



ISSN 1822-5721

2010/2

MEDICAL PHYSICS in the BALTIC STATES

PROCEEDINGS OF THE 8th INTERNATIONAL
CONFERENCE ON *MEDICAL PHYSICS*

14-16 October , 2010
Kaunas, Lithuania





ALTECHNA



LUND
UNIVERSITY



Research Council of Lithuania

ISSN 1822-5721

KAUNAS UNIVERSITY OF TECHNOLOGY

MEDICAL PHYSICS IN THE BALTIC STATES

**Proceedings of the 8th International Conference on Medical
Physics**

**Kaunas, Lithuania
14 – 16 October, 2010**

*This conference has been accredited by EFOMP as a CPD event for Medical
Physicists*

Executive editor **D.Adlienė**

CONFERENCE IS ORGANIZED BY:

Kaunas University of Technology
Malmö University Hospital, Lund University
Lithuanian Radiation Protection Centre
Kaunas Medical University Hospital

PROGRAM COMMITTEE

Diana ADLIENĖ – Kaunas University of Technology (Lithuania), *chairwoman*
Sören MATTSSON – Lund University, Malmö University Hospital (Sweden), *chairman*
Carmel J. CARUANA – University of Malta (Malta)
Yuri DEKHTYAR – Riga Technical University (Latvia)
Elona JUOZAITYTĖ – Medical University of Kaunas (Lithuania)
Kalle KEPLER – University of Tartu (Estonia)
Igor KADENKO – National Taras Shevchenko University of Kyiv (Ukraine)
Marius LAURIKAITIS – Kaunas Medical University Hospital branch Oncology Hospital (Lithuania)
Albinas MASTAUSKAS – Lithuanian Radiation Protection Centre (Lithuania)
Saulius RAILA – Kaunas University of Technology (Lithuania)
Ričardas ROTOMSKIS – Vilnius University (Lithuania)

ORGANIZING COMMITTEE

Lena ANCEVIČIENĖ – Kaunas University of Technology
Gediminas ADLYS – Kaunas University of Technology
Inga CIBULSKAITĖ – Kaunas Medical University
Reda ČERAPAITĖ – TRUŠINSKIENĖ – Kaunas Medical University
Karolis JAKŠTAS – Kaunas University of Technology
Jurgita LAURIKAITIENĖ – Kaunas Medical University Hospital branch Oncology Hospital
Rita PIKAITĖ – Kaunas University of Technology

CONFERENCE IS SUPPORTED BY:

Research Council of Lithuania
Kaunas University of Technology
Lund University
Malmö University Hospital
The European Federation of Organisations for Medical Physics
Lithuanian Radiation Protection Centre
Medical Physicists Society
Lithuanian Radiation Protection Society

Papers included in the Proceedings were referred by independent peer referees

© Kaunas University of Technology, 2010

CONFERENCE & WORKSHOP PROGRAM

Thursday, 14 October 2010

13.30-14.00 Registration of participants at
Kaunas Medical University Hospital branch Oncology Hospital
Volungiu str. 16, Kaunas

Session 1. Chair: Jurgita Laurikaitienė

- 14.00-14.15** Welcome to the Oncology Hospital: *Artūras Andrejaitis, Vice-Director; Dr. Marius Laurikaitis, Medical physicist*
- 14.15-14.45** *Tommy Knöös*. Lessons learned from accidents in radiation therapy: how to prevent them?
- 14.45-15.00** *A. Miller, L. Kasulaitytė*. IMRT for craniospinal irradiation: challenges and results
- 15.00-15.15** *E. Jakubovskij, R. Griškevičius, A. Miller*. IMRT commissioning: Baltic institutions planning and dosimetry comparisons
- 15.15-15.30** *Fredrik Nordström, Sacha AF Wettersted, Sven ÅJ Bäck*. Quality assurance methods in radiotherapy
- 15.30-15.45** *R. Vilkas, M. Laurikaitis, D. Adlienė, V. Andrijaitienė*. Implementation of the patient plan checking in radiotherapy

15.45-16.00 Coffee break

Session2. Chair: Dr. Marius Laurikaitis

QUALITY ASSURANCE SEMINAR

- 16.00-16.15** *Miglė Šniurevičiūtė*. Quality assurance in brachytherapy
- 16.15-16.30** *Romas Griškevičius*. Quality assurance of modern radiotherapy procedures
- 16.30-16.45** *Marius Laurikaitis*. Quality assurance of distance radiotherapy
- 16.45-17.00** *Tim Thurn (LAP GmbH Laser Applikationen)*. Virtual simulation and patient positioning in the field of radiotherapy
- 17.00-17.45** Visit to the Radiotherapy department
- 18.00-19.00** ANNUAL MEETING OF LITHUANIAN MEDICAL PHYSICISTS SOCIETY

Friday, 15 October 2010

- 9.00-9.30** Registration of participants at
**Kaunas University of Technology,
Studentų str. 50–325F, Kaunas**
- 9.15-9.30** Conference opening: *Vytautas Janilionis*, Dean of the Faculty of Fundamental Sciences; *prof. Sören Mattsson*, Lund University, Malmö University Hospital; *prof. Diana Adlienė*, Kaunas University of Technology

Session 3. Chair: prof. Diana Adlienė

- 9.30-10.00** *Sören Mattsson, Marcus Söderberg*. Patient dose management in CT, SPECT/CT and PET/CT imaging
- 10.00-10.15** *Anatoli Vladimirov, Kalle Kepler*. Analysis of AEC calibration methods for computed radiography by estimating TCDD at different tube potentials
- 10.15-10.30** *Lada Bumbure, Yuri Dekhtyar, Alexey Katashev, Tatyana Kirsanova, Ella Pacukevich, Lubova Shuvalova*. Digital QA method's calibration in digital radiography
- 10.30-10.45** *Hanna Holstein, Anders Tingberg, Marie-Louise Olsson*. Optimization of image quality and determination of effective dose to assisting persons in veterinary radiology
- 10.45-11.00** *Raju Srivastava, Sofie Gillis, Carlos de Wagter*. Radiographic film: still a viable dosimeter?

Coffee break 11:30-11:45

Session 4. Chair: prof. Carmel J. Caruana

- 11.00-11.15** *Jurga Valančiūnaitė, Ričardas Rotomskis*. Quantum dots as energy donors for photosensitizers: perspectives for photodynamic therapy of cancer
- 11.15-11.30** *Vytautas Kulvietis, Ričardas Rotomskis*. Accumulation of quantum dots in Ehrlich ascites tumours in mice
- 11.30-11.45** *Juras Kišonas, Vytautas Kulvietis*. Spectroscopic study of quantum dots distribution *in vivo*
- 11.45-12.00** *Artiom Skripka, Jurga Valančiūnaitė, Ričardas Rotomskis*. Spectral study of the formation of quantum dots and chlorin E6 complex in the presence of protein
- 12.00-12.15** *Vilius Poderys, Algirdas Selskis, Adelina Ilie, Ričardas Rotomskis*. Ring like TPPS₄ J-aggregate structure
- 12.15-12.30** *Matulionytė Marija, Vilius Poderys, Ričardas Rotomskis*. Influence of surface coating on CdTe quantum dots stability and interaction with bovine serum albumin
- 12.30-12.45** *Simona Petrošiūtė, Rasa Purvinienė, Vita Pašukonienė, Simona Lukoševičiūtė, Petras Juzėnas, Ričardas Rotomskis*. Characterization of cancer stem cells and their response to CdTe quantum dots
- 12.45-13.00** *Karolis Stašys, Vitalijus Karabanovas, Ričardas Rotomskis, Mindaugas Valius*. Surface modification of (CdSe)ZnS quantum dots using thiols – characterization, photo-physical and biological studies

Time for the lunch 13:00 – 14:00

Session 5. Chair: prof. Sören Mattsson

- 14.00-14.15 *Maksims Polakovs, Nina Mironova-Ulmane, Andrejs Pavlenko, Tija Zvagule, Natalija Kurjane, Natalija Gabrusheva.* The investigation of Chernobyl clean - up workers blood by EPR technique
- 14.15-14.30 *Alevtina Leice, Yuri Dekhtyar, Natalya Britzina.* Behaviour of blood cells being in contact with hydroxyapatite-coated titanium plate within an hour
- 14.30-14.45 *Andrej Rožkov, Ruslan Jerenkevič, Vadim Česonis.* Method of the radionuclide activity determination in nuclear medicine sources of complex geometries
- 14.45-15.00 *Dmitrijus Styra, Ana Usovaitė, Jelena Stankevič.* Data processing for connection between hard cosmic ray flux variations and human health disorder analyzing
- 15.00-15.15 *Rita Plukienė, Artūras Plukis, Laurynas Juodis, Vidmantas Remeikis.* The radiation safety of educational neutron laboratory
- 15.15-15.30 *Gediminas Adlys.* Physical aspects of neutron generation in medical accelerators

Coffee break 15:30-15:45

Session 6. Chair: prof. Tommy Knöös

- 15.45-16.30 *Carmel. J. Caruana.* European Commission Project ‘Guidelines on MPE’: proposed qualification and curriculum frameworks
- 16.30-16.45 *Vojtěch Mornstein, Daniel Vlk, Carmel. J. Caruana.* Teaching of medical physics to medical, dental, health care and biomedical engineering students in the Czech Republic
- 16.45-17.00 *Daniel Vlk, Vojtěch Mornstein, Carmel. J. Caruana.* Medical physics and biomedical engineering at the Faculty of Medicine, Masaryk University, Brno
- 17.00-17.15 *Sören Mattsson.* Education and training of medical physicists in Sweden
- 17.15-17.30 *Kalle Kepler.* Education and training of medical physicists in Estonia
- 17.30-17.45 *Lada Bumbure.* Education and training of medical physicists in Latvia
- 17.45-18.00 *Diana Adlienė.* Highlights from IAEA seminar & workshop “Synergy of nuclear sciences and medical physics: Education and training of medical physicists in the Baltic States”. Kaunas, 22-24 September 2010
- 18.00-18.15 *C.J. Caruana, M. Wasilewska-Radwanska, A. Aurengo, P.P. Dendy, V. Karenauskaitė, M.R. Malisan, J.H. Meijer, D. Mihov, V. Mornstein, E. Rokita, E. Vano, M. Weckstrom, M. Wucherer.* EFOMP project ‘Biomedical physics education for the medical/healthcare professions’ – an update for MEDPHYS2010
- 18.15-19.00 **Discussion:** The Proposed Qualification and Curriculum Frameworks of the European Commission Project “Guidelines on Medical Physics Expert” and Education and Training of Medical Physicists in the Baltic States

19:30-22:00 Get-together party
M. Valančiaus str. 9, Kaunas

Saturday, 16 October 2010

9.00-9.30 Registration of participants at
**Kaunas University of Technology,
Studentų str. 50-325F, Kaunas**

Session 7. Chair: Dr Kalle Kepler

- 9.30-9.45** *Joosep Kepler, Kalle Kepler, Tiiu Tomberg, Pilvi Ilves.* Uncertainty in functional magnetic resonance imaging methods for cortex motor and language area examinations
- 9.45-10.00** *Carl Siversson, Carl-Johan Tiderius, Leif Dahlberg, Jonas Svensson.* Early diagnosis of osteoarthritis using contrast enhanced 3-dimensional MRI
- 10.00-10.15** *Therese Geber, Mikael Gunnarsson, Sören Mattsson.* Dosimetry for the lens of the eye, applications for medical staff involved in interventional radiology procedures
- 10.15-10.30** *Aušra Urbonienė, Birutė Gricienė.* Extremity and eye lens doses of the interventional radiology and cardiology workers
- 10.30-10.45** *Agnė Usaite, Julius Žiliukas, Leonidas Krynke, Jonas Marcinkevičius.* Survey of pediatrics patient exposure in radiography examinations
- 10.45-11.00** *Rita Pikaitė, Jurgita Laurikaitienė, Diana Adlienė.* Patients' dose assessment in digital diagnostic radiography
- 11.00-11.15** *S. Luchkovsky, I. Kadenko. Yu. Spizhenko.* The assessment of absorbed dose value for calculations of irradiation plan for patients lungs cancer tumours with application of CyberKnife system

Coffee break 11:15-11.30

Session 8. Chair: prof. Nina Mironova-Ulmane

- 11.30-11.45** *Karolis Jakštas, Miglė Šniurevičiūtė.* Dosimetric comparison between linked and strand seeds for I-125 permanent seed prostate brachytherapy
- 11.45-12.00** *Nikolajus Medvedevas, Diana Adlienė, Jurgita Laurikaitienė.* Distribution of scattered radiation in superficial X-ray therapy
- 12.00-12.15** *Vaida Pupkaitė, Jurgita Laurikaitienė, Diana Adlienė.* Optimization of 3D and 2D treatment planning for palliative patients with lumbar spine metastasis.
- 12.15-12.30** *Virgilijus Minialga, Rolandas Paulauskas.* Heat dissipation investigation by thermovision
- 12.30-12.45** *Algimantas Meškauskas, Gediminas Adlys, Simona Mačiulaitienė.* Radiation impact on polymer structures
- 12.45-13.00** Final remarks (*prof. Sören Mattsson*)

IMRT FOR CRANIOSPINAL IRRADIATION: CHALLENGES AND RESULTS

A. Miller, L. Kasulaitytė
Institute of Oncology, Vilnius University

Abstract: To develop, investigate and implement IMRT method for Craniospinal irradiation (CSI) into the clinical environment. The study was performed for patients required either CSI or only extracranial (spinal) irradiation. IMRT plans with multiple isocenters without couch rotation and with overlap of field edges as well as standard technique 3D CRT plan were generated for each patient. The planning dose distributions for both methods and effect of patient set up uncertainties were investigated. As expected the IMRT treatment plans provided much better dose coverage and homogeneity in the target volume. Treatment verification proved, that interfractional movement of the field isocenters relative to the patient anatomy was within 3 mm limits in all cases. The IMRT plans provide much better dose distribution stability for these movements in comparison with 3DCRT plans. Dose bath in the dose range over 10 Gy within the “cancerous” distance from the fields’ edges was significantly lower for all IMRT plans created. The developed IMRT method for CSI and spinal irradiation provides superior dose coverage throughout the target volume, simplifies the technical performance, is less dependent on intrafractional movements of the patient and potentially reduce the risk of deterministic secondary cancer incidence. This method is recommended for use in the clinic for all CSI patients.

Key words: IMRT, CSI, setup verification

1. Introduction

Craniospinal irradiation is very important part in the treatment of patients with primitive neuroectodermal tumors such as medulloblastoma. Craniospinal irradiation (CSI) is technically very challenging because of the difficult geometry of the treatment fields, high radiosensitivity of the spinal cord and other critical structures around. The mechanical properties of standard linacs make possible treatment only with treatment field junctions and several isocenters. Thus causing potential problems – under/over dosage of the spinal cord in the areas of field junction and over dosage of adjacent structures. The most commonly used technique to reduce this potential problem is manual shift of the fields between fractions.

Intensity modulated radiotherapy technique (IMRT) has the advantage of modulating photon beam fluence in each treatment field and achieve more homogenous dose distribution in the target volume. This technique can be used in craniospinal and extra-cranial tumor treatment due to better dose coverage, more homogenous dose distribution and fewer doses to adjacent normal tissues [1].

The aim of this study was to develop IMRT technique for CS irradiation, to measure patient set-up errors during treatment and to compare possible affection of these uncertainties to the dose statistics of 3D CRT and IMRT treatment plans.

2. Methods and materials

Hereafter two representative cases are demonstrated: two young patients (age 35-31 years) with medulloblastomas were treated between 2009-2010. One patient had craniospinal treatment administered, and the second only extracranial (spinal) treatment. The patients were imaged with CT scanner in the prone position with the standard head and fit fixation and treatment plans were generated with treatment planning system. A dose of 32,4 Gy was prescribed to the PTV with 18 fractions. The PTV was created by adding 1,0 cm margin to CTV in all directions. Outlined organs at risk (OAR) included eyes, lenses and kidneys.

There were three plans generated for each patient - two 3D CRT and one IMRT treatment plans. Two 3DCRT plans had differences in field junction. First plan had field junction with 3 mm gaps in cranial-spinal area and spinal-spinal area. It was set on even days. Second treatment plan had no gaps (exact match) in cranial-

spinal and spinal-spinal junction areas, and it was set on odd days. Therefore, this technique was intended to reduce the effect of patient set-up errors and smear out the dose distribution and avoid cold or hot spots in field junction area [2,4].

Both created treatment plans – 3D CRT and IMRT, had comparable dose statistics.

3D CRT treatment plan consisted of 2 opposing cranial fields for craniospinal case and three spinal fields – one upper and two lower fields [3]. All spinal treatment fields had couch rotation to 90 degrees. Extracranial treatment plan consisted of three spinal treatment fields.

IMRT treatment plan consisted of 2 cranial fields and 6 spinal fields. No spinal field had couch rotation [4].

Both treatment plans had additional perpendicular setup fields for everyday set-up verification. Field arrangement for 3D CRT and IMRT plans is given in Fig. 1.

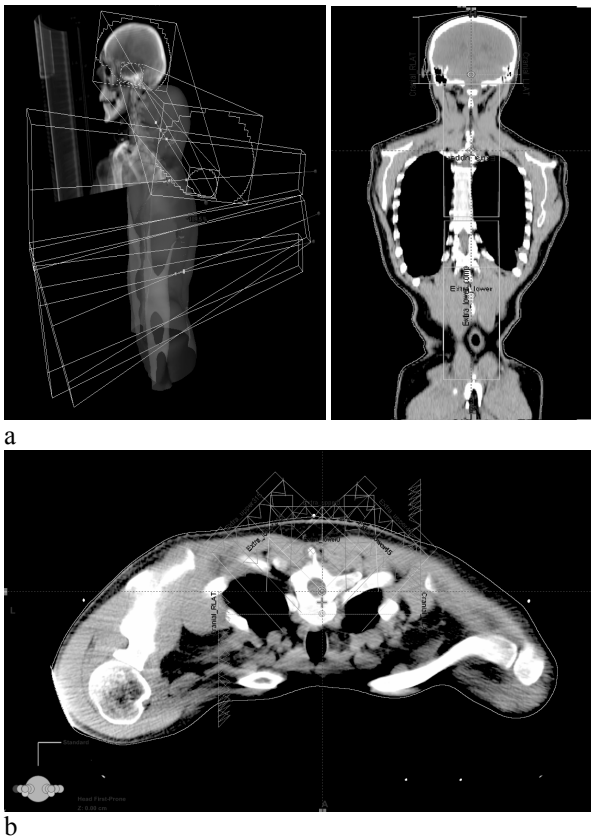


Fig.1. Field arrangement of 3D CRT (a) and IMRT (b) plans.

The IMRT plans were normalized so that 95 percent isodose was covering 100 percent of target volume. For dose optimization objectives, the minimum dose to PTV was set to be greater than 98 %, and the maximum dose less than 106 %. Additional optimization constrains were set for given OAR's. Optimized dose was calculated using AAA algorithm. The actual treatment of the patients was carried out with IMRT technique.

Patient related IMRT QA was performed before treatment. Verification plan created within the treatment planning system with portal dose prediction algorithm was verified on linac portal imaging system. During the treatment on-line verification was performed before every session, and subsequently required adjustment of the patient position was made before plan delivery.

Analysis of set-up errors was performed with estimation of the effect of these errors on the dose distribution

3. Results and discussion

Both patients completed treatment successfully. The IMRT and 3D CRT treatment plans comparison reveals the apparent advantage of IMRT plan in terms of dose distribution homogeneity in the target volume [5]. The resulting dose distributions for both treatment methods are given in Fig.2.

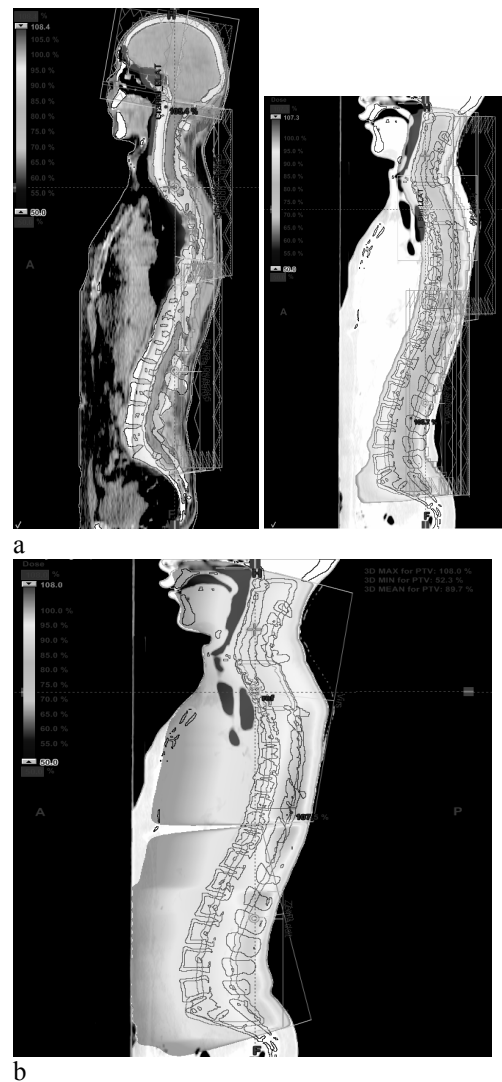


Fig.2. CSI and extracranial (spinal) IMRT (a) treatment cases and extracranial 3D CRT treatment plan.

Better dose homogeneity is achieved within entire treatment volume and spinal cord and in field junction areas. Also, it is evident that, adjacent normal tissues and OAR's receive fewer doses [6].

It has been proven in many published dosimetry studies that IMRT method, rightfully applied, provide noticeably better dose distribution for targets and critical organs for many different sites under consideration [7]. Therefore, there is no clinically important point to demonstrate this, ones again for this localization.

More important in our view is to demonstrate the IMRT plan stability and robustness to every day variation in patient position.

Therefore, the data of on-line patient setup errors was analyzed. The example of on-line setup verification is presented in Fig.3.

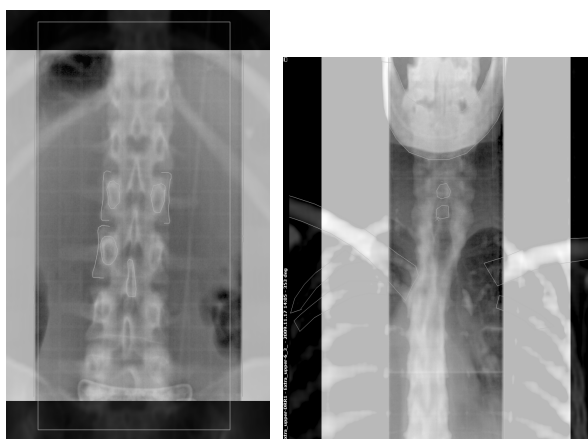


Fig.3. On-line setup view with PI.

Maximum setup error was found to be in our case 3mm in LNG and VRT directions. Influence of these maximum shifts on the plans dose distribution was evaluated. Resulting change in the maximum and mean doses are given in Table 1.

Table 1. Changes in dose statistics for IMRT plan.

	Max dose	Mean dose
Original plan	108%	96 %
Cranial isocenter		
3 mm lateral shift	111,3%	99%
3mm vertical shift	120%	94,6%
Upper spinal isocenter		
3 mm lateral shift	109,7%	94%
3 mm vertical shift	108,4%	94,6%
Lower spinal isocenter		
3 mm lateral shift	109,5%	93%
3 mm vertical shift	107,5%	94,3%

Simulated change in isocenter position for 3D CRT plans in order of 3mm magnitude gives rise of up to 147% maximum dose in the junction area.

Additionally, 3D CRT plans might have more than 3 mm isocenter move as soon as field setup involves table rotation to 90-degree angle. One can also see from this data that IMRT plans are sufficiently stable in rage of random isocenter position shift except, probably vertical shift of the cranial isocenter, were somewhat lager increase in maximum dose was observed.

The last point that we considered separately in this study was the whole body dose for these two techniques. This issue is of paramount importance in case of medulloblastoma treatments, because of young patient age and relatively good prognosis. The dose to the normal surrounding tissues depends strongly on the number of field involved and because of the interleaf leakage, partially on the number of monitor units for the particular plan. It is possible to produce sufficiently good IMRT plan with number of fields that do not differ much from the number of fields in 3D CRT plans. Therefore, dose to the surrounding tissue is in all cases much better than for the 3D CRT plans. Representative curves are shown in Fig. 4

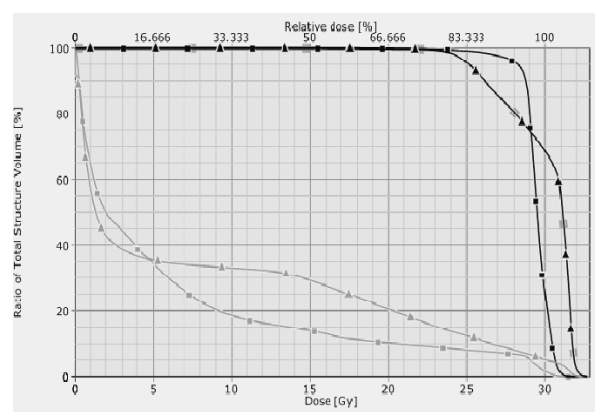


Fig. 4. Dose volume histograms of Body and PTV for IMRT treatment plan.

Thought, the body dose from 1 to approximately 5 Gy is slightly lower for 3D CRT plan, the difference is small and the risk of secondary cancer incidence in this dose range is still unclear. The difference in body dose up from this point, however, is around two fold in favor of IMRT plan. The risk of secondary cancer development in this dose range (up to 4 cm from the field edges) is well known and depends strongly on the dose-volume parameter [8].

4. Conclusions

The target volume of medulloblastoma is usually very complex. Due to target long shape and different distance from skin surface it is possible to achieve homogenous dose distribution in the target only using IMRT treatment technique. IMRT technique also enables to ensure good treatment accuracy as this

technique seems to be less sensitive to patient set-up uncertainties and there is no need for couch rotation during the treatment.

Surrounding normal tissues receive much smaller doses in the IMRT treatment plan rather than 3D CRT. It is especially important, because of radiotherapy toxicity, the young age of the patients and involved risk of secondary cancer development.

5. References

1. Seppälä J., Kulmala J., Lindholm P., Minn H., A method to improve target dose homogeneity of craniospinal irradiation using dynamic split field IMRT. *Radiotherapy and Oncology* 2010, 96:209-15
2. Michalski J. M., Klein E., Gerber R., Method to plan, administer, and verify supine craniospinal irradiation. *J Appl Clin Med Phys* 2002, 3:310-6
3. Parker W.A., Freeman C. R., A simple Technique for craniospinal radiotherapy in supine position. *Radiotherapy and Oncology* 2006, 78:217-22
4. Yom S., Frija E. K., Mahajan A., et al. Field-in-field technique with intrafractionally modulated junction shifts for craniospinal irradiation. *Int J Radiat Oncol Biol Phys* 2007, 69:1193-8
5. South M., Chiu J.K, The B.S., et al. Supine craniospinal irradiation using intrafractional junction shifts and field-in-field dose shaping: early experience at Methodist Hospital. *Int J Radiat Oncol Biol Phys* 2008, 71:477-83
6. Wilkinson J.M, Lewis J., Lawrence G.P, et al. Craniospinal irradiation using a forward segmented field technique. *Br J Radiol* 2007, 80:209-15
7. Sharma D.S., Gupta t., Jalali R., et al. High-precision radiotherapy for craniospinal irradiation: evaluation of three-dimensional conformal radiotherapy, intensity-modulated radiathiontherapy and helical TomoTherapy. *Br J Radiol* 2009 Jul 6
8. Parker W., Fillion E., Roberge D., et al. Intensity-modulated radiotherapy for craniospinal irradiation: target volume considerations, dose constraints and competing risks. . *Int J Radiat Oncol Biol Phys* 2007, 69:251-7
9. Hall E.J., Intensity-modulated radiation therapy, protons, and the risk of second cancers. . *Int J Radiat Oncol Biol Phys* 2006, 6:1-7

IMRT COMMISSIONING: BALTIC INSTITUTIONS PLANNING AND DOSIMETRY COMPARISONS

E. Jakubovskij, R. Griskevicius, A. Miller
Vilnius University Institute of Oncology, Santariskiu st. 1, 08660 Vilnius, Lithuania

Abstract: The purpose of this study was to investigate applicability of the new AAPM TG119 protocol for IMRT commissioning and use it for verification of IMRT planning and delivery accuracy in Vilnius University Institute of Oncology. The results were also compared with main hospitals in Baltic States. Results from Vilnius University Institute of Oncology and main hospitals from Baltic states shows agreement with trend lines from new AAPM TG119 protocol in chamber and Field by field measurements. Verification data of composite plan showed deviation from AAPM TG119 protocol. To conclude AAPM TG119 protocol is good tool to verify IMRT planning and delivery accuracy.

Keywords: IMRT, film verification, commissioning, measured dose.

1. Introduction

Intensity Modulated Radiation Therapy (IMRT) has become over the last ten years a standard radiotherapy treatment in many hospitals. However, more complex treatment technique could be associated with larger uncertainties in dose delivery. In 2008, the Radiological Physics Center reported that of the 250 irradiations of a head and neck phantom as part of an IMRT credentialing process, 71 (28%) had failed to meet accuracy criteria of 7% for dose in a low gradient region and/or 4 mm distance to agreement in a high gradient [1]. The purpose of this study was to investigate applicability of the new AAPM TG119 protocol for IMRT commissioning and use it for verification of IMRT planning and delivery accuracy in Vilnius University Institute of Oncology. This protocol includes tests of different complexity and helps evaluate the overall accuracy of the IMRT system. The results were also compared with main hospitals in Baltic States.

2. Materials and Methods

AAPM TG119 test package was used to verify the accuracy of IMRT implementation. The images of slab phantom with drawn structures in DICOM-RT format were uploaded to local treatment planning system and 5 different clinical test cases were planned according to description provided in the protocol. The planar dose distributions were assessed using gamma criteria of 3%/3 mm. The test cases included:

1) Three cylinders to be irradiated with different dose levels (multitarget) (Fig.1). Three cylindrical targets are stacked along the axis of rotation. Each has a diameter of approximately 4 cm and length of 4 cm [2];

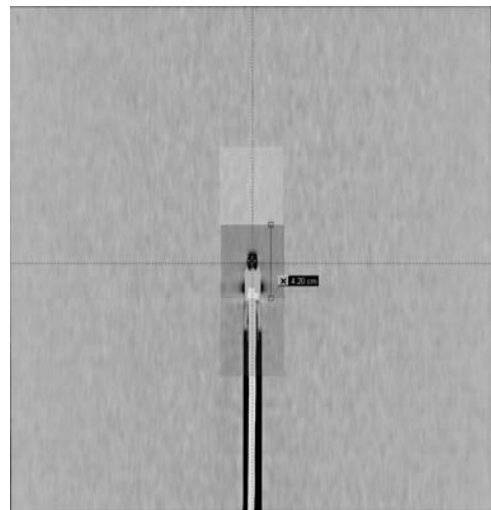


Fig. 1 Three cylindrical targets, multitarget case.

2) Prostate test case (Fig.2). The prostate CTV is roughly ellipsoidal with RL, AP, and SI dimensions of 4.0, 2.6, and 6.5 cm, respectively. The prostate PTV is expanded 0.6 cm around the CTV. The rectum is a cylinder with diameter 1.5 cm that abuts the indented posterior aspect of the prostate [2].

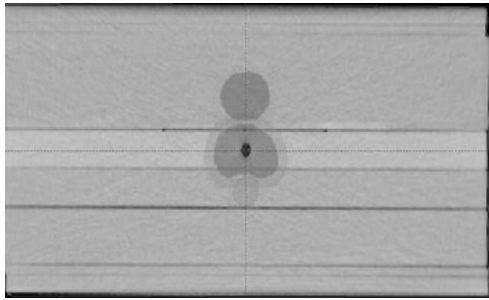


Fig. 2 Prostate test case.

3) Typical head and neck test case (Fig.3). The HN PTV includes all anterior volume from the base of the skull to the upper neck, including the posterior neck nodes. The PTV is retracted from the skin by 0.6 cm. There is a gap of about 1.5 cm between the cord and the PTV [2];

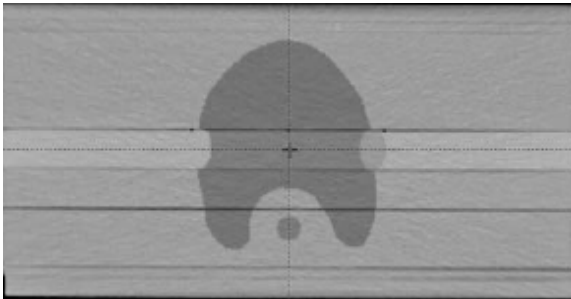


Fig. 3 Head and neck case.

4) C-shaped target with OAR (Fig.4). The target is a C-shape that surrounds a central avoidance structure. The center core is a cylinder 1 cm in radius. The gap between the core and the PTV is 0.5 cm, so the inner arc of the PTV is 1.5 cm in radius. The outer arc of the PTV is 3.7 cm in radius. The PTV is 8 cm long and the core is 10 cm long [2];

5) C-shaped target with OAR (hard constraints) (Fig.4). The agreement between calculated and measured doses for each test case was determined using small volume ion chamber (0.125 cm³), film dosimetry for composite plan and for each field perpendicular to central axis using EPID or 2D array [2].

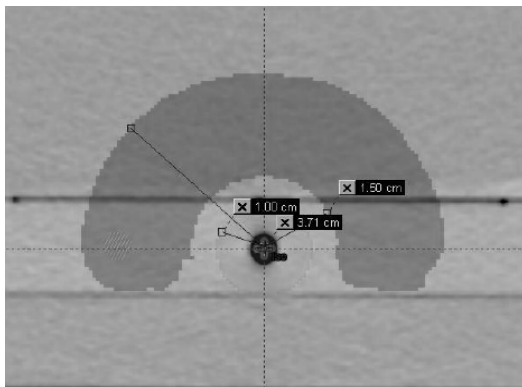


Fig. 4 C-shape case.

IMRT test cases were optimized using Eclipse v.8.1 software package. The water-equivalent plastic phantom slabs with a total thickness of 20 cm were used for chamber and film measurements. Reference dose measurements were performed with a Farmer type 0.125 cm³ ionization chamber. Measurements were performed as described in test package in high and low dose region. Field by field verifications was performed using Varian Electronic Portal Imaging Device aS1000. Portal dose calculation on the EPID was made with Eclipse Portal Dose Prediction algorithm. Dose evaluation of Field by field measurements was done within Eclipse v. 8.1 gamma evaluation module. Composite plan measurements were carried out using radiographic Kodak X-Omat V films. The film was positioned in the middle plane of phantom and posterior or anterior depending on the case requirements. Films were developed with Kodak -35 developing machine and scanned with Vidar 16 scanner. For films gamma pass evaluation Dose Lab v 4.11 software package was used.

3. Results and discussion

As result of IMRT optimization process the requirements for dose distribution were met in all of the package test cases except most difficult case of the C-shape (hard) target. Here we failed to satisfy the required constrains. Communication with other hospitals from Baltic countries reveals the same experience in all institutions. The measurements were repeated several times to reduce the measurements uncertainty. The differences between planned and measured doses are within the range of [-0.005, 0.051] for point dose measurements. The test result are tabulated in the Table 1

Table1. High dose point and low dose point in the PTV measured with ion chamber: [(measured dose-plan dose)/prescription dose].

Test (High dose region)	Location	[(measured dose-planned dose)]/ prescribed dose
Multitarget	Izocenter	0.0425
Prostate	Izocenter	0.051
Head/Neck	Izocenter	0.01765
C-shape(easy)	2.5cm anterior	0.04
C-shape(hard)	2.5cm anterior	0.0364
Test (Low dose region)	Location	[(measured dose-planned dose)]/ prescribed dose
Multitarget	4cm inferior	0.0022
Prostate	2.5cm posterior	-0.005
Head/Neck	4.0cm posterior	-0.0215
C-shape(easy)	Izocenter	0.0255
C-shape(hard)	Izocenter	0.0005

The range of mean gamma values using 3%, 3mm criteria for all test cases is [99.18, 99.99] for field by field planar measurements. For other hospitals the range of mean gamma values was [94.3-99.8] [3]. The results of field by field measurements demonstrate reliability and accuracy of used verification technique. For composite plans the range of mean gamma values is [80.6-94.1]. For Baltic countries the range of mean gamma values is [88-95.5] [3]. Results of composite plans measurements show a nonlinear sensitivity of film caused by dependence on accumulated dose, inaccuracy of development process, and expression of scanning device. This technique is not the best option on purpose to perform IMRT plan verification before patient treatment. The same measurements performed in other hospitals for several composite test cases have given slightly worse result than the protocol baseline values. The short summary of these results in all three countries is listed in Table 2.

Table 2. Comparison of results from Lithuania and Baltic countries.

Country	Lithuania	Baltic countries
<i>Chamber</i>	-0.5, 5.1	-1.9-5.1
<i>Filed by field</i>	99.18-99.99	94.3-99.8
<i>Film</i>	80.6-94.1	88-95.5

4. Conclusion

AAPM TG119 test package is a useful tool to verify and improve IMRT delivery. This report provides uniform baseline for IMRT commissioning. The results from VUOI and other Baltic States major hospitals shows reasonable agreement between calculated and measured doses, but have also indicated that there is a room for improvements in our institution for planar composite IMRT plan verification.

5. References

1. G. S. Ibbott, D. S. Followill, H. A. Molineu, J. R. Lowenstein, P. E. Alvarez, and J. E. Roll, "Challenges in credentialing institutions and participants in advanced technology multi-institutional clinical trials," *Int. J. Radiat. Oncol., Biol., Phys.* 71, S71–S75 (2008);
2. G. A. Ezzell, J. W. Burmeister, N. Dogan, T. J. LoSasso and J. G. Mechalakos, D. Mihailidis, A. Molineu, J. R. Palta, Ch. R. Ramsey, B. J. Salter, J. Shi, P. Xia, N. J. Yue, Y. Xiao, "IMRT commissioning: Multiple institution planning and dosimetry comparisons, a report from AAPM Task Group 119", *Med. Phys.*, Vol. 36, No. 11, November (2009)
3. E. Gershkevitch, S. Popovs, A. Meijers, A. Miller, R. Griskevicius "IMRT VERIFICATION IN BALTIC STATES", *Radiotherapy and Oncology*, Vol 96, Supp 1, S459, September 2010

QUALITY ASSURANCE METHODS IN RADIOTHERAPY

Fredrik NORDSTRÖM*, Sacha AF WETTERSTEDT**, Sven ÅJ BÄCK***

*Medical Radiation Physics, Institution of Clinical Sciences, Malmö, Skåne University Hospital, Sweden

** Radiation Physics, Skåne University Hospital, Malmö, Sweden

Abstract: The rapid development and implementation of new technology over the last decades has greatly increased the complexity of the radiotherapy process and potentially made it more error-prone. Independent checking has been identified as an intervention that could reduce the risk of errors. This paper discusses four quality control methods which all fall into the concept of independent checking.

Keywords: Quality assurance (QA), quality control (QC), patient safety, independent checking, monitor unit (MU) verification, data integrity, gel dosimetry.

1. Introduction

Preparation and delivery of radiotherapy is a complex procedure (figure 1), involving many different technologies and groups of professionals. The rapid development and implementation of new technology (eg. three-dimensional computed tomography based treatment planning, multi-leaf collimator / MLC, intensity modulated radiotherapy / IMRT) over the last decades have greatly increased the complexity of the radiotherapy process and potentially made it more error-prone.

A high level of accuracy in all steps of the process is required in order to deliver treatments resulting in a high tumour control probability (TCP) and minimal risk to normal tissue. Based on TCP data, ICRU has stated in its Report No. 24 that the overall uncertainty in the delivery of absorbed dose to a target volume should be within 5% [1]. The confidence level which this value represented was not explicitly stated. Goitein have suggested 5% dose accuracy at the 1.5 s.d. level which is in agreement with Mijnheer et al. which stated 3.5% at the 1 s.d level [2, 3].

In order to reduce uncertainties and errors in the steps of radiotherapy treatment preparation and delivery, a comprehensive quality assurance program is needed. Quality assurance in radiotherapy is according to the World Health Organization (WHO) all procedures that ensure consistency of the medical prescription, and safe fulfillment of that prescription, as regards to the dose to the target volume, together with minimal dose to normal tissue, minimal exposure of personnel and adequate patient monitoring aimed at determining the end result of the treatment [4].

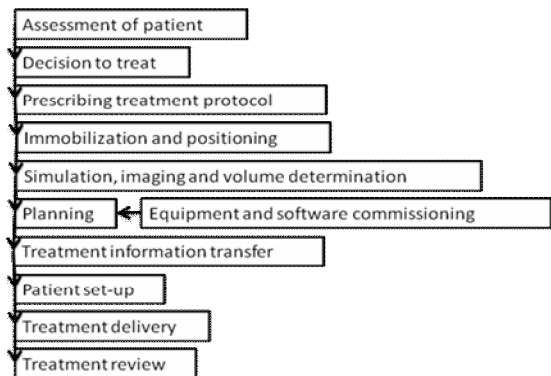


Fig. 1. The radiotherapy process of care as defined by WHO.

In a recent study initiated and founded by the WHO, three high impact risk reduction interventions were identified: planning protocol checklists, competency certification and independent checking [5, 6]. Planning protocol checklists is relevant in all preparation steps of the radiotherapy process. They are low resource demanding and easy to develop and implement. Competency certification requires more resources but will have an impact on the quality in all steps of the process.

The focus of this paper is on the third intervention, independent checking. This intervention is resource intensive but it is also a minimum standard in radiotherapy delivery in order to avoid errors from involuntary automaticity [7]. The simplest form of independent checking is to have two persons performing the same procedure separately. This could for instance be two radiotherapy technicians (RTT) verifying the setup of the patient on the treatment

couch independently of each other. A higher level of independent checking could be accomplished by utilizing two different methods. In the above example, the positioning of the patient could be performed using external positioning lasers and also positioning verification by planar x-ray imaging.

2. Independent dose calculation

In the process of patient specific quality assurance of radiotherapy plans, monitor unit (MU) verification is considered to be a central part [8, 9]. The monitor units are directly proportional to the absorbed dose in the patient for linac based deliveries, in a similar manner as the treatment time for cobalt treatments. The calculation method used for verification of the number of MU:s required to delivered the prescribed dose to the patient should be independent from that of the primary treatment planning system (TPS). Independent refers both to the data utilized to characterize the treatment unit, the implementation of the calculation algorithms, as well as the derivation of geometrical data (source-to-surface distance, depth and radiological path length) from the patient anatomy. Several calculation methods have been proposed for the purpose of MU verification [10-13]. Clinical implementation of MU verification software usually includes only a single tolerance level for dose or MUs, rather than complete tools for evaluation of calculation results. Control charts is a tool within statistical process control (SPC) which can be used to distinguish between common cause variations (data points inside control chart limits) and special cause variations (data points outside control chart limits). Control charts have been proven useful for analysis of results from independent dose calculations as well as for results from quality control of linac parameters (output, flatness, etc.) [14-16].

3. Data integrity

Software and computer systems from more than one vendor are often used in the preparation and delivery of the treatment. To allow different medical systems to communicate with each other a global information-technology standard, Digital Imaging and Communications in Medicine (DICOM) has been developed. In 1997, the standard was extended to cover radiotherapy information objects. Today DICOM-RT has been widely accepted and has a major role in the communication between different RT systems. Undoubtedly the absence of manual transfer ensures a higher level of data integrity. However, manual input might be difficult to avoid at some steps of the treatment chain, which inevitably leads to an increased risk. Comparisons between the data in different systems have previously been made manually by one or two professionals. Modern computer systems often relies on checksums, which are fixed-sized signatures calculated from a block of digital data. By comparing

checksums before and after transmission or storage, communication errors may be detected.

However, this method is not applicable for verification of the interpretation of data in systems from different vendors. For this purpose, independent tools that compare DICOM-RT data objects or database entries between different systems could be employed [17].

4. In-vivo dosimetry

In-vivo dosimetry acts as a final check of the treatment data and patient geometry. In vivo dose measurements can be divided into entrance dose measurements, exit dose measurements and intracavitary dose measurements. Through entrance dose measurements, the output and performance of the treatment unit as well as the accuracy of patient set-up can be examined. An exit dose measurement also checks the dose calculation, including volumetric information and heterogeneity corrections. Further, in-vivo dosimetry can not only provide information on the absorbed dose to the target, but also dose information for risk organs, such as the lens of the eye. Thermoluminescence dosimeters (TLD) and semiconductor detectors (silicon diodes) are the types of dosimeters that are most commonly employed for in-vivo dosimetry purposes.

The entrance dose is usually defined at the depth of dose maximum below the surface. In-vivo dosimetry detectors should be covered with a buildup cap appropriate to the photon beam energy. The drawback of this build-up cap is that it introduces an underdosage, up to 5%, in the shadow region beneath the detector [18]. Therefore, it is not recommended to use in-vivo dosimetry with this type of detector placed in front of the target during the whole treatment delivery, but instead only for a part of the treatment or the detector can be moved between treatment fractions.

5. Dosimetric verification of the whole process

When introducing new technologies and methods, the need for verification of the whole treatment process is imminent. The new advanced technologies such as intensity-modulated radiotherapy (IMRT) and volumetric arc therapy (VMAT), where the beam intensity is varied over the plane perpendicular to the central axis demands a full 3D dosimetric verification information. One detector system that could provide this information is gel dosimeters. Polymer gel dosimetry can be used to measure absorbed dose distributions in a complete volume with high spatial resolution [19, 20]. The use of gel dosimetry has also been found feasible for verification of dynamic delivery [21, 22]. For verification purposes, the patient could be substituted with the gel phantom, which can be manufactured in any shape. The phantom is passed through the radiotherapy treatment process and the dosimetric information is afterwards read-out using magnetic resonance imaging or optical computed tomography in 3D. The measured dose can be compared with the TPS calculated dose distribution,

verifying both the dosimetric and geometric delivery of the treatment.

6. Evaluating the effectiveness of the QC

In order to evaluate the effectiveness of the QC procedures, the use of simulated errors could be employed [23]. Note that this method should never be used in combination with real patients and treatments, where it would increase the risk for error tremendously. The method is useful in combination with phantom measurements, especially for determination of tolerance levels. Pre-treatment verification of IMRT using 2D detector arrays of either diodes or ionization chambers has become a standard verification method. A central part of this verification method is to adopt clinically relevant tolerances. If known errors are introduced into the treatment plan and then delivered to the detector, one can directly determine at which level these errors are detectable. Further, due to the fact that the errors are known, the TPS could be used to compare the erroneous plan with the correct plan and the clinical relevance of the error can be determined.

7. References

- International Commission on Radiation Units and Measurements (ICRU). Determination of absorbed dose in a patient irradiated by beams of X or gamma rays in radiotherapy procedures. ICRU Report no. 24. Bethesda, MD: ICRU; 1976.
- Goitein M. Nonstandard deviations. *Med Phys* 1983;10:709-711.
- Mijnheer B.J., Battermann J.J., Wambersie A.. What degree of accuracy is required and can be achieved in photon and neutron therapy? *Radiother Oncol* 1987;8(3):237-252.
- World Health Organization (WHO). Quality Assurance in Radiotherapy. Geneva: WHO, 1988.
- World Health Organization (WHO). Radiotherapy Risk Profile – Technical Manual. Geneva: WHO, 2008.
- Shafiq J., Barton M., Noble D., Lemer C., Donaldson L.J.. An international review of patient safety measures in radiotherapy practise. *Radiother. Oncol.* 2009;92:15-21.
- Toft B., Mascie-Taylor H. Involuntary automaticity: a work-system induced risk to safe health care. *Health Services Management Research*, 18: 211–216.
- Nyholm, T.. Verification of dose calculations in radiotherapy. Ph.D. thesis; Umeå University; 2008. URL <http://umu.diva-portal.org/>.
- Sellakumar P., Arun C., Sanjay, S.S., Ramesh S.B.. Comparison of monitor units calculated by radiotherapy treatment planning system and an independent monitor unit verification software. *Phys. Med.* 2010.
- Kung J.H., Chen, G.T., Kuchnir F.K.. A monitor unit verification calculation in intensity modulated radiotherapy as a dosimetry quality assurance. *Med. Phys* 2000;27(10):2226-2230.
- Dutreix A., Bjärngård B.E., Bridier A., Mijnheer B., Shaw J.E., Svensson H. Monitor unit calculation for high energy photon beams, *Physics for clinical radiotherapy – ESTRO booklet No.3.* European Society for Therapeutic Radiology and Oncology (Brussels); 1997.
- Nyholm T., Olofsson J., Ahnesjö A., Karlsson M.. Photon pencil kernel parameterization based on beam quality index. *Radiother Oncol* 2007;78(3):347-351.
- Pisaturo O., Moeckli R., Mirimanoff R.O., Bochud F.O.. A monte carlo-based procedure for independent monitor unit calculation in IMRT treatment plans. *Phys. Med. Biol.* 2009;54(13):42999-4310.
- Nordström F., af Wetterstedt S., Johnsson S., Ceberg C., Bäck S. Control chart analysis of data from a national monitor unit verification study. *Radiother. Oncol.* 2010;96(suppl. 1):152-153.
- Pawlicki T., Yoo S., Court L.E., McMillan S.K., Rice R.K., Russell J.D., et al. Moving from IMRT QA measurements toward independent computer calculations using control charts. *Radiother. Oncol.* 2008;89(3):330-337.
- Pawlicki T., Whitaker M., Boyer A.L.. Statistical process control for radiotherapy quality assurance. *Med. Phys.* 2005;32(9):2777-2786.
- Nordström F., Gustavsson H., Ceberg C., Wittgren L., Björk P., Johansson S., Bäck S. Development and evaluation of a method to verify the integrity of treatment data throughout the radiotherapy process. *Radiother. Oncol.* 2008;88(suppl. 2):491-492.
- Podgorsak E.B., et al.; sponsored by IAEA. Radiation oncology physics: a handbook for teachers and students. Vienna: International Atomic Energy Agency; 2005.
- Vergote K., De Deene Y., Duthoy W., De Neve W., Achten E., De Wagter C.. Validation application of polymer gel dosimetry for the dose verification of an intensity-modulated arc therapy (IMAT) treatment. *Phys. Med. Biol.* 2004;49:287-305.
- Isbakan F., Ülgen Y., Bilge H., Ozen Z., Agus O., Buyuksarac B.. Gamma Knife 3-D dose distribution near the area of tissue inhomogeneities by normoxic gel dosimetry. *Med. Phys.* 2007;34:1623-30.
- Gustavsson H., Karlsson A., Bäck S.Å.J., Olsson L.E.. MAGIC-type polymer gel for three-dimensional dosimetry: Intensity-modulated radiation therapy verification. *Med. Phys.* 2003;30:1264-70.
- Ceberg S., Karlsson A., Gustavsson H., Wittgren L., Bäck S.Å.J.. Verification of dynamic radiotherapy: the potential for 3D dosimetry under respiratory-like motion using polymer gel. *Phys. Med. Biol.* 2008;53:387-96.

23. Bengtsson-Scherman J. Development and evaluation of methods for comparison of dose distributions in radiotherapy using calculated, synthetic and simulated measured dose distributions. M.Sc. thesis; Lund University; 2009. URL <http://www.radfys.lu.se/>.

PATIENT DOSE MANAGEMENT IN CT, SPECT/CT AND PET/CT IMAGING

Sören MATTSSON and Marcus SÖDERBERG

Medical Radiation Physics Malmö, Lund University, Skåne University Hospital Malmö, SE-205 02 Malmö, Sweden

Abstract: New imaging technologies that use x-rays or radiopharmaceuticals are continuously developed. The techniques are now also often combined into a single investigation, such as PET/CT and SPECT/CT – so called “hybrid imaging”. The benefits of the new techniques are so dramatic that there is a tendency to overuse them. The increasing radiation exposure from CT has been of concern for some years and is now given increased attention by health professionals, authorities, manufacturers and patient groups. The relatively high doses from PET and SPECT investigations have only recently been discussed. The aim is to inform about developing technologies and clinical techniques for 3D imaging using ionizing radiation, and their associated radiation dose to patients and staff. The presentation includes a discussion on tools for improved dose management. Patient dose is a critical parameter for justification and optimization and there is a need to improve collection of patient (and staff) dose data.

Persons educated and trained in medical physics and radiation protection have to be fully involved in planning, absorbed dose estimations and optimisation of the diagnostic procedures and have to initiate radiation safety training for the medical staff. Guidelines need to be developed so that referring physicians carefully weigh the benefits against the potential risks and base their decisions on medically relevant data.

Keywords: CT, SPECT, PET, hybrid imaging, radiation dose, optimisation.

1. Introduction

There is a tremendous and undeniable benefit of medical imaging. During the last few years there have been a dramatic development and this development continues. Since its introduction in the 1970s and 1980s respectively, CT and MR has become two important tools in medical imaging to supplement planar X-ray-nuclear medicine and ultrasound imaging. The evolution of diagnostic imaging now goes from standalone techniques to “hybrid imaging” using SPECT/CT and PET/CT for many applications – and now also PET/MR and MR/CT.

The significant increase in the use of CT scanners, alone or in combination with SPECT or PET, has raised concerns about the radiation doses that patients are exposed to and the consequent increase in the probability of occurrence of cancers later in life [1, 2]. The concept of PET/CT has been so successful that none of the major medical imaging manufacturers now offers stand-alone PET scanners. This has also stimulated the use of SPECT/CT devices within nuclear medicine. The complementary anatomical, functional and molecular information provided by these hybrid techniques has been found clinically very important. A problem with CT as a complimentary anatomical

imaging modality is that it, like some of the PET- and SPECT- investigations, gives a comparatively high patient dose. Another problem is that CT provides relatively poor soft tissue contrast in the absence of oral and intravenous contrast media. This has stimulated the development of prototype PET/MRI devices, which are now under clinical tests.

A report from the Swedish Radiation Safety Authority showed that CT and nuclear medicine constitute 16% of the number of radiological investigations (mammography not included) and contribute with 64% to the collective dose in Sweden 2005 [3]. The National Council on Radiation Protection and Measurements in USA reports that CT and nuclear medicine constitute 22% of all radiological investigations, but 75% of the collective dose in USA 2006 [4].

The introduction of the PET and PET/CT-techniques and the increasing use of positron emitters have increased the doses to the staff at the hospital as well as at the cyclotrons and the hot labs for production of the radiopharmaceuticals. The aim of this work is to discuss various methods to reduce the radiation exposure to patients and staff in connection with CT-, SPECT- and PET-investigations.

2. CT

The effective dose from a single slice CT-investigation is typically from about 2 mSv (head) to 10 mSv (abdomen and pelvis) (Table 1). A total body investigation (brain, chest, abdomen and pelvis) gives around 20 mSv [5]. This is roughly a factor of ten higher than conventional planar X-ray investigations (range 0.01-10 mSv). The CT-doses are highly dependent on the characteristics of the CT-scanner, the size of the patient, the anatomical region under investigation and the technical factors used in each examination. The local doses from a CT-investigation can come up to hundred mSv [5]. For PET investigations, the effective doses are also considerable. An investigation with 350 MBq of ^{18}F -FDG gives for example an effective dose of 7 mSv [6]. The highest organ doses are 20-50 mGy. If this PET-study is combined with a CT-investigation of for example chest, abdomen, and pelvis, which gives an additional dose of 10 mSv, this together comes up to an effective dose of 20 mSv. If the PET-study instead is combined with a "low-dose" CT just for attenuation correction and anatomical orientation, the CT contribution can be reduced to 2-3 mSv and the total to around 10 mSv.

Table 1. Typical effective dose and organ dose values for common diagnostic single detector CT (SDCT) and multi detector CT (MDCT) investigations.

Investigation	Effective dose (mSv) [2, 5]	Organ absorbed doses (mGy) [7]
Head CT	2	Lens of the eye: 50, Thyroid: 1.9
Chest CT	6	Breast: 21, Thyroid 2.3, Lens of the eye: 0.14
Abdomen CT	16	Uterus and ovaries: 8
Pelvis CT	8	Uterus and ovaries: 25
Total body	20-30	

2.1. Methods to reduce CT doses

The slowly growing awareness of the increasing radiation doses from CT has forced the manufacturers to development several methods and techniques to reduce CT doses. The following section will review various dose reduction strategies. The implementation of these methods requires close collaboration between medical physicists, manufacturers, radiologists, technologists and referring physicians to be effective.

2.1.1. Optimise scanning parameters

There is an amount of scanning parameters that influence the radiation dose and the image quality: tube current, tube voltage, filtration, collimation, reconstruction filter, slice thickness, pitch and scanning length. The operator can monitor most of these parameters and modify them to obtain the necessary

image quality with a minimum radiation dose to the patient.

Except minimising the number of scans, tube current and tube voltage are important factors that affect the radiation dose. There is a simple relationship between the tube load (the product of tube current and the exposure time per rotation, mAs) and the radiation dose to the patient. A 50% reduction in tube load reduces the radiation dose by half but also causes an increase in the noise level by a factor of $\sqrt{2}$. Which mAs level that is adequate can be studied by using quite recently available dose reduction simulation software [8-10]. The software adds artificial noise to measured CT raw data with the intention to simulate a scan acquired with lower dose (mAs).

The tube voltage determines the energy of the emitted photons from the x-ray tube and a variation in tube voltage causes a change in radiation dose and image quality. Several studies have shown various levels of dose reduction or image quality improvement by using lower tube voltage [11, 12].

2.1.2. Automatic exposure control (AEC)

AEC is a technique that adapts the tube current relative the patient attenuation in the x-y plane (angular modulation), along the scanning direction (z-axis; longitudinal modulation), or both (combined modulation). The principle is that the operator selects an indicator of the image quality that is required and then the system adapts the tube current to obtain the predetermined image quality with improved radiation efficiency [13]. Use of an AEC system is an effective method for patient dose reduction and several studies have shown its potential. Results from a study performed by Söderberg et al. [14], valid for an anthropomorphic chest phantom representing a standard male patient, showed dose reductions in the range of 35-60%.

2.1.3. Iterative image reconstruction

Iterative image reconstruction methods have been used for a long time in SPECT and PET, but first recently been available also for CT. The conventionally used filtered back projection (FBP) procedure becomes now more and more replaced. The iterative algorithms have potential advantages as yielding lower image noise, improved spatial resolution, and reduced image artefacts (beam hardening, "windmill" and metal artefacts), which bring opportunities to reduce the radiation dose. Recently published clinical studies have shown dose reductions above 25% and improved image quality with iterative reconstruction compared to FBP [15, 16].

2.1.4. Organ based dose reduction

Protection of radiosensitive organs such as the breast, eye lenses and gonads is especially important in paediatric patients and young adults. Hidajat et al. [17]

have shown reduction in radiation dose to the testes with up to 95% using testis capsules during abdominal CT investigation. Several studies have shown the efficacy of using bismuth shield for reduction of the dose to the lens of the eye and dose to the breast without excessively affecting the image quality [18, 19], while other groups have questioned its value and even pointed out it as a dose-increasing factor [20]. Recently organ-based tube current modulation was developed where the x-ray tube switches off for a certain range of the rotation phase to protect radiosensitive organs from direct exposure. This is the method to recommend. Schmidt et al. [21] have shown dose reductions to the breast by about 30% and nearly the same noise level achieved using constant tube current by using noise-optimised image reconstruction techniques in combination with organ-based tube current modulation.

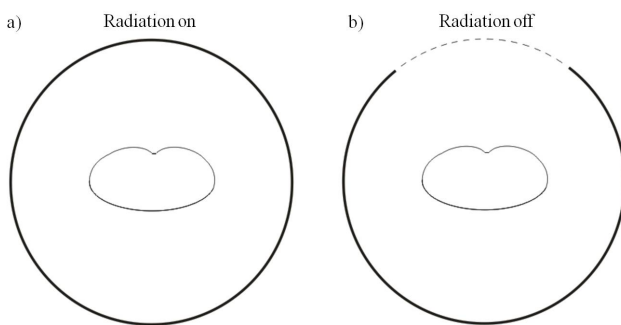


Fig. 1. The x-ray tube can now be switched off for a certain range of the rotation to protect radiosensitive organs like breasts, thyroid and eye lenses from direct exposure.

2.1.5. Adaptive collimation to reduce effect of “overscanning”

With overscanning means exposure of tissue volumes for which no reconstruction of tomographic images is done. Overscanning is required for helical CT scans to provide sufficient data on each side of the volume to be imaged to allow image reconstruction. As the X-ray beams in modern CT-scanner have become broader, consequently more and more wasted radiation dose is delivered to the patient by overscanning [22]. Both a software solution [23] and a hardware solution to this issue have been presented. Christner et al. [24] have shown dose reductions of up to 40% (using high pitch and short scan length) by using dynamically adjustable z-axis collimation.

3. Hybrid imaging

In PET/CT and SPECT/CT, the two techniques give complimentary information on structure and function, anatomy and physiology/biochemistry respectively. Hybrid imaging with PET/CT and SPECT/CT, in combination with more and more advanced reconstruction software, respiratory or cardiac gating and new tracer substances has increased the accuracy

of imaging and enable diagnosis in earlier stages of the disease. In PET/CT and SPECT/CT systems, attenuation mapping is performed based on available CT transmission data. Earlier techniques using different types of flat sources and line sources [25] have now been replaced by CT, as the improved attenuation correction in PET and SPECT gives a superior quantification.

Using PET/CT and SPECT/CT there are two levels of ambition for the CT part of the investigation: to use it for diagnosis (“diagnostic CT”) or just for attenuation correction or CT for imaging. From the radiation protection point of view, it is essential that if a “diagnostic” CT is needed, this be taken as part of the PET or SPECT/CT investigation to avoid that two CT investigations are done on the same patient. This creates a need for good cooperation between radiology and nuclear medicine departments if they are separated.

3.1. PET/CT

PET/CT has now replaced the standalone PET for many applications and is used mainly in oncology, but also more and more in neurology and cardiology. For PET-investigations, there are few observer performance studies, which relates diagnostic outcome to administered activity for an investigation. There is a work on diagnostic reference levels (administered activity) parallel to that in X-ray imaging.

For radiation protection PET/CT means an addition of two high-dose investigations, with effective doses of 20-30 mSv and organ doses, which for some organ could reach 100 mSv as seen in Tables 1 and 2 for the mean absorbed dose to the urinary bladder wall at a PET/CT investigation with ^{18}F -FDG. The use of ^{11}C -labelled substances generally gives a factor of two to three lower dose contributions.

3.2. SPECT/CT

SPECT is superior to planar imaging with gamma camera. SPECT/CT is used for bone scintigraphy, myocardial perfusion imaging, functional brain imaging, somatostatin receptor scintigraphy, parathyroid scintigraphy, adrenal gland scintigraphy, detection of sentinel nodes, etc.

Like in PET, there are few observer performance studies, which relates diagnostic outcome to administered activity for an investigation.

4. Justification

The topic of justification for medical exposures and the role of the referring physician and the radiologist at the radiology department are currently widely discussed. The meaning of justification of an investigation and the role of the involved staff is clarified in ICRP Publication 103 [26] and is further discussed and developed in the new European basic safety standards.

5. Occupational exposure

The areas within medical use of radiation, which today generates the highest personnel doses, are interventional

x-ray investigations, fluoroscopy outside the radiology department and PET.

Table 2. Typical effective dose values for common PET/CT investigations (PET contribution) [6].

Study	Radionuclide	Radio-pharmaceutical	Activity (MBq)	Effective dose (mSv)	Examples of organ doses (mGy)
Tumour	^{18}F	FDG	400	7.6	Bladder wall: 50; Ovary: 6; Testes: 5, Red bone marrow: 4
Tumour	^{18}F	Choline	300	6.0	Bladder wall: 22; kidneys: 25
Tumour	^{11}C	Choline	300	1.4	
Alzheimer	^{11}C	PiB	300	1.4	
Tumour	^{11}C	Acetate	400	1.4	
Tumour	^{11}C	Methionine	800	6.7	

Table 3. Typical effective dose values for common SPECT/CT investigations (SPECT contribution) [6, 27].

Study	Radionuclide	Radio-pharmaceutical	Activity (MBq)	Effective dose (mSv)	Examples of organ doses (mGy)
Bone	$^{99\text{m}}\text{Tc}$	Phosphonates	600	3.4	Bladder wall 30, Red bone marrow 6, Ovary 2, Testes 1.4
Myocardial perfusion	$^{99\text{m}}\text{Tc}$	Tetrofosmin; sestamibi	600	4.2-4.6	Bladder wall: 10-16, Gall bladder: 16-22-
Brain	$^{99\text{m}}\text{Tc}$	HMPAO	800	7.4	
Tumour	^{123}I	MIBG	400	5.2	
White cell	^{111}In ; $^{99\text{m}}\text{Tc}$	<i>In vitro</i> labelled leucocytes	18; 185	6.5; 2.0	

The shielding of PET and PET/CT facilities presents special challenges as the 0.511 MeV annihilation photons have much higher energy than other types of radiation used for diagnostics. Barrier shielding may be required in floors and ceilings as well as adjacent walls. However, shielding requirements, facility design, site planning, workflow, etc are not yet standardized. Therefore dose measurements for staff members show different values. From filling of syringe to patient departure the effective dose to technicians from ^{18}F -FDG is around 15 nSv/MBq ([28-33], with an essential part coming from interaction with the radioactive patient. For an annual number of less than 500 patients, an annual individual dose for the technicians would realistically be less than 3 mSv, which is still low but around 50% higher than that of technologists performing general nuclear medicine. Contributions to staff in wards may be about the same 15 nSv/MBq. The exposure of hands and especially fingers may, however, be a greater problem in ordinary nuclear medicine laboratories. Finger doses to technicians working under good normal nuclear medicine laboratory standard is around 2-3 $\mu\text{Sv/MBq}$ [33,34]. The use of syringe drawing device and semiautomatic injector can reduce this value to 0.2-0.6 $\mu\text{Sv/MBq}$ [30] and with fully automatic dispensing technique it can almost be totally eliminated ($< 0.02 \mu\text{Sv/MBq}$). For an average injected activity of 350 MBq per patient and for the three categories mentioned, the dose limit (500 mSv to

fingers) is reached after handling of 500, 2400 or many more patients annually.

7. Conclusion

The reduction of CT-doses during the last years, mainly due to improved technology from the manufacturers has been significant. Today CT-colon investigations can be done of an effective dose less than 2 mSv. There is a trend towards more individualised investigations. In PET and SPECT, more observer performance studies should be done to find optimal activities for various patients and investigations.

Cooperation between nuclear medicine and radiology departments are necessary to use CT investigations in the best way, both for diagnosis and for attenuation and scatter corrections in PET- and SPECT investigations. Efforts should be made to make patients better informed why a radiological examination is being performed, if there are alternative techniques and if the investigation is optimised.

8. References

1. Brenner D J, and Hall E J. Computed tomography-an increasing source of radiation exposure. *N Engl J Med*, 357, 2007.p. 2277–2784.
2. ICRP, International Commission on Radiological Protection. Managing patient dose in multi-detector computed tomography (MDCT). ICRP Publication 102, Ann ICRP, 37(1). 2007.

3. Almén A, Richter S and Leitz W. Swedish Radiation Protection Authority report 2008:03 number of radiological examinations in Sweden; 2008 (in Swedish).
4. NCRP, National council on radiation protection and measurements (USA). Ionizing radiation exposure of the population of the United States. Report No. 160, 2009
5. ICRP, International Commission on Radiological Protection. Managing patient dose in computed tomography. ICRP Publication 87, Ann ICRP, 30(4). 2000.
6. ICRP, International Commission on Radiological Protection. Radiation dose to patients from radiopharmaceuticals. ICRP Publication 106, Ann ICRP, 38(1-2). 2008.
7. Shrimpton P C, Jones D G, Hiller M C, Wall B F, LeHeron J C and Faulkner K. Survey of CT practice in the UK. Part 2: Dosimetric aspects, Chilton, UK, Report NRPB-R249, 1991
8. Söderberg M, Gunnarsson M and Nilsson M. Simulated dose reduction by adding artificial noise to measured raw data: a validation study. *Radiat Prot Dosimetry*, 139(1-3), 2010. p.71-77.
9. Mayo J. R, Whittall K. P, Leung A. N, Hartman T. E, Park C. S et al. Simulated dose reduction in conventional chest CT: validation study. *Radiology*, 202 (2), 1997. p. 453-457.
10. Massoumzadeh P, Don S, Hildebolt C. F, Bae K. T and Whiting B. R. Validation of CT dose-reduction simulation. *Med Phys*, 36 (1), 2009. p. 174-189.
11. Kalender W. A, Deak P, Kellermeier M, van Straten M and Vollmar S. V. Application- and patient size-dependent optimization of x-ray spectra for CT. *Med Phys*, 36 (3), 2009. p. 993-1007.
12. Funama Y, Awai K, Nakayama Y, Kakei K, Nagasue N et al. Radiation dose reduction without degradation of low-contrast detectability at abdominal multisection CT with a low-tube voltage technique: phantom study. *Radiology*, 237 (3), 2005. p. 905-910.
13. Kalra M. K, Naz N, Rizzo S. M and Blake M. A. Computed tomography radiation dose optimization: scanning protocols and clinical applications of automatic exposure control. *Curr Probl Diagn Radiol*, 34 (5), 2005. p. 171-181.
14. Söderberg M and Gunnarsson M. Automatic exposure control in computed tomography - an evaluation of systems from different manufacturers. *Acta Radiol*, 51(6), 2010. p. 625-634.
15. Prakash P, Kalra M. K, Kambadakone A. K, Pien H, Hsieh J, et al. Reducing abdominal CT radiation dose with adaptive statistical iterative reconstruction technique. *Invest Radiol*, 45 (4), 2010. p.202-210.
16. Prakash P, Kalra MK, Digumarthy S. R, Hsieh J, Pien H, et al. Radiation dose reduction with chest computed tomography using adaptive statistical iterative reconstruction technique: initial experience. *J Comput Assist Tomogr*, 34 (1), 2010. p. 40-45.
17. Hidajat N, Schröder R. J, Vogl T, Schedel H and Felix R. The efficacy of lead shielding in patient dosage reduction in computed tomography. *Rofo Fortchr Geb Rontgenstr Neuen Bildgeb Verfahr*, 165 (5), 1996. p. 462-465.
18. Coursey C, Frush D. P, Yoshizumi T, Toncheva G, Nguyen G and Greenberg S. B. Pediatric chest MDCT using tube current modulation: effect on radiation dose with breast shielding. *Am J Roentgenol*, 190 (1), 2008. p. 54-61.
19. Colombo P, Pedroli G, Nicoloso M, Valvassori L and Vanzulli A. Evaluation of the efficacy of a bismuth shield during CT examinations. *Radiol Med*, 108 (5-6), 2004. p. 560-568.
20. Geleijns K, Salvadó Artells M, Veldkamp W J H, López Tortosa M, Calzado Cantera A. Quantitative assessment of selective in-plane shielding of tissues in computed tomography through evaluation of absorbed dose and image quality. *Eur Radiol* 16, 2006, 2334–2340
21. Schmidt B, Raupach R and Flohr T, G. Assessment of image quality and dose for CT acquisitions with organ-based tube current modulation. Presented at: European Congress of Radiology, Vienna, Austria, 4-8 March 2010.
22. Tzedakis A, Damilakis J, Persinakis K and Stratakis J. The effect of z overscanning on patient effective dose from multidetector helical computed tomography examinations. *Med Phys*, 32 (6), 2005. p. 1621-1629.
23. Tang X, Hsieh J, Dong F, Fan J and Toth T, L. Minimization of over-ranging in helical volumetric CT via hybrid cone beam image reconstruction—Benefits in dose efficiency. *Med Phys*, 35 (7), 2008. p. 3232-3238.
24. Christner J. A, Zavaletta V. A, Eusemann C. D, Walz-Flannigan A. L and McCollough C. H. Dose reduction in helical CT: dynamically adjustable z-axis X-ray beam collimation. *Am J Roentgenol*, 194 (1), 2010. p. 49-55.
25. Mattsson S and Skretting A. Sealed radionuclide and X-ray sources in nuclear medicine. In: *Physics in nuclear medicine*. Ed by M C Cantone and Ch Hoeschen, Springer (in press)
26. ICRP, International Commission on Radiological Protection. The 2007 recommendations of the international commission on radiological protection. ICRP Publication 103, Ann ICRP 37(2-4), 2007.
27. ICRP, International Commission on Radiological Protection. Radiation dose to patients from radiopharmaceuticals. Addendum to ICRP 53. ICRP Publication 80, Ann ICRP 28(3), 1998.
28. Chiesa C, De Sanctis V, Crippa F, Schiavini M, Fraigola C E, Bogni A, Pascali C, Decise D, Marchesini R, and Bombardieri E. Radiation dose to technicians per nuclear medicine procedure: comparison between technetium-99m, gallium-67, and iodine-131 radiotracers and fluorine-18 fluorodeoxyglucose. *Eur J Nucl Med* 24, 1997, p 1380–1389
29. Benatar N A, Cronin B F and O'Doherty M J. Radiation dose rates from patients undergoing PET: implications for technologists and waiting areas. *Eur J Nucl Med* 27, 2000, p 583-589

30. Guillet B, Quentin P, Waultier S, Bourelli M, Pisano P and Mundler O. Technologist radiation exposure in routine clinical practice with ^{18}F -FDG PET. *J Nucl Med Technol* 33 (3), 2005, p 175-179
31. Roberts F O, Gunawardana D H, Pathmarai K, Wallace A, Paul L U, Tian M, Berlangieri S U, O'Keefe G J, Rowe C C and Scott A M. Radiation dose to PET technologists and strategies to lower occupational exposure. *J Nucl Med Technol* 33 (3), 2005, p 44-47
32. Seierstad T, Stranden E, Bjering K, Evensen M, Holt A, Michalsen H M, and Wetteland O. Doses to nuclear technicians in a dedicated PET/CT centre utilizing ^{18}F fluorodeoxyglucose (FDG). *Radiation Protection Dosimetry* 123 (2), 2007, p. 246–249
33. Leide-Svegborn S. Radiation exposure of patients and personnel from a PET/CT procedure with ^{18}F -FDG. *Rad Prot Dosim* 139 (1-3), 2010, p 208-213
34. Linemann H, Will E, Beuthien-Baumann B. Investigations of radiation exposure of the medical personnel during ^{18}F -FDG PET studies. *Nuklearmedizin*;39(3), 2000, p 77-81.

ANALYSIS OF AEC CALIBRATION METHODS FOR COMPUTED RADIOGRAPHY BY ESTIMATING TCDD AT DIFFERENT TUBE POTENTIALS

Anatoli VLADIMIROV*, Kalle KEPLER*

* University of Tartu, Institute of Physics, Training Centre of Medical Physics, Tartu, Estonia

Abstract: In the present work the threshold contrast-detail detectability (TCDD) estimated with a CDRAD test phantom by using $H_T(A)$ index at different tube potentials, with keeping constant detector entrance dose, phantom entrance surface dose (ESD) and time-current product (MAS) which correspond to different strategies in dose-quality optimisation practice. During the experiments also statistical component of image receptor dose uncertainty was evaluated when using AEC control.

Keywords: computed radiography, threshold contrast-detail detectability (TCDD), contrast-to-noise ratio (CNR), CDRAD

1. Introduction

During past years most of radiographic departments in European Union have been successfully moved from film-screen (FS) based technology to filmless digital technology. The digital technology in diagnostic radiography in Estonia is mostly presented by computed radiography (CR) systems, with slowly increasing number of digital radiography (DR) systems [1]. At the present work only CR systems as most conventional digital imaging systems in the radiology departments in Estonia have been covered, whereas DR systems have remained out of the scope. The transition from a film-screen environment to a digital is not a simple matter. In this process, patient radiation doses could increase from 40 to 100% [2]. However European directive (MED) 97/43/Euratom requires that medical exposures have to be justified and carried out in an optimized fashion. [3]. The CR systems are much more tolerant of inappropriate technique because of high latitude of digital detectors and phosphor plates which makes possible systematic over-expose or unnecessary high doses with a good or even perfect image quality. With increasing awareness of the need for radiation protection, a paradigm shift can be observed from the principle of “image quality as good as possible” to “image quality as good as needed”. The problem is that in digital radiography until now there is no certain approach how to keep constant image quality at

different tube potentials in order to calibrate the automatic exposure control (AEC) and this makes urgent need to find out appropriate practical image quality test methods. At this moment different types of parameters for image quality optimisation have been proposed by medical physics researchers: detector entrance dose, pixel value, detector dose indicator (DDI), signal-to-noise ratio (SNR), contrast-to-noise ratio (CNR), threshold contrast-detail detectability (TCDD). The behaviour of CNR at different tube potentials was recently examined in Marshall study [4]. As result of that work the method of constant entrance surface dose for AEC calibration was proposed in order to keep same value of CNR. Fig. 1 shows entrance surface dose (ESD) for the constant air kerma and constant CNR modes according to Marshall experiments [4].

Unfortunately CNR does not give information on the perceptibility of details of different size, although it does provide data on how well objects of different attenuation can be imaged, the question is if that method is good enough for evaluation and maintenance of an adequate image quality. In the present work comparison of the suggested CNR method with alternative strategies have been presented for dose-quality optimization, including introduction of the method by using physical measurements of threshold contrast-detail detectability (TCDD).

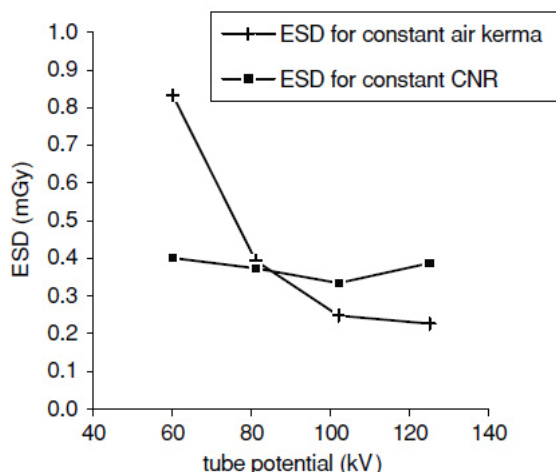


Fig. 1. Entrance surface dose (ESD) measured at the input to the 20 cm tissue equivalent phantom for the constant air kerma at the CR cassette (~3 µGy) and for the constant target CNR method [4].

2. Materials and methods

2.1. Imaging system

All test were performed in X-ray room equipped with overtable fluoroscopy system Iconos R100 Axiom (Siemens Medical Solutions, Erlangen, Germany) assembled with X-ray tube Optitop 150/40/80HC (tungsten target, anode angle 16°) and additional filtration of 0.1 mm Cu with total inherent filtration equivalent to 6.7 mm of aluminium (Al) and vertical bucky with moving antiscatter grid (focus distance 180 cm, 70 lines cm⁻¹, grid ratio 7:1). Images were acquired with storage phosphor plates of type MD 4.0 (35 cm x 43 cm, effective pixel pitch of 0.167 mm) (Agfa Healthcare, Mortsel, Belgium) and the phosphor plates were scanned by Agfa CR-35X digitizer with software version Agfa NX 1.0 (build 1.0.3203).

2.2. Contrast-detail phantom

The threshold-contrast detectability was assessed using the CDRAD contrast-detail phantom (Artinis Medical Systems BV, Zetten, The Netherlands). The CDRAD phantom consists of a 10 mm thick, 265 x 265 mm² wide polymethyl metacrylate (PMMA) support in which circular holes of 15 different diameters (ranging from 0.3 mm to 8 mm) have been drilled of 15 different depths (ranging from 0.3 mm to 8 mm) (Fig. 2). The holes have been arranged in a 15 x 15 matrix. Rows contain holes of identical diameter and exponentially increasing depth.

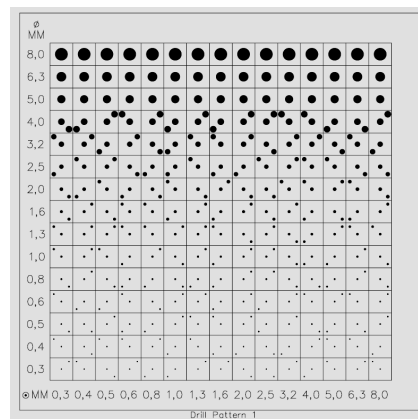


Fig. 2. Pattern of the CDRAD 2.0 phantom.

Columns contain holes of identical depth and exponentially decreasing diameter. Square matrix element of the first three rows contains one hole in the centre. Each square matrix element of the remaining 12 rows contains two identical holes; one in the centre and a second one randomly placed in one of the four corners. The detail depths are such that within a reasonable range of exposures some, but not all, of the details should be visible at all detail diameters.

In this work the CDRAD phantom was placed between two 75 mm (3 x 25 mm) PMMA plates to provide scatter and give attenuation similar to an adult patient. This gives the total thickness of the CDRAD-PMMA phantom of 160 mm PMMA.

All exposures were made in the vertical bucky stand with a moving antiscatter grid and a focal spot to detector distance of 200 cm in order to reduce parallax effect as much as possible. Large focal spot (1.0 mm) of the x-ray tube was selected. In order to have the x-ray beam collimated into the CDRAD-PMMA phantom area, the field size of 19 x 19 cm² (projected on the phosphor plate plane) was chosen on the collimator. The setup geometry is shown in Fig. 3.

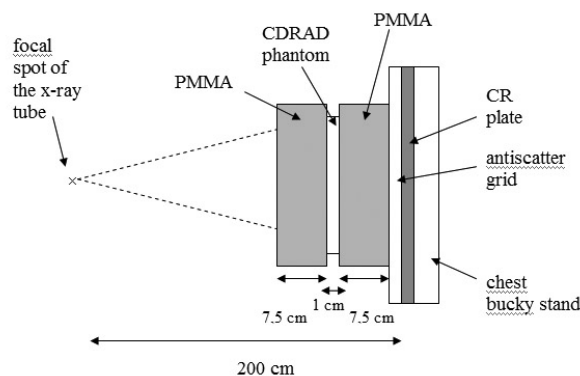


Fig. 3. A schematic diagram of the experimental setup.

2.3. Detector constant entrance dose setup

At first stage of experiment the tube potential of 81 kVp and central sensor for AEC system was chosen, together with high speed sensitivity settings (speed class "H"). Detector entrance dose of 3.9 μGy was used as the reference to obtain images with as close as possible entrance dose at 60 kVp, 100 kVp and 125 kVp (Table 1). Image receptor entrance dose with the phantom in place was measured with a Keithley TRIAD dosimeter and a 15 cm³ ionization chamber (Keithley Instruments Inc., USA) placed directly inside the bucky cassette holder.

Table 1. Setup for constant detector dose measurements.

Tube potential, kVp	Tube charge, mAs	Detector entrance dose, μGy
60	110	3.8
81	28	3.9
100	11	3.8
125	5	3.8

Reference exposure at 81 kVp was repeated 10 times in order to estimate uncertainty in the measurements.

2.4. Phantom constant entrance dose setup

At second stage in order to keep constant CNR according to Marshall method the constant value of ESD about 0.38 mGy at phantom entrance surface was selected and set as the reference dose level for obtaining images at potentials of 60 kVp, 100 kVp and 125 kVp (Table 2).

Table 2. Setup for constant ESD measurements.

Tube potential, kVp	Tube charge, mAs	Phantom entrance surface dose, mGy	Detector entrance dose, μGy
60	65	0.38	2.3
81	28	0.39	3.9
100	16	0.37	4.9
125	10	0.39	6.3

Phantom entrance dose was measured with a same Keithley ionization chamber placed directly at the centre of CDRAD-PMMA phantom entrance plane. At last stage the setup values of 81 kVp and 28 mAs were used as the reference to obtain images with same time-current product (MAS) at 60 kVp, 100 kVp and 125 kVp (Table 3).

Table 3. Setup for constant MAS measurements.

Tube potential, kVp	Tube charge, mAs	Detector entrance dose, μGy
60	28	1.1
81	28	3.9
100	28	10.2
125	28	21.6

The CR plates were read out in Agfa CR-35X scanner without clinical post-processing by using the "system diagnostics" and "flat field" settings. The DICOM greyscale image window and level were adjusted manually such that the visibility of the details appeared to be maximized and the background noise remained perceptible. The contrast of detail is defined as:

$$C = \frac{|I - I_D|}{I} \quad (2.1)$$

where I is the primary transmission through the full phantom thickness of 160 mm and I_D is primary transmission through the contrasting detail of the CDRAD phantom and the PMMA phantom of 150 mm. To estimate the detail contrast, the transmitted air kerma (the phantom output) was calculated for the particular CDRAD detail with the PMMA phantom at different tube potentials by using relevant tube data (tungsten target, anode angle 16°, ripple of the generator voltage 5%) and spectral data derived from IPEM Report 78 [5]. An X-ray spectrum calculated for the reference potential of 81 kVp is given in Fig. 4.

The CDRAD phantom was used to measure the lowest contrast detectable (C_T) as a function of detail size. All CDRAD DICOM images were evaluated (including finding threshold contrast-detail curves) with CDRAD Analyzer software v1.1 (Artinis Medical Systems BV, Zetten, The Netherlands) [6].

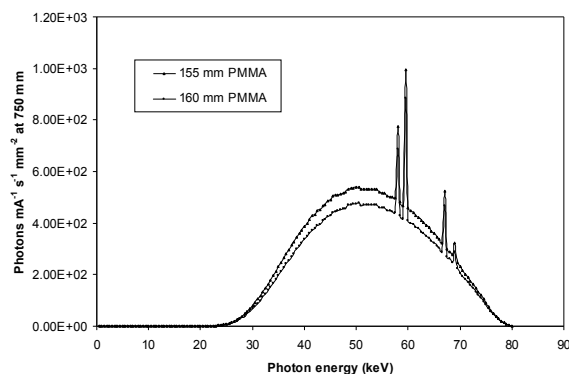


Fig. 4. Calculated X-ray photon spectrum for 155 mm and 160 mm of PMMA (tube voltage 81 kVp, ripple 5 %, total filtration 4.4 mm Al, anode angle 16°, target material W).

The lowest contrast detectable (the threshold contrast level) was determined by the computer analysis. Using the Student t-test with Welch correction the program determines if the contrast-detail combination in a certain square is positively seen. The same Alpha level of significance ($\text{Alpha}=1\text{e-}008$) was selected for all evaluations. This level set for automated software evaluation has a best correlation with a visual scoring by an average observer [7]. The contrast detail curve of mean value with maximum and minimum deviations of ten measurements of the CDRAD phantom, DICOM image acquired at 81 kVp with 15 cm PMMA are given in Fig. 5.

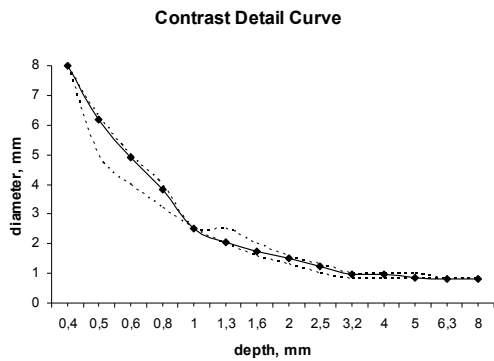


Fig. 5. Contrast detail curve of the CDRAD phantom at 81 kVp, 15 cm PMMA.

The data were presented graphically as the TCDD index $H_T(A)$ against the square root of detail area A (in mm) by the formula [8]

$$H_T(A) = \frac{1}{C_T \cdot \sqrt{A}} \quad (2.2)$$

where C_T is the detected threshold contrast.

The ideal $H_T(A)$ curve was also calculated by using ideal conditions where CDRAD phantom holes are fully visible and the maximum lowest contrast is detectable over every detail size.

3. Results and discussion

The aim of this work is to compare the different methods of AEC calibration through comparison of threshold contrast-detail index. Fig. 6 shows comparison of $H_T(A)$ index at different tube potentials with keeping constant detector entrance dose of 3.9 μGy .

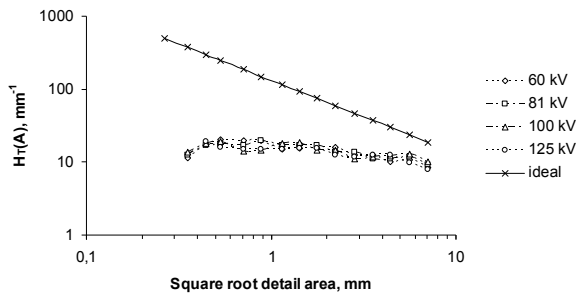


Fig. 6. Comparison of the threshold contrast-detail index at different tube potentials by using same 3.9 μGy detector entrance dose (15 cm PMMA + CDRAD).

Standard deviations of the single measurements of each value of $H_T(A)$ index for 60 kVp, 100 kVp and 125 kVp from reference 81 kVp was calculated. The average standard deviation for constant detector entrance dose method was 1.7 mm^{-1} . Fig. 7 shows the comparison of threshold contrast-detail index at different tube potentials when using constant patient entrance dose or ESD which could be corresponded according to Marshall study to the constant contrast-to-noise ratio (CNR) [4]. In order to do that the constant patient entrance dose ESD was kept around level of 0.39 mGy

which corresponds to well optimized system according the previous studies [9].

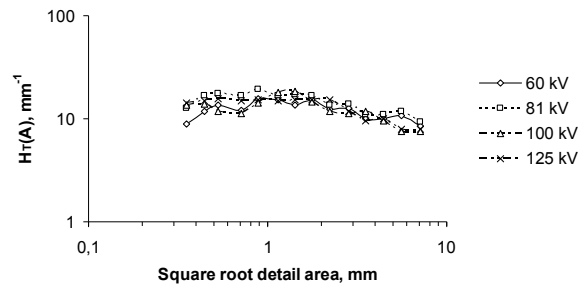


Fig. 7. Comparison of the threshold contrast-detail index at different tube potentials using the same 0.39 mGy entrance surface dose (ESD) in order to keep constant CNR (15 cm PMMA + CDRAD).

For constant CNR method the average standard deviation of $H_T(A)$ index for 60 kVp, 100 kVp and 125 kVp from reference 81 kVp curve is 2.4 mm^{-1} which is 41% more compare to constant detector dose method. In the same time the average absolute value of $H_T(A)$ index is about 10% more for constant dose detector method. Fig. 8 shows the effect of tube potential to the contrast-detail index curve without any AEC calibration and by using constant time-current product.

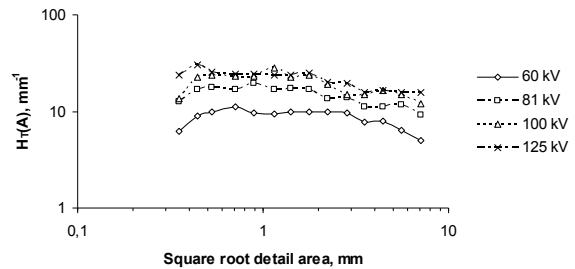


Fig. 8. Comparison of the threshold contrast-detail index at different tube potentials using same time current product (28 mAs) (15 cm PMMA + CDRAD).

Because lower tube potentials produce lower tube output it is clear, that lower KV will produce significantly lower ESD when MAS value is kept constant and as result the lower image quality as well. Fig. 9 demonstrates how the AEC detectors could be practically calibrated in order to keep same detector entrance dose or ESD.

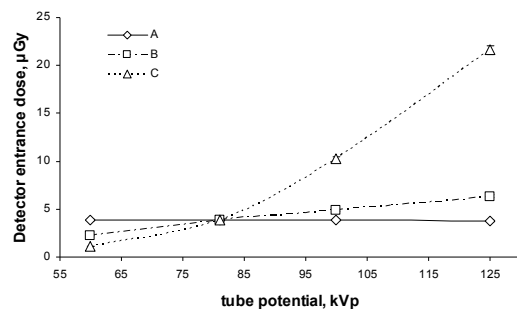


Fig. 9. Comparison of detector entrance dose at different optimisation methods (15 cm PMMA + CDRAD): constant detector entrance dose (A); constant CNR (B); constant time-current product (MAS) (C).

In Fig. 10 the threshold contrast-detail index for two different methods is compared at 60 kVp. The average standard deviation of $H_T(A)$ index at 60 kVp from reference 81 kVp curve is 1.5 mm^{-1} for constant dose detector method and 2.4 mm^{-1} for constant CNR method. Fig. 10 shows that for 60 kVp at lower spatial frequencies or large details absolute value of $H_T(A)$ index for the constant detector entrance dose method compared to the constant CNR method differs from 26% to 63%. In the same time at higher spatial frequencies (small details) the values of $H_T(A)$ index are almost equal. In the same way in Fig. 11 the threshold contrast-detail index for two different methods is compared at 125 kVp. The average standard deviation of $H_T(A)$ index from reference 81 kV curve is 1.9 mm^{-1} for constant dose detector method and 2.0 mm^{-1} for constant CNR method.

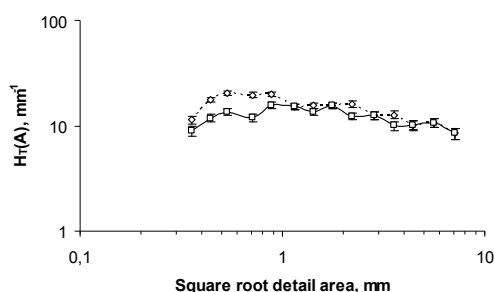


Fig. 10. Comparison of the threshold contrast-detail index at 60 kVp with method based on constant detector entrance dose (A) and method based on constant CNR (B) (15 cm PMMA + CDRAD).

Fig. 11 shows that at higher spatial frequencies (i.e. smaller detail objects) absolute value of $H_T(A)$ index for the constant detector entrance dose method compared to the constant CNR method differs from 26% to 30% and is almost equal at lower spatial frequencies.

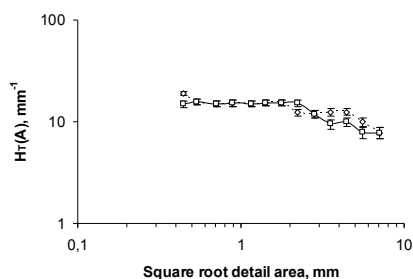


Fig. 11. Comparison of the threshold contrast-detail index at 125 kV with method based on constant detector entrance dose (A) and method based on constant CNR (B) (15 cm PMMA + CDRAD).

The expanded uncertainties were found for detector dose measurements at 81 kVp, entrance surface dose measurements (ESD) and dose measurements with

automatic expose control (AEC). The statistical uncertainty component for $3.9 \mu\text{Gy}$ of detector dose measurements was $0.0012 \mu\text{Gy}$, type B uncertainty was $0.07 \mu\text{Gy}$; combined standard uncertainty is $0.07 \mu\text{Gy}$. The measured detector dose value with expanded uncertainty at 95% level of confidence (3.90 ± 0.17) μGy . The statistical uncertainty component for ESD measurements was 0.00012 mGy , type B uncertainty was 0.007 mGy ; combined standard uncertainty is 0.007 mGy . The measured ESD value with expanded uncertainty at 95% level of confidence $\text{ESD} = (0.390 \pm 0.016) \text{ mGy}$. During experiment it was also evaluated statistical component of image receptor dose when using AEC control, which was $0.05 \mu\text{Gy}$. Using AEC instead of manual mode could give rise to additional 1.0% of relative uncertainty in detector dose measurements.

For $H_T(A)$ index the maximum measured expanded uncertainty at 95% level of confidence was 1.2 mm^{-1} which corresponds to relative uncertainty of 7.5%.

4. Conclusions

Two methods of automatic exposure control (AEC) setup based on threshold contrast-detail detectability measurements on CDRAD phantom have been examined as a function of x-ray beam quality in a computed radiography (CR) system. It was found that the constant CNR method did not maintain constant TCDD when the x-ray energy has been increased. The constant detector entrance air kerma strategy was more successful at maintaining constant detectability. Deviation between on spatial frequency dependences of the constant CNR method and the constant detector entrance dose method at lower and higher tube potentials was found. It was found that for $H_T(A)$ index the maximum measured expanded uncertainty at 95% level of confidence was 1.2 mm^{-1} which is lower than average standard deviation of $H_T(A)$ index from reference 81 kVp curve for both constant detector dose and constant CNR methods which was 1.7 mm^{-1} and 2.4 mm^{-1} correspondently. The results show that TCDD evaluation method is reliable and could be used for the optimisation practice. It was also found that usage of automatic AEC instead of manual setting could give rise to additional 1% of relative uncertainty in detector dose measurements, which shows that if AEC is used during image quality optimisation the repeatability of AEC control needs to be taken into account, that was absent in the previous studies [9]. However the idea to keep constant contrast-to-noise ratio for every patient independently from tube potential is good, the physical parameter of CNR itself does not give information on the perceptibility of details with different size. Following the Marshall method [4] the detector entrance dose would decrease at lower tube potentials, but the threshold-contrast detail detectability would also drop down up to 63%. For CR system optimisation the Marshall method could be developed if the constant detector dose method is combined with the constant CNR method to achieve the golden mean. For higher

tube potentials the constant CNR method could be fully implemented which will slightly decrease the TCDD at higher spatial frequencies, and at the same time ESD will be slightly increased. For lower tube potentials it is suggested not to decrease fully the detector dose in order to keep constant CNR but decrease it up to 30% of TCDD deviation at lower spatial frequencies. It will maintain slightly increased CNR and slightly decreased ESD. Also according to the previous publication the $H_1(A)$ index is more sensitive to dose reduction at lower tube potentials than higher tube potentials [9]. Although the dependence of both CNR and TCDD on tube potential has been examined in this work, the optimum absolute value of detector entrance dose still needs future investigations. It could be also necessary to calculate effective patient doses for optimised AEC curves by using for example PCMCX software [10]. Still the new optimisation methods using objective physical parameters need further justification by the human observer evaluation methods for medical image quality such as ROC or VGA analysis.

5. References

1. Ust M., Aavik A., Käpp R., Paats A. ESTONIA-PACS – integral part of national e-Health Program. Presented at the Baltic Radiology Congress, Tartu, Estonia, 24-25 October 2008.
2. Vano E., Fernandez J.M., Ten J.I et al. Transition from screen-film to digital radiography: evaluation of patient radiation doses at projection radiography. *Radiology*, 243, 461-466, 2007.
3. Commission of the European Communities (CEC). Council Directive 97/43/Euratom of 30 June 1997 on health protection of individuals against the dangers of ionizing radiation in relation to medical exposure, and repealing Directive 84/466/Euratom. *Official Journal of the European Communities*, L 180, 22-27, 1997.
4. Marshall N. W. An examination of automatic exposure control regimes for two digital radiography systems. *Physics in Medicine and Biology*, 54, 4645-4670, 2009.
5. Cranley K., Gilmore B. J., Fogarty G. W. A. and Desponds L. Catalogue of diagnostic X-ray spectra and other data. IPEM Report 78. [CD-ROM]. York (UK): Institute of Physics and Engineering in Medicine (IPEM), 1997.
6. Artinis Medical Systems. CDRAD Analyser – manual. Version 1.1, March 2006. Zetten (The Netherlands): Artinis, 2006. <http://www.artinis.com>
7. Pascoal A., Lawinski C.P., Honey I., Blake P. Evaluation of a software package for automated quality assessment of contrast detail images – comparison with subjective visual assessment. *Physics in Medicine and Biology*. 50, 5743-5757, 2006.
8. Gallacher D.J., MacKenzie A., Batchelor S., Lynch J. and Saunders J.E.. Use of a quality index in threshold contrast detail detection measurements in television fluoroscopy. *The British Journal of Radiology*, 76, 464-472, 2003.
9. Kepler K., Vladimirov A. Optimisation strategies introduced for CR at health care centres in Estonia. *Radiation Protection Dosimetry*, 129, 127-131, 2006.
10. Tapiovaara M., Siiskonen T., PCXMC, A Monte Carlo program for calculating patient doses in medical x-ray examinations. 2nd Ed. STUK-A231. Helsinki: Radiation and Nuclear Safety Authority, 2008.

DIGITAL QA METHOD'S CALIBRATION IN DIGITAL RADIOGRAPHY

Lada BUMBURE, Yuri DEKHTYAR, Alexey KATASHEV, Tatyana KIRSANOVA, Ella PACUKEVICH,
Lubova SHUVALOVA
Biomedical Engineering and Nanotechnology Institute of Riga Technical University, Riga, Latvia

Abstract: A digital x-ray imaging technology allows making of quality assurance of x-ray images digitally. There was found that a brightness histogram is a tool, which correlates with digital x-ray image quality parameters. Usage of brightness histograms become an important method of digital x-ray images quality assurance. A calibration of the method would allow using digital quality assurance in any hospital where digital radiography is in use.

Keywords: a digital x-ray image quality, a brightness histogram.

1. Introduction

Quality assurance of an x-ray machine and an x-ray image is an integral part of today's digital radiography quality assessment. A digital x-ray imaging technology allows making the quality assurance digitally.

In the previous works a digital x-ray image data array was in use to produce a pixel distribution over brightness related to the quality parameters of the x-ray image. There was found that a variance and an average of brightness histograms correlate to the contrast of x-ray image which in turn depends on high voltage. The previous results demonstrated that image brightness digitalization could be a useful method for quality assessment of digital x-ray imaging.

The aim of this work was to establish an approach of the brightness digitalization method's calibration that would allow determination of a basic value of standard deviation with some confidence intervals for each specific x-ray machine. In future the method could be used by medical physicists in any x-ray diagnostics department for quality assessment of digital radiography.

2. Materials and methods

The x-ray machine „Digital Diagnost” was employed to supply a flow of radiation to acquire the digital x-ray images.

The images were acquired using an automatic exposure control (AEC) mode. The x-ray tube was provided with the voltage equal to 71 kV.

The test plate “ETR-1” from the set “QC Kit Roland 8” was used as the test object.

The Source Image Distance (SID) was 1m. The irradiated field was sized to 19x25 cm for each exposure. A large, a medium and a small focal spot size were in use. A total of 10 exposures were done for each focal spot size.

All the digital x-ray images were acquired in the DICOM (Digital Imaging and Communications in Medicine) format. White and black areas of the images (Fig.1) were analysed.

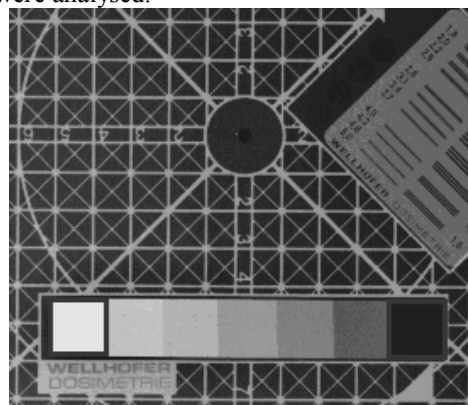


Fig. 1. The analyzed areas of the digital image

The DICOM images of each area were transferred to TIFF (Tagged Image File Format) format images 75x75 pixels, and digitized using software, designed for this purpose. Histograms of pixel distribution over brightness for all 10 exposures of each area and each focus were constructed using “Microsoft Excel” program (Fig.2 - 7).

An average of brightness (x_{vid}) for each histogram was calculated using formula (1) [1]:

$$x_{vid} = \frac{\sum_{i=1}^k x_i n_i}{n}, \quad (1)$$

where: x_{vid} – average brightness, x_i - brightness value “ i ”, n_i - pixels number of value “ i ”, n – total number of pixels

A variance of each histogram was calculated using formula (2):

$$\sigma^2 = \frac{\sum_{i=1}^k n_i (x_i - x_{vid})^2}{n - 1}, \quad (2)$$

where: x_{vid} – average brightness, x_i - brightness value “ i ”, n_i - pixels number of value “ i ”, n – total number of pixels, σ – variance

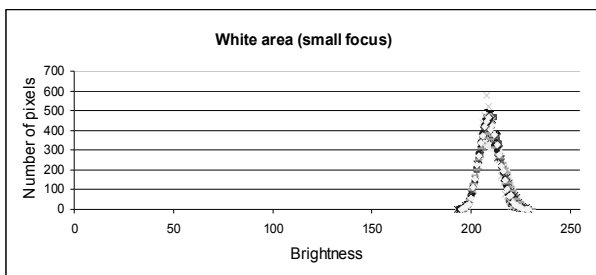


Fig. 2. White area small focus brightness histograms

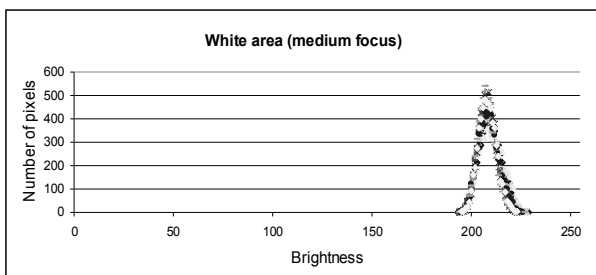


Fig. 3. White area medium focus brightness histograms

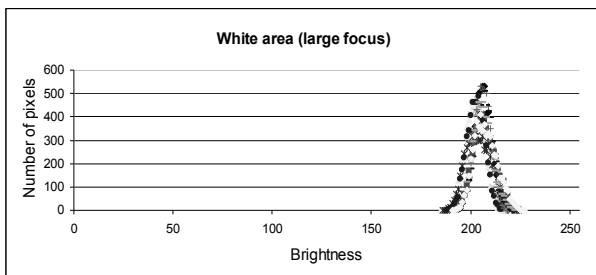


Fig. 4. White area large focus brightness histograms

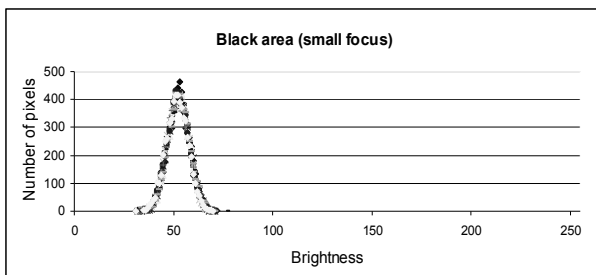


Fig. 5. Black area small focus brightness histograms

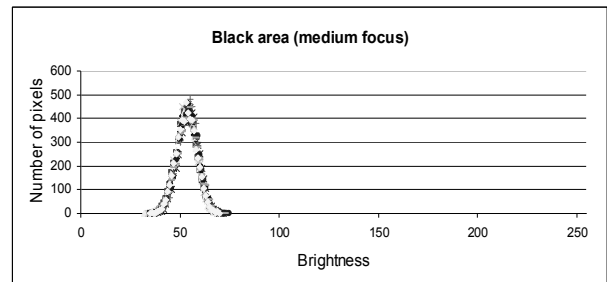


Fig. 6. Black area medium focus brightness histograms

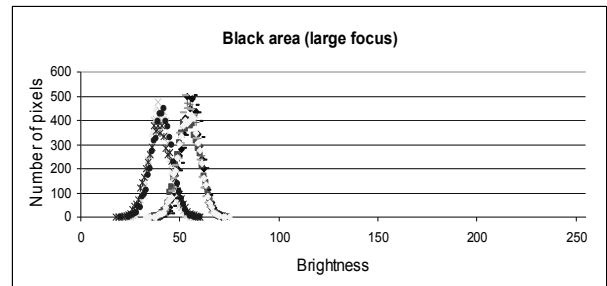


Fig. 7. Black area large focus brightness histograms

A standard deviation (σ) was calculated for each variance. Then confidence intervals of the standard deviations were calculated using χ^2 test (significance level of 0.01). After that an average value of standard deviation and of the limits was calculated for each area and each focal spot.

3. Results

The results of the calculations are shown in Tables 1-6. The values of standard deviations are shown in the figures 8 and 9.

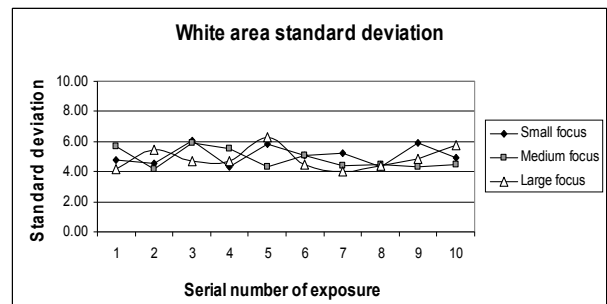


Fig. 8. White area standard deviations

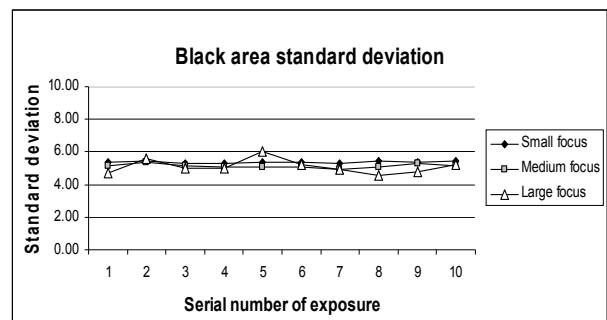


Fig. 9. Black area standard deviations

Table 1. White area's standard deviation (small focus)

White area (small focus)				
Nr. of image	σ^2	σ	1 st limit	2 nd limit
1	23.05	4.801	0.121	0.113
2	20.93	4.575	0.115	0.107
3	36.55	6.046	0.152	0.142
4	18.52	4.303	0.108	0.101
5	34.04	5.834	0.147	0.137
6	25.55	5.055	0.127	0.118
7	27.71	5.264	0.133	0.123
8	18.92	4.350	0.110	0.102
9	35.04	5.920	0.149	0.139
10	24.35	4.935	0.124	0.116
Aver.	26.47	5.108	0.129	0.120

Table 2. White area's standard deviation (medium focus)

White area (medium focus)				
Nr. of image	σ^2	σ	1 st limit	2 nd limit
1	32.43	5.695	0.144	0.133
2	17.40	4.171	0.105	0.098
3	34.63	5.885	0.148	0.138
4	30.79	5.549	0.140	0.130
5	18.91	4.348	0.110	0.102
6	26.08	5.107	0.129	0.120
7	19.40	4.404	0.111	0.103
8	20.31	4.506	0.114	0.106
9	18.48	4.299	0.108	0.101
10	20.19	4.493	0.113	0.105
Aver.	23.86	4.846	0.122	0.114

Table 3. White area's standard deviation (large focus)

White area (large focus)				
Nr. of image	σ^2	σ	1 st limit	2 nd limit
1	17.40	4.171	0.105	0.098
2	29.91	5.469	0.138	0.128
3	21.73	4.661	0.118	0.109
4	22.22	4.714	0.119	0.110
5	39.45	6.281	0.158	0.147
6	19.70	4.439	0.112	0.104
7	16.41	4.052	0.102	0.095
8	19.63	4.430	0.112	0.104
9	23.48	4.845	0.122	0.114
10	33.11	5.754	0.145	0.135
Aver.	24.30	4.882	0.123	0.114

Table 4. Black area's standard deviation (small focus)

Black area (small focus)				
Nr. of image	σ^2	σ	1 st limit	2 nd limit
1	28.83	5.369	0.135	0.126
2	29.49	5.430	0.137	0.127
3	28.40	5.330	0.134	0.125
4	27.67	5.260	0.133	0.123
5	29.04	5.389	0.136	0.126
6	28.81	5.367	0.135	0.126
7	28.09	5.300	0.134	0.124
8	30.00	5.477	0.138	0.128
9	29.14	5.398	0.136	0.127
10	29.75	5.454	0.137	0.128
Aver.	28.71	5.360	0.135	0.126

Table 5. Black area's standard deviation (medium focus)

Black area (medium focus)				
Nr. of image	σ^2	σ	1 st limit	2 nd limit
1	26.66	5.164	0.130	0.121
2	28.86	5.372	0.135	0.126
3	26.43	5.141	0.130	0.120
4	25.57	5.057	0.127	0.119
5	25.54	5.054	0.127	0.118
6	26.10	5.109	0.129	0.120
7	24.60	4.960	0.125	0.116
8	25.65	5.065	0.128	0.119
9	27.72	5.265	0.133	0.123
10	26.29	5.127	0.129	0.120
Aver.	25.54	5.054	0.127	0.118

Table 6. Black area's standard deviation (large focus)

Black area (large focus)				
Nr. of image	σ^2	σ	1 st limit	2 nd limit
1	22.47	4.741	0.119	0.111
2	30.90	5.559	0.140	0.130
3	25.17	5.017	0.126	0.118
4	25.16	5.016	0.126	0.118
5	36.74	6.061	0.153	0.142
6	27.25	5.220	0.132	0.122
7	24.51	4.950	0.125	0.116
8	20.64	4.543	0.115	0.106
9	22.59	4.753	0.120	0.111
10	27.36	5.231	0.132	0.123
Aver.	26.28	5.126	0.129	0.120

4. Conclusions

The achieved results demonstrate that standard deviation of white area is less constant than standard deviation of black area. The tendency is observable in all cases i.e. using small, medium or large focal spot size. The most stable standard deviation appears using small focus and black area. So the recommendation is to use small focal spot for exposures and to process only black areas of digital x-ray images in calibration

process. When the standard deviation with some confidence intervals is acquired, it would serve as a basic value for quality assurance for a specific x-ray machine. All the further measurements would be compared with the basic value.

5. References

1. Arhipova I., Bāliņa S. „Statistika ar EXEL ikvienam”, Datorzināibu centrs – 1999.

OPTIMIZATION OF IMAGE QUALITY AND DETERMINATION OF EFFECTIVE DOSE TO ASSISTING PERSONS IN VETERINARY RADIOLOGY

Hanna Holstein*, Anders Tingberg* and Marie- Louise Olsson*

*Department of clinical sciences Malmö, Lund University, Skåne University Hospital, Malmö

Abstract: Diagnostic radiology of horses is rarely optimized in terms of image quality and dose to the assisting person. The effective dose to the assisting person has been measured and techniques have been developed with different characteristics to increase the image quality by shaping the x-ray beam for homogeneous exposure of the thoracic spine.

Keywords: Veterinarian radiology, dose assisting person, image quality, horses, wedge.

1. Introduction

In Sweden, there are approximately 300 licenses and a total of 430 x-ray systems for veterinary diagnostic radiology[1]. There are about 2000 professional veterinarians, a third of them are employed by the government and the remainder works in the private sector. Radiographic examinations are performed on about 40 veterinary clinics in Scania. The clinics are divided into small and large animal clinics, and they vary in size from small clinics with two to three persons employed up to large clinics with several employees. X-ray examinations of horses are investigated in this study and evaluated which are categorized as large animals.

The veterinarian decides which x-ray examinations should be performed and the treatment of the animal is based on the diagnostic information from the radiographs. It is important that the x-ray diagnosis is accurate and that the dose to the animals and the persons assisting during the examination is kept as low as reasonably achievable. Currently, radiographic examinations on horses are rarely optimized in terms of image quality and dose. Generally, no medical physicists are involved in the clinical routine.

Veterinarians use mainly conventional radiographic equipment, developed for diagnosis of humans, and these devices are adapted to be used for horses. Direct digital systems (DR), and, more frequently, computed radiography system (CR), are used. In some applications, the delayed image formation with CR (due to the cassette handling and image readout), can be problematic and thus DR is advantageous. On the other hand a DR system is more expensive than a CR system. Frequently at veterinary clinics, a veterinary assistant has special training in veterinary radiography and

radiation physics, and is therefore responsible for acquiring the x-ray images. During the examination it is often the animal owner who holds the detector and is involved as much as possible in the x-ray examinations in order to reduce the radiation dose to the staff. This means that the animal owner is close to the primary x-ray beam which makes radiation protection aspects important [2]. In most cases there is another assisting person who holds the horse, and who is also subject to the scattered radiation, however to a lesser degree.

The image quality varies between different clinics due to different radiographic systems and the degree of training and experience of the person who takes the images. The image quality at most examinations is relatively good and adequate diagnostic information is generally achieved.

The thoracic spine of the horse presents a special problem due to the large variation in thickness of the animal of this area. Without special arrangements during the image acquisition, it is difficult to achieve correct exposure of both the lower and upper parts of the vertebral bodies. Details may be underexposed or burnt-out, which causes information loss in those parts of the image. Multiple images, at different dose levels, are often produced to circumvent this problem and give rise to higher effective dose to the assisting person.

Due to the necessary sedation of the horse and possible movement of the horse between the images, multiple images are highly undesirable. Furthermore, this is an urgent field of interest, since back problems are frequent among horses.

There are no established standards for determining image quality in veterinary radiology (e.g. with criteria on image quality)[3], which makes it hard to evaluate

and compare image quality from different exposure parameters or x-ray systems.

2. Material and method

Two different x-ray systems were used in this study: One DR system (at Saxtorp equine clinic, Saxtorp, Sweden), and one CR system (at the Swedish University of Agricultural Sciences, Uppsala, Sweden).

The equipment used in Saxtorp is equipped with a Sound Techniques True DR 1x detector (Sound-Ekline™, Carlsbad, California, USA) and a Varian x-ray system (Type RAD-14, Varian Medical System, Palo Alto, California, USA). At Uppsala, a Siemens generator (Siemens Health, Erlangen, Germany) used with a Fuji computed radiography system (FCR xG1, Fuji Film, Tokyo, Japan).

An effort was made to minimize bias due to exposure geometry and size of the horses. The geometries used were as similar as possible for the two systems and the horses examined were similar with respect to size, about 550 kg and 1.65 m at the withers. The most common examinations are the examination of the phalanx (the leg) of the horse. Other common examinations are the examination of the hock joint, stifle joint, the thoracic spine and the cervical spine (c-spine). The effective dose to the assisting person was determined during normal daily work examining horses. A direct detector (Educational Direct Dosimeter, EDD, Unfors, Billdal, Sweden) was placed at the trunk, inside of the lead apron (0.25 mm Pb equivalent), of the assisting person. The dosimeter converts the measured absorbed dose to effective dose with built-in conversion factors. The effective dose to the assisting person is determined on a per-image basis as well as for a full investigation.

In Uppsala, the absorbed dose to the trunk of the assisting person (the horse owner) was measured for 190 single images at 30 examinations. At Saxtorp equine clinic the absorbed dose was measured at 20 examinations with a total of 116 images. The exposure parameters are based on parameters commonly used in the daily routine in the clinic. In figure 1 a typical position of the assisting person are shown.

The visibility of normal anatomy can be used as a measure of image quality. By formulating criteria with respect to the visibility of defined anatomical structures, the image quality can be assessed in clinical trials [4]. Such criteria exist for diagnostic radiology of humans but not for horses.

Similar image criteria for horses would be useful to evaluate the image quality resulting from different x-ray systems, exposure parameters and techniques, in the optimization of veterinary radiological examinations.

Image criteria were developed for four common and important examinations, cranial thoracic spine, central thoracic spine, caudal thoracic spine and caudal lumbar spine; examinations which are considered to be difficult to get accurate diagnostic information from.



Fig. 1. The position of the assisting person holding the detector (near the horse) when examining the hock joint.

When defining the criteria, the veterinarians studied images of different types of horses and with the support of the image criteria for humans[3], developed the new image criteria. For each of the four examinations, defined anatomical structures are mentioned together with a level of visibility: “visually sharp reproduction”, “visualization” and “reproduction”. These visibility levels show the importance of various image quality aspects (e.g. spatial resolution or contrast) for this particular examination.

By letting observers judge the confidence regarding the fulfillment of the image criteria (e.g. based on the confidence scale), a score related to the clinical image quality can be calculated. This image criteria score can thus be used as a measure of the image quality of different x-ray systems and different exposure parameters.

The observer (radiologist or veterinary) judge the images based on the fulfillment of criteria, often on a five-grade scale ranging from “not fulfilled” to “definitely fulfilled”. Based on these scores, an image criteria score, ICS, was calculated for each image, and each examination technique [5].

Development of image criteria for horses was done in collaboration with Margaret Uhlhorn of Agricultural Sciences, Uppsala University animal hospital, and with help of Anne Haglund, Saxtorp equine clinic.

One veterinarian and two medical physicists observed all the images with the developed image criteria in a visual grading analysis [6] study with the software package ViewDEX [7]. Fifty central thoracic spine radiographs and forty lumbar thoracic spine radiographs from different horses were evaluated. For each radiograph the observers judged the visibility of the defined anatomical structures of the criteria according to five-grade scale ranging from “not fulfilled” to “definitely fulfilled”. Five different techniques to shape the x-ray beam were manufactured within this project. The different techniques consist of wedges that have different design. Two of the wedges are patent pending and the designs of the wedges are confidential. The techniques were constructed for imaging the central thoracic spine, cranial thoracic spine, caudal thoracic spine and caudal lumbar spine.

The image observations took place at two different workstations but the viewing conditions were kept as constant as possible.

3. Results

The effective dose to the assisting person is based on measurements performed at every examination of horses in Uppsala and Saxtorp during one typical work-week, a total of 30 resp. 20 complete examinations. The effective dose to the assisting person per image for four different examinations and for a whole examination (7-20 radiographs) is presented in Figure 2.

There are a significant difference between the examination at Uppsala and Saxtorp of the thoracic spine and the stifle joint (t-test $p < 0,05$). There are no significant difference between the examination of the phalanx, c-spine and a whole examination.

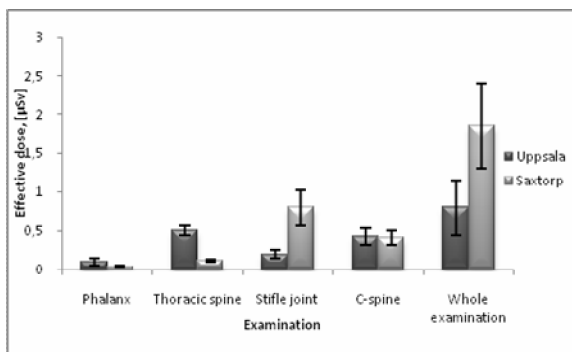


Fig. 2. Mean effective dose to the assisting person per image for four different examinations and for a whole examination (multiple images). The error bars show the standard deviation of the mean.

Image criteria scores were calculated based on image quality evaluation of images from seven horses that had central thoracic spine and the caudal lumbar spine examinations, without and with one of the custom-made wedges (See Figure 3 and Figure 4).

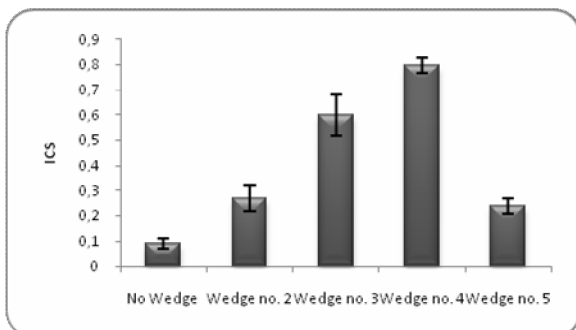


Fig. 3. Image criteria score without a wedge and with four different wedges used at the central thoracic spine examination.

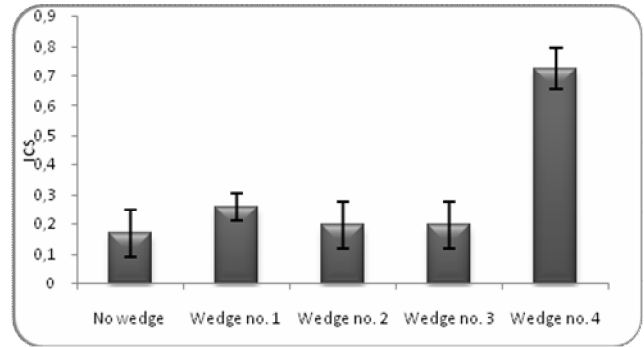


Fig. 4. Image criteria score without a wedge and with four different wedges used at the lumbar thoracic spine examination.

All wedges, except no. 3 in figure 4 improved the ICS. There are a significant improvement of the ICS (Wilcoxon, $p < 0,05$) when use wedge no. 4 both for the central thoracic spine and the caudal lumbar spine. The wedge that gave rise to the highest ICS was wedge no. 4 for both the central thoracic spine and the lumbar thoracic spine examinations.

4. Conclusions

The average effective dose to the assisting person ranged from 0.8 μSv to 1.85 μSv per examination (provided that protective clothing is worn), i.e. the effective dose is negligible. It is of big importance that the lead aprons are adapted well to minimize gap between the lead apron and the assisting person that could appear if the lead apron does not fit properly. Image criteria for spine examinations were developed and used in an image quality study. The image criteria proved to be a good method to quantify clinical image quality.

The use of a novel wedge significantly improves the image quality for the thoracic spine examination and makes it possible to image the whole spine with a single exposure.

5. References

1. Jönsson, H., Veterinärinspektioner 2005. SSI Rapport.
2. Hupe, O. and U. Ankerhold, Dose to persons assisting voluntarily during X-ray examinations of large animals. *Radiat Prot Dosimetry*, 2008. 128(3): p. 274-8.
3. European guidelines on quality criteria for diagnostic radiographic images. Commission of the European Communities, 1996.
4. Almen, A., et al., The use of reference image criteria in X-ray diagnostics: an application for the optimisation of lumbar spine radiographs. *Eur Radiol*, 2004. 14(9): p. 1561-7.
5. Lanhede, B., et al., The influence of different technique factors on image quality of chest radiographs as evaluated by modified CEC image quality criteria. *Br J Radiol*, 2002. 75(889): p. 38-49.

6. Bath, M. and L.G. Mansson, Visual grading characteristics (VGC) analysis: a non-parametric rank-invariant statistical method for image quality evaluation. *Br J Radiol*, 2007. 80(951): p. 169-76.
7. Borjesson, S., et al., A software tool for increased efficiency in observer performance studies in radiology. *Radiat Prot Dosimetry*, 2005. 114(1-3): p.45-52.

RADIOGRAPHIC FILM: STILL A VIABLE DOSIMETER?

Raju SRIVASTAVA, Sofie GILLIS, Carlos De WAGTER

Radiation therapy and Experimental Cancer Research, Ghent University, De Pintelaan 185, 9000 Ghent, Belgium

Abstract: The dosimetric accuracy of EDR2 radiographic films has been evaluated using 3D-inverse pyramid shaped beam intensity patterns to investigate the film response over the full dynamic dose range in both parallel and perpendicular direction. In the present study, coherent information was gathered to differentiate the extent to which EDR2 film is useful for total treatment verification, and for deciding when what compromises have to be made and what precautions have to be taken.

Keywords: Inverse pyramid, radiographic film, dosimetry, perturbation, IMRT

1. Introduction

In intensity modulated radiotherapy treatments (IMRT), not only the beam shape is geometrically optimized – as is also the case for 3D-CRT – but also the photon intensity across the beam area is actively shaped. This additional feature enables treatment plans with increased dose conformality to the tumour and more appropriate dose restriction to the normal tissues and organs at risk [1, 2]. However, the demands on the performance of plan design and delivery are very high. Treatments might hold a high number of irregular shaped beamlets, each contributing in a small extent to the overall dose distribution and geometrically accurate steep dose gradients are often required. Additionally, the complicated underlying physics of IMRT makes accurate dose calculation an arduous task; e.g. the delivered dose to shielded organs at risk is a superposition of many contributions like head scatter, transmission through the collimators, photons scattered in the patient and electrons transported from the adjacent high dose regions. The complexity of IMRT planning and delivery makes verification of the intended dose distributions an important issue (IMRT Collaborative Working Group 2001).

Herein, two approaches can be followed: one option is the dose delivery verification of the separate beams; the other is verifying the whole treatment at once. Both have their arguments for and against. In the first approach, detected discrepancies between measured and calculated values can be directly related to the individual beams or even segments while this is not easily possible for complete treatment verification. However, the impact of the deviations revealed by

single-beam verification cannot be straightforwardly extrapolated to the composed dose distribution. For the second approach, the verification of complete treatments, three-dimensional information is expedient. Only one real three-dimensional technique is available: gel dosimetry [3]. However, due to its main drawback of complexity, gel dosimetry is only slowly becoming available in research centers. Alternatively, 2D dosimeters such as radiochromic [4] and radiographic films [5] provide in one plane dosimetric data with high spatial resolution. Dosimetric information in the third dimension can be obtained by placing several films parallel to each other [6]. Radiochromic film is advantageous by being tissue equivalent. Although this type of film does not require chemical processing and allows ambient light conditions, it is still hampered by low signal to noise ratios and film uniformity issues.

The second alternative, EDR2 radiographic film, yields high spatial resolution, is readily available and its extended dose range make MU rescaling of the treatment fraction superfluous. EDR2 films are now an integral part of dosimetric QA, particularly in intensity-modulated radiation therapy (IMRT), image-guided radiation therapy (IGRT), and stereotactic radiosurgery (SRS). A detailed description and applications have been described in radiological text books [7, 8] and rather recently published in the Task Group 69 (TG-69) report [9]. However, a lot of controversy in literature exists about the dosimetric accuracy that can be achieved.

The process of radiographic film dosimetry appears to be easy: the interaction of radiation with film results after development in a blackening of the film. Quantifying the resulting optical density (OD) and

relating it to the applied doses, yields a sensitometric curve. Hence inversely, the OD of film irradiated with an unknown dose can be converted to dose using this sensitometric curve. In principle, the sensitometric curve should reflect unambiguously the sensitivity of a specific film to dose. However, many parameters can further influence the registered OD of the film: photon energy, irradiation conditions, composition of the emulsion, film processing and characteristics of the film scanner (densitometer). Some parameters are controlled: the irradiation of a set calibration films within each experiment together with the use of films of the same batch within one experiment already reduce the variability to a large extent. In addition, strict procedures regarding the irradiation conditions and the use of the film digitizer guarantee a further reduction of variability [10]. The remaining issues are photon energy spectrum and irradiation conditions. It is known that the high silver content in the film enhances the photoelectric interactions when compared to biological tissue, resulting in an over-response of the film to low-energetic photons. Additionally, published results might be confounded by the great impact a variety of experimental conditions have on the film sensitivity: air gaps [11], the material surrounding the film when bare (e.g. cassette material) [12] and film orientation with respect to the incident beam [13]. Especially, irradiation in parallel geometry requires special care in experimental set-up. Gillis et al [14] showed that in parallel irradiation geometry, inadequate contact between film and surroundings induces a gradual increase of film response with depth which might be confounded with an increase in film response due to the growing relative amount of low-energy photons with depth. Despite these drawbacks and controversies, radiographic film is used in many IMRT verification studies [15, 16, 17].

In this study, we evaluated the dosimetric accuracy of EDR2 radiographic film in IMRT fields at different depths for perpendicular as well as parallel film irradiation geometries. Finally, the self-perturbation and intrinsic directional sensitivity of the film were investigated. In this way, lucid information was gathered to discriminate whether radiographic film is at all useful for specific total treatment verification and what compromises have to be made.

2. Materials and methods

All measurements were performed using the 6 and 18 MV photon beams from a SLiplus linear accelerator (Elekta, Crawley, UK) equipped with the standard multileaf collimator (MLC). In this study, the X- and Y-directions are defined according to the Elekta convention. The Y-direction is the travelling direction of the leaves of the MLC. A 3-level valley (Inverse Pyramid) dose patterns was realized by combining six partly overlapping beamlets that all measured 20 cm in the X-direction (Figure 1). Inverse pyramid field is a laborious and challenging test for radiographic film dosimetry due to (1) relatively high-dose region are irradiated by a greater number of beamlets and thus by a greater proportion of in-field photons (2) relatively low-dose regions are irradiated by a smaller number of beamlets and thus by a greater proportion of outside-*penumbra* photons. For this reason the photon fluence spectrum varies significantly across a single fluence map. The contribution of low energy is larger than in calibrations condition so that it increases in photographic effects in the film with respect to tissue. On the other hand, regions with large scatter contribution mostly correspond to low dose rate. These are the reasons why the 3-dimensional inverse pyramid field was chosen for this investigation.

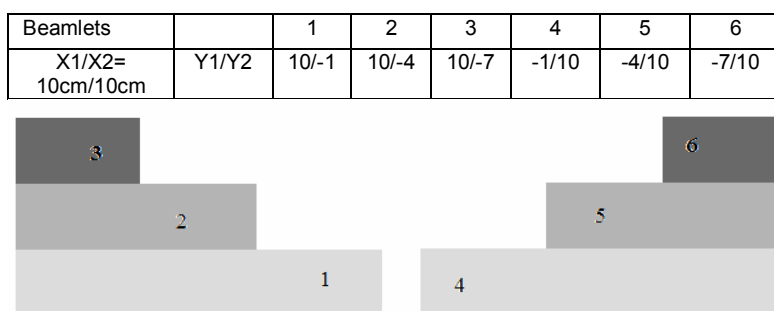


Fig. 1. Inverse pyramid field. Negative sign of beamlets in table indicates the MLC point which crosses the central axis. The moving direction of leaves is Y.

Film measurement: EDR2 (Eastman Kodak Co., Rochester, NY, USA) was used for this study. This film can handle a dose of more than 2 Gy without saturation [18]. This implies that a clinically applied fraction dose can be given to the film. All films were irradiated and calibrated in their ready-pack jackets. The films irradiated in one session were of the same batch, avoiding confounding effects by inter-batch differences [19]. As we always irradiated the films in

the evening and did not develop them before the next morning, we ensured that the films had reached their stable OD [20]. The film processor (Kodak RP X-Omat processor model M7B with standard RP X-Omat chemicals) was not dedicated to film dosimetry alone, so that one “dummy” film was processed before each development session to ensure proper working conditions of developer. Residual effects of drift in temperature or composition of the developer solution

during the development session were randomized by developing the films in arbitrary order. These rigorous precautions were taken to enhance consistency of the measurements.

Both calibration and measurement films were scanned using a VXR-12 film scanner (Vidar Systems Corporation, Herndon, VA, USA). The film scanner was operated with a resolution of 75 dpi (0.34 mm/pixel) an encoding depth of 12 bit/pixel, and a digitizing speed of 14 ms/line. The film scanner was switched on 15–20 min beforehand to avoid warm-up effects [10] and procedure followed as described by Martens et al [30]. Film analysis was performed using in-house written routines in the Matlab environment (The Math Works Inc., Natick, MA, USA, and Matlab 6.5).

Film calibration: All calibration films were irradiated by 5 cm x 5 cm fields in a polystyrene slab phantom of 30 cm x 30 cm x 20 cm in 'perpendicular' geometry (Figure 2a) – with the radiation beam incident at right angle to the film. For the 6 MV beam quality, the films were positioned at 5 cm depth in the slab phantom and the SSD was 95 cm. For 18 MV the films were located at 10 cm depth and a SSD of 90 cm was established.

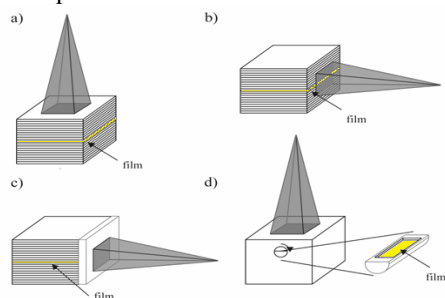


Fig.2. Experimental phantom geometries: a) perpendicular geometry b) parallel geometry c) geometry for assessment of self-perturbation d) intrinsic directional sensitivity.

Self perturbation: The response at a certain depth in parallel geometry might be influenced by the part of the film more upfront in the beam and the phantom [21] because radiographic film is not tissue equivalent. The experimental set-up to investigate this issue was similar to the set-up for parallel irradiation. The film was aligned with the edge of the horizontal slabs of the phantom. Then, various thicknesses of slabs were put vertically in front of this phantom: 0, 4, 9 and 14 cm (figure 2c) and table was adjusted laterally to keep the SSD equal. A rigorous junction without air gaps between the horizontal plates and the vertical ones upfront was complicated by the film. Therefore, the film, in its ready-pack jacket, was shortened beforehand at one side with a cutting machine in the dark room in order to achieve a clear border of film and its envelope. In that way the film could be aligned accurately with the border of the polystyrene slab. To avoid incoming light in the opened ready-pack jacket, the polystyrene plates, between which the film was inserted, were covered by black insulation tape. The gantry was rotated to a horizontal central axis orientation and a 5 cm x 5 cm field with a beam quality of 6 MV was set and 2.00 Gy was delivered to the isocentre. Each film exposure was repeated three times

and the images from the three films were averaged in terms of dose for reproducibility reasons.

Directional sensitivity: A cubic high-density polyethylene (0.94-0.98 g/cm³) phantom was designed and constructed (Figure 2d) with a hole in which a cylindrical holder fitted to discriminate local from distant directional effects. This holder, containing a small elongated piece of film along its diagonal, could be rotated in the phantom. In the dark room, three films were cut into 8 pieces of 3 cm x 20 cm, exactly fitting into the holder together with surrounding white paper and jacket. In this way, the same configuration is guaranteed as in the other experiments. The rotation axis of the cylindrical film holder is positioned in the isocentric plane. A dose of 1.5 Gy was delivered to the isocentre by a 6 MV 5 cm x 5 cm beam SSD of 95 cm was established. Eight different film orientations were considered: 0, 5, 10, 20, 30, 50, 70 and 90°. 0° implies a film orientation containing the central beam axis and, obviously, 90° means perpendicular irradiation of the film. For each film orientation three films were exposed. The OD in the middle of each film piece i.e. film response at the isocentre, was evaluated. The resulting OD values of the three films irradiated in the same configuration were then averaged.

The same procedure was followed for the inverse pyramid 6 MV beam as fig.1 at 20 cm depth in the phantom. Finally, this experiment was repeated for a 0.5 cm x 5 cm 6 and 18 MV beam at depth of 5 cm and SSD of 95 cm.

3. Results and discussion

Figure 3 shows the results of inverse pyramid irradiation in perpendicular and parallel geometries for 6MV and 18MV beam quality compared to diamond measurements.

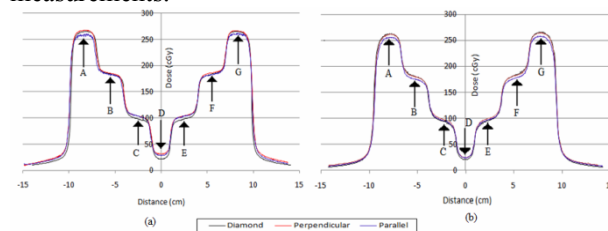


Fig.3. Inverse pyramid profiles measured with diamond detector, film in perpendicular geometry and film in parallel geometry: a) 6 MV SSD = 95 cm d = 5 cm (85 MU/segment) b) 18 MV SSD = 90 cm d = 10 cm (70 MU/segment). The letters A-G indicate the areas where dose has been evaluated quantitatively.

For the same IMRT beam in the same dose regions (Inverse Pyramid) for 6 MV, at evaluation spot A and G (i.e. minimal relative dose due to scatter), the local deviation from the diamond measurements varies from 0.2 to 0.5 % for perpendicular irradiated films. For parallel irradiated films, the local deviation varies from -2.4% to -2.2%.

In the central regions without primary dose contribution, (region D for the inverse-pyramid dose pattern in Figure 3) the over-response of perpendicular irradiated film varies from 27.8% for the 6 MV large inverse pyramid beam. In identical irradiation

geometry, parallel irradiated film over-responds by 23.2%.

For the same IMRT beam in the same dose regions but in an 18 MV beam quality, the local deviation from the diamond measurements vary from -0.4% to -0.2% for perpendicular irradiated films. For parallel irradiated films these local deviations vary from -2.9% to -2.7%.

We found that the parallel irradiated films show a lower response than the film irradiated in perpendicular geometry systematically.

Pragmatic methods to suppress low-energy over-response of radiographic film have been proposed in several papers. For open beams Williamson *et al* [22] presented a depth-dependent sensitometric curve fitted to a mathematical equation. However, this method is specific for each field size and does not correct fully the over-response in the outside-penumbra region. Another published approach to overcome the over-response problem to low-energy photons is a scintillation method [26]. Hereby, a film is sandwiched between two plastic scintillation screens to enhance the film response to upstream electrons, and therefore minimize the over-response caused by low-energy photons. Their method suffers from poor uniformity of the scintillation screens and has only been evaluated for percentage depth dose curves. Burch *et al* [25] proposed a filtration method: scattered low-energy photons are prevented from reaching the film by placing a lead foil parallel to the film. This method described and tested by Burch *et al* [25] and Yeo *et al* [26] for regular field profiles and depth dose curves and it was evaluated for more complicated IMRT beams by Yeo *et al* [23], Ju *et al* [27] and Bucciolini *et al* [28]. However, the optimal filter thickness is in principle dependent on depth, field size, energy and the orientation of the filter and film. The applicability of this filter technique needs therefore still more investigation for total treatment verification. Recently, a Monte Carlo based spectral and absorbed dose correction was presented by Palm *et al* [29]. They achieved good results but Monte Carlo simulations are needed for any verification rendering the method rather cumbersome. We thought that the cause of lower response of radiographic film in parallel orientation can be explained by a recombination effect. Radiographic film behaves as a solid-state process occurring in the silver bromide (AgBr) crystals of the film emulsion.

After ionization of AgBr, electrons are released into conduction band and trapped at imperfection sites. Recombination of electrons and holes at recombination centers (imperfection) would be expected to occur as a second-order process, being proportional to the product of the numbers of electrons and holes. The alternative process leading to the formation of silver (permanent hole-trapping, nucleation and growth of silver particles) would probably proceed with lower order kinetics. For this reason, it is to be expected that recombination is more probable under condition that large number of electrons and holes are simultaneously present in the grain. They probably released their energy in the form of lattice vibrations or heat energy.

The increasing recombination effect results in a reduced sensitivity.

Figure 4 represents a 6-MV central depth dose curve of a 5 cm x 5 cm field measured with film in a parallel geometry together with different partial depth dose curves obtained by placing the respective film edges at different depths: 0, 4, 9 and 14 cm. No significant response changes can be detected when placing the front edge of the film deeper into the phantom. The response of the film irradiated in parallel geometry at a certain depth is obviously not influenced by film material situated more upfront in the beam.

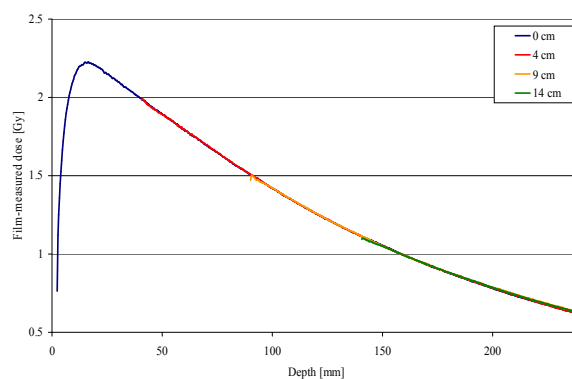


Fig. 4. Superposition of four partial depth dose curves measured with 4 sets of films retracted over 0, 4, 9 and 14 cm respectively in parallel irradiation geometry for a 6MV 5 cm x 5 cm beam. SSD = 95 cm. 2 Gy was delivered to the isocentre for all curves. The colors show the start of each set of retracted films.

Figure 5 represents the OD as function of incidence angle for four irradiation geometries: in the isocentre at 5 cm phantom depth in a 5 cm x 5 cm 6 MV and at position D of the 6 MV inverse pyramid beam at 20 cm depth in the phantom and in the isocentre in a 0.5 x 5 cm 6 and 18 MV beam.

For the 6 MV 5 cm x 5 cm beam, the film response gradually decreases by 3.5% when evolving from perpendicular to parallel film irradiation. Reducing the field size to 0.5 cm x 5 cm brings the gradual decrease up to 6%. For 18 MV this field size revealed no further decrease. Inverse-pyramid field shows less than 1% decrease.

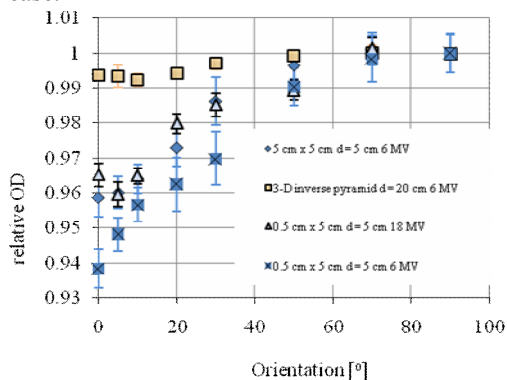


Fig. 5. Intrinsic directional sensitivity at 5 cm depth in a 6 MV 5 cm x 5 cm and 0.5 x 5 cm beam, 18 MV 0.5 cm x 5 cm beam and in the central region (D) of the 6MV inverse-pyramid dose pattern at 20 cm depth. Error bars are standard errors of the mean. 0° stands for perpendicular irradiation and 90° for perpendicular irradiation are normalised to 1.

4. Conclusion

While for the measurement in a parallel plane to the beam axis EDR2 film is reported to be lower response than perpendicular irradiated film for IMRT beams which involve great amount of low-energy scattered photons. This can be fully described to intrinsic directional sensitivity. This is a pure local effect that can be largely overcome by appropriate calibration measurements and choice of verification plane in total treatment verification. The film irradiated in parallel geometry at a certain depth is clearly not influenced by film material situated more upfront in the beam. There is no extra self absorption by the film itself.

5. References

- De Neve W, Claus F, Duthoy W et al. 2002 Intensity modulation techniques for improvement of normal tissue tolerance. *Front. Radiat Ther. Oncol* 37 163-173
- Chao K S C, Majhail N, Huang C-J, Simpson J R, Perez C A, Haughey B and Spector G 2001 Intensity-modulated radiation therapy reduces late salivary toxicity without compromising tumor control in patients with oropharyngeal carcinoma: a comparison with conventional techniques *Radiother. Oncol* 61 275-280
- Vergote K, De Deene Y, Duthoy W, De Gerssem W, De Neve W, Achten E, De Wagter C 2004 Validation and application of polymer gel dosimetry for the dose verification of an intensity-modulated arc therapy (IMAT) treatment *Phys. Med. Biol.* 49 287-305
- Cadman P, Bassalow R, Sidhu N P S, Ibbott G, Nelson A. 2002 Dosimetric considerations for validation of a sequential IMRT process with a commercial treatment planning system. *Phys. Med. Biol.* 47 3000-3010
- Low D A, Mutic S, Dempsey J F, Gerber R L, Bosch W R, Perez C A, Purdy J A 1998 Quantitative dosimetric verification of an IMRT planning and delivery system. *Radiother Oncol* 49 305-316
- Robar J L, Clark B G 2000 A practical technique for verification of three-dimensional conformal distributions in stereotactic radiosurgery *Med. Phys.* 27 978-987
- Attix F H Introduction to Radiological Physics and Radiation Dosimetry New York: John Wiley & Sons, 1986.
- Khan F. M. The Physics of Radiation Therapy Philadelphia, PA: Lippincott Williams & Wilkins, 2003.
- Pai S, Das I J, Dempsey J F, Lam K L, LoSasso T J, Olch A J, Palta J R, Reinstein L E, Ritt D, and Wilcox E 2007 TG-69: Radiographic film for megavoltage beam dosimetry *Med Phys* 34 2228-2258
- Mersseman B, De Wagter C 1998 Characteristics of a commercially available film digitizer and their significance for film dosimetry. *Phys. Med. Biol.* 43 1803-1812
- Suchowerska N, Hoban P, Butson M, Davison A, Metcalfe P 2001 Directional dependence in film dosimetry: radiographic and radiochromic film. *Phys. Med. Biol.* 46 1391-1397
- Fujisaki T, Saitoh H, Hiraoka T, Kuwabara A, Abe S, Inada T 2003 Contribution of Cerenkov radiation in high-energy X-ray and electron beam film dosimetry using water-substitute phantoms. *Phys. Med. Biol.* 48 N105-N109
- Danciu C, Proimos B S, Rosenwald J C, Mijnheer B J. 2001 Variation of sensitometric curves of radiographic films in high-energy photon beams. *Med. Phys.* 28 966-974
- Gillis S, De Wagter C 2005 Practical and dosimetric implications of a new type of packaging for radiographic film *Phys. Med. Biol.* 50 N63-N72
- Budgell G J, Perrin P A, Mott J H L, Fairfoul J, Mackay R I 2005 Quantitative analysis of patient-specific dosimetric IMRT verification. *Phys. Med. Biol.* 50 103-119
- Childress N L, Dong L, Rosen I, 2002 Rapid radiographic film calibration for IMRT verification using automated MLC fields. *Med. Phys.* 29 2384-2390
- Stock M, Kroupa B, Georg D 2005 Interpretation and evaluation of the γ index and γ index angle for the verification of IMRT hybrid plans. *Phys. Med. Biol.* 50 399-411
- Chetty I J and Charland P 2002 Investigation of Kodak Extended Dose Range EDR film for megavoltage photon beam dosimetry. *Phys. Med. Biol.* 47 3629-3641
- Bos L J, Danciu C, Cheng C W, Brugmans M J P, van der Horst A, Mincken A, Mijnheer B J 2002 Interinstitutional variations of sensitometric curves of radiographic dosimetric films. *Med. Phys.* 29 1772-1780
- Childress N L, Rosen I, 2004 Effect of processing time delay on the dose response of Kodak EDR2 film *Med. Phys.* 31 2284-2288
- Van Battum L J and Heijmen B J M Film dosimetry in water in a 23 MV therapeutic photon beam 1995 *Radiother. Oncol* 34 152-159
- Williamson J F, Khan F M, Sharma S C 1981 Film dosimetry of megavoltage photon beams: A practical method of isodensity-to-isodose curve conversion *Med. Phys.* 8 91-98
- Yeo I J, Beiki-Ardakani A, Cho Y, Heydarian M 2004 EDR2 film dosimetry using low-energy photon filters. *Med. Phys.* 31 1960-1963
- Yeo I J Wang C-K C, Burch S E A 1997 A filtration method for improving film dosimetry in photon radiation therapy *Med. Phys.* 12 1943-1953

25. Burch S E, Kearfott K J, Trueblood J H, Sheils W S, Yeo J I, Wang C K C 1997 A new approach to film dosimetry for high energy photon beams: lateral scatter filtering Med. Phys. 24 775-783
26. Yeo I J Wang C-K C, Burch S E 1999 A new approaches to film dosimetry for high energy photon beams using organic plastic scintillators. Phys. Med. Biol. 44 3055-3069
27. Ju S G, Qhn Y C, Huh S J, Yeo I J 2002 Film dosimetry for intensity modulated radiation therapy: dosimetric evaluation Med. Phys. 29 351-355
28. Bucciolini M, Buonamici F B, Casati M 2004 Verification of IMRT fields by film dosimetry Med. Phys. 31 161-168
29. Palm A, Kirov A S, LoSasso T 2004 Predicting energy response of radiographic film in a 6 MV x-ray beam using Monte Carlo calculated fluence spectra and absorbed dose. Med. Phys. 31 3168-3178
30. Martens C, Claeys I, De Wagter C, De Neve W 2002 The value of radiographic film for characterization of intensity-modulated beams Phys. Med. Biol. 47 2221-22

QUANTUM DOTS AS ENERGY DONORS FOR PHOTSENSITIZERS: PERSPECTIVES FOR PHOTODYNAMIC THERAPY OF CANCER

Jurga VALANČIŪNAITĖ*, Ričardas ROTOMSKIS***

*Laboratory of Biomedical Physics of Vilnius University Institute of Oncology, Baublio 3B LT- 08406, Vilnius, Lithuania; **Laser research center, Vilnius University, Sauletekio 9, Bldg. 3, LT-10222 Vilnius, Lithuania

Abstract: In this work we review the perspectives of using semiconductor quantum dots in the photodynamic therapy of cancer. The special attention is paid to studies where quantum dots were investigated as resonance energy donors to porphyrin-type photosensitizers. One example of self-assembled quantum dot-photosensitizer complex with the ability of energy transfer, which was examined by our group, is presented as well.

Keywords: Photodynamic therapy, PDT, quantum dots, nanocrystals, porphyrin, photosensitizer, resonance energy transfer, FRET, singlet oxygen.

1. Introduction

Cancer is a leading cause of death worldwide. Late diagnosis and inefficient treatment of cancer lead to large number of deaths every year. Nanotechnology can offer new solutions for fighting this disease. Due to nano-dimensions, unique optical properties, high stability and easy surface modification by binding different functional groups and biomolecules, semiconductor quantum dots (QDs) are considered as promising materials for many biological and medical applications. Recently it has been suggested to use QDs not only for diagnostic purposes but also in the photodynamic therapy (PDT) of cancer [1]. PDT is a treatment that uses a photosensitizing drug (PS), usually porphyrin-type molecules, and the light to cure the malignant tumors and certain non-malignant pathologies. Once the light is applied, the excited molecules of photosensitizer generate cytotoxic reactive oxygen species (ROS), such as singlet oxygen ($^1\text{O}_2$) (type II reaction) or free radicals (type I), which irreversibly damage cancer cells. Desired features for the ideal PDT sensitizer are chemical purity, simplicity of synthesis, significant absorbance in the red spectral region (in optical window of biological tissues), high quantum yield for generation of photochemical reactions, preferential tumor localization, minimal dark toxicity and rapid clearance from normal tissue. It is believed that using QD-PS system could improve PDT in many ways. First of all, due to tunable by QD size emission spectrum, high emission quantum yield and long lifetime, QDs can work as efficient energy donors for PS. The energy transmitted from QD to PS could

further be used for generation of $^1\text{O}_2$ or free radicals. It is established that the energy from QD to PS is transmitted by non-radiative Förster resonance energy transfer mechanism [1]. Moreover, in several recent papers it was shown that QDs are potential photosensitizers in their own i.e QDs can generate ROS [1-3]. Scheme in Fig. 1 illustrates processes, which could be induced after photoexcitation of QD-PS complex during PDT. The optical properties of QDs such as high extinction coefficient (10^5 - 10^6 $\text{M}^{-1}\text{cm}^{-1}$) and broad absorption spectrum would make easier to excite QD-PS complex. High extinction coefficient of QDs absorbing in red or NIR spectral region would allow achieving the photosensitization in deeper tissue layers. Further, high photostability of QDs as well as the ability to control the QDs encapsulation and surface functionalization for improved water solubility, biocompatibility and targeting make QDs favorable for PDT.

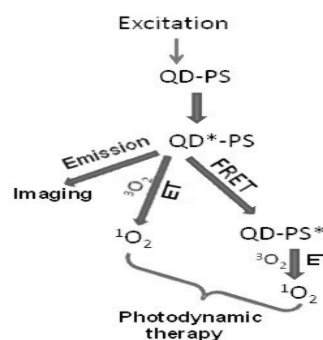


Fig.1. The processes induced after photoexcitation of QD in quantum dot-photosensitizer (QD-PS) complex.

The absorbed energy by QD could be returned by emission, which is an advantage when QDs are used for imaging. The excitation energy could also be transferred to bound photosensitizer molecule via Förster resonance energy transfer (FRET) mechanism. Photosensitizer excited by this indirect way can further pass the energy to surrounding oxygen molecules ($^3\text{O}_2$) by exciting them to singlet state ($^1\text{O}_2$) [1]. The third possible way is when photoexcited QD* directly generates $^1\text{O}_2$ [1, 2] or other reactive oxygen species [3]. The last two ways are desirable for PDT.

Several comprehensive reviews where the numerous investigations of different aspects using QDs for PDT are summarized have been published recently [4-7]. Here we will focus on QD-porphyrin systems where QD works as energy donor for porphyrins. One example of non-covalent QD-PS complex investigated by our group [8] will be presented as well.

2. Quantum dots as resonance energy donors for classical photosensitizers

Förster resonance energy transfer (FRET) is a non-radiative transfer of excitation energy from an excited donor fluorophore to a ground-state acceptor fluorophore [9]. FRET process results from dipole-dipole interactions and its rate is depended on: 1) the degree of spectral overlap between donor luminescence and acceptor absorption (Fig. 2) 2) the sixth power of the separation distance between the donor and acceptor pair, and 3) orientations of donor and acceptor transition dipoles. FRET efficiency is determined experimentally from the fluorescence quantum yields or lifetimes of the donor in the absence (Φ_D, τ_D) and presence of the acceptor ($\Phi_{\square D}, \tau_{\square D}$) using Eq. (1).

$$E = 1 - \frac{\Phi'_{\square D}}{\Phi_D} = 1 - \frac{\tau'_{\square D}}{\tau_D} \quad (1)$$

FRET efficiency is related to the distance between the donor and acceptor pair (r) by Eq. (2).

$$E = \frac{R_0^6}{R_0^6 + r^6} \quad (2)$$

where R_0 (the Förster distance) is the critical distance between the donor and the acceptor molecules for which efficiency of energy transfer is 50%. R_0 depends on the quantum yield of the donor, Eq. (3) as

$$R_0^6 = 8,8 \times 10^{23} \kappa^2 n^{-4} \Phi_D J \quad (3)$$

where κ^2 is the dipole orientation factor ($\kappa^2=2/3$ is often assumed, considering that both donor and acceptor are isotropically oriented during the excited state lifetime), n is the refractive index of the medium and J is the spectral overlap integral, calculated as

$$J = \int f_D(\lambda) \varepsilon_A(\lambda) \lambda^4 d\lambda \quad (4)$$

where f_D is the normalized donor emission spectrum, and ε_A is the acceptor molar extinction coefficient.

FRET between organic molecules is quite common process and is widely exploited in a variety of biological studies [9]. However, only recently FRET was reported in hybrid nanomaterials composed of inorganic semiconductor QDs and organic dyes.

The first demonstrations that QDs could efficiently transfer energy via FRET were reported in QD systems between the different sizes of QDs. In the pioneering works performed by Bawendi group it was shown that FRET occurs between closely-packed QDs of two different diameters: smaller (38.5 Å diameter) serving as exciton donors and larger ones (62 Å) functioning as energy acceptors [10]. Further studies demonstrated that inorganic QDs could perfectly function as FRET donors for different organic fluorophores [11, 12], including porphyrin-type photosensitizers used for PDT [1].

Using QDs as FRET donors to photosensitizer molecules are particularly attracting due to: 1) the ability to tune the emission wavelength by either simple manipulation of the nanocrystal dimension and/or modification of the composition of the inorganic core used, which can allow achieving a better spectral overlap with an acceptor absorption, 2) high quantum yield and long lifetime of emission, 3) resistance to photobleaching, 4) ease of surface modifications and subsequent possibilities of stable and controllable binding of donor molecules.

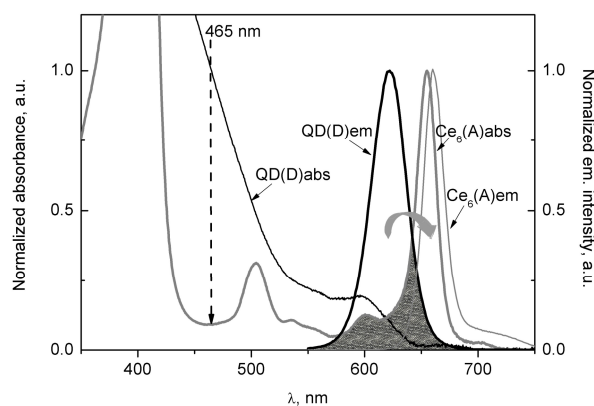


Fig. 2. Normalized absorption and emission spectra of CdSe/ZnS QDs and photosensitizer chlorin e_6 in phosphate buffer solution (PBS) of pH 7. Filled area indicates the overlap of QDs (donor) emission with the absorption spectrum of chlorin e_6 (acceptor). The arrow shows the excitation at $\lambda_{\text{ex}}=465$ nm, used for FRET studies.

In our studies, we used a second-generation photosensitizer, chlorin e_6 (Ce_6) and water-soluble CdSe/ZnS quantum dots with lipid-based coating bearing external amino groups (commercially available from eBioscience) [8]. QDs were chosen according to their emission maximum in the way to full fill the condition of spectral overlap between the emission of QD (donor) and absorption of Ce_6 (acceptor) for FRET to occur. Fig. 2 demonstrates the spectral overlap of studied QD- Ce_6 pair. The absorption spectrum of QD is

broad with gradual intensity decrease towards the red spectral side, while the emission band is narrow with the maximum at 620 nm. The emission of QDs partially overlaps two last absorption bands of Ce₆. For FRET studies, the excitation wavelength ($\lambda_{\text{ex}}=465$ nm) was selected to coincide with the minimum of Ce₆ absorption spectrum in order to reduce contributions resulting from the direct excitation of Ce₆.

2.1 Quantum dot-porphyrin systems in organic solvents

First studies on QD-photosensitizer complexes were performed in organic solvents [1, 13-15]. In the earliest work reported by Samia et al. the spectral measurements of trioctylphosphine oxide (TOPO) capped-CdSe QDs with linked silicon phthalocyanine (Pc) through an alkyl amino group on the photosensitizer's axial substituent were performed in toluene [1]. The primary condition for FRET to occur was fulfilled – the emission band of QDs overlapped with the absorption of Pc. Using excitation wavelength where only QDs absorbed, the authors observed a decrease in QD's emission, while the emission of Pc appeared in the spectrum. It was evaluated that QDs could work as FRET donors for conjugated Pc molecules with 77% FRET efficiency. In that work the key principles of using QDs for PDT were formulated. In the later works of Burda group, the efficiency of energy transfer between CdSe QDs and Si Pc molecules were studied as function of length of chain linkers, their functional groups, also thickness of capping layers of QDs. For example, it was noticed that the efficiency of energy transfer between QDs and Pc increased with the chain length of the linker. These findings were opposite to a FRET process, which efficiency depends on donor-to-acceptor separation distance with an inverse 6th power (Eq. 2.). However this contradiction was explained by the better interdigitization of the longer phthalocyanine linker chains into the organic capping layer of QDs [14, 15].

The formation of CdS/ZnS QDs capped with TOPO and pyridyl-substituted porphyrins non-specific conjugates in toluene solution was demonstrated by Zenkevich et al. [16, 17]. It was shown that the quenching efficiency of QD emission by porphyrins was dependent on the number and position of pyridyl rings, as well on the position of nitrogen atom within the pyridyl ring. This was related to the manner and orientation of pyridyl groups upon porphyrin attachment to the surface of QDs. It was concluded that pyridyl-substituted porphyrin molecules anchor on the CdSe/ZnS surface in a nearly perpendicular fashion with two nitrogen lone pair orbitals forming coordination bonds with the surface. Authors stated that FRET is a good qualitative tool to identify formation of QD-porphyrin complexes [16].

2.2. Quantum dot-porphyrin systems in aqueous medium

Although studies of QD-porphyrin complexes in organic solutions had confirmed the possibility of FRET in such

systems, however these complexes were not suitable for biological medium due to the lack of water solubility.

The first study on QD-porphyrin complex in aqueous solution was reported by Shi et al. [18]. Water-soluble CdTe QDs coated with 2-aminoethanethiol (cysteamine) and meso-tetra(4-sulfonatophenyl)porphine (TSPP) as a photosensitizer were used. It was proposed that QD-TSPP complex was formed via electrostatic interaction. The measurements of singlet oxygen in D₂O revealed that such complex was able to produce singlet oxygen with quantum yield of 0.43. Since QD-TSPP complex was excited at the wavelength where the absorption of free TSPP was minimal, the authors suggested that singlet oxygen was produced via excitation of QD followed by a FRET mechanism. No singlet oxygen was generated when QDs were excited in the absence of TSPP, this was in contrast to results obtained by Samia et al. who observed a small amount (5%) of singlet oxygen formed directly from excitation of CdSe QDs [1].

Further attempts to produce stable QD-porphyrin complexes in aqueous solutions via electrostatic interaction were reported [19-23]. However, in most of these studies the aggregation of formed QD-porphyrin complex arose as main instability problem. For instance, aggregation was obtained under formation of complex between CdTe(TGA) QDs and metal-free tetra(p-trimethylamino) phenylporphyrin [19] as well between CdTe(cysteamine) QDs and AlOH-tetrakisulfophthalocyanine [20]. Addition of CdTe(MPA) QDs also caused the aggregation of cationic zinc phthalocyanine in methanol-water solution [22].

The interesting results were obtained with TGA capped CdTe QDs and porphyrins having differently charged meso-substituents [23]. The quenching of QD luminescence was observed upon increasing concentration of both negatively and positively charged porphyrins, however the intensity of only negatively charged porphyrins increased and became higher than in the absence of QDs. The authors concluded, that the negatively charged porphyrins interact with QDs through energy transfer mechanism, while positively charged porphyrin molecules interacts through charge transfer mechanism [23].

The first covalent QD-PS conjugates were created by linking peptide-coated CdSe/CdS/ZnS QDs and photosensitizers, Rose Bengal and chlorin e₆ [24]. The dramatic increase of fluorescence of both Rose Bengal as well as chlorin e₆ in comparison to photosensitizers alone was observed after its covalent attachment to QDs. This observation was accompanied by a decrease in emission intensity and lifetime of QDs. Moreover, it was shown that such conjugates are able not only undergo FRET but also produce singlet oxygen. The highest quantum yield of singlet oxygen generation was obtained for QD-Ce₆ sample (0.31).

2.3. Complex of water-soluble CdSe/ZnS quantum dot and chlorine e₆

In this section, we will shortly present our results on non-covalent complex formation between water-soluble

CdSe/ZnS QDs and chlorin e₆ [8]. As was shown above, QDs were selected in the way to full fill the condition of spectral overlap between its emission and the absorption band of Ce₆ (Fig. 2). When Ce₆ was added to QD solution, the fluorescence band of Ce₆ underwent a bathochromic shift from 660 nm to 670 nm. Upon increase in Ce₆ concentration, the intensity of QDs emission significantly decreased, while the intensity of Ce₆ fluorescence at 670 nm was increasing simultaneously (Fig. 3). It should be noted that the excitation wavelength at 465 nm was used, which coincided with the minimum of Ce₆ absorption in order to reduce contributions resulting from direct excitation of Ce₆.

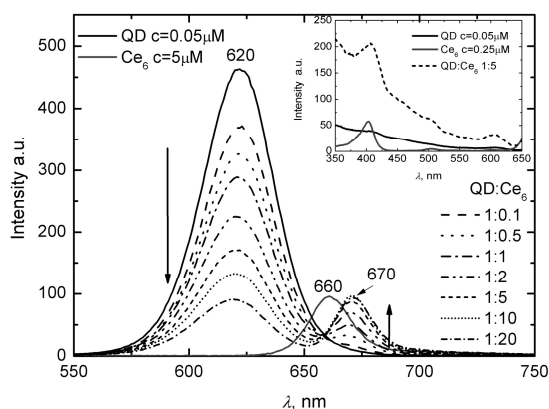


Fig. 3. Emission spectra of QD, Ce₆ and mixed QD-Ce₆ solutions at increasing QD:Ce₆ molar ratio from 1:0.1 to 1:20, λ_{ex} = 465 nm. The inset shows Emission excitation spectra of corresponding solutions recorded at λ_{em} = 670 nm.

The emission lifetime measurements of QDs showed a substantial shortening of QDs lifetime in the presence of Ce₆ (Fig. 4). These findings indicated that the efficient process of energy transfer from QDs to bound Ce₆ molecules occur within self-assembled QD-Ce₆ complex.

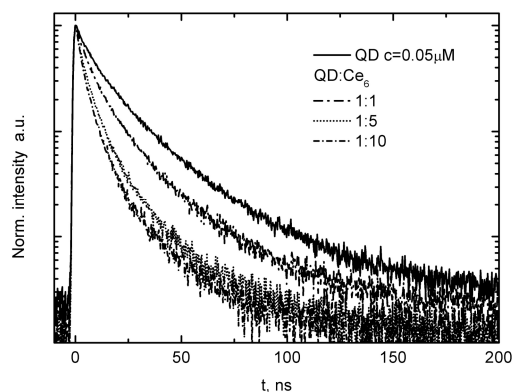


Fig. 4. Photoluminescence decay of QD and QD-Ce₆ solutions at increasing QD:Ce₆ molar ratio from 1:1 to 1:10 registered at λ_{em} = 620 nm.

In the first approach, we expected that the electrostatic interaction between the positively charged amino groups of QDs coating and negatively charged carboxyl groups of Ce₆ might be a pivotal force for QD-Ce₆ complex

formation. However, the experiments with similar QDs, except that terminal amino (positively charged) groups were changed to carboxyl (negatively charged) also revealed the formation of Ce₆ fluorescence band at 670 nm. Meanwhile, the measurements performed with QDs, which did not have lipid-based coating, but were capped with MSA or TGA did not result any changes in Ce₆ spectrum. This suggested that lipid-based coating plays the major role in QD-Ce₆ complex formation. Indeed, similar bathochromic shift of fluorescence band is observed upon binding of Ce₆ to plasma proteins, LDL and DOPC unilamellar vesicles [25], i.e. when Ce₆ molecules localize in hydrophobic environment. Most probably, upon binding to QD, the nonpolar part of Ce₆ molecule immerse in the hydrophobic part of lipid coating of QD. This is also in agreement with Ce₆ cellular localization studies, which demonstrated that Ce₆ molecules tend to localize in most cellular membranes [26] and membrane models [27]. By summarizing the above results we proposed the model of QD-Ce₆ complex formation with schematic illustration how Ce₆ molecules might be arranged within this complex in Fig. 5.

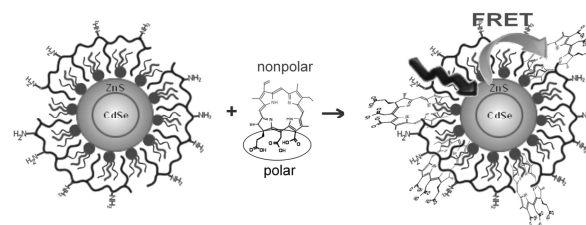


Fig. 5. Model of QD-Ce₆ complex formation. Ce₆ bears polar carboxyl groups on one side of the porphyrin macro cycle whereas the opposite side is rather nonpolar. Most probably upon binding to QDs, the nonpolar part of Ce₆ molecule immerse in the hydrophobic part of lipid coating of QD, while carboxyl groups are exposed to water surrounding.

Our findings imply that the hydrophobic interaction might be a promising way for creating QD-photosensitizer complexes for PDT.

3. Conclusions

As the primary step in the long cascade of photosensitization the effective energy transfer from QDs to photosensitizers is vital for using QDs in photodynamic therapy of cancer. Although, the first successive attempts in development of such QD-PS systems were made, however further efforts are needed to produce stable, biocompatible conjugates with a high quantum yield of singlet oxygen or ROS generation.

4. Acknowledgement

This work was supported by the project "Postdoctoral Fellowship Implementation in Lithuania" (VP1-3.1-ŠMM-01-V-01-001).

5. References

- Samia, A.C.S., Chen, X.B., and Burda, C., Semiconductor quantum dots for photodynamic therapy. *Journal of the American Chemical Society*, 2003, 125(51), p. 15736-15737.
- Zhang, Y., et al., Time-dependent photoluminescence blue shift of the quantum dots in living cells: Effect of oxidation by singlet oxygen. *Journal of the American Chemical Society*, 2006, 128(41), p. 13396-13401.
- Cho, S.J., Maysinger, D., Jain, M., Roder, B., Hackbarth, S., and Winnik, F.M., Long-term exposure to CdTe quantum dots causes functional impairments in live cells. *Langmuir*, 2007, 23(4), p. 1974-1980.
- Juzenas, P., et al., Quantum dots and nanoparticles for photodynamic and radiation therapies of cancer. *Advanced Drug Delivery Reviews*, 2008, 60(15), p. 1600-1614.
- Chatterjee, D.K., Fong, L.S., and Zhang, Y., Nanoparticles in photodynamic therapy: An emerging paradigm. *Advanced Drug Delivery Reviews*, 2008, 60(15), p. 1627-1637.
- Yaghini, E., Seifalian, A.M., and MacRobert, A.J., Quantum dots and their potential biomedical applications in photosensitization for photodynamic therapy. *Nanomedicine*, 2009, 4(3), p. 353-363.
- Biju, V., Mundayoor, S., Omkumar, R.V., Anas, A., and Ishikawa, M., Bioconjugated quantum dots for cancer research: Present status, prospects and remaining issues. *Biotechnology Advances*, 2010, 28(2), p. 199-213.
- Valanciunaite, J., Skripka, A., Streckyte, G., and Rotomskis, R. Complex of water-soluble CdSe/ZnS quantum dots and chlorin e6: interaction and FRET. in XII International Conference on Laser Applications in Life Sciences. 2010. Oulu.
- Lakowicz, J.R., Principles of Fluorescence Spectroscopy. 3 ed. 1999, New York: Springer Science+Business Media.
- Kagan, C.R., Murray, C.B., Nirmal, M., and Bawendi, M.G., Electronic energy transfer in CdSe quantum dot solids. *Physical Review Letters*, 1996, 76(9), p. 1517-1520.
- Clapp, A.R., Medintz, I.L., Mauro, J.M., Fisher, B.R., Bawendi, M.G., and Mattoussi, H., Fluorescence resonance energy transfer between quantum dot donors and dye-labeled protein acceptors. *Journal of the American Chemical Society*, 2004, 126(1), p. 301-310.
- Medintz, I.L., et al., A fluorescence resonance energy transfer-derived structure of a quantum dot-protein bioconjugate nanoassembly. *Proceedings of the National Academy of Sciences of the United States of America*, 2004, 101(26), p. 9612-9617.
- Samia, A.C.S., Dayal, S., and Burda, C., Quantum dot-based energy transfer: Perspectives and potential for applications in photodynamic therapy. *Photochemistry and Photobiology*, 2006, 82(3), p. 617-625.
- Dayal, S., et al., Femtosecond time-resolved energy transfer from CdSe nanoparticles to phthalocyanines. *Applied Physics B-Lasers and Optics*, 2006, 84(1-2), p. 309-315.
- Dayal, S., Lou, Y.B., Samia, A.C.S., Berlin, J.C., Kenney, M.E., and Burda, C., Observation of non-Förster-type energy-transfer behavior in quantum dot-phthalocyanine conjugates. *Journal of the American Chemical Society*, 2006, 128(43), p. 13974-13975.
- Zenkevich, E., Cichos, F., Shulga, A., Petrov, E.P., Blaudeck, T., and von Borczyskowski, C., Nanoassemblies designed from semiconductor quantum dots and molecular arrays. *Journal of Physical Chemistry B*, 2005, 109(18), p. 8679-8692.
- Zenkevich, E.I., Blaudeck, T., Shulga, A.M., Cichos, F., and von Borczyskowski, C., Identification and assignment of porphyrin-CdSe hetero-nanoassemblies. *Journal of Luminescence*, 2007, 122, p. 784-788.
- Shi, L.X., Hernandez, B., and Selke, M., Singlet oxygen generation from water-soluble quantum dot-organic dye nanocomposites. *Journal of the American Chemical Society*, 2006, 128(19), p. 6278-6279.
- Orlova, A.O., Maslov, V.G., Stepanov, A.A., Goukko, I., and Baranov, A.V., Formation of QD-porphyrin molecule complexes in aqueous solutions. *Optics and Spectroscopy*, 2008, 105(6), p. 889-895.
- Orlova, A.O., Maslov, V.G., Baranov, A.V., Goukko, I., and Byrne, S., Spectral-Luminescence Study of the Formation of QD-Sulfophthalocyanine Molecule Complexes in an Aqueous Solution. *Optics and Spectroscopy*, 2008, 105(5), p. 726-731.
- Idowu, M., Chen, J.Y., and Nyokong, T., Photoinduced energy transfer between water-soluble CdTe quantum dots and aluminium tetrasulfonated phthalocyanine. *New Journal of Chemistry*, 2008, 32(2), p. 290-296.
- Idowu, M. and Nyokong, T., Spectroscopic behavior of cationic metallophthalocyanines in the presence of anionic quantum dots. *Spectrochimica Acta Part a-Molecular and Biomolecular Spectroscopy*, 2010, 75(1), p. 411-416.
- Jhonsi, M.A. and Renganathan, R., Investigations on the photoinduced interaction of water soluble thioglycolic acid (TGA) capped CdTe quantum dots with certain porphyrins. *Journal of Colloid and Interface Science*, 2010, 344(2), p. 596-602.
- Tsay, J.M., et al., Singlet oxygen production by peptide-coated quantum dot-photosensitizer conjugates. *Journal of the American Chemical Society*, 2007, 129(21), p. 6865-6871.
- Mojzisoava, H., Bonneau, S., Vever-Bizet, C., and Brault, D., The pH-dependent distribution of the photosensitizer chlorin e6 among plasma proteins and membranes: A physico-chemical approach. *Biochimica Et Biophysica Acta-Biomembranes*, 2007, 1768(2), p. 366-374.

26. Bachor, R., Shea, C.R., Gillies, R., and Hasan, T., Photosensitized Destruction of Human Bladder-Carcinoma Cells Treated with Chlorin E6-Conjugated Microspheres. Proceedings of the National Academy of Sciences of the United States of America, 1991, 88(4), p. 1580-1584.
27. Vermathen, M., Louie, E.A., Chodosh, A.B., Ried, S., and Simonis, U., Interactions of water-insoluble tetraphenylporphyrins with micelles probed by UV-visible and NMR spectroscopy. Langmuir, 2000, 16(1), p. 210-221.

ACCUMULATION OF QUANTUM DOTS IN EHRlich ASCITES TUMOUR IN MICE

Vytautas KULVIETIS***, Ričardas ROTOMSKIS***

*Vilnius University, Faculty of Physics, Department of Quantum Electronics;

**Institute of Oncology Vilnius University, Laboratory of Biomedical Physics.

Abstract: Quantum dots (QD) are semiconductor nanoparticles which are widely used as fluorescence imaging probes in biomedicine. We investigated QDs distribution in mouse Ehrlich ascites tumour model *in vivo* using fluorescence microscopy. The results show limited QDs penetration into tumour cells and principal accumulation in cell membrane. Meanwhile, QDs are internalized inside the blood cells and are retained in vesicular structures indicating endocytotic uptake pathway.

Keywords: Fluorescence imaging, quantum dots, endocytosis, Ehrlich ascites, tumour.

1. Introduction

Nanobiotechnology has become an actively emerging research area because of the immense efforts in the biomedical applications of nanomaterials. Semiconductor quantum dots (QDs) have widely served as fluorescent probes to visualize the biological processes both *in vitro* and *in vivo*. These nanoparticles are easily functionalized using peptides, proteins, DNA and antibodies. QDs indeed showed high capacity to target and image tumours in living subjects by fluorescence based techniques [1-4].

Selective tumour imaging strategies can be divided into passive and active targeting. Passive targeting does not require nanoparticles specificity for tumour cells and is based on the enhanced permeability and retention (EPR) effect [1]. Tumour capillaries are leakier than healthy tissue vessels, which causes more intense QD extravasation into neoplastic tissue. Additionally, tumours usually have reduced lymphatic drainage and increased permeability of cell membranes, which determine nanoparticles retention in tissue.

Active targeting is reasoned on the selective interaction of specifically modified QD with biomolecules (antibodies, proteins, etc) expressed by the cancer cells. Tumour imaging can be performed by interaction of functionalized QDs with specific receptors located on the membranes of vascular endothelium cells [2,3]. This strategy doesn't require nanoparticles extravasation into tissue and is based on tumour vessel imaging.

On the other hand, QD can be targeted to the cancer cells directly. This strategy, however, needs QD to be transported from intravascular compartment through

vessel wall into tissue. This hurdle depends on tissue type

and becomes even more complicated in the brain tissue because of blood-brain barrier [4]. One of the QD delivery solutions is loading macrophages with nanoparticles. These cells actively phagocytize QD and accumulate in the inflammatory lesion and tumours. This technique was used with magnetic nanoparticles and QDs [5]. Another way to translocate nanoparticles through biological membranes is capping with cell penetrating peptides. For example Tat protein conjugated QDs successfully penetrated into brain tissue [6].

The other important group of QD applications involves intracellular imaging and organelle tracking. These applications require QD delivery through cell membrane. It was shown that QD enter the cells via the endocytotic pathway and remain entrapped in vesicular structures [7,8]. There are several endocytotic pathways shown to be involved in QD uptake: lipid raft mediated, G-protein coupled receptor dependant, clathrin based and caveolin based endocytosis. It is believed that QD size, surface coatings and charge could be the key determinants for nanoparticles recognition by certain receptor(s) [9]. On the other hand, QD uptake depends on the biological system parameters, namely, cell type, physiological state, endocytotic activity and other [8]. However, fairly little is known about how QDs are eliminated from cells after labeling. It was shown that QD may remain in the lysosomes, Golgi complex and even nuclei [10]. Meanwhile *in vivo* studies reveal that administered QDs are observed in the organism up to 2 years with additional changes in spectral properties indicating nanocrystal degradation and possible release

of toxic compounds [11]. QDs excretion from the cell was reported only in the stem cells [8].

Understanding the metabolism of QDs in individual cells could help us to prevent the cytotoxicity of QDs in different types of cells. Nanoparticles behavior in biological systems is little known and there is a need for extensive studies in order to optimize and control QD applications in biomedicine.

In this study we investigated QDs distribution and intracellular uptake in Ehrlich ascites tumour mouse model by the means of fluorescence microscopy.

2. Materials and Methods

Ehrlich ascites tumour model

Subcutaneous tumour models were generated by the subcutaneous inoculation of Ehrlich ascites carcinoma cells into peritoneum (200 μ l) using a 1 ml syringe.

After two weeks the tumour reached appropriate volume for nanoparticles distribution experiments. 0,3 ml of CdSe/ZnS QD capped with carboxy groups exposing ligands (QTracker-565, Invitrogen) at $5,3 \cdot 10^{-7}$ M in PBS were injected intraperitoneally. After different incubation times (1-24 hours) the Ehrlich ascites specimen were prepared (0,1-0,5 ml) and diluted up to 200 times with PBS. The cells were washed by centrifugation at 1000 rpm for 5 min and aspirating the supernatant and resuspending with PBS up to initial volume.

The cells were stained with 0,1 μ g/ml DiOC₆ for 10 min which is lipophylic and, therefore, stains cellular membranes.

Fluorescence microscopy

Microscopy experiments were performed using Nikon Eclipse TE-2000U microscope, equipped with Plan Fluor 20x/0,5 and Plan Apo VC 60x/1,4 (oil imm.) objectives. For brightfield and fluorescence image detection RGB CCD camera Leica "DFC 290" was used. Three excitation-emission filter blocks were used: BP330-380, BA420 for ultraviolet; BP450-490, BA520 for blue and BP510-560, BA590 for green excitation. Nikon mercury lamp was used for fluorescence excitation.

Confocal fluorescence microscopy was performed using the Nikon "Eclipse C1 Plus" confocal scanning system equipped with two detectors. For standard images the three channel RGB detector (bandpass filters: 515/30 for green and 605/75 for red channel) was used. For spectral imaging the 32-channel spectral detector was used (resolution: 5 nm). Specimens were excited with 488 nm Ar ion laser.

Image processing was performed using the "Nikon EZ-C1 Bronze version 3.80" and "ImageJ 1.41" software.

3. Results

3.1. Characterization of Ehrlich ascites tumour

The microscopic examination of Ehrlich ascites sample shows that the tumour is not a homogenous cell

population and consists of several cell types. Using the brightfield microscopy different cell types can be distinguished by their size and shape (Fig. 1.). The most abundant cells are ascites cells. They are largest in diameter (15-25 μ m), nearly spherical with weakly visible nucleus. However, the blood cells are present in the sample as well. They could be identified due to their size, 6-9 μ m in diameter, and shape: erythrocytes – characteristically concave and white blood cells – spherical. The quantity of blood cells varied among the animals. An increase could be observed if any bleeding occurred during sample preparation. The blood cells could be distinguished from ascites cells according to the images of healthy mouse plasma. The cellular heterogeneity was confirmed by differentiating the cells with Giemsa stain: ascites cells stained in blue, erythrocytes in red and white blood cells in purplish-reddish colors.

Using the fluorescence microscopy the tumour cells appeared bluish autofluorescent under UV excitation. There were seen single cells with greenish fluorescence under UV or blue excitation. However autofluorescence bleached in the order of seconds under lamp exposure.

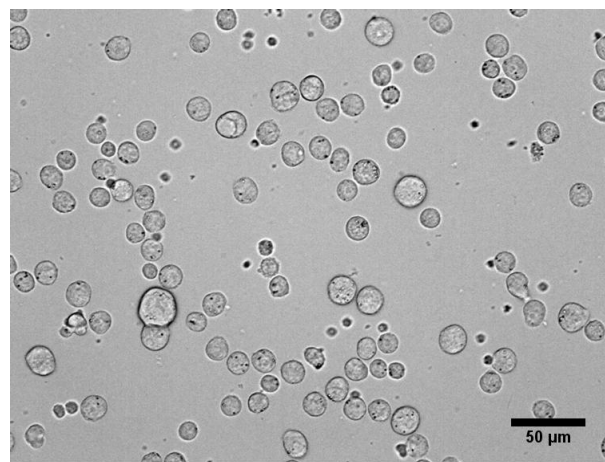


Fig. 1. Brightfield image of Ehrlich ascites sample showing heterogeneous cellular composition.

3.2. Quantum dots distribution in Ehrlich ascites tumour

The distribution of QD in Ehrlich ascites tumour is unambiguous. When a concentrated ascites sample (1:10 ascites:saline dilution) is investigated under fluorescence microscope, the extracellularly distributed QD can be observed. They can be detected in the interstitial cell connecting substance, which is predominantly rich in extracellular proteins.

Extracellular QD localization can be observed even better by diluting the ascites sample to a higher degree (1:100 -1:500 ascites:saline). When the cell aggregates are disrupted single cells can be analyzed (Fig. 2). Most of the Ehrlich ascites cells show no QD photoluminescence. Several cells appear having fluorescent membrane (fig. 2: the cell with numbers "2"

and "4") indicating limited or no QD intracellular uptake but mostly accumulated in the plasma membrane or the extracellular matrix. Since QDs are coated with carboxy groups exposing ligands, they possess negative charge. These polar groups may strongly interact with positively charged amino acids of the proteins. QD electrostatic interaction with proteins was shown earlier [12].

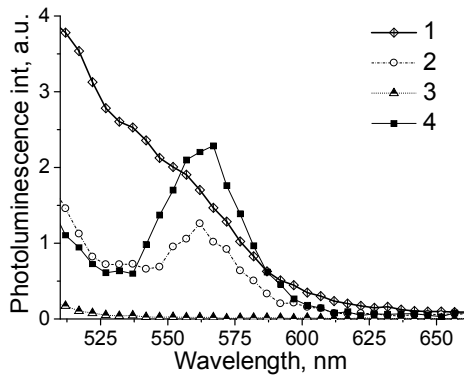
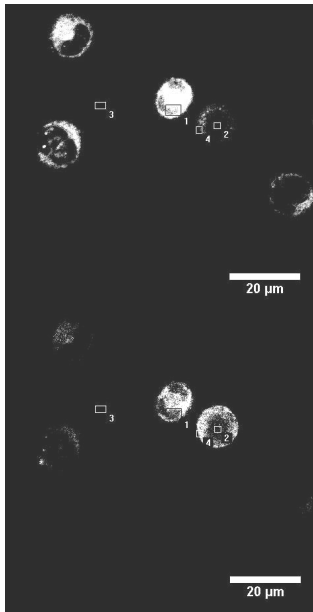


Fig.2. Confocal microscopy images of Ehrlich ascites cells 2 h after intraperitoneal QD (λ_{fl} =565 nm) injection. Membranes stained with DiOC₆ (λ_{fl} =510 nm). Left: "green" channel 510-560 nm for DiOC₆; right: "red" channel 560-660 nm for QD; bottom: fluorescence spectra of selected areas in the images. Note that one cell has more intense QD PL at 565 nm in the membrane "4" than in the cell centre "2".

However, single cells with internalized QDs can be found (Fig. 3.). These cells are rare in the sample and presumably are not healthy ascites cells. They are smaller in size (up to 10 µm) compared with Ehrlich ascites cells. According to the results of tumour characterization experiments it is most likely that these cells are phagocytes. The QD photoluminescence pattern is not homogenous but granulated. It shows that QDs are not monodispersed in the cytosol but rather

entrapped in certain cellular vesicular compartments. The QD PL was not observed in the nuclei of any cells.

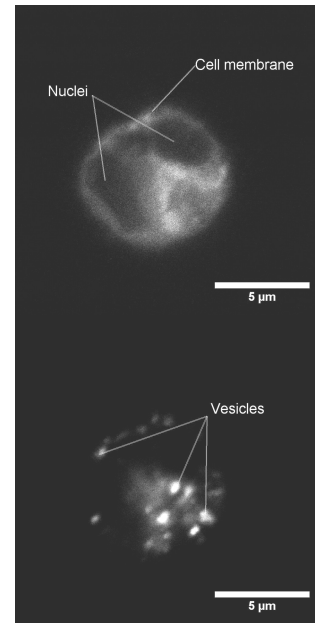


Fig. 3. Confocal microscopy images of a single cell from Ehrlich ascites tumour 2 h after incubation with QDs. Membranes stained with DiOC₆. Left: "green" channel 500-530 nm for DiOC₆, right: "red" channel 568-643 nm for QD

In the samples single fluorescent cells with continuous QD distribution could be found. However, they possess intact membrane, blebbing, nuclear fragmentation or other signs indicating damaged cells. The homogenous QD distribution could have been determined by passive migration through disrupted barrier.

The cell to cell variability in the sample could be determined by several factors: limited QD intraperitoneal diffusion and dispersion because of tumour viscosity, QD adhesion to non cellular tissue components, cellular migration and diversity of cell types with different metabolism and endocytotic activity.

The last factor should have played the major role in the observed QD distribution pattern. Macrophages and other phagocytes are the part of the reticuloendothelial system (RES) which is an essential component of the immune system. Phagocytes are able of engulfing substances, such as bacteria and viruses, rendering them incapable of causing harm to the body. They also ingest abnormal and old cells, thus clearing the body of their harmful presence. Increased endocytosis of nanoparticles by these cells was reported as well and is a key determinant in QDs uptake and clearance from blood [3,5]. The selective QD accumulation in phagocytes can be used for identification of inflammation process or tumour as these tissues are rich in phagocytic cells [5]. In general, QD intracellular uptake is determined by both: cellular (cell type, endocytotic activity, physiological state) [3,8] and

nanoparticles properties (size, surface chemistry, functionalization) [7, 13].

4. Conclusions

The complexity of the investigated biological system impedes the analysis of cellular QD distribution. However, it can be concluded, that intraperitoneally injected QDs adhere to extracellular tissue components and the membranes of ascites cells. QD intracellular uptake can be observed in non-ascites cells, predominantly in phagocytes. Vesicular QD cellular distribution indicates endocytotic QD uptake pathway and limited nanoparticle release from the vesicular structures. Cell type dependant QD uptake is related with different endocytotic activity and can be used for selective cell imaging.

5. References

1. Adisheshaiah P. P., Hall J. B., McNeil S. E. Nanomaterial standards for efficacy and toxicity assessment. *Wiley Interdisciplinary Reviews: Nanomedicine and Nanobiotechnology*, 2(1), 2010. p. 99-112.
2. Hu R., Yong K. T., Roy I., Ding H., Law W. C., Cai H., Zhang X., Vathy L. A., Bergey E. J., Prasad P. N. Functionalized near-infrared quantum dots for in vivo tumor vasculature imaging. *Nanotechnology*, 21(14), 2010. p. 145105.
3. Gao J., Chen K., Xie R., Xie J., Lee S., Cheng Z., Peng X., Chen X. Ultrasmall near-infrared non-cadmium quantum dots for in vivo tumor imaging. *Small*, 6(2) 2010. p. 256-261.
4. Kato S., Itoh K., Yaoi T., Tozawa T., Yoshikawa Y., Yasui H., Kanamura N., Hoshino A. Organ distribution of quantum dots after intraperitoneal administration, with special reference to area-specific distribution in the brain. *Nanotechnology*, 21, 2010. p. 335103 (7p).
5. Muhammad O., Popescu A., Toms S.A. Macrophage-Mediated Colocalization of Quantum Dots in Experimental Glioma. *Methods in Molecular Biology*, 374, 2007. p. 161-171.
6. Fonseca S.B., Pereira M.P., Kelley S.O. Recent advances in the use of cell-penetrating peptides for medical and biological applications. *Adv Drug Deliv Rev.*, 61(11), 2009. p. 953-964.
7. Kelf T.A., Sreenivasan V.K.A., Sun J., Kim E.J., Goldys E.M., Zvyagin A.V. Non-specific cellular uptake of surface-functionalized quantum dots. *Nanotechnology*, 21, 2010. p. 285105 (8p).
8. Pi Q.M., Zhang W.J., Zhou G.D., Liu W., Cao Y. Degradation or excretion of quantum dots in mouse embryonic stem cells. *BMC Biotechnology*, 10, 2010. p. 36.
9. Zhang L.W., Monteiro-Riviere N.A. Mechanism of Quantum Dot Nanoparticle Cellular Uptake. *Toxicological Sciences*, 110(1), 2009. p. 138-155.
10. Zhang Y., Mi L., Xiong R., Wang P.N., Chen J.Y., Yang W., Wang C., Peng Q. Subcellular Localization of Thiol-Capped CdTe Quantum Dots in Living Cells. *Nanoscale Res Lett*, 4(7), 2009. p. 606–612.
11. Fitzpatrick J. A., Andreko S. K., Ernst L. A., Waggoner A. S., Ballou B., Bruchez M. P. Long-term persistence and spectral blue shifting of quantum dots in vivo. *Nano letters*, 9(7), 2009. p. 2736-2741.
12. Liu W., Choi H.S., Zimmer J.P., Tanaka E., Frangioni J.V., Bawendi M. Compact cysteine-coated CdSe(ZnCdS) quantum dots for in vivo applications. *J Am Chem Soc.*, 129(47), 2007. p. 14530-14531.
13. Tan S.J., Jana N.R., Gao S., Patra P.K., Ying J.Y. Surface-Ligand-Dependent Cellular Interaction, Subcellular Localization, and Cytotoxicity of Polymer-Coated Quantum Dots. *Chem. Mater.* 22 (7), 2010. p.239–2247.

SPECTROSCOPIC STUDY OF QUANTUM DOTS DISTRIBUTION *IN VIVO*

Juras KIŠONAS*, Vytautas KULVIETIS**,**

*Vilnius University, Faculty of Medicine;

**Vilnius University, Faculty of Physics, Department of Quantum Electronics;

*** Institute of Oncology Vilnius University, Laboratory of Biomedical Physics

Abstract: In recent decade nanoparticles became very popular for biomedical applications. Biological imaging requires comprehensive knowledge about distribution and clearance patterns of nanoparticles for efficient clinical applications and for potential risks minimization. We used quantum dots (QDs) to investigate the biodistribution of nanoparticles in mouse model after subcutaneous and intravenous administration by the means of fluorescence spectroscopy. The results show that QD penetration through vessels is limited and distribution depends on the administration pathway.

Keywords: Quantum dots, fluorescence imaging, spectroscopy, clearance, biodistribution, lymph nodes mapping.

1. Introduction

Quantum dots (QDs) are semiconductor nanocrystals 1–10 nm in diameter [1]. Structurally they consist of a core and a shell. Exceptional QDs properties, like composition and size-dependent absorption and emission, high photostability makes them perfect for *in vivo* imaging. Organic coatings can be added to the surface of such QD to make them biologically compatible, stable and widely adaptable for biomedical research. Properly modified QD were numerously used for targeted *in vivo* imaging, drug delivery systems, therapeutic agents and others [2,3].

Recently subcutaneously injected QDs were used for lymph node (LN) mapping in order to locate LN during lymphonodectomy, which is an important part of radical cancer operation [4,5]. Subcutaneously injected QDs were detected in sentinel lymph nodes (SLN) already 5 minutes post injection. Their concentration reached a maximum at 60 min [5] or 4 h [6] after injection. Most of injected QDs remained in injection region with no migration into internal organs [5]. Contrary, other research group detected QDs in internal organs, but in very low and time depended concentrations [6,7].

Sentinel lymph node mapping was performed after QDs injection into pleural space [8], esophagus [9], gastrointestinal tract [10] etc. Inoue Y. et al. used abdomen compression with transparent, colorless tape, this markedly improved the visualization of the iliac LN [11].

QDs injected into different tumours models rapidly migrate to sentinel lymph nodes [12]. In the future this procedure can help to find tumor metastases in LN were tumours lymph drains.

The other promising group of QD applications relates tissue specific imaging after intravenous administration.

The majority of tumour targeting strategies involve QD functionalization with antibodies specific for receptors that are overexpressed by tumour cells. One such approach is targeting the integrin $\alpha v \beta 3$ receptors which are overexpressed in the endothelium of growing blood vessels associated with tumour growth (angiogenesis), using peptides containing the arginine-glycine-aspartic acid (RGD) sequence as the targeting agent [13].

However *in vivo* applications require comprehensive knowledge about QD distribution, non-specific accumulation and clearance from organism because of potential toxicity, due to QD toxic heavy metal composition. For today cadmium-free QDs are synthesized and already used for *in vivo* imaging [14].

It is known that QDs toxicity depends on multiple factors derived from both individual QD physicochemical properties and environmental conditions. QD size, charge, concentration, outer coating bioactivity (capping material, functional groups), and forthcoming oxidative, photolytic, and mechanical stability have each been shown to be determining factors in QD toxicity [15].

Low nanoparticle toxicity could be clinically tolerated if they would be cleared from organism in a short period of time. It was shown that the molecules with hydrodynamic diameter (HD) less than 6 nm are typically filtered through kidneys, while the particles with $HD > 8$ nm are not. The filtration of molecules 6-8 nm in size depends both on size and charge of the particle. Liver is physiologically capable to effectively capture the particles 10-20 nm in size for the clearance of viruses, pathogens and other small particles.

Consequently the agents within this size undergo rapid liver uptake and they have low circulation lifetimes [16,17]. QD presence in the organism was observed even 2 years after injection and long-term effects of accumulated QD are not studied well [18].

The aim of this study was to examine QDs distribution in mouse model after different administration routes using photoluminescence (PL) spectroscopy.

2. Materials and methods

Animal model

Experiments were carried out in the Institute of Oncology, Vilnius University. Permission for experiments with animals (no.0190) was given by The State Food and Veterinary Service. BALB/c mice were used for spectroscopy experiments and one Wistar rat was used for fluorescence microscopy. Animals were kept in a 12 h light/dark cycle and had access to food and water *ad libitum*.

Subcutaneous QD administration

For QD distribution after subcutaneous administration CdTe QD (*Plasmachem*) with 710 nm emission were used. QDs nanocrystals are capped with organic molecules and have carboxy groups in the outer layer. 100 μ l at 2,5 and 1,25 μ M solution of CdTe were injected into front left paw of mouse. As a positive control 200 μ l of photosensitizer AlPcS₄ at 55,6 μ M were injected subcutaneously. QD and photosensitizers distribution were evaluated by fluorescence spectroscopy.

Intravenous QD administration

For QD distribution after intravenous administration CdSe/ZnS quantum dots (QTracker-705, Invitrogen) with 705 nm emission were used. 200 μ l at 0,4 μ M solution (total dose: 40 pmol/animal) were injected into the tail vein of experimental mouse.

Fluorescence spectroscopy

Fluorescence spectra were measured by Varian Eclipse spectrophotometer. The fiber optics module was used for examination of mice skin *in vivo* and for measurements of internal organs after sacrificing the animals. Cuvette module was used for examination of prepared tissue homogenates. 450 nm excitation light was used.

Sample preparation

After examination of photoluminescence of mice skin animals were sacrificed at 20 min, 24 h and 5 days post injection. Internal organs (liver, heart, kidneys, lungs, brain, spleen, muscles) were removed and prepared for mechanical homogenization. Disruption was performed by T18 basic Ultra-Turrax disperser by *IKA* Afterwards homogenates were centrifuged for 15 min at 7000 RPM. Supernatants were used for spectroscopy.

Fluorescence microscopy

QD localization in tissue was examined by fluorescence microscopy. The rat was anesthetized by calipsol narcosis. The thoracic cavity was partially opened and QDs (100 μ l; 0,7 μ M; QTracker-655) were injected directly into heart (left ventricle). After 15 min the animal was sacrificed and organs were prepared, frozen (at -20°C)

and sliced with scalpel (thickness ~0,5mm) for fluorescence microscopy: Nikon Eclipse TE2000 microscope with Plan Fluor x20/0,5 objective and mercury lamp with dichroic filter set BP510-560, DM575, BA590 for QD PL detection.

3. Results

3.1 Quantum dots (QD) distribution after subcutaneous administration

Autofluorescence of mice skin was measured before the injection of QDs and is presented in Fig. 1. PL intensity of mice skin decreases with increasing detection wavelength, and there are no specific bands of PL intensity in this spectral region.

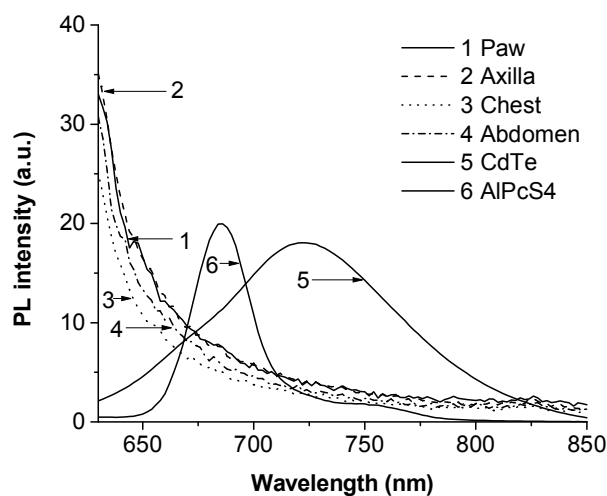


Fig. 1. Photoluminescence spectra of mouse skin, quantum dots and AlPcS₄ photosensitizer.

These are typical spectra of tissue autofluorescence caused by endogenous biomolecules. QDs have PL band with the peak at ~725 nm and AlPcS₄ at 684 nm, therefore these fluorophores can be clearly distinguished from the autofluorescence background.

After subcutaneous injection of AlPcS₄ characteristic PL of photosensitizer is visible in all regions of skin already 15 minutes after injection (Fig. 2).

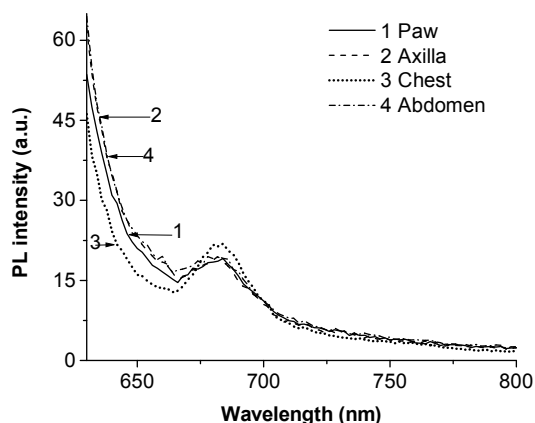


Fig. 2. PL spectra of the skin 15 min after injection of AlPcS₄, compared with AlPcS₄ PL.

AlPcS₄ PL was registered in the internal organs as well (data not shown). It indicates that sensitizer is rapidly absorbed from tissue to the blood vessels and distributes with blood throughout the organism.

These results show that sensitizer is easily detectable using optical fiber spectroscopy *in vivo*.

After subcutaneous injection of QDs characteristic PL band is observed only in the PL spectra of skin at injection site region. The signal could be registered during the whole investigation period, e.g. up to 5 days (Fig. 3).

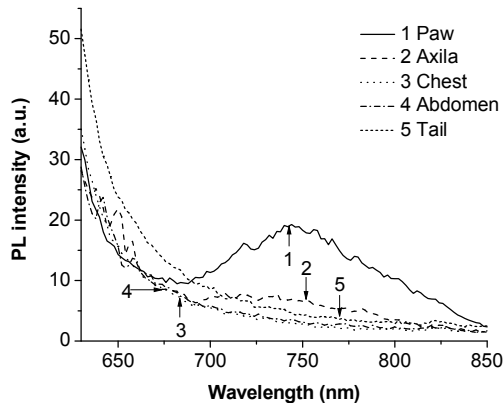


Fig. 3. Photoluminescence spectra of the skin 20min after subcutaneous injection of CdTe QDs.

However QD PL could not be detected in other skin sites located more than 1cm from the injection site. Fiber optics spectroscopy is limited because of limited penetration depth of excitation light into the tissue. Therefore, the signal comes only from the superficial skin layer and the information about QDs distribution in deeper tissues is not gathered.

After QDs photoluminescence evaluation *in vivo*, animals were sacrificed and internal organs were prepared for fluorescence spectroscopy. The PL spectra of internal organs didn't show characteristic QDs photoluminescence band up to 5 days after QDs injection (Fig. 4). These results indicate that QDs did not migrate from injection site and remained in the administration region during the whole investigation period.

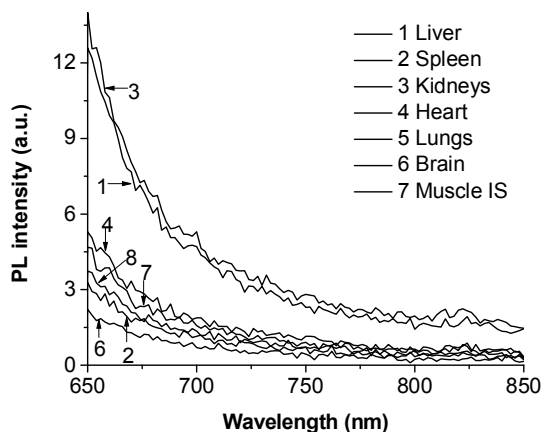


Fig. 4. Photoluminescence spectra of internal organs homogenates 5 days after CdSe/ZnS QDs injection.

The results show that photosensitizer molecules and QD nanocrystals distribute in organism differently. Photosensitizers molecules are small (MW=894 g/mol) and this allows them to be absorbed from interstitium to blood and afterwards they migrate to other organs (hematogenic migration). Meanwhile QDs are much bigger particles (MW≈4*10⁶g/mol) and their penetration into vessels is highly limited. More to add QDs interaction with biomolecules is reported which may cause the increase of hydrodynamic diameter, opsonization, aggregation and other effects [17]. These processes influence QD stability and pharmacokinetics which are essential for *in vivo* applications.

3.2 QD distribution after intravenous administration

After intravenous QD administration, characteristic QD PL band (at ~705 nm) could be observed in injection site and surrounding regions by the means of fiber optics spectroscopy (Fig. 5). However QD PL was not detected more than 1 cm from the injection point, similarly like after subcutaneous injection. The QD PL topical distribution pattern remained similar up to 1 hour.

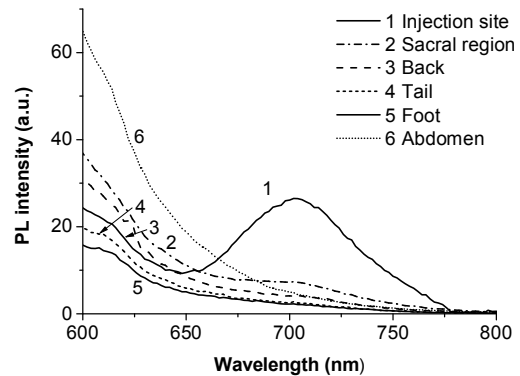


Fig. 5. Fluorescence spectra of mouse skin in different body positions 1 h after intravenous QD administration; measured with fiber optics module.

1 hour after injection the mouse was sacrificed, internal organs were prepared and examined by fiber optics spectroscopy. In most organs the QD PL band could be detected indicating QD presence in tissues (Fig. 6).

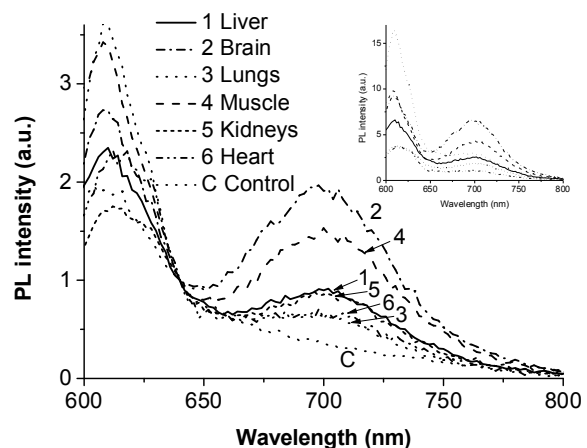


Fig. 6. Fluorescence spectra of mouse organs 1 h after intravenous QD administration; measured by fiber optics

module. The graph shows normalized spectra (at 640 nm), inset displays the original spectra.

The highest QD PL intensity was observed in the brain. It should be noticed, that highest PL intensity does not necessary reflect highest fluorophore concentration in tissue because the investigated organs have different optical properties and, therefore, light is absorbed and scattered differently. Kidney, liver and spleen are very dark due to the high pigmentation in these organs and, therefore, they have overall lowest fluorescence signals (fig. 6, inset). Therefore this method should be treated as semi-quantitative.

After fiber optics examination the organs were homogenized and prepared for cuvette-module based spectroscopy. The QD PL band was registered in the spectra of these samples as well (data not shown).

QD presence in internal organs after 1 hour indicates that nanoparticles migrate from injection site. The fast and systemic QD appearance in organs indicates that QD distribute with blood circulation. In general, intravenously administered agents may be a) retained in tissue vascular compartments, b) extravasate into interstitium and later c) be taken up by the tissue cells [16,17].

24 hours after injection QD PL could still be observed in the injection area during topical examination. QD PL traces were observed in the internal organs spectra as well (Fig. 7). However the QD PL was significantly lower when compared to 1 h samples and was comparable with autofluorescence level in liver, lungs, spleen and kidney. Meanwhile the spectra of brain, heart and control samples (no QD administration) do not exhibit 705 nm band.

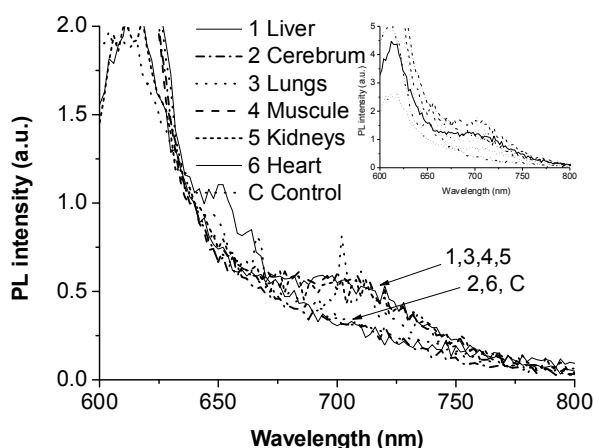


Fig. 7. Fluorescence spectra of mouse organs 24 h after intravenous QD administration, measured by fiber optics module. The graph shows normalized spectra (at 640 nm), inset displays the original spectra.

In the spectra of samples prepared after 24 h the QD PL intensity is significantly lower than in the samples prepared after 1 h. More to add, the spectrum of brain tissue overlaps with the control spectrum, which means that no QD PL was detected after 24 h, whereas it was most intense among investigated organs after 1h. Similarly, no QD PL was observed in the spectrum of

heart. These results are related with QD transport from blood vessel to tissue and can be explained as follows.

The diffusion of molecules across capillary wall is exceptionally limited in the brain by the blood-brain barrier, which does not exist in other tissues. Therefore QD uptake to the brain tissue is highly limited and remains a challenge for researchers [19]. The observed results could be associated with the intravascular QD retention in brain capillaries. The intensive QD PL in the brain should be attributed to the high cerebral blood flow, which constitutes ~15% of cardiac output.

QD presence in blood vessels was confirmed by fluorescence microscopy of brain section after QD injection into the circulation. Figure 8 shows blood vessel of the brain surface and QD PL (right) coming from the vascular compartment.

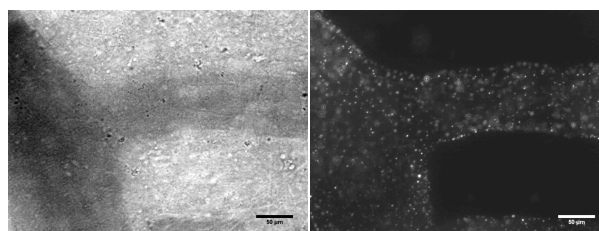


Fig. 8. Brightfield (left) and fluorescence (right) images of brain surface 15 min after QD injection indicating QD presence in blood vessel without extravasation to interstitium; scale bar - 50 μ m.

Consequently, measured QD PL intensity in brain and heart tissues correlates with QD concentration in blood and the absence of QD PL in brain and heart after 24 h represents QD clearance from blood. Contrary, weak QD PL remains in other organs indicating QD accumulation in tissue (muscle, liver, kidneys, lungs).

Rapid QD accumulation in liver and spleen was observed by others and is explained by QD retention in reticuloendothelial system. The other clearance pathway is renal filtration. However urinary clearance is most efficient for smaller particles (particularly up to 6 nm) and should not be significant in our case. On the other hand, QD interaction with biomolecules was reported earlier and possible QD PL quenching, nanoparticle aggregation or disruption in biological tissue should not be excluded [16,17,20].

The observed QD distribution is caused by several processes and more detailed study on QD pharmacokinetics and deposition pattern is needed in order to predict and control nanoparticle behaviour in biological systems.

4. Conclusions

Our results show that QD distribution depends on the administration pathway. Subcutaneously injected QDs diffuse locally and do not migrate with blood to other organs. QD remain in injection site up to 5 days indicating limited QD penetration into vessels. Intravenously injected QD migrate with blood and can be observed 1 h after injection in the vascular

compartments of internal organs. Meanwhile after 24 h QD are removed from blood and their distribution is more related to QD tissue uptake.

5. References

- Sutherland A. J. Quantum dots as luminescent probes in biological systems. *Current Opinion in Solid State and Materials Science*, 6(4), 2002. p. 365-370.
- Adisheshaiah P. P., Hall J. B., McNeil S. E. Nanomaterial standards for efficacy and toxicity assessment. *Wiley Interdisciplinary Reviews: Nanomedicine and Nanobiotechnology*, 2(1), 2010. p. 99-112.
- Gao J., Chen K., Xie R., Xie J., Lee S., Cheng Z., Peng X., Chen X. Ultrasmall near-infrared non-cadmium quantum dots for in vivo tumor imaging. *Small*, 6(2) 2010. p. 256-261.
- Maria I., Harrell A., Iritani B. M., Ruddell A. Lymph node mapping in the mouse. *Journal of Immunological Methods*, 332(1-2), 2008. p. 170-174.
- Robe A., Pic E., Lassalle H. P., Bezdetnaya L., Guillemin F., Marchal F. Quantum dots in axillary lymph node mapping: Biodistribution study in healthy mice. *BMC Cancer*, 8(111), 2008. Published online.
- Pic E., Pons T., Bezdetnaya L., Leroux A., Guillemin F., Dubertret B., Marchal F. Fluorescence Imaging and Whole-Body Biodistribution of Near-Infrared-Emitting Quantum Dots after Subcutaneous Injection for Regional Lymph Node Mapping in Mice. *Molecular Imaging and biology*, 12(4), 2010. p. 394-405.
- Gopee N. V., Roberts D. W., Webb P., Cozart C. R., Siitonen P. H., Warbritton A. R., Yu W. W., Colvin V. L., Walker N. J., Howard P. C. Migration of Intradermally Injected Quantum Dots to Sentinel Organs in Mice. *Toxicological sciences*, 98(1), 2007. p. 249-257.
- Soltész E. G., Sungjee K., Laurence R. G., DeGrand A. M., Parungo C. P., Dor D. M., Cohn L. H., Bawendi M. G., Frangioni J. V., Mihaljevic T. Intraoperative Sentinel Lymph Node Mapping of the Lung Using Near-Infrared Fluorescent Quantum Dots. *The Annals of Thoracic Surgery*, 79(1), 2005, p. 269-277.
- Parungo C. P., Ohnishi S., Kim S. W., Kim S., Laurence R. G., Soltész E. G., Chen F. Y., Colson Y. L., Cohn L. H., Bawendi M. G., Frangioni J. V. Intraoperative identification of esophageal sentinel lymph nodes with near-infrared fluorescence imaging. *The Journal of Thoracic and Cardiovascular Surgery*, 128, 2005. p. 844-850.
- Soltész E. G., Kim S., Kim S. W., Laurence R. G., DeGrand A. M., Parungo C. P., Cohn L. H., Bawendi M. G., Frangioni J. V. Sentinel Lymph Node Mapping of the Gastrointestinal Tract by Using Invisible Light. *Annals of Surgical Oncology*, 13(3), 2006. p. 386-396.
- Inoue Y., Kiryu S., Watanabe M., Oyaizu N., Ohtomo K. Fluorescence Lymph Node Mapping in Living Mice using Quantum Dots and a Compression Technique. *Journal of Fluorescence*, 20(2), 2010. p. 599-606.
- Ballou B., Ernst L. A., Andreko S., Harper T., Fitzpatrick J. A. J., Waggoner A. S., Bruchez M. P. Sentinel Lymph Node Imaging Using Quantum Dots in Mouse Tumor Models. *Bioconjugate Chemistry*, 18 (2), 2007. p. 389-396
- Hu R., Yong K. T., Roy I., Ding H., Law W. C., Cai H., Zhang X., Vathy L. A., Bergey E. J., Prasad P. N. Functionalized near-infrared quantum dots for in vivo tumor vasculature imaging. *Nanotechnology*, 21(14), 2010. p. 145105.
- Li L., Daou T. J., Texier I., Kim Chi T. T., Liem N. Q., Reiss P. Highly Luminescent CuInS₂/ZnS Core/Shell Nanocrystals: Cadmium-Free Quantum Dots for In Vivo Imaging. *Chemistry of Materials*, 21(12), 2009. p. 2422-2429.
- Hardman R. A Toxicologic Review of Quantum Dots: Toxicity Depends on Physicochemical and Environmental Factors, *Environmental Health Perspectives*. 114(2), 2006. p. 165-172.
- Choi H.S., Liu W., Misra P., Tanaka E., Zimmer J. P., Ipe B. I., Bawendi M. G., Frangioni J. V. Renal clearance of quantum dots. *Nature Biotechnology*, 25, 2007. p. 1165-1170.
- Longmire M., Choyke P. L., Kobayashi H. Clearance properties of nano-sized particles and molecules as imaging agents: considerations and caveats. *Nanomedicine (Lond)*, 3(5), 2008. p. 703-717.
- Fitzpatrick J. A., Andreko S. K., Ernst L. A., Waggoner A. S., Ballou B., Bruchez M. P. Long-term persistence and spectral blue shifting of quantum dots in vivo. *Nano letters*, 9(7), 2009. p. 2736-2741.
- Kato S., Itoh K., Yaoi T., Tozawa T., Yoshikawa Y., Yasui H., Kanamura N., Hoshino A. Organ distribution of quantum dots after intraperitoneal administration, with special reference to area-specific distribution in the brain. *Nanotechnology*, 21, 2010. p.335103 (7p).
- Karabanovas V., Zakarevičius E., Sukackaitė A., Streckytė G., Rotomskis R. Examination of the stability of hydrophobic (CdSe)ZnS quantum dots in the digestive tract of rats. *Photochemical & photobiological sciences*, 7(6), 2008. p.725-729.

**SPECTRAL STUDY ON THE FORMATION OF QUANTUM DOTS AND CHLORIN E6
COMPLEX IN THE PRESENCE OF PROTEIN**

Artiom SKRIPKA¹, Jurga VALANČIŪNAITĖ², Ričardas ROTOMSKIS^{1,2}

¹Vilnius University Physics faculty, Saulėtekio 9, c.3, LT-10222, Vilnius, Lithuania

²Laboratory of Biomedical Physics of Vilnius University institute of Oncology, Baublio 3B LT- 08406, Vilnius

Abstract: In this work we present the spectral study on complex formation between CdSe/ZnS-amino (PEG) (545 nm) quantum dots and second-generation photosensitizer chlorin e₆ in the presence of bovine serum albumin.

Keywords: Photodynamic therapy, quantum dots, photosensitizer, porphyrin, chlorin e₆, complex, energy transfer, FRET, protein, bovine albumin serum.

1. Introduction

Luminescent semiconductor quantum dots (QDs) have received considerable interest due their unique optical properties leading to various applications in some biological and biomedical fields. Several years ago it was suggested that QDs could also be used in the photodynamic therapy (PDT) of cancer to enhance the efficiency of conventional porphyrin-type photosensitizers (PS) [1]. Although there are numerous studies on different QD-PS systems in organic and aqueous solutions reported until now [2, 3], however the formation and stability of QD-PS complex in biological medium were not investigated yet.

In this work, we present the spectral study on the formation of complex between CdSe/ZnS-amino(PEG) (545 nm) QDs and second-generation photosensitizer chlorin e₆ (Ce₆) in the presence of protein, bovine serum albumin (BSA).

2. Materials and methods

Chlorin e₆ tetrasulfonic acid was purchased from Frontier Scientific Inc. (USA). CdSe/ZnS coated with amphiphilic (AMP) polymer and polyethylene glycol (PEG) amine (NH₂ 100%) were obtained from Invitrogen Corp. (USA). Bovine albumin serum was purchased from Sigma (Germany). All materials were used without further purification.

Working solution of QD (0.05 μM) was prepared by diluting the stock solution of QD (8 μM) provided directly by manufactures (Invitrogen Corp., USA). The stock solutions of Ce₆ and BSA were freshly prepared before experiments. All solutions were prepared in

phosphate buffer solution (PBS) of pH 7. A small amount of BSA was added to working QD solution to reach QD:BSA molar ratio of 1:100. Further, concentrated Ce₆ solution was titrated to QD-BSA solution until QD:BSA:Ce₆ molar ratio of 1:100:15 was achieved. Similarly, solution of QD-Ce₆ without BSA was prepared (QD:Ce₆ 1:15). For control measurements, unmixed Ce₆ and QD solutions were prepared without (0.75 μM Ce₆, 0.05 μM QD) and with BSA (Ce₆:BSA 15:100, QD:BSA 1:100).

Fluorescence measurements were performed on Cary Eclipse fluorescence spectrophotometer (Varian Inc., USA). To determine if FRET from QDs to Ce₆ molecules occurs, the excitation wavelength at 465 nm was used, which coincides with the minimum of Ce₆ absorption (in order to reduce contributions resulting from direct excitation of Ce₆).

3. Results and discussion

The fluorescence spectra of QD, Ce₆ and mixed QD-Ce₆ solutions in the absence and presence of BSA are shown in Fig. 1. The emission maximum of QD was at 545 nm and upon addition of BSA the change in QD emission was negligible. Meanwhile, the fluorescence maximum of Ce₆ in the presence of BSA shifted to red side of the spectrum from 660 nm to 670 nm. Similar spectral shift of Ce₆ was reported upon binding to human serum albumin [4]. Further addition of Ce₆ into QD-BSA solution reduced the intensity of QD emission, while the intensity of Ce₆ fluorescence at 670 nm became higher than in Ce₆-BSA solution. Upon addition of Ce₆ to pure QD solution, the intensity of QD emission decreased almost twice as in QD-BSA-Ce₆ solution, while the

intensity of Ce_6 fluorescence increased five folds. Interestingly, the position of Ce_6 fluorescence band in QD- Ce_6 solution was at 670 nm, similar as in the presence of BSA (in Ce_6 -BSA and QD-BSA- Ce_6 solutions). The bathochromic shift of Ce_6 fluorescence band to 670 nm was reported not only upon binding to serum albumin, but also in LDL and DOPC unilamellar vesicles[4].

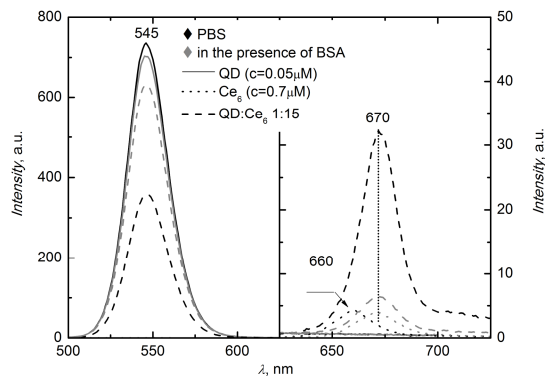


Fig. 1. Fluorescence spectra of QD ($0.05\mu\text{M}$), Ce_6 ($0.75\mu\text{M}$) and QD- Ce_6 (QD: Ce_6 molar ratio 1:15) solutions in PBS and in the presence of BSA (QD:BSA 1:100, Ce_6 :BSA 15:100, QD:BSA: Ce_6 1:100:15). The excitation was at 465 nm. The spectral region from 625 to 725 nm is shown in different scale.

Structurally similar chlorin p_6 was shown to undergo red shift of its fluorescence band due to the interaction with surfactants (SDS and CTAB) [5]. These studies disclose that the spectrum of Ce_6 molecules is very sensitive to the polarity of environment and changes significantly in the hydrophobic surrounding. The amphiphilic nature of Ce_6 might favor the binding affinity to nonpolar molecules. The principal function of serum albumin is to transport fatty acids, which bind in hydrophobic pockets capped by polar side chains [6]. Most probably that upon binding to BSA, Ce_6 molecules localize in the hydrophobic parts of protein as well. The explanation for similar position of Ce_6 fluorescence band in the presence of QDs might be that Ce_6 molecules immerse into the hydrophobic region of amphiphilic polymer, which is the main constituent of QD coating. The interaction study with PEG (another constituent of QD coating) did not reveal any changes in Ce_6 spectrum (not shown here). In this approach, upon binding to AMP polymer, Ce_6 molecules became situated at a short and fixed distance from QD core. This might lead to high FRET efficiency. The quenched intensity of QD emission after addition of Ce_6 and the increased intensity of Ce_6 (Fig. 1, QD- Ce_6 in PBS) confirm that the energy transfer from QD to bound Ce_6 molecules occur within QD- Ce_6 complex. However, when BSA was added into QD solution before Ce_6 (QD-BSA- Ce_6), the efficiency of energy transfer was significantly lower. The decreased intensity of QDs indicated that some Ce_6 molecules reached QD coating. The higher intensity of fluorescence band at 670 nm in QD-BSA- Ce_6 solution in comparison to that in Ce_6 -BSA solution reinforced the fact that some Ce_6 molecules were excited by energy transfer from QDs. The reduced efficiency of energy

transfer in the presence of BSA could be resulted not only from the decreased number of potential acceptors because some Ce_6 molecules were bound to BSA, but also from the fact that BSA molecules could bind to QDs thus increasing the interaction distance for Ce_6 . The study with CdTe QDs with similar core size (emission maximum at 550 nm) revealed that the interaction of QDs with BSA led to the formation of additional quantum dot coating layer [7].

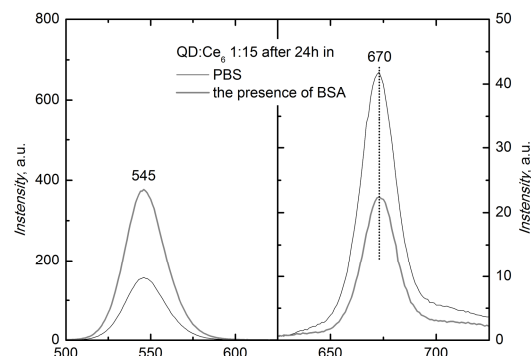


Fig. 2. Fluorescence spectra of QD: Ce_6 (QD: Ce_6 1:15) solutions in PBS and in the presence of BSA (QD:BSA: Ce_6 1:100:15) 24h after the preparation.

Moreover, the presence of protein molecules could simply increase the viscosity of solution thus reducing the speed of the reaction between QDs and Ce_6 . To test the last assumption, the fluorescence spectra of QD- Ce_6 solutions in PBS and in the presence of BSA were measured after 24 hours (Fig. 2.). After 24 hours the spectral changes were registered not only in QD-BSA- Ce_6 solution but also in QD- Ce_6 solution. The same tendency of intensity redistribution between QD and Ce_6 emission bands was observed in both solutions: the intensity of QD emission further decreased, while the intensity of Ce_6 fluorescence raised. However, in the presence of BSA, the quenching of QD emission was not so intensive as in the absence of protein. The level of QD emission in the presence of BSA almost dropt to that observed in freshly prepared QD- Ce_6 solution without BSA. On the contrary, the increase in Ce_6 fluorescence after 24h was more pronounced in the presence of protein, however the intensity of Ce_6 fluorescence did not reach the value obtained in the absence of BSA. These results indicate that the presence of protein slows down the binding reaction between QD and Ce_6 and reduces its yield. Consequently, the FRET efficiency is lower in QD-BSA- Ce_6 solution. However, the higher ratio of QD emission decrease in respect to the ratio of Ce_6 increase obtained in the absence of protein after 24h suggests that besides FRET there might be another quenching mechanism of QD emission, which in the presence of protein is eliminated. It was demonstrated that the interaction with BSA prevents CdTe QDs from aggregation [7]. Although, the coating of AMP polymer and PEG should insure good solubility for QDs, however the aggregation might be the case.

4. Conclusions

We conclude that photosensitizer Ce₆ can form a stable complex with CdSe/ZnS-amino(PEG) quantum dots in the presence of protein. The interaction responsible for Ce₆ binding to QDs in the presence of BSA reveals the hydrophobic character, similar as in PBS solution. In formed QD-Ce₆ complex, energy transfer from QD to bound Ce₆ molecules occur, however with lower efficiency.

5. Acknowledgements

This work was supported by the project "Postdoctoral Fellowship Implementation in Lithuania" (VP1-3.1-ŠMM-01-V-01-001) and Lithuanian Science Council Student Research Fellowship Award (A.S).

6. References

1. Samia, A.C.S., Chen, X.B., and Burda, C., Semiconductor quantum dots for photodynamic therapy. *Journal of the American Chemical Society*, 2003, 125(51), p. 15736-15737.
2. Yaghini, E., Seifalian, A.M., and MacRobert, A.J., Quantum dots and their potential biomedical applications in photosensitization for photodynamic therapy. *Nanomedicine*, 2009, 4(3), p. 353-363.
3. Juzenas, P., et al., Quantum dots and nanoparticles for photodynamic and radiation therapies of cancer. *Advanced Drug Delivery Reviews*, 2008, 60(15), p. 1600-1614.
4. Mojzisova, H., Bonneau, S., Vever-Bizet, C., and Brault, D., The pH-dependent distribution of the photosensitizer chlorin e6 among plasma proteins and membranes: A physico-chemical approach. *Biochimica Et Biophysica Acta-Biomembranes*, 2007, 1768(2), p. 366-374.
5. Datta, A., Dube, A., Jain, B., Tiwari, A., and Gupta, P.K., The effect of pH and surfactant on the aggregation behavior of chlorin p(6): A fluorescence spectroscopic study. *Photochemistry and Photobiology*, 2002, 75(5), p. 488-494.
6. Curry, S., Mandelkow, H., Brick, P., and Franks, N., Crystal structure of human serum albumin complexed with fatty acid reveals an asymmetric distribution of binding sites. *Nature Structural Biology*, 1998, 5(9), p. 827-835.
7. Poderys, V., Matulionyte, M., Selskis, A., and Rotomskis, R., Interaction of Water-Soluble CdTe Quantum Dots with Bovine Serum Albumin, in *Nanoscale Research Letters*. 2010, Springer New York. p.1-6.

RING LIKE TPPS₄ J-AGGREGATE STRUCTURE

Vilius PODERYS * **, Algirdas SELSKIS ***, Adelina ILIE ****, Ričardas ROTOMSKIS* **

* Institute of Oncology Vilnius University, Laboratory of Biomedical Physics;

** Vilnius University, Physics Faculty, Quantum Electronics Department, Biophotonics laboratory

*** State Research Institute Centre for Physical Sciences and Technology, A. Goštauto 9, LT-2600 Vilnius, Lithuania

**** University of Bath, Department of Physics, Bath BA2 7AY, United Kingdom

Abstract: Self assembling nanostructures of Meso-tetra (4-sulfonatophenyl) porphine (TPPS₄) were investigated using atomic force microscope (AFM) and scanning tunneling microscope (STM). It was shown that TPPS₄ forms long up to 1 μm length 19 nm diameter nanotubes. Also short „standing“ nanotubes (10 nm height) were observed. Investigations with STM showed that TPPS₄ molecules forms 17,5 nm diameter ring like structures. These ring like structures are primary TPPS₄ J-aggregate structures formed by stacking TPPS₄ molecules by zigzag model. We propose a new TPPS₄ nanotube formation model – winding of linear threads to a 18 nm diameter spiral.

Keywords: Porphyrin, aggregation, atomic force microscopy.

1. Introduction

Organized self-assembly of molecules and self-organization is the central issue to the utilization of nanoscaled materials in the “bottom-up” approach of nanotechnology for future manufacturing [1]. Self-assembled porphyrin nanostructures have recently gained considerable attention as a technique for the fabrication of nanoscale functional structures, for the electronic and photonic devices and solar energy conversion [2].

It is believed that in the future nanodevices will be created using self-assembling nanostructures. One of possible building blocks for nanodevices is molecular aggregates. It is known, that ordered structures are used in nature (and can be used in nanodevices) to perform specific functions like light harvesting complexes in the chlorosomes of green bacteria. Molecular aggregates also could be used for manufacturing photo converters [3] and biosensors [4]. Optical properties of molecular aggregates with a cylindrical geometry currently draw considerable attention since they are model substances for aggregates of the light harvesting antenna chlorophyll with a ‘storage-ring’ configuration and of primary charge-separation systems in photosynthesis. The molecules in such aggregates are bound to each other by noncovalent bonds, such as hydrogen bonds, van der Waals interactions, and π - π stacking and they are highly ordered. Water-soluble 5,10,15,20-tetrakis-(4-sulfonatophenyl)porphyrin (TPPS₄) (fig 1.) has been largely investigated by many authors [5, 6] mainly because its diacid form is able to self-aggregate, leading to formation of porphyrin nanotubes [7, 8].

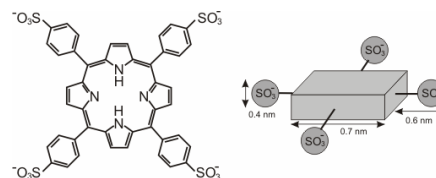


Fig. 1. Structure of TPPS₄ at pH=7 [9].

Aggregate nanotube model is confirmed by AFM [10], TEM [11], small angle X-ray scattering [12] and theoretical modeling [13] results. Structure, deposition, preparation of TPPS₄ nanotubes is widely investigated using various methods, but detailed molecular structure and aggregation model of TPPS₄ aggregates still remains unclear.

In this paper we present investigation of TPPS₄ aggregates structure by means of Atomic force microscopy (AFM) and scanning tunneling microscopy (STM).

2. Materials and methods

Meso-tetra (4-sulfonatophenyl) porphine (TPPS₄) was obtained from Frontier scientific (Logan, UT, USA). J-aggregate solutions were prepared by dissolving TPPS₄ in a drop of distilled water and then diluted with hydrochloric acid (HCl) till the required concentration. Concentration of all solutions was 10⁻⁴ M medium pH=1.3. TPPS₄ molecules assemble into small

aggregates immediately, but it takes at least several hours to form large aggregates.

Glass and self-assembled monolayers (SAMs) were used as substrates for measurements with atomic force microscope (AFM). Glass slides were degreased and washed in distilled water. Gold substrates, used for SAM's preparation were prepared by first precoating the Si substrates with 25 Å of Ti adhesion layer and then by evaporating 2000 Å of Au. Gold substrates were washed in aqueous solution of 3,6% NH₃ and 4,0% of H₂O₂ at 85° C for 5 minutes. SAMs were prepared by dipping gold substrates into diluted solutions of hexadecanethiol (hydrophobic surface). Substrates were left in solution for at least 12 hours. Afterwards, the samples were washed in the MilliQ water in ultrasonic bath for 3-10 minutes. Gold wafers were used as substrates for STM measurements.

Samples for AFM measurements were formed by casting a droplet (20–60 µl) of solution of J-aggregates onto the glass/SAM substrate. The droplet was removed after 30 seconds. Drop of solution covered 0,5 – 1 cm² of the substrate surface. Then the sample was dried in ambient air. Samples for STM were prepared by putting a drop (20 µm) of TPPS₄ J-aggregate solution on gold substrate and, 30 s later, spun at 5000 rpm. This procedure was repeated six times.

Atomic force microscopes Explorer (ThermoMicroscopes, Sunnyvale, CA) and Nano Scope IIIa (Digital Instruments, Santa Barbara, CA) were used to produce surface images in ambient air. Measurements were performed in constant force contact mode using silicon nitride cantilevers (type: MLCT-EXMT-A, Thermomicroscopes, Sunnyvale, CA) and in the tapping mode with a point probe silicon tip (type: NCH-W) of radius <15 nm (Nanosensors GmbH&Co.KG, Norderfriedrichskoog, Germany) at oscillation frequencies of 250-350 kHz. Omicron UHV AFM/STM (Omicron NanoTechnology GmbH Taunusstein, Germany) was used to produce images in ultra high vacuum (10⁻¹¹ Torr). Tungsten tips were used.

Spectral measurements were carried out using PC1000 (Ocean Optics Inc., Dunedin, FL, USA) spectrometer.

3. Results and discussion

It is suggested that TPPS₄ does not stack in neutral water solution because the negative charges at the sulfonato groups cause electrostatic repulsion. The changes observed in the absorption spectrum in aqueous solution of TPPS₄ with increasing medium acidity are result of diprotonated species formation, which are the ones forming the J-aggregates. Figure 2 presents the normalized absorption spectra of TPPS₄ in neutral solution (dotted line), acidic solution (solid line), and film of TPPS₄ deposited on glass substrate (dashed line) prepared by the drying a drop of an acidic aqueous solution of TPPS₄ at room temperature. In neutral solution (pH=7) TPPS₄ molecules has intense Soret absorption band at 413nm and four Q bands in visible region (516 nm, 553 nm, 582 nm and 636 nm). In acid

medium spectrum of TPPS₄ changes: intensity of Soret band decreases, new absorption bands at 489 nm (J-band) and at 706 nm appears. Absorption band peaks at 489 nm and 706 nm both indicate the formation of J-aggregates [14]. Spectrum of TPPS₄ aggregates film deposited on glass substrate (40 µl of acid TPPS₄ solution dried on glass slide) is very similar to spectrum of acidic TPPS₄ solution. It has absorption bands at the same positions (489nm and 706nm). This indicates that the J-aggregates remained structurally intact on glass substrate after drying 40µl of TPPS₄ acidic solution in ambient air.

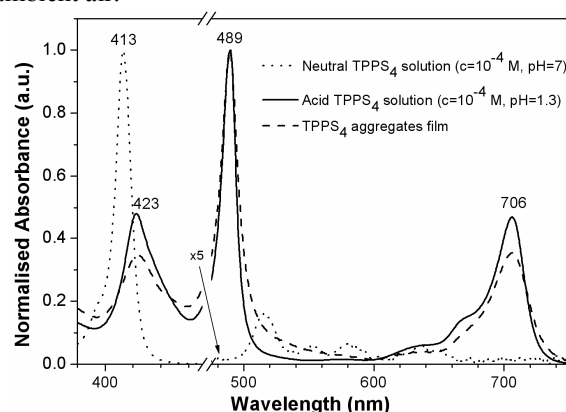


Fig. 2. Normalized absorption spectra of neutral TPPS₄ solution ($c=10^{-4}$ M, pH=7) (dotted line), TPPS₄ J-aggregates in aqueous acidic solution ($c=10^{-4}$ M, pH=1.3) (solid line), and in thin layer on glass substrate (dashed line), prepared by the drying a drop of an acidic aqueous solution of TPPS₄ at room temperature.

The stability of the optical properties in general indicates that deposition and drying of J-aggregates on the substrate does not destroy them. A slight broadening of the absorption band at 489nm may appear because of possible distortion of the spatial structure of the aggregates deposited on glass substrate.

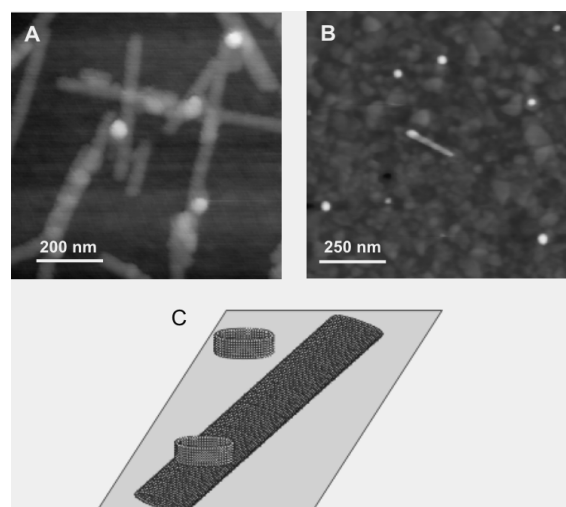


Fig. 3. TPPS₄ J-aggregates dispersed on glass (A) and hydrophobic SAM (B) substrates topography images and model (C)

AFM images of J-aggregates on glass substrate (fig. 3 A) show that TPPS₄ molecules form rod-like aggregates. Their height (~ 4nm) and width (~ 40 nm) is uniform, but length of the aggregates varies in quite broad range (from 200 - 1000 nm). This indicates that aggregates growth direction is along the rod. In AFM images presented in fig. 3 A, B besides rod-like aggregates, cylinder-like objects that are about 10 nm in height and 40 nm in diameter were observed. In literature [7] such structures were presented and described as not ordered “floculated” structures. But these structures recur in AFM images of TPPS₄ aggregates and have approximately equal size; width of these cylinder-like objects is approximately the same as width of TPPS₄ aggregates. In solution small TPPS₄ aggregates should also be present. In case of very short aggregates it could be energetically more favorable to “stand” rather than lay on the surface. It was previously reported [15], that TPPS₄ aggregates interact stronger with hydrophilic surfaces. This shows, that surface of aggregates is hydrophilic and small aggregates should tend to stand on hydrophobic surfaces so minimizing interaction surface. Our results shows, that these cylinder-like objects lay on the top of TPPS₄ aggregates when aggregates are dispersed on hydrophilic substrate (glass). In case of hydrophobic substrate (SAM of hexadecanethiol molecules) these cylinder shaped objects lay not on the surface of aggregate but on the hydrophobic SAM. These results confirms idea, that these cylindrical objects are „standing“ TPPS₄ J-aggregates (short nanotubes) (fig. 3 C). Absence of the hollow could be explained by too low resolution of used AFM.

Measurements with UHV STM showed that width of aggregate dispersed on gold substrate is around 25 nm, height – around 2 nm (fig. 4 A). Surface of aggregates is covered by small structures (fig. 4. A). On the surface of some aggregates bending threads can be seen. One almost complete ring-like structure is presented in (fig. 4, B, C). Diameter of this ring-like structure is around 17,5 nm, width of a thread is approximately 5 nm, height ~1 nm.

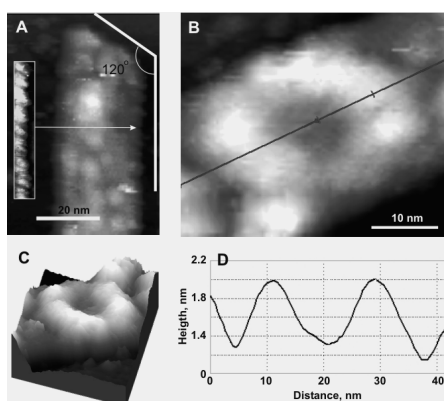


Fig. 4. STM image of TPPS₄ aggregate (insert shows side of the aggregate) (A), ring-like structure on surface of aggregate (B), 3D view of ring-like structure (C), cut of ring-like structure (D).

Width of aggregate measured with UHV STM is about 15 nm smaller than width measured with AFM in air. This difference could appear because of UHV STM has greater resolution and sharper tips were used so “tip imaging” had less effect. Width of TPPS₄ aggregates (nanotubes) presented in literature [11] measured with cryo-EM is equal to 18 nm. Our measurements with STM show 6 nm wider aggregates. Difference of aggregates width measured with STM could be explained by nanotube flattening on the gold surface. TPPS₄ aggregates deforms (flattens) after deposition on the surface (height of aggregate is equal to bilayer of TPPS₄ molecules) so width of aggregate increases. Flattened 18 nm diameter nanotube on the surface should appear as 28 nm width rod-like aggregate. These results are in good agreement with previously reported studies of TPPS₄ aggregates using AFM [7, 8, 10, 16], small angle X-ray scattering [12], theoretical modeling [13]. The most relevant structure based on spectroscopic data and mathematical modeling supports the formation of linear TPPS₄ J-aggregates [17]. The polar sulfonic groups exhibit strong intermolecular interactions with positive charge of the protonated nitrogen atoms at the center of neighboring porphyrin molecules. Theoretical modeling [13] results shows that that porphyrin ring of TPPS₄ molecule is flat in neutral solutions and it loses its flatness in acid solutions. Asymmetry of zwitterions (building blocks of the thread) leads to bending of the whole thread approximately 5° for each monomer. In literature there are presented several TPPS₄ nanotubes formation models [7, 12]. These models states, that bending threads forms rings, and nanotube is composed of these rings. However there are no data presented in literature that would show a closed ring formed of TPPS₄ molecules. Friesen et. al. [18] reported that TPPS₄ rods are composed of disk-like building blocks approximately 6 nm in diameter. They speculated that these disks are rings formed from TPPS₄ molecules. But these rings are too small to form a 18 nm diameter nanotube seen in SPM images.

Size of ring-like structure, we observed, presented in fig. 4 B perfectly coincides with SPM measurement, theoretical modeling [13] and small angle X-ray scattering [12] experiment results.

Another interesting fact is that aggregates end is diagonal (fig. 4 A). It makes 120 degrees angle with longitudinal axis of aggregate. It was impossible to determine how threads of TPPS₄ molecules are oriented in TPPS₄ aggregate because surface of aggregate was covered by small structures (TPPS₄ monomers or small aggregates), but we observed that side of aggregate is toothed (fig. 4 A insert). This toothed side is made of oblong structures approximately 2.2 nm in width and oriented same direction (approximately 117 degrees to the longitudinal axis of aggregate) as end of the aggregate. Periodicity of these structures is ~4.6 nm. In literature presented models states that aggregate is formed from rings. In this case end of the aggregate should be perpendicular to the longitudinal axis of aggregate. Nanotube could also form when a bending

thread, formed of TPPS₄ molecules, winds up to a spiral. In this case end of aggregate should be diagonal to aggregate longitudinal axis, threads formed of TPPS₄ molecules should be oriented same direction as end of aggregate. Structures observed on the side of aggregate are oriented the same direction as end of the aggregate. "Spread deck of cards", "zigzag" and "helical" models were proposed for formation of linear threads of TPPS₄ molecules [14, 17]. Size of TPPS₄ molecule is approximately 1.9 nm x 1.9 nm x 0.4 nm [9]. Width and height of threads formed agreeably to these models would approximately be 1.9 nm x 1 nm, 4.2 nm x 1 nm and 3 nm x 3 nm respectively for "Spread deck of cards", "zigzag" and "helical" models. Height of nanotube made of threads formed by helical model should be at least 6 nm. Height of TPPS₄ nanotube measured with STM is 2 nm. Regarding to these results helical formation model can be rejected. It was shown [10] that TPPS_{2a} (adjacent form) forms rodlike structures, similar to the ones formed by TPPS₄, while the aggregates TPPS_{2op} (opposite form) do not exhibit any regular features. This suggests that adjacent SO₃ groups interact with neighboring TPPS₄ molecules when TPPS₄ molecules are forming linear threads. Opposite SO₃ groups are necessary to form linear thread of TPPS₄ molecules by spread deck of cards model. In case of zigzag model – adjacent SO₃ groups are needed. We propose that thread of TPPS₄ molecules is formed by zigzag model. Toothed aggregate side confirmed confirms this model. Periodicity of structures observed on the edge of the aggregate (4.6 nm) is very similar to the width of thread of TPPS₄ molecules formed by zigzag model (4.2 nm). On base of these results we suggest, that primary TPPS₄ aggregate structure is linear bending thread formed by staircase model. TPPS₄ nanotube (meso aggregate) forms when this bending thread winds up to 18 nm diameter spiral. One winding should contain about 80 TPPS₄ molecules.

4. Conclusions

Self assembling TPPS₄ J-aggregates structure was investigated. It was shown that besides long rod-like aggregates, on the surface also some short "standing" aggregates are present. These small "standing" aggregates tend to participate on the hydrophobic surface. We noticed that aggregate surface is covered with smaller structures - bending threads that form 18 nm diameter ring-like structures. These ring like structures are primary TPPS₄ J-aggregate structures formed by stacking TPPS₄ molecules by zigzag model. We propose new TPPS₄ nanotube formation model – winding of linear threads to a 18 nm diameter spiral.

5. Acknowledgements

This study has been supported by the European Structural funds, the grant No BPD2004-ERPF-1.5.0-12-05/0035 / BPD-222.

6. References

1. Philp D, Stoddart J.F. Self-assembly in natural and unnatural systems. *Angewandte Chemie-International Edition in English*, 1996, 35:1155-1196.
2. Golubchikov O.A., Berezin B.D. Applied Aspects of the Chemistry of the Porphyrins. *Russian Chemical Reviews*. 1986, 768
3. Haruo Inoue†, Shigeaki Funyu, Yutaka Shimada, and Shinsuke Takagi. Artificial photosynthesis via two-electron conversion:Photochemical oxygenation sensitized by ruthenium porphyrins with water as both electron and oxygen atom donor. *Pure Appl.Chem.*, Vol.77, No.6, pp.1019–1033, 2005.
4. Ciplys D., Rimeika R., Sereika A., Poderys V., Rotomskis R., Shur M.S. Effect of substrate piezoelectricity on surface acoustic wave propagation in humidity –sensitive structures with porphyrin layers. *Appl. Phys. Lett.* 2009, 95, 171903.
5. Rubires R., Crusats J., El-Hachemi Z., Jaramillo T., Lopez M., Vaals E., Farrera J.A., Ribo J.M. Self-Assembly in Water of the Sodium Salts of meso-Sulfonatophenyl-Substituted Porphyrins. *NewJ.Chem.* 1999, 189-198.
6. Drain C.M., Varotto A., Radivojevic I. Self organized porphyrinic materials. *Chem. Rev.* 2009, 1630-1659.
7. Rotomskis R., Augulis R., Snitka V.Valiokas R., Liedberg B., Hierarchical structure of aggregates on substrate revealed by atomic force microscopy. *J. Phys. Chem.* 2003, 108, 2833-2838.
8. Schwab A. D., Smith D.E., Rich C.S., Young E.R., Smith W.F., Paula J.C. Porphyrin nanorods, *Phys. Chem. B.* 2003, V. 107, 11339.
9. Rubires, R.; Farrere, J.-A.; Ribo, J.M. Stirring Effects on the Spontaneous Formation of Chirality in the Homoassociation of Diprotonated meso-Tetrasulfonato Porphyrins. *Chem.s Eur. J.* 2001, 7,436 – 446.
10. Poderys, V., Selskis, A., Rotomskis, R. Solid State Phenomena. The polar sulphonic groups influence on structure of self-assembled tetrapyrrolic molecules. 2004, V. 97-98, 221-224.
11. Vlaming S. M., Augulis R., Stuart M.C.A., Knoester, J., van Loosdrecht P.H.M. Exciton Spectra and the Microscopic Structure of Self-Assembled Porphyrin Nanotubes. *Journal of Physical chemistry B.* 2009, V. 113, Issue 8, p. 2273-2283.
12. Gandini S. C. M., Gelamo E. L., Itri R., Tabak M. Small Angle X-Ray Scattering Study of Meso-Tetrakis (4-Sulfonatophenyl) Porphyrin in Aqueous Solution:A Self-Aggregation Model. *Biophysical Journal.* 2003, V. 85, 1259
13. Augulis R., Tamulienė J., Tamulis A., Rotomskis R.. Theoretical Modeling of TPPS₄ J-Aggregates. *Solid State Phenomena.* 2004, V. 97-98

14. Ohno O, Kaizu Y, Kobayashi H: J-Aggregate Formation of a Water-Soluble Porphyrin in Acidic Aqueous-Media. *Journal of Chemical Physics* 99:4128-4139, 1993
15. Augulis R., Valiokas R., Liedberg B., Rotomskis R. Atomic Force Microscopy of Self-Assembled Nanostructures of TPPS₄ on SAM Substrates. *Solid State Phenomena*. 2004, V. 97-98,
16. Snitka V., Rackaitis M., Rodaite R. Assemblies of TPPS₄ porphyrin investigated by TEM, SPM and UV-vis spectroscopy. *Sensors and Actuators B-chemical*. 2005, V. 109, Issue 1, 97-101
17. Ribo J., Crusats J., Farera J.A., Valero M. L. Aggregation in water solutions of tetrasodium diprotonated mezo-Tetrakis(4-sulfonatophenyl) porphyrin. *J. Chem soc.* 1994.
18. Friesen B.A., Nishida K.R.A., McHale J.L. Mazur U. New Nanoscale Insights into the Internal Structure of Tetrakis(4-sulfonatophenyl) Porphyrin Nanorods. *Journal of Physical Chemistry C*. 2009, V. 113, Issue 5, p. 1709-1718.

INFLUENCE OF SURFACE COATING ON CdTe QUANTUM DOTS STABILITY AND INTERACTION WITH BOVINE SERUM ALBUMIN

Marija MATULIONYTE¹, Vilius PODERYS^{1,2}, Ricardas ROTOMSKIS^{1,2}

¹*Quantum Electronics Department, Faculty of Physics, Vilnius University, Sauletekio ave. 9, c. 3, 10222, Vilnius Lithuania*

maria.matte@gmail.com

²*Laboratory of Biomedical Physics, Vilnius University Institute of Oncology, Baublio 3A, 08406, Vilnius, Lithuania*
vilius.poderys@ff.stud.vu.lt, ricardas.rotomskis@ff.vu.lt

Abstract: Quantum dots – fluorescent semiconductor nanoparticles are very promising fluorescent markers for biomedical imaging due to their exceptional optical properties. It is very important to know all the effects of quantum dots interaction with biological molecules before applying them in medicine. In this work effect of quantum dots coating on interaction with bovine serum albumin (BSA), stability and spectral properties of quantum dots were investigated. Steady state and time resolved fluorescence spectroscopy results showed that CdTe quantum dots coated with mercaptosuccinic acid (MSA) are more stable in aqueous solution than CdTe quantum dots coated with thioglycolic acid (TGA). Bovine serum albumin appeared to stabilize CdTe-TGA quantum dots and prevent from aggregating. In the case of CdTe-MSA quantum dots, addition of BSA induced decrease of photoluminescence intensity though quantum dots remained stable and did not precipitate even after two months.

Keywords: quantum dots, coating, thioglycolic acid, mercaptosuccinic acid, bovine serum albumin, interaction, stabilization, aggregation.

1. Introduction

Quantum dots – fluorescent semiconductor nanoparticles - are more resistant to photobleaching than nowadays for biomedical imaging used organic dyes. For their broad absorption spectra and narrow photoluminescence spectra they are perfectly suitable for multicolor imaging. Tunable photoluminescence wavelength and easy modified surface makes quantum dots very promising fluorescent markers [1].

The best quality of quantum dots is achieved when they are synthesized in organic solutions though for imaging biological objects they have to be made water-soluble. Coating with specific molecules that have hydrophilic ends makes quantum dots water soluble and affects many other properties like photoluminescence quantum yield [2, 3], stability (toxicity) [4] and interaction with biological molecules.

In earlier studies interaction of CdTe quantum dots with bovine serum albumin was investigated [5]. It was shown that CdTe quantum dots coated with thioglycolic acid (TGA) are not stable in aqueous solution. Bovine serum albumin appeared to stabilize CdTe-TGA quantum dots and prevent from aggregating.

In this paper effect of coating on quantum dot-protein interaction was investigated. Results of CdTe

TGA-coated quantum dots are compared with the ones of CdTe quantum dots coated with mercaptosuccinic acid. Both TGA and MSA have same hydrophilic groups and differ only in structure – thioglycolic acid has one carboxylic acid group and mercaptosuccinic acid has two branches both ending with carboxylic acid groups. However, stability and interaction with BSA are different to CdTe-TGA and CdTe-MSA quantum dots.

2. Materials and methods

Samples for spectroscopic measurements were prepared by dissolving CdTe quantum dots ($\lambda = (550 \pm 5)$ nm, PlasmaChem GmbH, Germany) in saline (0.9 %, pH=5.6). CdTe quantum dots coated with thioglycolic acid (TGA) and CdTe quantum dots coated with mercaptosuccinic acid (MSA) were used. Investigating interaction of quantum dots with protein, bovine serum albumin (V fraction, $M = 69000$ g/mol Sigma, Germany) was added to CdTe solutions in saline.

Spectral measurements were performed immediately after preparation of solutions.

Absorbance spectra were measured with Varian Cary Win UV (Varian Inc., Australia) absorption spectrometer. Photoluminescence spectra were measured with Varian Cary Eclipse (Varian Inc.,

Australia) and PerkinElmer LS 50B (PerkinElmer, USA) fluorimeters. Photoluminescence excitation wavelength was 405 nm. Measurements were done in 1 cm path length quartz cells (Hellma, Germany). Cells were hermetically sealed and between measurements kept in dark at room temperature.

Photoluminescence decay measurements were performed with FLS920 (Edinburgh instruments, UK) using time correlated single photon counting technique. EPL-405 (Edinburgh instruments, UK) laser, emission wavelength 405nm and pulse repetition rate 500 kHz was used for excitation. Photoluminescence decay was measured at peak of photoluminescence band (550 nm).

3. Results

CdTe quantum dots coated with thioglycolic acid (TGA) appeared to be not stable in aqueous solution – after 144 hours photoluminescence intensity of quantum dots solution in saline started to decrease, photoluminescence band started getting narrower and shifted to longer wavelength region (Fig. 1). Simultaneously absorption slightly decreased. This indicates aggregation of quantum dots. At 270th hour photoluminescence intensity was close to zero and after nine days precipitate was observed.

Spectral properties of CdTe quantum dots coated with mercaptosuccinic acid (MSA) remained stable for 250 hours. After that time photoluminescence intensity started slightly decreasing, slow shift to longer wavelength region was observed. Width of photoluminescence band remained intact. No precipitate was observed even after 2 weeks.

Addition of bovine serum albumin changed dynamics of CdTe-TGA quantum dots in saline. A sudden increase followed by further growth of photoluminescence intensity was observed after bovine serum albumin was added. Photoluminescence intensity increased for 64 hours and after that started decreasing, but even after two months did not drop below half of the value of initial intensity, no precipitate was observed [5].

In case of CdTe-MSA quantum dot solution with bovine serum albumin photoluminescence intensity started decreasing straight away, but after 50 hours slowed down and stabilized. Photoluminescence band maximum over the 336 hours shifted to longer wavelength region by 5 nm. Width of photoluminescence band remained intact.

Time resolved spectroscopy measurements showed that photoluminescence of CdTe-TGA quantum dots without protein decays faster. Decay is described with four exponents ($\chi^2=1.018$) while photoluminescence decay of quantum dots with bovine serum albumin is tri-exponential ($\chi^2=1.063$) (Fig. 2). Photoluminescence lifetime analysis showed that in case of quantum dots with BSA the fastest relaxation component ($\tau_1=3.4$ ns) disappeared.

In case of MSA coating photoluminescence decay of CdTe quantum dots is described best not with four but with three exponents. Addition of bovine serum

albumin to CdTe-MSA quantum dots solution does not change photoluminescence decay. It remains tri-exponential ($\chi^2=1.09$).

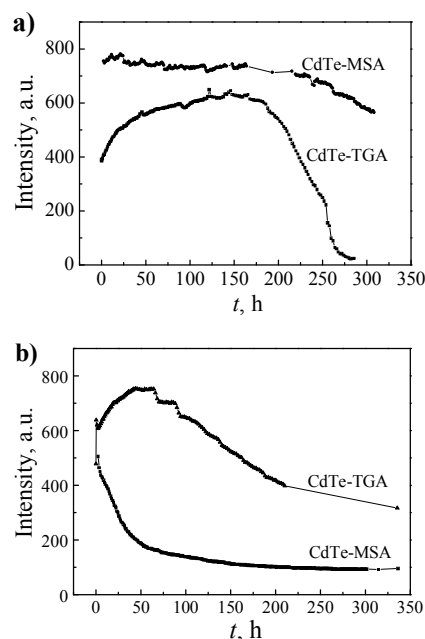


Fig. 1. Photoluminescence intensity dynamics of CdTe quantum dot solutions. a) CdTe quantum dot solutions without bovine serum albumin, b) CdTe quantum dot solutions with bovine serum albumin

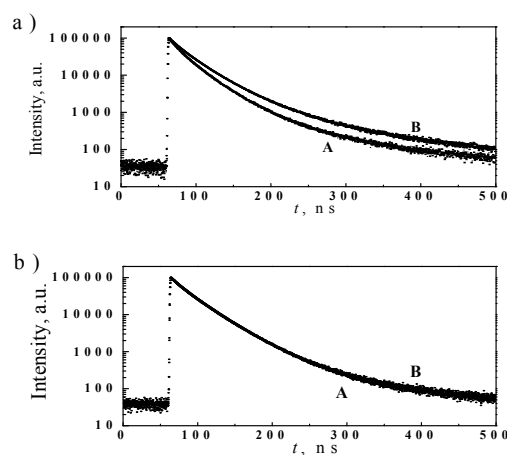


Fig. 2. Photoluminescence decay of a) CdTe-TGA quantum dots and b) CdTe-MSA quantum dots solutions ($c=6 \times 10^{-6}$ mol/l) without bovine serum albumin (curve A) and with bovine serum albumin ($c=3 \times 10^{-5}$ mol/l) (curve B)

4. Discussion

Our proposed model, explaining spectral dynamics of CdTe-TGA quantum dots in aqueous solution with and without BSA is presented in figure 3.

After dissolution of CdTe quantum dots coated with thioglycolic acid in aqueous media, increase of photoluminescence intensity was observed (Fig. 1, a), but absorption spectra and photoluminescence band position did not change [5]. This showed that quantum

dot core remained intact. Photoluminescence intensity increase (from preparation of solution till 144th hour) should be caused by increasing photoluminescence quantum yield of CdTe quantum dots. Photoluminescence quantum yield of quantum dots could increase if number of quantum dots surface defects decreases [4]. This could be caused by rearrangement of quantum dots coating (TGA) molecules (Fig. 3, IA). Since thioglycolic acid molecules are not covalently bound to the quantum dot core (they are attached to it by coordinating bonds [5]) they can be washed out from the quantum dots. This would lead to reduced quantum dot coating quality and decrease of quantum dots photoluminescence quantum yield (Fig. 3, IIA). Due to washout of surface molecules hydrophobic core of quantum dot is exposed to water. Such quantum dots tend to aggregate (Fig. 3, IIIA). This is confirmed by observed photoluminescence band shift to longer wavelength region and decrease of absorption. Atomic force microscopy measurements done 40 min, 5 hours and 24 hours after preparation of CdTe quantum dots solution also confirmed aggregation of quantum dots [5]. CdTe quantum dots in aqueous media precipitated nine days after preparation of solution (Fig. 3, IVA), photoluminescence intensity and absorption was close to zero.

Addition of bovine serum albumin changed dynamics of spectral properties of CdTe-TGA quantum dots. A sudden increase of photoluminescence intensity was observed after BSA was added to CdTe quantum dots solution. Time resolved spectroscopy measurements showed that addition of BSA to CdTe-TGA quantum dots solution eliminated the fastest excitation relaxation pathway. The fastest non-radiative relaxation path should be related with surface defects of quantum dots [8], so elimination of the fastest component increased photoluminescence quantum yield of CdTe-TGA quantum dots.

Increase of photoluminescence intensity might be caused by formation of additional quantum dots coating (bovine serum albumin) layer (Fig. 3, IB) that enhanced photoluminescence quantum yield of quantum dots. Further growth of photoluminescence intensity (observed from sample preparation till 40th hour) is related to rearrangement of surface coating (TGA) molecules (Fig. 3, IIB) which led to increasing photoluminescence quantum yield. Later photoluminescence intensity of quantum dots started to decrease but even after 300 hours did not drop below half of the value of initial intensity. Decrease of photoluminescence intensity is caused by slow wash out of TGA molecules (Fig. 3, IIIB) that reduces quality of surface coating and led to reduced photoluminescence quantum yield. Atomic force microscopy measurements confirmed that CdTe-TGA quantum dots in aqueous solution with BSA remained stable and did not precipitate.

Model, explaining spectral dynamics of CdTe-MSA quantum dots in aqueous solution with and without bovine serum albumin, is presented in figure 4.

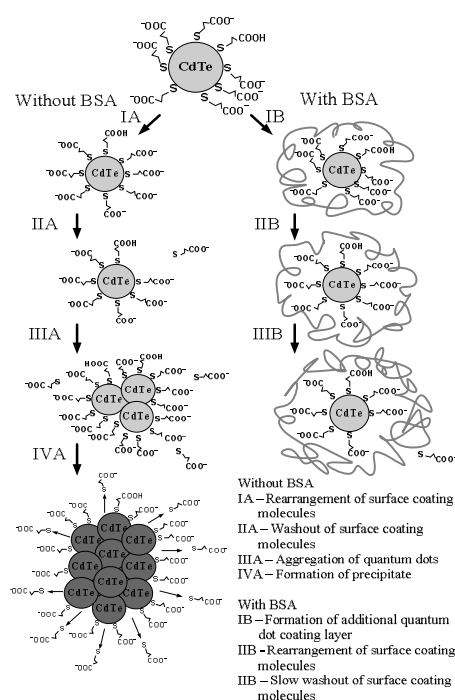


Fig. 3. Model of water soluble CdTe-TGA quantum dots aggregation in aqueous solution (A processes) and stabilization with bovine serum albumin (B processes)

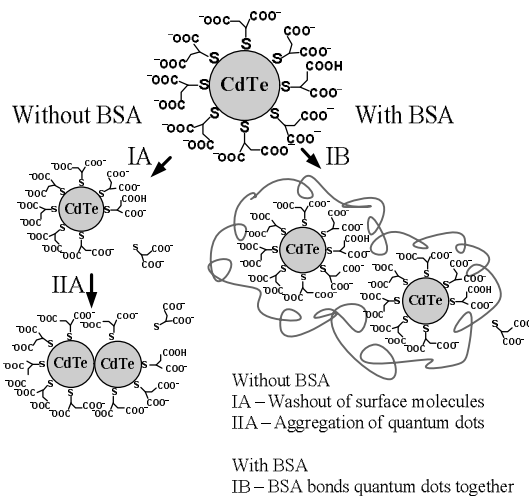


Fig. 4. Model of water soluble CdTe-MSA quantum dots aggregation in aqueous solution (A processes) and interaction with bovine serum albumin (B process)

Photoluminescence intensity of CdTe-MSA quantum dots in aqueous solution remained stable for approximately 250 hours after preparation of solution. After that time photoluminescence intensity started slowly decreasing. This indicated that surface molecules of quantum dots are slowly washing out (Fig. 4, IA) as they are attached to the core by coordinating bonds [7]. Washout of surface molecules led to formation of small aggregates (Fig. 4, IIA) and slow photoluminescence band shift to longer wavelength region though photoluminescence band width remained intact and no precipitates were observed even after two months. These results show, that CdTe quantum dots coated with

mercaptosuccinic acid are more stable than CdTe quantum dots coated with thioglycolic acid.

Photoluminescence decay of CdTe-MSA quantum dots is described best not with four but with three exponents. Compared with CdTe-TGA quantum dots photoluminescence decay the fastest non-radiative relaxation path is absent. This shows that CdTe-MSA quantum dots may have less surface defects [7] as in case of CdTe-TGA quantum dots the fastest relaxation component disappeared after addition of BSA, which increased photoluminescence quantum yield.

Addition of bovine serum albumin strongly changes dynamics of photoluminescence intensity of CdTe-MSA quantum dots solution. Photoluminescence intensity of CdTe-MSA quantum dots solution starts immediately decreasing after addition of BSA (Fig. 1, b). This might be explained by BSA molecules wrapping several quantum dots together (Fig. 4, IB). After 50 hours decrease of photoluminescence intensity slows down and CdTe-MSA quantum dots do not precipitate even after two weeks though photoluminescence intensity is close to zero. However, addition of bovine serum albumin to CdTe-MSA quantum dots solution does not change photoluminescence decay. It remains tri-exponential ($\chi^2=1.09$). This shows that bovine serum albumin does not influence photoluminescence decay of CdTe-MSA quantum dots. Reduction of photoluminescence intensity may be related to decrease in quantum yield of CdTe-MSA/bovine serum albumin complex.

5. Conclusions

Experiments showed that CdTe-TGA quantum dots are not stable in aqueous media and aggregate. Addition of bovine serum albumin stabilizes CdTe-TGA quantum dots and prevents from aggregating. CdTe-MSA appeared to have fewer surface defects. CdTe-MSA quantum dots are stable in aqueous media but addition of BSA decreases photoluminescence intensity. This shows that different coatings of quantum dots may cause different effects on quantum dot – protein interaction.

6. Acknowledgements

This work was supported by the project “Multifunctional nanoparticles for specific non-invasive early diagnostics and treatment of cancer” (No. 2004-LT0036-IP-1NOR).

7. References

1. Rotomskis R., Streckytė G., Karabanovas V. Nanodariniai diagnostikai ir gydymui: nanomedicinos link. *Medicina* 42 (7), Kaunas, 2006, p. 542-558.
2. Kloepfer J.A., Bradforth S. E., Nadeau J. L.. Photophysical Properties of Biologically Compatible CdSe Quantum Dot Structures, *J. Phys. Chem. B* 109, 2005, p. 9996-10003.
3. Li C., Murase N., Surfactant-dependent Photoluminescence of CdTe Nanocrystals in Aqueous Solution, *Chem Lett* 34, 2005.
4. Ma J., Chen J.Y., Guo J., Wang C.C., Improvement of the Photostability of Thiol-Capped CdTe Quantum Dots in Aqueous Solutions and in Living Cells by Surface Treatment. *Nanotechnology* 17, 2006, p. 5875–5881.
5. Poderys V., Motekaitis D., Rotomskis R., CdTe Quantum Dots Stabilization by Protein in Aqueous Solution. *Proceedings of the 7th International Conference “Medical Physics in the Baltic States”, Kaunas, 2009.*
6. Karabanovas V., Zakarevicius E., Sukackaite A., Streckyte G., Rotomskis R.. Examination of the Stability of Hydrophobic (CdSe)ZnS Quantum Dots in the Digestive Tract of Rats. *Photochem. Photobiol. Sci.* 7, 2008, p. 725-729.
7. Mandal, A., Tamai, N.. Influence of Acid on Luminescence Properties of Thioglycolic Acid-Capped CdTe Quantum Dots. *J. Phys. Chem. C* 112, 2008, p. 8244–8250.
8. Kim D., Miyamoto M., Nakayama M., *J. of Electron Microscopy* 54, 2005, i31-i34.

CHARACTERIZATION OF CANCER STEM CELLS AND THEIR RESPONSE TO CdTe QUANTUM DOTS

Simona PETROŠIŪTĖ^{1, 2}, Rasa PURVINIENĖ³, Vita PAŠUKONIENĖ³, Simona LUKOŠEVIČIŪTĖ⁴,
Petras JUZĖNAS⁴, Ričardas ROTOMSKIS^{1,2}

¹Institute of Oncology Vilnius University, Laboratory of Biomedical Physics, Vilnius, Lithuania

²Vilnius University, Laser Research Center, Laboratory of Biophotonics, Vilnius, Lithuania

³Institute of Oncology Vilnius University, Laboratory of Immunology, Vilnius, Lithuania

⁴Institute for Cancer Research, Oslo University Hospital – Radiumhospital, Oslo, Norway

Abstract: Cancer stem cells display extensive differentiation potential and can give rise to new tumours. Therefore, an important attention must be paid for cancer stem cell identification, characterization and investigation of for novel targeted therapies. Quantum dots are promising tools in fighting against cancer. However, there is not much known about accumulation and cytotoxicity of quantum dots in cancer stem cells. It is important to know that before we use quantum dots as therapy agents.

Keywords: Quantum dots, cancer stem cells, flow cytometry, FACS, CD133, CD44, nanoparticles.

1. Introduction

Human tumours exhibit intra-tumoural heterogeneity at genetic and epigenetic level. The existence of functional heterogeneity between defined sub-populations of tumour cells has also been described in clonogenic and xenotransplantation studies. Numerous studies have used cell surface markers to isolate sub-populations of cancer cells, which possess enhanced tumorigenicity and self-renewal potential when injected into immunodeficient mice. Cells with such properties have been termed ‘cancer stem cells’ (CSC) [1,2].

It has been reported that CSCs are more likely to survive chemotherapy or radiotherapy. Low efficiency of chemotherapy is associated with CSC ability to extrude a drug from the cytosol through transcytosis [3]. Other studies have documented that CSCs are also more resistant to radiotherapy than non-stem cells [4, 5]. Reduced radiosensitivity is associated with activated defence mechanisms against radiation induced reactive oxygen species (ROS) and accelerated repopulation of CSCs. These studies also indicate that CSCs could be the main targets in cancer therapies.

Nanomaterials create new possibilities in targeted anti-cancer therapies. One of them is a quantum dot (QD) with possibility for easy manipulation of surface chemistry and ability to fluoresce at a desired spectral range [6]. It has been reported that QDs can be used for detection and imaging of cancer cells *ex vivo* [7] and for labelling healthy and cancerous cells *in vivo* [8]. Cancer

treatment can be performed using QDs as photodynamic therapy (PDT) agents [9, 10].

In this study we investigated if QDs could be new multifunctional agents with potential to identify and treat cancer stem cell. Accumulation and cytotoxicity of CdTe-MPA (mercaptopyropionic acid) QDs in cancer stem cells were assessed using flow cytometry and fluorescence-activated cell sorting (FACS) techniques as well as colorimetric cell viability assay.

2. Materials and methods

Pancreatic adenocarcinoma (Mia-PaCa-2, Panc-1), glioblastoma (U87) cells and human fibroblasts (F11-hTERT) were cultured in DMEM medium. Prostate adenocarcinoma (Du145, PC3) and melanoma (FEMX-I) cells were cultured in RPMI-1640 medium. Both growth mediums contained 10% fetal bovine serum, FBS (20% FBS for F11-hTERT), 100 U/ml penicillin, 100 mg/ml streptomycin and 2 mM L-Glutamine. In case of U87 cells DMEM medium was additionally supplemented with 3% MEM non-essential amino acids. The cells were routinely cultivated in 25 cm² Nunc culture dishes under standard conditions subculturing them twice a week and keeping them in a humidified incubator at 37°C. For experiments the cells were harvested bringing them into suspension by trypsinization and seeding a necessary amount of cells into multiplates.

Stock QD solution was prepared by dissolving 1 mg CdTe-MPA (fluorescence $\lambda_{max} = 710 \pm 5$ nm, PlasmaChem GmbH, Germany) in 1 ml PBS (pH=7.4) or saline (0.9% w/v NaCl). The stock solution was further diluted until a desired concentration in DMEM or RPMI-1640 medium and poured over the cells growing in the multiplates. The medium without QDs was poured in a few wells to keep control cells in the same multiplate. After incubation at 37°C for 4 or 24 h the cells were washed with ice-cold PBS+ (pH 7.4, standard PBS supplemented with 0.9 mM CaCl₂ and 0.5 mM MgCl₂ to prevent cell detachment at this step) to remove any free QDs. Immediately after washing, the cells were brought into suspension by trypsinization for further analysis using monoclonal antibodies.

Up to 10⁶ cells were labelled in PBS solution with mouse anti-human monoclonal CD44 antibody conjugated with fluorescein isothiocyanate (FITC) (BD Biosciences Pharmingen) and mouse anti-human monoclonal CD133 antibody conjugated with phycoerythrin (PE) (eBioscience, Inc.,) for 20 min. at room temperature. Respective mouse immunoglobulin and dye conjugates, IgG2b-FITC (Dako Denmark AS) and IgG1-PE (BD Biosciences), were used as unspecific binding controls. Flow cytometric analysis was carried out with a FACSsort or LSR II analyzer (BD Biosciences). The data were analyzed with Cyflogic (CyFlo Ltd, Finland) or FCS Express (De Novo, CA) software. A minimum of 10 000 viable cells were measured per sample. Using forward and side scatter profiles and propidium iodide (PI) staining, debris, cell doublets and dead cells were gated out, respectively. Fluorescence-activated cell sorting was performed on a BD FACSAria or FACSsort Cell Sorter (BD Biosciences). Purities of the sorted populations, as determined by post-sorting flow analysis, were generally >90%.

The cytotoxicity of QDs was determined using methylene blue (MB) assay on FEMX-I cell line. The same amount of the cells in each well was seeded in a 96-well plate and incubated with different concentrations of QDs. After 24 h incubation the old medium was carefully aspirated and the cells were supplemented with fresh medium and left for further growth under standard culture conditions. After 3 days the cells were washed with ice-cold PBS and fixed with 70% ethanol. After 10 min 100 μ l of filtered 1% w/v MB aqueous solution was added to each well. After 20 min, the excess dye was removed by washing the wells with distilled water. To elute the dye, 200 μ l of 0.2% Triton X-100 solution was added to each well and left overnight at 37°C. The plates were then gently shaken and the absorbance at 650 nm was measured for each well by a microplate photometer (BioTek Instruments, VT). The photometer was blanked on the first column of the control wells containing the elution solvent alone.

3. Results

We have investigated heterogeneity of six cancer cell lines using putative stem cell markers CD133 and CD44. The cell-surface associated CD44 is an adhesion glycoprotein. The function of CD133 is still unknown but it has been shown to be involved in dynamics of membrane protrusions and to mark cancer stem cells. Flow cytometry technique was performed to detect fluorescence from single cells after combined staining with antibody-dye conjugates against CD133 and CD44. All cell lines express CD44 to a similar degree, from 96.2% to 99.9% (Fig. 1). However, the expression of CD133 was very low among these cell lines (0% - 0.03%) with slightly higher prevalence in Du145 cells (0.35%, Fig. 1A) and U87 cells (1.94%, Fig. 1D). Only FEMX-I cells exhibited high expression of CD133 (99.1%, Fig. 1F).

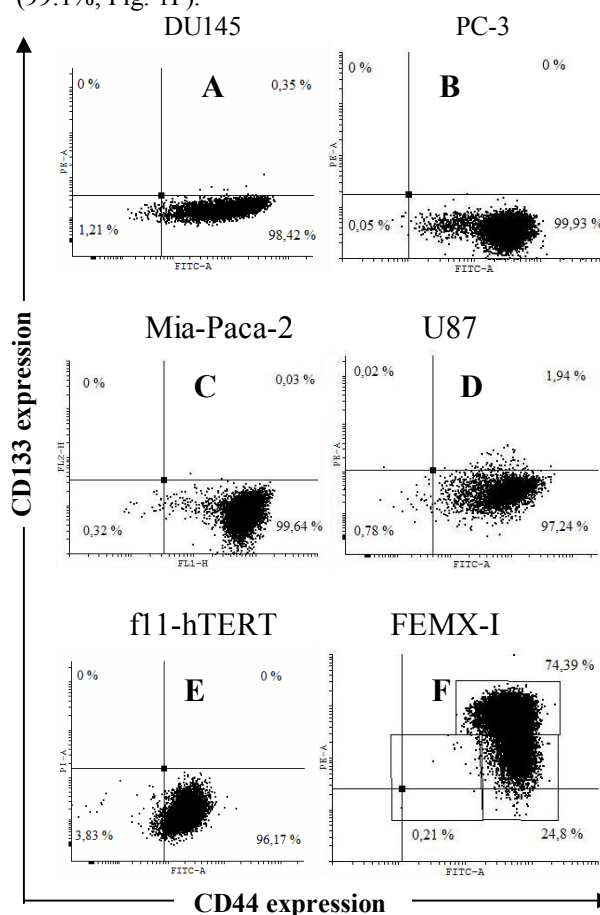


Fig. 1. A representative example of CD133 and CD44 expression in different human cell lines. A) and B) prostate adenocarcinoma cells, C) pancreatic adenocarcinoma, D) glioblastoma cells, E) non-cancerous human fibroblasts and F) melanoma cells.

The response to CD markers is not enough to determine heterogeneity of the cell lines. Therefore, we have further analyzed the shape of their phenotypical patterns (Fig. 1), which indicate the expression levels of CD133

and CD44. Du145 (Fig. 1A) and U87 (Fig. 1D) cells show nearly uniform semi-horizontal oval-shaped cloud distribution. PC-3 (Fig. 1B) and Mia-PaCa-2 (Fig. 1C) cells show two clouds, indicating two subpopulations, circular-shaped dense cloud with high CD44 expression ($CD44^{high}$) and horizontal oval cloud with low/none CD44 expression ($CD44^{low/-}$). FEMX-I cells appear to consist of three different subpopulations: $CD44^{high}CD133^{high}$, $CD44^{high}CD133^{low/-}$ and $CD44^{low/-}CD133^{low/-}$ (Fig. 1F). Since FEMX-I cells showed both high expression of two CD markers and possibility to be divided into distinct subpopulations, they were chosen for further investigations.

To examine the specificity of the used markers to cancer cells, we investigated CD44 and CD133 expression in normal human fibroblast cells f11-hTERT. Interestingly, one can obviously see CD44 expression in f11-hTERT cells (96.2%, Fig. 1E) but there was no perceptible CD133 expression. This shows that anti-CD133 is more selective for cancer cells than anti-CD44.

For correct analysis of flow cytometry data, it is important to discriminate between debris, dead cells and cell doublets. Measurements of forward scattered light (FSC) together with side scattered light (SSC) aid such separation.

Location of dead cells and cell doublets on a dot plot of forward and side scatter, B) forward and side scatter give information about live cells, dead cells and debris, C) SSC-Width vs. SSC-Area plot gives information about two or more cells agglomerated together, D) whole image of CD133 and CD44 expression in live cells together with debris, dead cells and cell doublets, E) gated image of CD133 and CD44 expression only in live cells.

As can be seen from Fig. 2A, the dead cells in Du145 population as detected by PI fluorescence are nicely located in a SSC-FSC dot plot and, therefore, can be distinguished even without additional PI staining (Fig. 2B). Cell doublets do not have exact location on SSC-FSC dot plot and usually are detected by the width of a scatter signal (Fig. 2C). Two or more cells lumped together give a wider signal. Debris is usually situated at the very left corner of a SSC-FSC plot (Fig. 2B). If one does not eliminate debris, dead cells and cell doublets, false-positive expression of CD133 and CD44 markers may be detected (Fig. 2D). However, once debris, dead cells and cell doublets are gated out, no CD133 positives are left (Fig. 2E).

We have examined the most heterogeneous cell line FEMX-I consisting of three subpopulations. To examine their capability of growing and restoring initial population, each subpopulation ($CD44^{high}CD133^{high}$, $CD44^{high}CD133^{low/-}$ and $CD44^{low/-}CD133^{low/-}$) was isolated and plated under usual growing conditions. $CD44^{low/-}CD133^{low/-}$ cells did not grow after sorting. $CD44^{high}CD133^{high}$ cells grew after sorting but after 10 days of growth the cells did not show significant changes in their phenotypical composition.

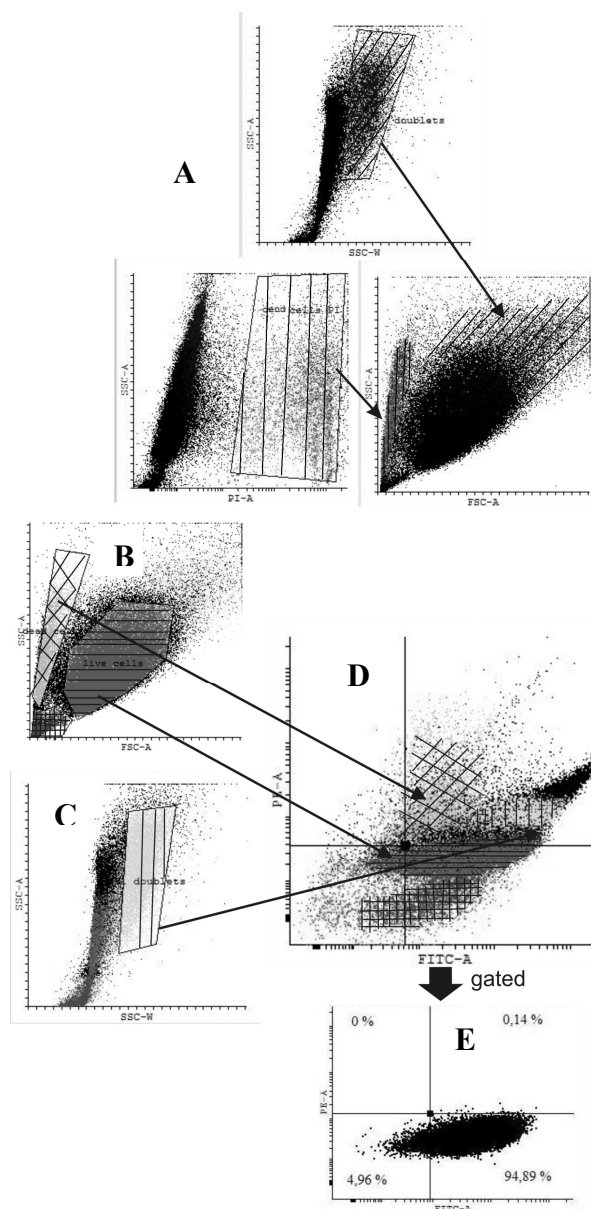


Fig. 2 Schematic representation of debris, dead cells and cell doublets determined by flow cytometry of Du145 cells. A)

Immediately after sorting the subpopulation was composed of around 95% $CD44^{high}CD133^{high}$ cells (results are not shown) and remained unchanged after 10 days of growth (Fig. 3B) suggesting that $CD44^{high}CD133^{high}$ subpopulation was unable to restore its progeny. However, $CD44^{high}CD133^{low/-}$ cells were able to grow and change their phenotypical composition. Immediately after sorting the cells were composed of around 80 % $CD44^{high}CD133^{low/-}$ cells (results are not shown) and after 10 days of growth the same cells were composed of around 58,85 % $CD44^{high}CD133^{low/-}$ and around 40,90 % $CD44^{high}CD133^{high}$ cells (Fig. 3C) thus approaching the phenotypical composition of unsorted cells (Fig. 3B).

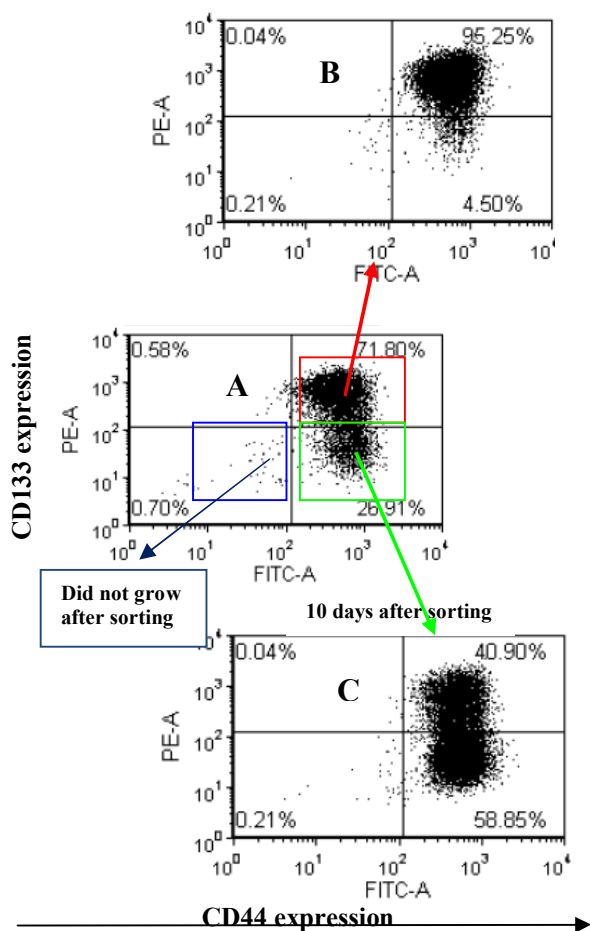


Fig.3. The CD profile of CD44^{high} CD133^{high}, CD44^{high} CD133^{low/-} and total population of FEMX-I cells. A) phenotype of the total population of the cells, B) phenotype of CD44^{high} CD133^{high} and C – CD44^{high} CD133^{low/-} cells after 10 days of growth.

To determine the cytotoxicity of CdTe-MPA on FEMX-I cells, the unsorted cells were incubated with different concentrations of QDs for 24 h. The cell viability was determined using colorimetric MB assay. As can be seen from Fig. 4, the viability decreases increasing CdTe-MPA concentration, suggesting that QDs are cytotoxic to the cells. To investigate the response of each defined subpopulation to such cytotoxic QDs, a concentration of CdTe-MPA QDs was chosen to be high enough to induce death for approximately half of the cells (Fig. 4, dotted line). Immediately after the incubation flow cytometry was performed to observe any changes in a phenotypical composition of the treated FEMX-I cells.

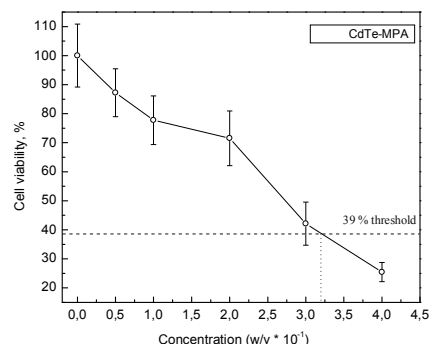


Fig. 4 FEMX-I cell viability after treatment with different concentrations of CdTe-MPA QDs. The viability was calculated as a percentage from the viability of the control untreated cells. The results are means \pm SD from three independent experiments.

When compared to the control untreated cells, QD-treated cells contained 1.25 times more CD44^{high}CD133^{low/-} cells (42% vs. 34% in the control) and 1.4 times less CD44^{high}CD133^{high} cells (41% vs. 59% in the control). The percentage of CD44^{low/-}CD133^{low/-} cells increased after the treatment, which might be associated with CdTe induced apoptosis.

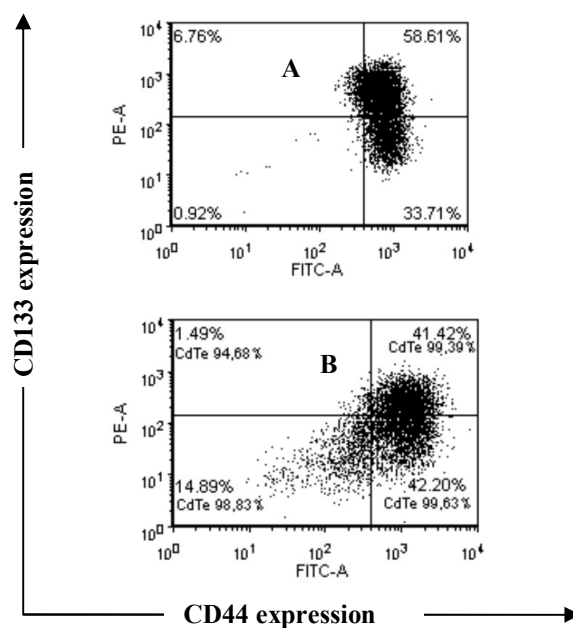


Fig. 5. The CD profile of FEMX-I cells: plot A – untreated cells, plot B – treated with CdTe QD. Quadrants divide cells into subpopulations: CD44^{high}CD133^{high}, CD44^{high}CD133^{low/-} and CD44^{low/-}CD133^{low/-}. Percentages marked with “CdTe” are CdTe positives in a defined subpopulation.

Accumulation of CdTe-MPA QDs in FEMX-I cells was also examined by flow cytometry. The number of CdTe-MPA positives was calculated as a percentage from all CD44^{high}CD133^{high}, CD44^{high}CD133^{low/-} and CD44^{low/-}CD133^{low/-} subpopulations. Interestingly, approximately 99% of each subpopulation exhibited CdTe-MPA fluorescence (Fig. 5B) showing no differences in QD uptake by different FEMX-I subpopulations.

4. Discussion

In this study, we have investigated population heterogeneity of normal fibroblasts, prostate and pancreatic adenocarcinoma, glioblastoma and melanoma cancer cell lines using putative CSC markers CD44, an adhesion molecule, and CD133, which has been recently considered as a common marker of tumour stem cells [11]. All studied cell lines exhibited high expression of CD44 (Fig. 1), while CD133 was highly expressed only in FEMX-I cells (Fig. 1E). Therefore, the latter cells were chosen for further examination of their stem-like properties.

Our experiments demonstrate that FEMX-I cells consist of three distinct subpopulations with different CD133 and CD44 expression levels: CD44^{high}CD133^{high}, CD44^{high}CD133^{low/-} and CD44^{low/-}CD133^{low/-}. Rappa and colleagues also have shown CD133 expression in FEMX-I cells and stated that downregulation of CD133 in FEMX-I cells results in decreased growth rate and migratory capacity, which suggests CD133 to be essential in tumour formation and regression [12-13]. Interestingly, we can suggest that the subpopulation with lower expression of CD133 antigen possibly represents tumorigenic stem cells since only CD44^{high}CD133^{low/-} cells were capable of progeny restoration after their isolation and were also resistant to the toxic effect of CdTe-MPA QDs. The toxicity of CdTe is associated with release of Cd²⁺ ions and generation of ROS products [14]. The concentration of QDs was chosen to correspond to lethal concentration LC40, *i.e.* high enough to induce obvious QD-associated cell death (Fig. 4) and thus to examine whether QD-resistant subpopulation exists. Although no significant differences in CdTe-MPA accumulation among CD44^{high}CD133^{high}, CD44^{high}CD133^{low/-} and CD44^{low/-}CD133^{low/-} subpopulations was observed (Fig. 5B), these populations showed different behaviour: The percentage of CD44^{high}CD133^{low/-} cells actually increased after CdTe-MPA treatment. However, our results cannot be directly compared with the studies of Rappa and colleagues who have experimented with whole CD133⁺ population while we have divided CD133⁺ into CD133^{high} and CD133^{low/-}.

When considering novel targeted therapies it is important to know whether a potential therapeutic agent can accumulate inside a cell. In our study we have shown that although FEMX-I cell line is heterogeneous, CdTe-MPA QDs accumulate equally in different subpopulations. To our knowledge, this the first time

when QD accumulation in different subpopulations of cancer stem-like cells was evaluated.

5. Conclusions

Our experiments show that FEMX-I cell line is heterogeneous and can be divided into subpopulations with higher and lower expression of CD44 and CD133. The subpopulation with lower expression of CD133 (CD44^{high}CD133^{low/-}) displays characteristics of cancer stem cells by being more resistant to QD cytotoxicity and capable to restore its progeny. There is no difference in the accumulation of CdTe-MPA QDs among different FEMX-I subpopulations. These interesting results encourage for further investigations on applicability of QDs in CSC targeting therapies.

6. Acknowledgements

This study has been supported by the Research Council's of Lithuania grant No. LIG-15/2010, the EU and Norwegian grant No. 2004-LT0036-IP-1NOR.

Simona Petrosiute has participated in ERASMUS Lifelong Learning Programme, which was organized by Vilnius University and funded by the European Commission and the Republic of Lithuania.

Petras Juzenas and Simona Lukoseviciute were supported by the Research Council of Norway (grant No. 182058) and the South-Eastern Norway Regional Health Authority (grant No. 20100068).

We are grateful to dr. Lina Prasmickaite for helpful advices and to Idun Dale Rein for technical support.

7. References

1. Cho RW, Clarke MF. Recent advances in cancer stem cells. *Curr Opin Genet Dev* 2008;18:48–53.
2. Shipitsin M, Polyak K. The cancer stem cell hypothesis: in search of definitions, markers, and relevance. *Lab Invest* 2008;88:459–463.
3. Bertolini G., Roz L., Highly tumorigenic lung cancer CD133+ cells display stem-like features and are spared by cisplatin treatment, *PNAS*, vol.106, no.38, 16281–16286. September 22, 2009.
4. Phillips, T. M., McBride, W. H. & Pajonk, F. The response of CD24^{-low}/CD44⁺ breast cancer-initiating cells to radiation. *J. Natl Cancer Inst.* **98**, 1777–1785 (2006).
5. Woodward, W. A. *et al.* WNT/ β -catenin mediates radiation resistance of mouse mammary progenitor cells. *Proc. Natl Acad. Sci. USA* **104**, 618–623 (2007).
6. Rotomskis R., Streckytė G., Karabanovas V.. Nanodariniai diagnostikai ir gydymui: nanomedicinos link [Nanoparticles in diagnostics and therapy: Towards nanomedicines]. *Medicina* (Kaunas), 2006, 42 (7) p.542-558.

7. Rotomskis R. Optical biopsy of cancer: nanotechnological aspects, *Tumori* 2008; 94: p.200-205.
8. Gao X., Cui Y., Levenson R.M., Chung L., Nie S.. In vivo cancer targeting and imaging with semiconductor quantum dots, *Nature Biotechnology* 2004; 22:969 – 976.
9. Bakalova R., Ohba H., Zhelev Z., et. al. Quantum dots as photosensitizers?, *Nature Biotechnology* 2004; 11: 1360-1361.
10. Juzenas P., Chen W., Sun YP., et al. Quantum dots and nanoparticles for photodynamic and radiation therapies of cancer, *Advanced Drug Delivery Reviews* 2008, 60:1600–1614.
11. Mizrak D, Brittan M, Alison MR. CD133: molecule of the moment. *J Pathol* 2008;214:39.
12. Rappa G., Mercurio J., et al. Growth of cancer cell lines under stem cell-like conditions has the potential to unveil therapeutic targets, *Exp Cell Res.* 2008; 314:2110-2122.
13. Rappa G., Fodstad O., et al. The stem cell-associated antigen CD133 (Prominin-1) is a molecular therapeutic target for metastatic melanoma, *Stem Cells.* 2008; 26(12):3008-3017.
14. Cho SJ, Maysinger D, Jain M, et al. Long-term exposure to CdTe quantum dots causes functional impairments in live cells, *Langmuir.* 2007; 23(4):1974-1980.

SURFACE MODIFICATION OF (CdSe)ZnS QUANTUM DOTS USING THIOLS – CHARACTERIZATION, PHOTOPHYSICAL AND BIOLOGICAL STUDIES

Karolis Stašys^{* **}, Vitalijus Karabanovas^{****}, Ričardas ROTOMSKIS^{* ****}, Mindaugas Valius^{***}

^{*}Laboratory of Biomedical Physics of Vilnius University institute of Oncology;

^{**}Vilnius University, Physics Faculty, Quantum Electronics Department, Biophotonics laboratory;

^{***}Institute of Biochemistry, Department of Developmental biology;

^{****}Laser Research Center of Vilnius University.

Abstract: In this work surface modification of (CdSe)ZnS-TOPO QDs using three different thiols was performed. Stability, spectral properties, and QDs behavior in immortalized mouse embryonic fibroblasts NIH3T3 cells was investigated. It is shown that depending on surface coating, QDs stability and behavior differs in various pH buffers and biological environment. Observation in biological media showed that the localization and uptake of QDs in NIH3T3 cells differs with each type of surface modification.

Keywords: Quantum dots, mercaptopropionic acid (QDS-MPA), thioglycol (TGA), QDs-CYSteamine (QDS-CYS), fluorescence spectroscopy.

1. Introduction

Quantum dots are fluorescent semiconductor nanoparticles that are widely explored due to their possible applications in many fields such as molecular and cellular biology, hybrid nanobiosensors and drug delivery systems and medicine. Tunable emission wavelength, broad absorption and sharp emission spectra, high quantum yield (QY), resistance to chemical degradation and photobleaching, versatility in surface modification makes quantum dots very promising fluorescent markers [10].

QDs can be used for live cell labeling, detection and imaging of cancer cells and for treatment of cancer using photodynamic therapy [11]. Despite all unique photophysical properties, some problems must be solved before QDs can be successfully applied in medicine. QDs are synthesized in organic solutions, are water insoluble and made of materials (Cd, Se) that are toxic for biological objects. The main strategies to make QDs soluble include silanization and surface exchange with bifunctional molecules. Such molecules have a hydrophobic side (e.g., a thiol group) that binds to the ZnS layer of the QDs and a hydrophilic side (e.g., a carboxyl group –COOH). A next strategy involves encapsulation of QDs within phospholipids micelles, polymer beads or block-copolymer micelles, which are composed of synthetic polymers containing hydrophilic and hydrophobic parts. The hydrophilic part is commonly poly[ethylene oxide], while the hydrophobic part may utilize amino acids and polyesters.

At present, most of the related efforts on the ligand chemistry of semiconductor QDs are focused on the development of new types of ligands and different passivation strategies. However, it remains an open question as to how the decay behavior and surface morphology change by changing the pH of the solution, and more experiments are still required to understand the influence of the surface structure on the luminescence properties of the thiols capped QDs. Therefore, studies of the surface structure of thiol-stabilized nanoparticles continue to be of great importance in understanding the control of the optical properties of nanoparticle materials. And it's still important to know about thiol-stabilized QDs interaction with biological surrounding, cytotoxicity, stability and distribution in the cells.

One problem that occurs is low quality of surface coating after modification that reduces photophysical properties. However, Ravindrans group showed how surface modification using cysteamine and mercapto groups affect cell localization and quantum yield by increasing both qualities [2].

Secondly, QDs usage as probes and dyes occurs uncertain. One scientific group showed how using cysteamine and protein groups for coating, QDs managed to dye cytoplasm [3]. Thou many unanswered questions remains, especially how QDs tend to localise in cells.

The biggest problem remains is QDs hazardousness to cells. After injection of hydrophobic quantum dots to live organisms they tend to agglomerate and obstruct

vital veins. Uptaken by OS hydrophobic QDs do not permeate through gastric wall [10]. This might lead to the destruction of the quantum dots core and to the release of Cd^+ ions that are highly toxic. It is very important to know how different ways of modification influences the biological effects and photophysical properties of QDs before using them in medical applications. Nowadays there are three main ways to make QDs water soluble using different thiol groups but there were no attempts to compare all of them together. It was showed that both the physicochemical properties and the cellular toxicity of surface modified quantum dots are dependent on the surface molecules not the core material [1]. It was also showed that coating made from mercapto group molecules allows the QDs to pass into cells and localizes them in vesicles [2] One scientific group made water soluble nanocrystals using MPA and MUA (11-*mercapto*-undecanoic acid) and received greater full width at half maximum (FWHM) but lower photoluminescence (PL) than original [4]. Some authors also observed QDs-TGA temporal PL decrease and bathochromic shift using different pH buffers [5]. In this work the surface of hydrophobic (CdSe)ZnS-TOPO QDs was modified using thiols, such as MPA, TGA, CYS and compared their stability and spectral properties in different pH solutions then observed uptake and localization in NIH3T3 cells.

2. Materials and methods

Quantum dots solutions were prepared by evaporating toluene from (CdSe)ZnS-TOPO ($\lambda = (595 \pm 5)$ nm, Evident Technologies, USA, $c=19.67 \mu\text{M}$) solution. Then the dry QDs were resuspended in chloroform and mixed with the same amount of liquid MPA (10:4 QDs:MPA; Sigma-Aldrich, Germany), TGA (10:4 QDs:TGA; Fluka, Germany) and CYS (10:4 QDs: CYS; Sigma-Aldrich, Germany) and all three samples were left to vortex for 48 hours. The obtained solutions were purified using a centrifuge at 14000 rpm for 15 minutes three times using ethanol (98%) to precipitate. Then the products were desiccated to remove all traces of ethanol and then dissolved in distilled water. Spectral measurements of modified QDs ($c=98 \text{ nM}$) were performed in PBS (pH 7.4) immediately after preparation of solutions.

The same concentration of QDs dissolved in different pH (6.6-8) PBS solution was used in stability experiments.

(CdSe)ZnS-TOPO QDs dissolved in toluene were used to compare how certain properties have changed after modification with different thiol groups.

Absorbance spectra were measured with Varian Cary Win UV (Varian Inc., Australia) absorption spectrometer. Photoluminescence spectra were measured with Varian Cary Eclipse (Varian Inc., Australia) fluorimeters. Photoluminescence excitation wavelength was 405 nm, excitation slits were 2.5 nm, and emission slits 5 nm for Varian Cary Eclipse. Hellma Optik (Jena, Germany) cell with 1 cm length optical path was used for all optical measurements.

PL lifetime experiments were performed with a FLS920 Steady State and Fluorescence Lifetime Spectrometer (Edinburg instruments, United Kingdom). This system is equipped with a 405nm GaN laser diode, which produce 66ps pulses at a repetition rate of 20MHz and time correlated single photon counting system. "FAST" software package for the advanced analysis of QDs PL multi-exponential decay kinetics was used. Photoluminescence decay was measured at different peaks of photoluminescence band according to different coating (595 nm for QDs-MPA and QDs-TGA and 600 nm for QDs-CYS).

Cell culture line: NIH-3T3 – immortalized mouse embryonic fibroblast cell line. Cell line have been cultured in the presence of CO_2 (5 % v/v) at 37°C in Dulbecco's Modified Eagle's (DME) Medium supplemented with foetal bovine serum (10 % v/v), 0.1 % antibiotics (stock: 1000 U/mL Penicillin, 1000 $\mu\text{g}/\text{mL}$ Streptomycin) to get ~60 % of confluence.

Living cells were *in vitro* imaged with a confocal Nikon Eclipse TE2000-S, C1 plus microscope equipped with Leica CCD camera DFC 290. NIH-3T3 cells were washed 3 times with 37°C DME medium before imaging.

DIOC₆ (Invitrogen, USA, 1 $\mu\text{g}/\text{mL}$) was used to label cells endoplasmic reticulum, vesicles membranes and mitochondria.

All cell specimens were incubated for 24 hours with the same concentration ($c=60\text{nM}$) of differently modified QDs.

3. Results

3.1. Spectroscopic studies

During the first stage of our experiments the influence of surface modification with MPA, TGA and CYS of QDs on optical properties was investigated by using steady state and ultrafast spectroscopy techniques. Study of optical properties (optical density, PL intensity, position and width of PL band and PL decay) after three different thiol groups modification was investigated in phosphate buffer (PBS, pH 7.4) solution (Fig. 1 A,B,C).

Decrease of absorbance at the interval ranging from 400 up to 630nm was detected in both QDs-MPA and QDs-CYS solutions. (Fig. 1A). The cysteamine modified QDs absorbance decreased rapidly and even the absorption excitonic peak at 583 nm is not clearly visible. After dissolving QDs-CYS start to aggregate and precipitation of large aggregates was detected. On the other hand, the absorption bands for QDs-TGA and QDs-MPA are detectable and sharper than original QDs. Spectral positions of the absorption bands remained constant. There for it can be suggested that QDs surface coating changes do not affect their absorption peak position only determine the solution colloidal stability. PL decreased to about 80% of its initial intensity value for QDs-CYS, 11% – for QDs-MPA and to 15% – for QDs-TGA, as shown in Fig. 1 B Inset of Fig. 1 B shows

how the spectral position and measured FWHM depended on the surface modification.

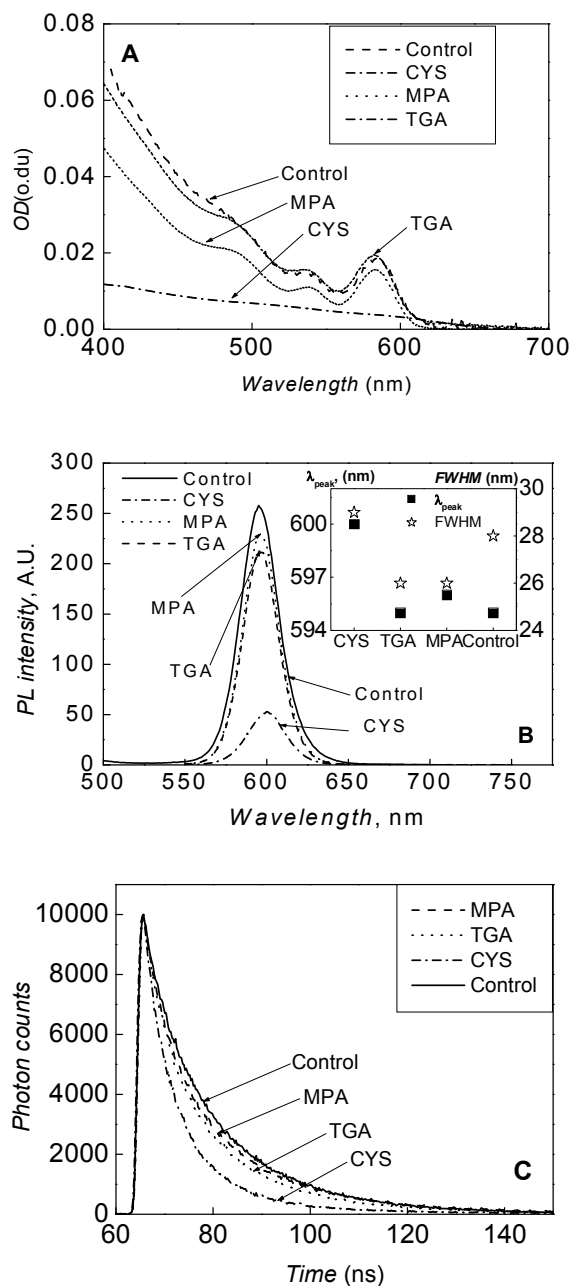


Fig. 1. Optical properties of (CdSe)ZnS QDs after modification with MPA, TGA and CYS. All samples were dissolved in PBS with pH of 7.4. (A) - Absorption spectra of modified QDs (98 nM). (B) - PL spectra of modified QDs, Inset: peak of PL band and FWHM of modified QDs. (C) - The time-resolved PL decays of each QDs

The results show that PL peak remained the same for QDs-TGA and QDs-MPA as for QDs-TOPO. Only for QDs-CYS slight bathochromic shift about 5 nm of PL band was detected. This PL band shift might be caused by QDs aggregation, which is a result of bad surface passivation by cysteamine molecules after ligand

exchange reaction. The same 27 nm FWHM means good polydispersity in size for all modified QDs. Fig. 1 C compares the time-resolved PL decays of the QDs after surface modification measured at the exciton emission peak for each modified QDs.

The decay profiles of all modified QDs dissolved in PBS are shorter than for QDs-TOPO suspended in toluene.

These data were modeled with 3 exponential decay components according to:

$$I(t) = \sum_{i=1}^4 A_n e^{-\frac{t}{\tau_n}}$$

Where τ_n represents a decay time, and A_n the amplitude of this component. The best-fit results are presented in Table 1.

Table 1. Best-fit results of PL decay with the reduced χ^2 values.

QDs	τ_1 (ns)	τ_2 (ns)	τ_3 (ns)	χ^2
QDs-MPA	6.303	19.025	114.139	1.074
QDs-CYS	5.299	13.003	78.213	1.060
QDs-TGA	6.193	17.251	81.701	1.054
Control	5,02	15,86	35,88	1.050

Changes of fast components are not as dramatic as the slow component. From table 1. it is seen that for modified QDs τ_3 lifetime component is from 2 to 3 times longer than QDs-TOPO. It is possible that τ_3 lifetime component is longer because of the formation of trap sites on the surface of QDs after modification. The longest τ_3 lifetime is for QDs-MPA and the shortest is for QDs-CYS. This might be caused that CYS barely passivates the QDs surface that is already not perfect, has a huge numbers of defects. As a result, probability of non-radiation relaxation increases and PL quantum yield decreases. It correlates with steady state spectroscopy results and shows that MPA ligand passivates the surface of QDs better than CYS molecules.

The stability of QDs-ligand complexes has become a focus of study nowadays because of several promising applications of QDs. QDs stability can be monitored by the following PL spectra parameters: the maximum peak position, the maximum peak intensity and the spectral width of the band. The effect of the medium pH (6.6–8) on the physicochemical properties of modified QDs was spectroscopically evaluated in the present study. We observed that the PL intensity of QDs are highly sensitive to surface modification quality and the pH level of the solution. Fig 2. illustrates how PL intensity depends on surface modification and solution pH value.

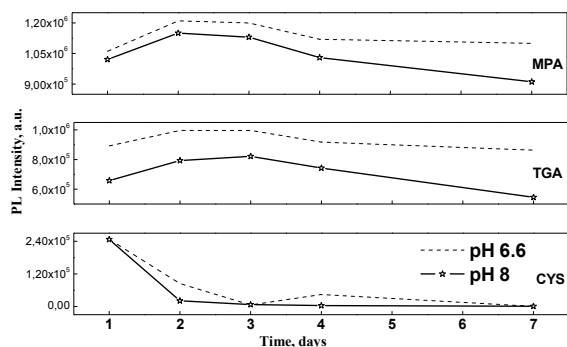


Fig. 2. PL intensity changes of each modified QDs dissolved in the two different pH value solutions.

It was observed that initial PL intensity for different modification QDs enhanced at neutral pH values (6.6). The PL intensity increase for MPA and TGA modified QDs in both pH solutions was detected after 24 h. Temporal stability study show, that after 7 days PL intensity slightly decreased to its initial values for MPA and TGA coated QDs solutions, which pH=6.6. The most visible decrease of PL intensity was registered for TGA and MPA coated QDs in PBS solution, which pH=8. At day 7 it was about 82% of its initial PL intensity value for QDs-TGA and about 89% for QDs-MPA.

The most unstable were cysteamine coated QDs, their PL intensity decrease rapidly from preparation till 3 day. After it the temporal stabilization of PL intensity of QDs-CYS was detected. Moreover spongy, red precipitates were obtained after 7 days in both QDs-CYS solutions. After mixing them the same PL intensity as the day 1 occurred. FWHM and PL peak position was also taken into consideration. No bathochromic and hypsochromic shifts and no FWHM changes of QDs-MPA, QDs-TGA PL spectra were observed during all time of examination. Notwithstanding, after 5 days the FWHM and PL peak position of QDs-CYS changed rapidly. The PL spectra has broadened what means that different size of QDs-CYS aggregates formed in the solution.

3.2. Confocal microscopy studies

Confocal microscopy was employed to examine the subcellular localization of QDs. To examine differently modified QDs cellular interaction, their uptake and localization, NIH3T3 cells was used as model cell lines. Imaging studies illustrated that the cellular uptake and localization of QDs were sensitive to their surface properties.

First QDs-MPA accumulated inside the NIH3T3 cells were detected after 1h of normal incubation conditions (Fig. 3A.). Discrete pattern of intracellular QDs-MPA PL implied that QDs-MPA were encapsulated in vesicular structures that initially concentrated in perinuclear region and later localized uniformly through the cytoplasm. After 3h the number of QDs-MPA containing vesicles per cell increased, as well their size and PL intensity. QDs containing vesicles formation assume that process of QDs-MPA accumulation is

controlled by endocytosis, but not by diffusion through cytoplasmic membrane. Detailed investigation of single cells, showed fully filled with QDs-MPA vesicles varying size ranging from 0.5 μm to 2 μm in diameter.

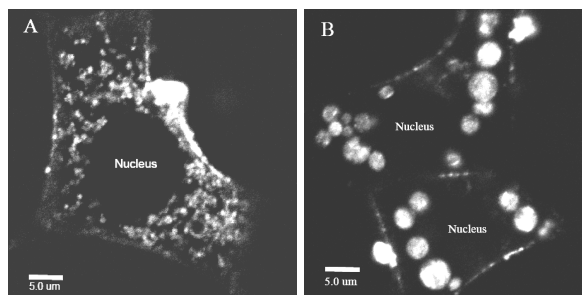


Fig. 3. Confocal fluorescence images for the NIH3T3 cells taken after 1h (A) and 24h (B) incubation with QDs-MPA. intercellular transport of QDs-MPA vesicles between NIH3T3 cells(C).

These vesicles were moving rapidly into the cytoplasm in a “stop and go” manner, but vesicle fusion with the cytoplasmic membrane was never observed. No traces of QDs were found in nucleus as the release of vesicles content was never observed. Intercellular transport of QDs-MPA vesicles mediated by intercellular junctions was detected (Fig. 3B). Size of vesicles increased to 3-5 μm in diameter after 24h incubation with QDs-MPA. These larger vesicles revealed to be multi-vesicular bodies composed of many small vesicles fully filled with QDs-MPA.

On the contrary, no QDs-TGA observed inside the NIH3T3 cells even after 24h of incubation. Rather they tend to localize in the cell cytoplasmic membranes, were they remained stable and homogeneous (Fig. 4). It seems that QDs-TGA surface still more hydrophobic even after surface ligand exchange. These TGA coated QDs were stuck to the cell membrane and did not enter the NIH3T3 cells.

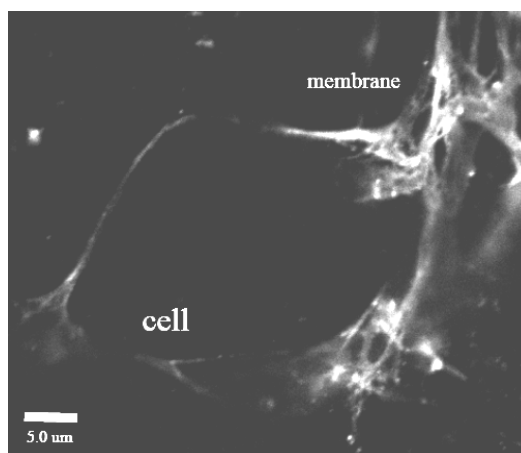


Fig. 4. Confocal fluorescence image of NIH3T3 cells incubated with QDs-TGA for 24 h.

Cationic QDs-CYS had weaker interactions with NIH3T3 cells, than QDs-MPA and QDs-TGA, because

they were unstable and tend to agglomerate in NIH3T3 cells incubation media (Fig 5).

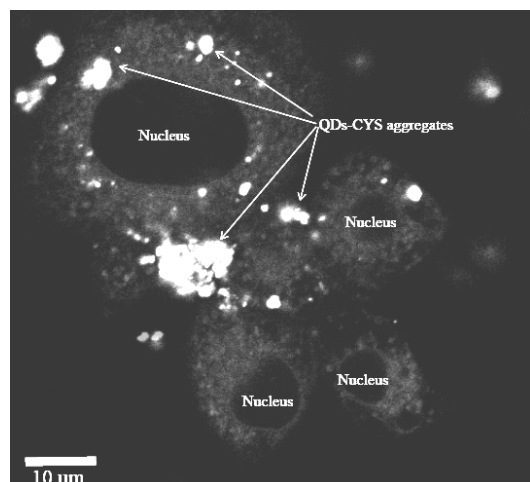


Fig. 5. Confocal fluorescence image of NIH3T3 cells incubated with QDs-CYS QDs. DIOC_6 was used for the staining cells endoplasmic reticulum. Large aggregates of QDs-CYS appeared after 24h incubation and none of them were enter cells. However no significant changes in the cells viability were detected.

4. Conclusions

This study showed that (CdSe)ZnS quantum dots coated with three thiol groups (TGA, CYS, MPA) have different photophysical and biological properties. The least successful modification was for QDs-CYS as their PL band intensity rapidly decrease, they became unstable and tend to agglomerate in biological environment. PL decay spectra suggest poor surface passivation for QDs-CYS in comparison with others. QDs modified with MPA and TGA showed similar results to QDs-TOPO photophysical properties though QDs-MPA was more stable. However they differed greatly in biological medium. NIH3T3 cells tended to uptake QDs-MPA via endocytosis process and after 24 h. they localize in multivesicular bodies while QDs-TGA localize in membranes and none were uptaken inside the cells.

5. Acknowledgements

This work was supported by the project "Postdoctoral Fellowship Implementation in Lithuania" (VP1-3.1-ŠMM-01-V-01-001).

6. References

1. Hoshino et al., Physicochemical Properties and Cellular Toxicity of Nanocrystal Quantum Dots Depend on Their Surface Modification *Nano Letters*, 2004, 4 (11), pp 2163–2169.
2. Ravindran S., Sunran K., R., Martin. Quantum dots as bio-labels for the localization of a small plant adhesion protein. *Nanotechnology* 16 (2005) 1–4.
3. Sukhanova A., Devy J., Lydie V. Biocompatible fluorescent nanocrystals for immunolabeling of membrane proteins and cells. *Analytical Biochemistry* 324 (2004) 60–67.
4. Takashi J., Fumihiko F., Hiroshi S. Calixarene-coated water-soluble CdSe–ZnS semiconductor quantum dots that are highly fluorescent and stable in aqueous solution. *Chemical Communications Issue: 22. 2005. 2829-2831*
5. Boldt K., Bruns O., Gaponik N., CoQDs-MPARative Examination of the Stability of Semiconductor Quantum Dots in Various Biochemical Buffers. *The journal of physical chemistry*, 2006, 110, 1959-1963.
6. Wuister S., Swart I., Van Driel F. Highly Luminescent Water-Soluble CdTe Quantum Dots. *Nano Letters*, 2003, Vol. 3, No. 4, 503-507.
7. Sperling R. A., Parak W. J. Surface modification, functionalization and bioconjugation of colloidal inorganic nanoparticles. *Phil. Trans. R. Soc. A* 2010 368, 1333-1383
8. Mazumder S., Dey R., Mitra K. Biofunctionalized Quantum Dots in Biology and Medicine. doi:10.1155/2009/815734.
9. Karabanovas V., Zakarevicius E., Sukackaite A., Streckyte G., Rotomskis R. Examination of the stability of hydrophobic (CdSe)ZnS quantum dots in the digestive tract of rats. *Photochem. Photobiol. Sci.* 2008. 7:725 – 729.
10. Poderys V., Motekaitis D., Rotomskis R., CdTe quantum dots stabilization by protein in aqueous solution *Medical physics in the Baltic states 7 2009, Proceedings of International Conference "Medical Physics 2009" 8-10 October 2009, Kaunas, Lithuania, p.24-29.*
11. Rotomskis R., Gražalienė G., Kulvietis V., Zakarevičius E., Lapienis J., Žalgevičienė V. Accumulation of exogenous sensitizers in rat brain. *Acta medica Lituanika*, 2007, 14(3): 219–224
12. Karabanovas V., Damalakiene L., Bagdonas S., Rotomskis R., Ger M., Valius M. Influence of growth factor on internalization pathway of quantum dots into cells. *Nanotechnology*, 2009. IEEE-NANO 2009. 9th IEEE Conference. 465 – 46

EUROPEAN COMMISSION PROJECT 'GUIDELINES ON MPE': PROPOSED QUALIFICATION AND CURRICULUM FRAMEWORKS

Carmel J. CARUANA *

*EFOMP Representative on the EC 'Guidelines on MPE' Project and Biomedical Physics, Faculty of Health Sciences, University of Malta, Malta

Abstract: The objectives of EC project 'Guidelines on Medical Physics Expert' are to provide for improved implementation of the provisions relating to the Medical Physics Expert of Council Directive 97/43/EURATOM and the proposed recast Basic Safety Standards directive. This includes harmonisation of mission statement, education and training among the Member States of the EU. This paper will present the current thinking of the project members on qualification and curriculum frameworks for the Education and Training of the Medical Physics Expert in Europe.

Keywords: Medical physics expert, qualifications, curriculum

1. Introduction

The main objectives of the European Commission project 'Guidelines on Medical Physics Expert' (TREN/09/NUCL/SI2.549828) is to provide for improved implementation of the provisions relating to the Medical Physics Expert (MPE) of Council Directive 97/43/EURATOM (Medical Exposures Directive, MED) and the recently proposed recast Basic Safety Standards (BSS) Directive. This includes harmonisation of the mission statement, education and training of the MPE among the Member States of the European Union. In this way, the project will support the European Commission in its actions relating to the optimisation of radiation doses to individuals submitted to medical exposures. This paper will present the current thinking of the project consortium on the qualification framework for attainment of MPE status and also for the curricular framework for Education and Training.

2. Principles guiding the development of the document

The principles guiding the development of the qualification and curriculum frameworks were the following:

- The new proposed qualification framework for the MPE will be based on the levels defined by the European Qualifications Framework (EQF)¹ for lifelong learning which is the most recent document proposed by the EC on qualification frameworks. For the purpose of this project the appropriate Levels are EQF Level 6 (e.g., Bachelor) and EQF Level 7 (e.g., Masters)^{1,2}.
- The qualification framework will facilitate the mobility of the MPE in Europe through an agreed

set of minimum criteria for achievement of MPE status (whilst keeping in mind the safety of the patient).

- The qualification framework will make it possible for more individuals to achieve MPE status through its flexibility, cost-effectiveness and lifelong learning approach (whilst keeping in mind the safety of the patient).
- The curriculum framework must be such as to make it possible for MPEs to move easily from one area of medical physics practice (i.e., Diagnostic Radiology, Nuclear Medicine and Radiotherapy) to another, according to national and professional needs, with a minimum amount of additional education and training.
- The determination of the content will be guided by a mission statement for Medical Physics Services derived from the MED and recast BSS. The consortium has developed the following mission statement: "Medical Physics Services will contribute to maintaining and improving the quality³, safety^{4,5} and cost-effectiveness⁶ of healthcare services through patient-oriented activities requiring expert action, involvement or advice regarding the selection, acceptance, commissioning, quality assurance and optimised clinical use of medical devices and risks from associated physical agents (including radiation); all activities will be based on current best evidence or own scientific research when the available evidence is not sufficient" This mission includes the following key activities: General Physics Service, Physical Agents Dosimetry Service, Development of Service Quality, Clinical Involvement, Expert Consultancy, Patient Safety and Risk Management, Occupational / Public

Safety and Risk Management (when associated with patient safety), Education of Healthcare Professionals, Clinical Medical Device Management, Economic Issues / Health Technology Assessment (HTA) and Innovation.

- Learning outcomes (LO) for MPE programmes will be expressed in terms of Knowledge, Skills and Competences (KSC) as stipulated and defined in the EQF document. These are:
 - a. Knowledge (facts, principles, theories, practices)
 - b. Skills as the ability to use knowledge and know-how to complete tasks and solve problems (both cognitive skills involving the use of logical, intuitive and creative thinking and practical skills involving manual dexterity and the use of methods, materials, tools and instruments)
 - c. Competence (in the EQF meaning responsibility and autonomy)¹.

3. Qualification framework for the MPE in Europe

The current thinking of the consortium regarding the qualification framework for the MPE is shown in Fig. 1.

4. Curricular framework for MPE programmes in Europe

The curricular framework proposed can be seen in Fig. 2. LO are classified into two categories: Generic and Subject Specific⁷. Generic LO consist of skills which are transferable across professions. They are further classified into three sub-categories⁷:

- a. Instrumental skills: cognitive, methodological, technological, linguistic
- b. Interpersonal skills: individual abilities involving social and co-operational aspects
- c. Systemic skills: involving combinations of understanding, sensibility and knowledge and usually involving prior acquisition of instrumental and interpersonal skills

Subject Specific LO are those which are specific to a profession. These would be further classified into sub-categories as determined by the particular profession. The following classification is based on proposals by the EFOMP Board and Caruana⁸ and Caruana⁹:

- a. Medical Physics Core LO (these LO are expected from all medical physicists)
 - LO appropriate for the medical physicist as physical scientist (these are fundamental physics knowledge and measurement skills expected of all physicists)
 - LO for the medical physicist as healthcare professional
 - LO for the medical physicist as clinical medical device / physical agents expert (these are common to all medical devices and safety from all associated physical agents)
- b. LO for specific medical physics areas (these LO would consist of the application of the Medical Physics Core LO to the three areas of medical physics relevant to this project e.g., Diagnostic and

Interventional Radiology, Nuclear Medicine, Radiotherapy.

5. Conclusion

The whole curriculum document will be forwarded to medical physicists in Europe for their feedback. A workshop is being held 9-10 May 2011 in Seville, Spain for medical physicists and stakeholders. The website for the project is

Acknowledgment: The members of the consortium would like to thank the European Commission for providing the funds to make this project possible.

6. References

1. European Parliament and Council (2008) Recommendation 2008/C 111/01 on the establishment of the European Qualifications Framework for Lifelong Learning. Official Journal of the European Union 6.5.2008. (<http://eur-lex.europa.eu/LexUriServ/LexUriServ.do?uri=oj:c:2008:111:0001:0007:en:pdf>)
2. A Framework for Qualifications of the European Higher Education Area. http://www.bologna-bergen2005.no/Docs/00-Main_doc/050218_QF_EHEA.pdf
3. Helena Legido-Quigley, Martin McKee, Ellen Nolte, Irene A Glinos (2008). Assuring the quality of health care in the European Union. http://www.euro.who.int/_data/assets/pdf_file/0007/98233/E91397.pdf
4. Luxembourg Declaration on Patient Safety - Making it Happen. http://www.eu2005.lu/en/actualites/documents_travail/2005/04/06Patientsafety/Luxembourg_Declaration_on_Patient_Safety_05042005-1.pdf
5. Standing Committee of European Doctors and other stakeholders (2005). Stakeholders' position paper on patient safety. http://www.ehtel.org/forum/tasks-sources/tf-patient-safety-emedication/stakeholders_position_on_patient_safety.pdf
6. EC (2007) Together for Health: A Strategic Approach for the EU 2008-2013. http://eur-lex.europa.eu/LexUriServ/site/en/com/2007/com2007_0630en01.pdf
7. Tuning - Universities' contribution to the Bologna Process. 2nd ed. (<http://www.tuning.uni-deusto.org/tuningeu/>)
8. Christofides S et al (EFOMP Officers) and Caruana CJ. An Initial EFOMP Position on the Tuning Process for Masters Programs in Medical Physics in Europe. In Dössel O and Schlegel WC (Eds.): WC 2009, IFMBE Proceedings 25/XIII, pp. 70–73, 2009. Springer
9. Caruana CJ (2010). The Tuning process and the Masters in Medical Physics in Europe - a personal vision. Book chapter in book by Tabakov S. (ed). Book title still not finalised.

Qualification Framework for the MPE in Europe

Medical Physics Expert: An individual having the knowledge, training and experience to act or give advice on matters relating to radiation physics applied to medical exposure, whose competence to act is recognized by the competent authorities (Recast BSS)

EQF = European Qualifications Framework KSC = Knowledge, Skills, Competences (2008/C 111/01)



- (i) 'Equivalent' here meaning EQF Level 6 with a high level of physics and mathematics content
- (ii) 'Equivalent' here meaning EQF Level 7 with a high level of physics and mathematics content, plus further additional education which includes the core KSC of Medical Physics and the KSC of the specific area/s of Medical Physics practice as stipulated in this project.
- (iii) The EQF level for the MPE has been set at Level 7 because to provide effective, safe and economical practice based on current best evidence, the MPE requires highly specialized knowledge, critical awareness of knowledge issues in the field, specialized problem-solving skills, ability to manage work contexts that are complex and ability to review the performance of teams (2008/C 111/01).
- (iv) Accredited clinical training that has a credentialing system based on defined demonstrable skills and competences in specific area/s of Medical Physics practice; skills / competences gained prior to the start of the formal training period should be recognized and credited.

Fig. 1. Qualification framework for the MPE in Europe

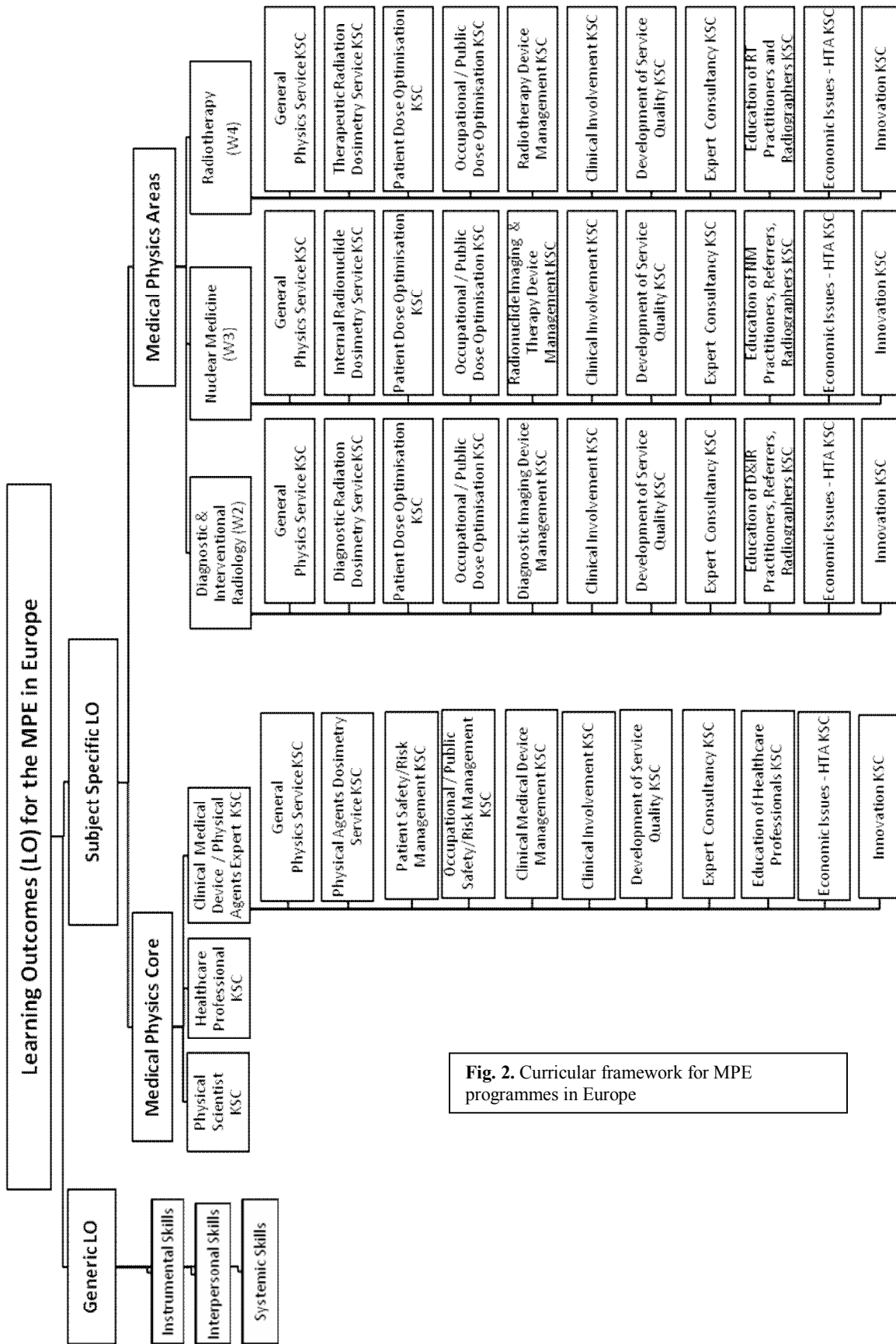


Fig. 2. Curricular framework for MPE programmes in Europe

**MEDICAL PHYSICS AND BIOMEDICAL ENGINEERING AT THE FACULTY OF
MEDICINE, MASARYK UNIVERSITY, BRNO**

Daniel VLK*, Vojtěch MORNSTEIN*, Carmel. J. CARUANA**

*Department of Biophysics, Medical Faculty, Masaryk University, Brno, Czech Republic

**Biomedical Physics, Faculty of Health Sciences, University of Malta, Malta

Abstract: We describe the biomedical physics component of the study programmes for General Medicine, Dentistry and Biomedical Engineering at the Faculty of Medicine, Masaryk University, Brno, Czech Republic. In comparison with other biomedical subjects, biomedical physics has less curriculum time in the case of General Medicine and Dentistry programmes. However, it has a higher number of hours in the case of the programme in Biomedical Technology. Practical tasks play an important role in all our programmes.

Keywords: Biomedical physics, Biophysics, Biomedical engineering, Practical tasks, Education, Czech Republic

1. Introduction

At the Department of Biophysics, Faculty of Medicine, Masaryk University, Brno we teach students of three different faculties, who represent several healthcare professionals. Table 1. shows all specialisations and the number of students in each of them for the academic year 2009-10. About one fifth of the General and Dental Medicine students are enrolled in the English study programme (identical with the Czech programme but the students are taught in English and pay fees). The biggest group involves students of General Medicine, followed by other healthcare professional groups from the Medical Faculty. A small group of students comes from the Biophysics and Medical Physics programmes of the Faculty of Science. Since the academic year 2008/2009 we also started education of students from the newly designed BSc programme “Biomedical Technology and Bioinformatics” of the Faculty of Electrical Engineering and Communication (FEEC), University of Technology, Brno.

We have prepared individual syllabi for students for the different programmes. We focus on the effective and safe use of biomedical devices (students of Medical Faculty), medical and technical aspects of biomedical physics (students of Medical Physics and Biophysics from the Faculty of Science) and general biophysics (students from FEEC). These syllabi were designed in agreement with the latest recommendations published by Caruana et al. [1,2]

Table 1.

Faculty	Specialisation	Number of students
Faculty of Medicine Masaryk University, Brno	General Medicine	480
	Dentistry	90
	Nurse – midwife	30
	General Nurse	40
	Physiotherapy	40
	Optometry	40
	Human Nutrition	20
	Laboratory Assistant	50
	Radiology Assistant	10
Faculty of Science, Masaryk Uni., Brno	Biophysics	15
	Medical physics	8
FEEC, Technical University, Brno	Biomedical Technology and Bioinformatics	70

2. Biomedical physics and other theoretical subjects

Lectures and practicals are held during the first semester of the first year of the programmes as biomedical physics is considered fundamental. The number of hours for the three biggest groups of students are shown in Table 2. Physics is assigned less than half the time compared to Chemistry (and biochemistry), anatomy and physiology in the case of students of General Medicine (GM) and Dentistry. This is not ideal, but better than in most European countries [3,4]. The situation in the case of the Biomedical Technology and Bioinformatics (BTB) study programme is the reverse – together with Physiology we have the biggest number of hours.

Table 2.

Theoretical subject	Study programme Hours per semester (number of semesters)		
	GM	Dentistry	BTB
Medical physics	105 (1)	90 (1)	75 (1)
Chemistry and Biochemistry	225 (3)	165 (3)	60 (1)
Biology	135 (2)	90 (2)	60 (1)
Anatomy	240 (3)	195 (3)	30 (1)
Physiology	232 (2)	120 (2)	75 (1)
Histology and Embryology	150 (2)	105 (2)	30 (1)

3. Practical exercises

The practical exercises usually represent about 60% of the complete course of biomedical physics. Moreover, practical exercises (tasks) include also an introduction to healthcare informatics (only in the courses for students of Faculty of Medicine). The latter involves a wide range of topics starting from PC hardware and software to data mining, sharing and processing with emphasis on web tools, resources and scientific databases (e.g. Medline, Scopus). The time available for practical tasks oriented on biomedical physics proper (i.e., without informatics) is the same for GM, Dentistry and BTB – 45 hours. The intended learning objectives of the practical sessions are: the development of the measurement and instrument user skills, the awareness of the scientific, effective, efficient and safe use of biomedical devices (as required by EU Directives and healthcare policies), basics of the biophysical quantities behind clinical diagnostics and the fundamentals of medical imaging and physiological monitoring techniques. One of the target learning outcomes of the practical tasks is for all

healthcare professions to share a common conceptual understanding and unified terminology regarding medical devices. Our syllabus is based on the theoretical model which considers Biomedical Physics as a discipline that creates an important bridge between physics, technology and medicine.

The practical programme consists of three sets of tasks: (1) a basic set which is common to all professions and which ensures a solid foundation to all students, (2) specialized sets chosen according to the future specific healthcare profession of the students. More details about the rationale for this arrangement can be found in [5].

Most of the tasks are involve laboratory measurements, some have the character of demonstrations performed by the teacher, which can be followed by student operation/measurement; a few hours are theoretical seminars.

Examples of tasks:

Basic set:

Illuminance

Spectrophotometry (absorption curve and concentration measurement)

Viscometry (different types of viscometers)

Thermometers (thermistor, thermocouple, IR camera)

Signal processing (oscilloscopy, filtering, etc.)

Specialised set:

Audiometry (hearing threshold measurement)

Ultrasound induced haemolysis (see below)

X-ray imaging (a group of tasks performed with a student laboratory X-ray device Phywe)

Membrane potential measurement (a model)

Sound level measurement

Medical set (mostly demonstrations):

Ultrasound diagnostic methods (B-scan, Doppler blood flow measurement)

Optometry (e.g. applanation tonometry, refraction measurement, visual acuity measurement)

Endoscopy (operation of a technical endoscope)

MRI (seminar)

Electrotherapy (electrostimulation etc.)

Example task:

Ultrasound induced haemolysis

Main task:

Determine the effect of ultrasound on erythrocytes in suspension in the dependence on duration of sonication (application of ultrasound). The students acquire information about ultrasonic cavitation, conventional microscopy and cell counting, and basic digital acquisition and processing of images.

Equipment for the measurement:

Ultrasound generator BTL-07 (Fig. 1.), microscope with a digital camera connected to computer (Fig. 2.), Bürker counting cell, stand with test tubes, pipettes, flat bottom test tube for sonication, suspension of

erythrocytes, saline, cellulose tissues, acoustic contact medium (paraffin oil).

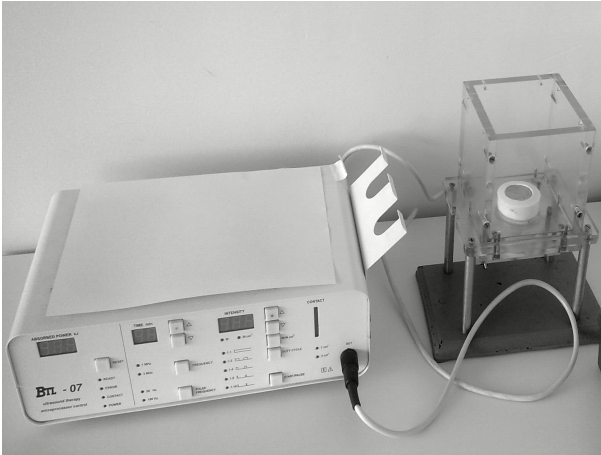


Fig. 1. Ultrasound generator



Fig. 2. Microscope connected with computer

Procedure:

Suspension of erythrocytes (50-times diluted non-coagulable horse blood) is prepared in the beaker.

- 1) After a mild stirring pour approximately 3mL of the suspension of erythrocytes into a flat-bottom test tube (half of test tube).
- 2) Count number of erythrocytes in this control suspension. Dilute the suspension 10-times: 0.1 mL of suspension + 0.9 mL of saline. Take the erythrocyte suspension into the Bürker cell and count erythrocytes at least in 20 small squares of the grid. Calculate number of unsonicated erythrocytes in 1 mL of the suspension. Stir the suspension before each manipulation!
- 3) Switch the ultrasound generator. Spread the ultrasound application head with a little of paraffin oil. The application head is fastened in the stand.
- 4) Before the actual accomplishment of haemolysis, set the sonication time – 30 seconds is sufficient. Push

start button and gradually increase intensity of ultrasound. During sonication one can observe ultrasonic cavitation taking place on the head in the paraffin oil. Time switch will automatically switch off the device.

5) Put carefully the flat-bottom test tube with erythrocyte suspension on the ultrasound application head. Set the ultrasound intensity – 0.1 W/cm^2 – and the time of sonication – 30 seconds. After that take 0,1mL from the sonicated erythrocyte suspension and dilute by addition of 0.9 mL of saline. Count the erythrocytes - see point 2.

6) Sonicate the suspension in the flat-bottom test tube for 30 seconds again. Count number of erythrocytes after sonication - see point 2.

7) Repeat the previous step several times. If the average number of erythrocytes in one small square drops under 5, do not dilute the suspension and fill the Bürker cell with undiluted suspension.

8) Accomplish at least 6 sonications. If the full hemolysis happens (e.g. after four thirty-second sonications), finish the experiment.

9) Write down numbers of erythrocytes recounted for 1mL of full blood into a table and percentage (level) of hemolysis in dependence on the time of sonication. Based on this table, plot a graph showing the level of haemolysis vs. the time of sonication.

10) To calculate the number of erythrocytes N in 1mm^3 of undiluted suspension (full blood) use this equation:

$$N = nz/Shx$$

Where n is number of erythrocytes in x squares (usually 20), z – dilution of suspension, S – area of a small square of the Bürker cell ($0,0025\text{mm}^2$) and thickness (height) of the Bürker cell h is 0,1mm).

4. Student's responsibility

The practical exercises in Biophysics are compulsory and a missing practical has to be substituted. Theoretical knowledge of the principles of the methods used is regularly checked by oral examination. For each task the students have to write a comprehensive report which is marked. From, this year, students are to hand in reports via the website of Masaryk University Information system, and they receive the corrected script through the same system. At the end of the course students sit for a multiple-choice test which consists usually of 20 questions and must achieve 50% of the mark to be considered successful.

Students will only be allowed to sit for the final exam if successful in the multiple choice test. The exam consists of a written test consisting of 25 multiple choice questions and an oral part. The student can continue with the oral part only when the number of correctly answered questions in the multiple choice test is at least 15. The oral part consists of two questions. The examined student must be able to explain physical and biophysical problems and explain their clinical importance.

Acknowledgment: This contribution is supported by a development project of the Czech Ministry of Education, Youth and Sports entitled “C42 - Inter-university co-operation in biomedical techniques and biomedical engineering using state-of-the-art technologies”.

5. References

1. Caruana C.J., Wasilewska-Radwanska M., Aurengo A., Dendy P.P., Karenauskaite V., Malisan M.R., Meijer J.H., Mornstein V., Rokita E., Vano E., Wucherer M., The role of the biomedical physicist in the education of the healthcare professions: An EFOMP project. *Physica Medica*, 2009, vol. 25, no. 3, p. 133-140.
2. Caruana C.J., Wasilewska-Radwanska M., Aurengo A., Dendy P.P., Karenauskaite V., Malisan M.R., Meijer J.H., Mihov D., Mornstein V., Rokita E., Vano E., Weckstrom M., Wucherer M., A comprehensive SWOT audit of the role of biomedical physicist in the education of healthcare Professional in Europe, *Physica Medica: European Journal of Medical Physics*, 2010, vol. 26, p. 98-110.
3. Caruana C.J., A strategic development model for the educator role of the biomedical physics-engineering academic in faculties of health science in Europe, PhD Thesis, Charles University, Prague, 2006.
4. Dusek, T., Bates, T., Analysis of European medical school's teaching programs, *Croat. Med. J.*, 2003, vol. 44(1), p. 26-31.
5. Vlk D., Mornstein V., Caruana C. J. A medical biophysics conceptual base for medical / healthcare / technology students at the Department of Biophysics, Faculty of Medicine, Masaryk Uni., Brno. IFMBE Proceedings, Volume 25, Issue 12, 2009, ISSN:16800737, ISBN:978-364203892-1, Pages 54-56.

MEDICAL PHYSICS IN THE BALTIC STATES 8 (2010)

Proceedings of International Conference "Medical Physics in the Baltic States"
14 - 16 October 2010, Kaunas, Lithuania

EFOMP PROJECT 'BIOMEDICAL PHYSICS EDUCATION FOR THE MEDICAL / HEALTHCARE PROFESSIONS' – AN UPDATE FOR MEDPHYS2010

C.J. Caruana¹, M. Wasilewska-Radwanska², A. Aurengo³, P.P. Dendy⁴, V. Karenauskaitė⁵, M.R. Malisan⁶, J.H. Meijer⁷, D. Mihov⁸, V. Mornstein⁹, E. Rokita¹⁰, E. Vano¹¹, M. Weckstrom¹², M. Wucherer¹³

¹ EFOMP SIG 'Biomedical Physics Education for the Healthcare Professions', Chair and Faculty of Health Sciences, University of Malta, Malta, ² AGH University of Science and Technology, Krakow, Poland, ³ Faculty of Medicine, Uni. Pierre et Marie Curie, Paris, France, ⁴ Formerly Faculty of Chemistry and Physics and Faculty of Medicine, Cambridge University, Cambridge, England, UK, ⁵ Faculty of Physics, Vilnius University, Vilnius, Lithuania, ⁶ University Hospital, University of Udine, Udine, Italy, ⁷ VU University Medical Center, Amsterdam, Netherlands, ⁸ Department of Medical Physics and Biophysics, Medical University of Sofia, Bulgaria, ⁹ Faculty of Medicine, Masaryk University, Brno, Czech Republic, ¹⁰ Faculty of Medicine, Jagiellonian University, Krakow, Poland, ¹¹ Faculty of Medicine, Complutense University, Madrid, Spain, ¹² Department of Physical Sciences, Faculty of Science, University of Oulu, Finland., ¹³ Klinikum Nuremberg, Nuremberg, Germany

Abstract: The policy statements describing the role of the biomedical physicist (and engineer) published by organizations representing biomedical physicists in Europe include the responsibility of contributing to the education of healthcare professionals. But the role of the biomedical physicist in the education of the medical/healthcare professions has never been studied systematically. The EFOMP SIG 'Biomedical Physics Education for the Healthcare Professions' has been conducting research aimed at producing a development model for this increasingly important subrole of the biomedical physicist.

Keywords: Biomedical physics education, medical education, academic role development, curriculum development.

1. Introduction

Although biomedical physicists provide educational services in most medical/healthcare faculties (and hospitals) in Europe, the role of the biomedical physicist in the education of the medical/healthcare professions has never been studied systematically. In 2005, the EFOMP council set up a Special Interest Group to develop the role of the biomedical physics educator in such faculties and to work with other healthcare professional groups to produce updated European curricula for them. The group seeks to provide a basis for the progress of the role, enhance its relevance to contemporary healthcare professional education and provide input for future EFOMP policy documents. The educational aspect of the physicist's role is becoming progressively more important owing to the rapid increase in the number and sophistication of medical devices used by these professions.

This article presents a research project aimed at developing the role of biomedical physics (BMP) educators in the teaching of the non-physics healthcare

professions (HCP). The methodology used was based on the well-established SWOT analytical framework. SWOT is a two-step process: an audit of SWOT themes relevant to the role under study is first carried out and then a development model is constructed by matching the internal Strengths and Weaknesses of the role to Opportunities and Threats arising from the external Political, Economic, Social-Psychological and Technoscientific environments. SWOT themes were identified through a survey of 120 faculties across Europe and document analysis of the medical/healthcare educational literature. Two papers have already been published, the first presenting a survey of the literature on the subject and the second presenting the results of the SWOT audit [1, 2]. The third paper with the proposed role development model has been submitted for publication. A fourth paper which will include a curriculum development model is also planned. The set of papers will strengthen the role and help bring about convergence of biomedical physics curricula for the medical/healthcare professions in Europe.

2. Background to the project

A scrutiny of the medical and healthcare professional literature provides relatively few references on the educational role of the biomedical physicist in Faculties of Medicine / Health Science (FMHS). Current curricular content varies tremendously across Europe. Even for a single profession such as that of physician content ranges from general physics to physical biochemistry, biomolecular and cellular biophysics, physiological physics, the effects of physical agents on the human organism and medical devices. From the personal experience of the members of the group there are various causes for this variability. Remits presented to BMP educators by HCP programme leaders are sometimes quite vague as the latter are often unsure on what the learning requirements of their students are. Choice of curriculum content is often subjective with BMP educators simply choosing learning objectives based on those areas of their expertise that in their opinion are most relevant to the particular HCP. Research-based curriculum development and international networking on the issues are lacking. This ad-hoc approach to curriculum development may lead to learning objectives that are far removed from the everyday practicalities in the exercise of the HCP, hence leading to a low level of satisfaction and motivation on the part of the students. There are also indications that the BMP academic is not perceived by the various HCP to have a clear, valuable and easily identifiable role with respect to the education of their students - an issue which if not addressed with urgency by the profession could lead to a reduction of curriculum time devoted to BMP in the various HCP curricula.

At the same time, the gradual construction of the European Higher Education Area (often referred to as the 'Bologna' process) is encouraging institutions involved in higher education to take a critical look at their curricula and ensure that the latter are more in agreement with the present and future learning needs of the professions [3]. BMP educators cannot play a significant role in this process unless they have a clear updated role mission statement, are in possession of research based role and curriculum development models to guide their work, and increase the degree of harmonization of their activities at the European level.

3. Summary of the literature review regarding the role

Almost all articles found in the literature focus on the role within programmes for physicians, diagnostic radiographers / radiation therapists and the postgraduate medical specializations of radiology, radiotherapy, interventional radiology and cardiology. There are very few articles regarding the physics component of medical curricula even though it is a component of many medical programmes. The only work that has been described in detail is that of J. K. Robertson, teaching at Queen's University Faculty of Medicine, Canada in the

years 1909 - 1951. The pedagogical approach of this educator demonstrates the remarkable vision of some early biomedical physics educators.

At that time the medical curriculum was very linearly structured with strict separation of basic and applied science. Robertson challenged this system and produced a very successful course combining physics principles with clinical applications in a single unit. "Robertson's success in this endeavor was based largely on two factors: his sympathetic understanding of the needs of medical students and his innovative combination of basic and applied science in one course - factors that are as important to medical teaching today as they were 50 years ago" [4]. However it seems that this initial flash of educational initiative was not followed up by the international biomedical physics community.

Moreover there have been indications that the absence of systematic research and publication has resulted sometimes in unsatisfactory learning with a high theory-practice gap. In 2001, an interesting attempt to introduce problem-based learning to medical students was reported [5]. In 2005, EFOMP published a radiation protection syllabus for medical undergraduates. Some authors have appealed for a widening of content to include topics such as biosignals. In 2005, a survey of the physics component of European undergraduate medical curricula led to the following results: (a) in general a compulsory physics contribution is included in the pre-clinical stage with further optional units in the clinical years (b) there is wide variation in the compulsory physics pre-clinical curriculum time ranging from 0 - 90 hours (c) in some countries physics is a national legal requirement whilst in others not (d) there is wide variation in curriculum content, in some countries legal instruments specify detailed content whilst in others these provide only general direction (e) delivery is still mainly presentation based though in some countries practicals are mandated by law (f) there is a lack of systematic, research-based curriculum development (g) most departments have not yet reacted to developments such as competence-based curricula and problem-based-learning [6]. In a subsequent paper the same authors developed a biomedical physics competence inventory for undergraduate medical education.

Physics has been included in the curriculum for diagnostic radiographers since the beginning of formal radiography education. However, the first research-based inventory of physics competences for diagnostic radiography education in Europe was only published recently [7]. Physicists have always been involved in international initiatives regarding radiation protection education. These have always included reference to radiographers [8]. Physicists are presently involved in an ICRP group working on a document entitled 'Radiation protection training for diagnostic and interventional procedures' to be published in 2009 (Vano E., personal communication, Feb. 2008). Therapeutic radiology is an area in which physicists and

other healthcare professions have worked together to produce European curricula including one for radiation therapists.

Physics has always been a component of the curriculum of the postgraduate medical specializations of radiology and radiotherapy. It has been argued that it is the superior knowledge that radiologists have of physics that gives them an advantage over other clinicians who attempt to read medical images. Some have argued that owing to the pressures on radiologists' learning time only physics knowledge that is derived from the clinical practice should be taught.

This was countered by the argument that it is more important to use the time available to build firm broad conceptual foundations as concepts that were not seen as relevant at the time of learning could become so at a later date. A more recent debate involved a discussion on whether the rapid increase in the number of imaging modalities implies that the physics taught to radiologists would need to be expanded and become more quantitative. The arguments in favour of the proposition tended to be statements on the lines that more technology requires more physics. Arguments against the proposition were that there is simply no available curriculum time and that medical students do not tend to be mathematically inclined. Some recent experiences in the teaching of the practical aspects of radiation protection to interventional radiologists and cardiologists have been well received by clinicians.

Although there are indications of increasing interest [9-12] the literature indicates that the precise role of the biomedical physics educator in Faculties of Medicine / Health Science has never been studied in a systematic manner. The complete literature review has been published in *Physica Medica - European Journal of Medical Physics* [1].

4. Subsequent research

The group has finished conducting a SWOT analysis for the role. Strengths and Weaknesses have been identified through a survey of 120 faculties across Europe whilst Opportunities and Threats through a systematic survey of the healthcare, healthcare professional education and higher education literature. The SWOT themes indicate that (a) the biomedical physicist's role in the education of the healthcare professions is blessed with many opportunities and if biomedical physicists rise to the challenge a good future for the role is achievable (b) however, in the past the role has been generally weakened in some countries either through neglect from role holders who have not practiced proper role-balance amongst their various sub-roles or through lack of opportunity. In the case of university based physicists the educator role has not been given its due importance owing to over-emphasis on the research role. In the case of clinically based physicists there is a lack of opportunity when the educational role is considered subsidiary to the service role. The major strengths of the

role are its strong medical device competences and its competences regarding protection from physical agents associated with medical devices.

SWOT themes identified in the study [2]

Strengths of the role

- S1) Highly qualified academics
- S2) Strong medical device competences
- S3) Strong competences regarding safety with regard to physical agents
- S4) Strong Information and Communication Technology competences
- S5) Strong research competences

Weaknesses of the role

- W1) Absence of a clear mission
- W2) Poorly determined scope
- W3) Absence of international networking and curricular harmonization
- W4) Absence of a unique internationally agreed title for the discipline
- W5) Low level of pedagogical expertise, pedagogical materials and educational research
- W6) Narrow range of client groups
- W7) Role overlaps
- W8) Absent departments
- W9) Low marketing competences
- W10) Conflict between the self-perceived role and the role expectations of the HCP
- W11) Insufficient awareness of the ethical and humanistic aspects of healthcare

Opportunities for the role

- O1) The European Higher Education Area and recognition of professional qualifications
- O2) The European Research Area
- O3) EC directives
- O4) The escalating cost of health care and health technology assessment
- O5) Human resource requirements in the HCP sector
- O6) Increased public awareness of quality and safety standards in healthcare
- O7) The rise of the new HCP
- O8) Increased regulation of the HCP
- O9) Increased awareness of occupational safety issues
- O10) The explosion in the number and sophistication of biomedical devices

Threats to the role

- T1) The escalating cost of higher education
- T2) Low incentives for biomedical physicists to join academia
- T3) Resistance to multi-disciplinarity in HCP education
- T4) Insufficient curriculum time
- T5) The perception of physics as a difficult subject

Many members of the profession consider that the major function of the role is to act as a 'bridge' across the divide between biomedical device providers / medical device research literature and the HCP (Fig.1). The BMP is the biomedical science professional who is comfortable using the terminologies of both technology and medicine. A significant component of this bridging

role is to 'translate' technical knowhow (e.g., that found in device user manuals) into a form that can be useful to the HCP. It is also important to ensure that future HCP have at least the basic physics concepts required to be able to achieve understanding during the training sessions provided by device manufacturers.

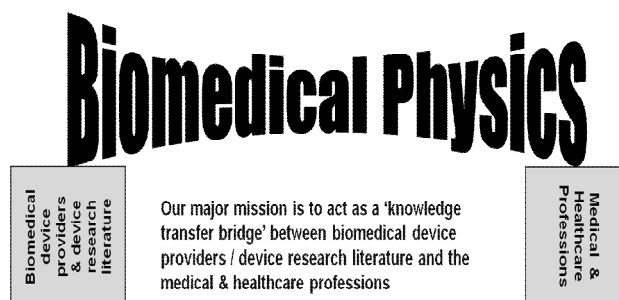


Fig. 1. Major mission of Medical Physicists for HCP education

Following the SWOT audit, the group has been working on a strategy for the development of the role based on the outcomes of the audit. The research methods adopted focus on the importance of strategic planning at all levels in the provision of educational services. The analytical process used in the study is a pragmatic blend of the various theoretical frameworks described in the literature on strategic planning research as adapted for use in academic role development. Important results include identification of the core competences of the biomedical physicist in this context; specification of bench-marking schemes based on experiences of other biomedical disciplines; formulation of detailed mission and vision statements; gap analysis for the role (i.e., the discrepancies between the current position and desired vision for the role). The study concludes with a set of strategies and specific actions for gap reduction.

5. Conclusions

The literature review showed that in this field, there was a need to focus research on the following areas: (a) carrying out a comprehensive Europe-wide SWOT position audit for the role, including curricular challenges within higher and healthcare professional education (b) proposing a strategic role development model for the perusal of role holders which would ensure the future well-being of the role (c) putting forward a curriculum development model structured enough for systematic curriculum development yet generic enough to be applicable to all the HCP and easily modifiable to national and local needs. The Group's recent work has addressed the first objective and the results of the study have been submitted for publication to *Physica Medica - European Journal of Medical Physics*. In the coming year the Group will be focusing its efforts on addressing the two remaining research objectives, that is constructing role development and curriculum development models.

6. References

1. Caruana CJ, Wasilewska-Radwanska M, Aurengo A, Dendy PP, Karenauskaite V, Malisan MR, et. al. The role of the biomedical physicist in the education of the healthcare professions: an EFOMP project. *Physica Medica/EJMP* 2009;25:133-40.
2. Caruana CJ, Wasilewska-Radwanska M, Aurengo A, Dendy PP, Karenauskaite V, Malisan MR, et al. A comprehensive SWOT audit of the role of the biomedical physicist in the education of healthcare professionals in Europe. *Physica Medica/EJMP* 2010;26(2):98-110.
3. Tuning (2008) Universities' contribution to the Bologna Process. 2nd ed. Available from <http://www.tuning.unideusto.org/tuningeu/>.
4. Hayter C R. Physics for physicians: integrating science into the medical curriculum. 1910-1950 *Acad Med.*, 1996, 71:1211-7.
5. Fasce E, Calderon M, Braga L, De Orue M, Mayer H, Wagemann H, Cid S (2001) Problem based learning in the teaching of physics to medical students - Comparison with traditional teaching. *Rev Med Chil* 129:1031-7.
6. Caruana C J, Plasek J. A systematic review of the biomedical physics component within undergraduate medical curricula in Europe. *Biomedizinische Technik*, 2005, 50 Suppl. Vol 1 Pt 2:931-2.
7. Caruana C J, Plasek J. An inventory of biomedical imaging physics elements-of-competence for diagnostic radiography education in Europe. *Radiography*, 2006, 12:189-202.
8. European Commission. Directorate General Environment, Nuclear Safety and Civil Protection (2000) Radiation Protection 116 - Guidelines on education and training in radiation protection for medical exposures. Luxembourg. Retr. April 8 2007 from <http://www.csfm.cz/fileadmin/csfm/rp-116-en.pdf>.
9. Caruana C J. A summary account of the historical development and present state of the role of biomedical physics-engineering in the education of the healthcare professions. *Proc. GIREP-EPEC Conf. 2007, Frontiers in Physics Education, Opatija, Croatia.*
10. Caruana C J (2007) A strategic role development primer for physics educators in higher education: some general principles and their application to the case of a physicist teaching in a Faculty of Medicine / Health Science. *Proc. GIREP-EPEC Conf. 2007, Frontiers in Physics Education, Opatija, Croatia.* pp 276-82.
11. Caruana C J, Plasek J (2006) A SWOT Audit for the Educator Role of the Biomedical Physics Academic within Faculties of Health Science in Europe. *Proceedings GIREP 2006. Modeling in*

- Physics and Physics Education, Amsterdam, Netherlands, pp 899–903.
12. Karenauskaite V, Dikcius G, Macyte A, Rotomskis R. (2006) The Systematic Approach to a Biomedical Physics Course: a Case Study at Vilnius University. Proc. GIREP 2006. Modeling in Physics and Physics Education. Amsterdam, Netherlands, pp 979–85.

UNCERTAINTY IN FUNCTIONAL MAGNETIC RESONANCE IMAGING METHODS FOR CORTEX MOTOR AND LANGUAGE AREA EXAMINATIONS

Joosep KEPLER*, Kalle KEPLER**, Tiiu TOMBERG***/***, Pilvi ILVES***

* Diagnostics Department, Pärnu Hospital, Pärnu, Estonia; ** Training Centre of Medical Physics, Institute of Physics, University of Tartu, Tartu, Estonia; *** Radiology Clinic, Tartu University Hospital, Tartu, Estonia; ****Neurology Clinic, Tartu University Hospital, Tartu, Estonia

Abstract: Inter- and intrasubject uncertainty in functional magnetic resonance imaging examinations at cortex motor and language area was studied. The highest Z-scores were identified and mean weighted lateralisation index (LI_w) were calculated using a combined bootstrap/histogram analysis by Wilke and Schmithorst within prescribed Brodmann areas (BA). LI_w (with standard deviation) for right hand motor task of adults was 0,77(0,04) for BA 1-2-3, 0,88(0,02) for BA 4 and 0,71(0,04) for BA 6.

Keywords: functional magnetic resonance imaging (fMRI), statistical parametrical mapping (SPM), neuroimaging studies, data analysis, reproducibility.

1. Introduction

Since 1990, when blood-oxygen-level-dependent (BOLD) technique [1] was first used for imaging brain functions, functional magnetic resonance imaging (fMRI) method has spread to many university hospitals, as indispensable clinical tool. Since fMRI methods has not been systematically introduced in Estonia, this is the first methodology adaption carried out in Tartu University Hospital. A short overview about processing and analyzing techniques, which were chosen for making clinical evaluation of motor cortex reorganisation of patients with hereditary spastic paraplegia and compensatory reorganisation of language network of children with perinatal and early childhood stroke, is given. In addition, the purpose of this study was to assess inter- and intrasubject reproducibility of the used methodology. Due to the fact that subject will get tired and bored after repeating the same task, fMRI repeatability can only be estimated exactly by an appropriate phantom [2]. Thus only reproducibility assessment was carried out and it was assessed both between subjects (inter-) and for one subject (intrasubject). This study was approved by the local ethics committee.

2. Materials and methods

2.1. Subjects and tasks

Twelve right-handed healthy subjects (aged between 22 and 70, with mean age of 45) with no history of neurological or psychiatric illness were studied while

performing hand and foot motor task. Ten right handed healthy children (aged between 9 and 14, with mean age of 11) were studied while performing two cognitive tasks. For assessing intrasubject reproducibility one healthy 23 year old right handed male subject was studied at both motor and both cognitive tasks.

All tasks were employed in a block design. Motor task of the hand was flexion/extension of the right-hand fingers and for the feet was flexion/extension of the right ankle. Hand and feet motor tasks were run separately. Cognitive task comprised also of two tasks, where activation block comprised of verb generation task or sentence comprehension task and during the rest block subject were asked to do motor task of finger tapping.

Length of a block was 10 TR-s with the TR of 4 s. For motor task 3 blocks of motor task and 3 blocks of resting was done alternately. For cognitive task 5 blocks of verb generation tasks or sentence comprehension tasks was used with 5 motor tasks alternately.

2.2. Image Acquisition

Before examination the subjects were informed about the procedure, tasks and length of the examination. Images were obtained on a 1,5 T MR scanner Magnetom Symphony (Siemens Medical Systems, Erlangen, Germany). Prior to the functional scans, high resolution T1 weighted anatomical image was obtained with gradient echo FLASH sequence (TR=12 ms, TE=5,68 ms, flip angle 15°, resolution 224×256, voxel size 1×1×1 mm³, 176 sagittal planes). Functional T2* weighted images were obtained using gradient echo EPI sequence (TR=4 s, TE=50 ms, spin flip angle 90°,

resolution 64×64, voxel size 3×3×3 mm³, slice gap 0,75 mm, 36 axial planes, interleaved scan). 60 whole brain functional images were acquired for each patient and control subject while the subjects were performing the motor tasks and 100 images while performing cognitive tasks.

2.3. Image Processing

All of the image processing steps were performed using Statistical Parametrical Mapping (SPM8, Wellcome Trust Centre for Neuroimaging, London, UK) software [3], which is a suite of MATLAB (The MathWorks, Inc., Natick, MA, USA) functions to process and analyse functional neuroimaging data. First step of spatial pre-processing was realignment of functional images, where movement effects were discounted. After realignment high resolution anatomical images were coregistered with functional images, which maximized the mutual information. Pre-processing continued with segmentation of high resolution anatomical images, where the MNI452 white matter, grey matter and cerebro-spinal-fluid probability maps [4] were used to yield a parametric description for normalisation. In normalisation process the images were normalised and bias corrected. Image pre-processing ended with smoothing by 8×8×8 mm³ full width at half maximum (FWHM) isotropic Gaussian kernel.

2.4. Statistical Analysis

Image processing was followed by a general linear model based statistical analysis of the functional images.

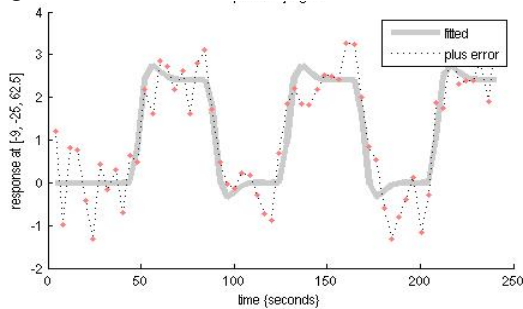


Fig. 1. Box car function convolved with hemodynamic response function (bold line) and pre-processed signal readings at a single voxel during motor task (red dots).

Modelling was done with box car functions convolved with hemodynamic response function [7]. An example of pre-processed data points with response function are shown in fig. 1. Low frequency noise was eliminated by using 160 s high-pass filter. Estimation of model parameters was done by using SPM 8, after which task vs. rest activation was assessed by applying t-test to the parameter estimates, resulting statistical parametric t-maps for each subject. Multiple comparisons problem was corrected by masking images with Brodmann area (BA) masks (fig. 2) from MRICro [8] and by doing ROI analysis using WFU PickAtlas [9, 10]. BA masks a), b)

and c) were used for motor task and d), e) for cognitive task results.

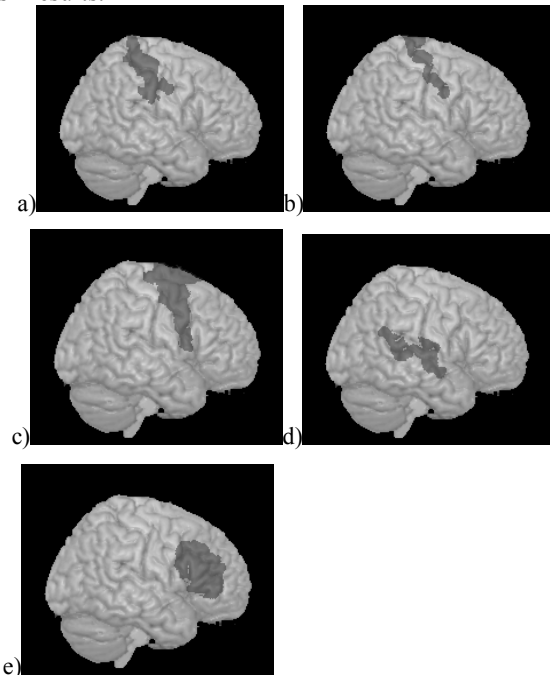


Fig. 2. Brodmann area masks (regions of interest) defined on a normalized MNI single_subject_T1 template using modified Brodmann area templates by MRICro [8] and visualized within 10 mm below the surface: a) BA 1-2-3; b) BA 4; c) BA 6; d) BA 22; e) BA 44-45.

From resulting masked t-maps, weighted lateralisation index (LI_w) was calculated using combined bootstrap/histogram analysis approach by Wilke and Schmithorst [11]. Bootstrap algorithm helps to evaluate sampling distribution of a sample by repeatedly resampling, with replacement, the original sample which would give approximately the “real” distribution of the original sample. By using bootstrap algorithm, 10 000 indices were iteratively calculated with equation (1) at different thresholds, where Q_{LH} is the sum of all the t-map values in masked area of left hemisphere and Q_{RH} is the similar sum for right hemisphere:

$$LI = \frac{Q_{LH} - Q_{RH}}{Q_{LH} + Q_{RH}} \quad (1)$$

For each threshold a trimmed mean lateralisation index was calculated by finding the mean value of lateralisation indices where 25% of upper and lower values were excluded. Weighted lateralisation index LI_w was calculated by equation (2), where $LI_{25,i}$ is the trimmed mean lateralisation index and W_i is the weighting factor or threshold, where trimmed mean was calculated:

$$LI_w = \frac{\sum_{i=1}^n W_i \cdot LI_{25,i}}{\sum_{i=1}^n W_i} \quad (2)$$

To avoid statistically not important results, limits for minimum cluster size of 5 “activated” voxels and minimal number of 10 “activated” voxels per hemisphere were established. By using same BA masks and by doing ROI analysis with WFU PickAtlas in SPM 8, maximum Z-scores in each BA were found.

3. Results

3.1. Intersubject repeatability of motor task

Motor task was run in two parts, at first with right hand and then with right ankle. Weighted lateralisation indices of right hand motor task for each subject are in fig. 3. As the lateralisation is usually [12] assessed to be left lateral when the LI_w is higher than 0,2 all of the patients right hand motor task results at each BA were assessed to have left lateralisation.

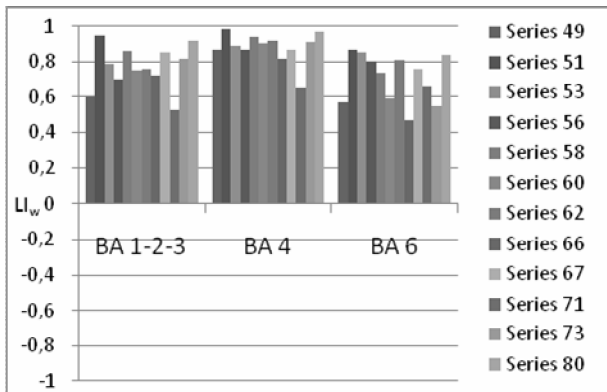


Fig. 3. Weighted lateralisation indices of right hand motor task of right handed healthy subjects in respective Brodmann areas (BA).

Z-score relative standard uncertainty for right hand motor task was 5% for BA 1-2-3 and BA 4 and 6% for BA 6.

The results of right ankle motor task are shown in fig. 4. Ankle motor task had bigger variation in results, thus some of the results were yielded bilateral (with $|LI| \leq 0,2$) and some of the results right lateral (with $LI < -0,2$). The best reproducibility of ankle test was found in BA 4, where standard deviation of mean was 0,04. This was expected by physicians because BA 4 is thought to be primary motor cortex. Bigger variation of other BA-s was thought to be caused by inhomogeneity of the subjects group or as well as moving right ankle without moving left ankle might have been difficult for some subjects, which might have led to different results.

Relative standard uncertainty of mean Z-score of the ankle motor task was 6% for BA 1-2-3, 8% for BA 4 and 6% for BA 6.

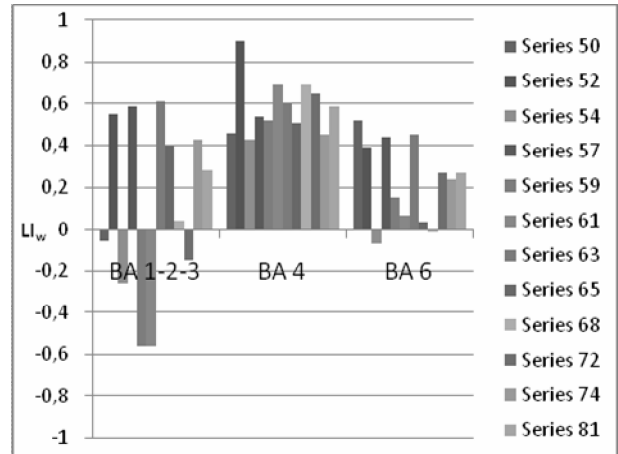


Fig. 4. Weighted lateralisation indices of right ankle motor task of right handed healthy subjects in respective Brodmann areas (BA).

3.2. Intersubject reproducibility of cognitive task

Cognitive task was also run in two parts where at first subjects had to think about the word which they were told, and finally they had to listen different sentences and to decide whether it is true or false.

The results for word generation task are at fig. 5. It was concluded that for cognitive task much higher subject group homogeneity requirements should be in place and as results in fig. 5 and 6 are for children aged between 9 and 14 a big variation is seen.

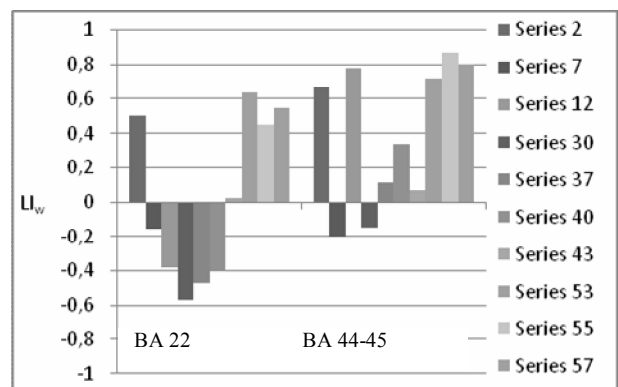


Fig. 5. Weighted lateralisation indices of word generation task of right handed healthy subjects in respective Brodmann areas (BA).

The results for sentence comprehension test are in fig. 6. While comparing results of different test of single subject, for example 40 and 41, it can be seen that word generation and sentence comprehension can have opposite laterality at BA 22.

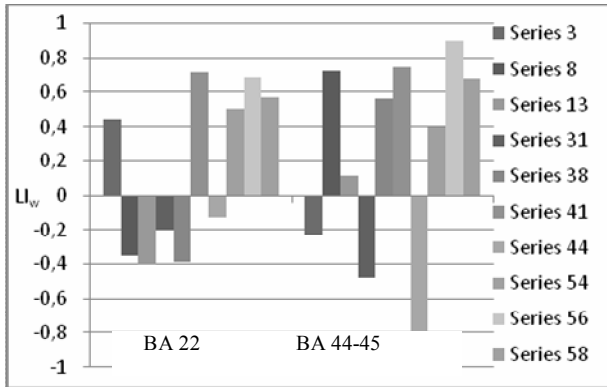


Fig. 6. Weighted lateralisation indices of sentence comprehension task of right handed healthy subjects in respective Brodmann areas (BA).

Z-score relative standard uncertainty of cognitive task for word generation was 11% for both BA-s, and for sentence comprehension task 8% for BA 22 and 10% for BA 44-45.

3.3. Intrasubject reproducibility of motor task

From the word generation and the sentence comprehension data 8 motor task contrast t-maps were acquired, which LI_w values are in fig. 7. For intrasubject reproducibility a motor task of finger tapping was used. Though all the results are connected to left lateralisation, one can see increasing trend of lateralisation due to adaptation of motor task.

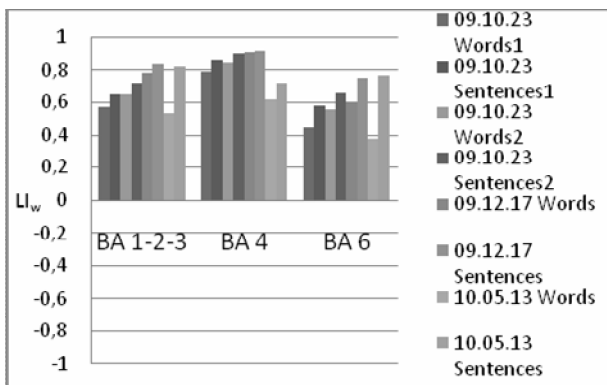


Fig. 7. Weighted lateralisation indices of finger tapping motor task of one right handed healthy subject in respective Brodmann areas (BA).

Relative standard uncertainty of mean maximum Z-score in intrasubject reproducibility study of the motor task was 15% for BA 1-2-3, 13% for BA 4 and 14% for BA 6.

3.3. Intrasubject reproducibility of cognitive task

The results of 4 word generation and 4 sentence comprehension tasks are in fig. 8. Due to the fact that subject under study was more tired in one day than the other and due to cognitive adaptation, results tend to yield pseudobilaterality as mentioned in literature [12].

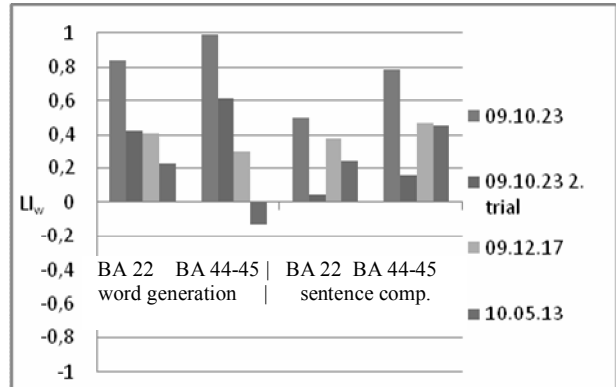


Fig. 8. Weighted lateralisation indices of word generation and sentence comprehension task of one right handed healthy subject in respective Brodmann areas (BA).

4. Discussion

The aim of this work was to compare inter- and intrasubject variability of motor and language area examinations. It is not right to compare the exact mean results of inter- intrasubject motor tasks because one of the tasks comprised flexion extension of right hand and the other finger tapping, respectively. As intersubject cognitive task examinations were held on children and intrasubject cognitive task examinations on adult, language task results are not directly comparable either. For this reason only standard deviations are compared.

4.1. Motor task reproducibility

In fig. 9 standard deviation of mean inter- and intrasubject LI_w values are compared. Even although the tasks where different the mean values of hand motor tasks only slightly differ with finger tapping task results having 7-16% lower lateralisation. Standard deviations of mean LI_w values of intersubject reproducibility were 0,04 for BA 1-2-3, 0,02 for BA 4 and 0,04 for BA 6 and for intrasubject reproducibility 0,04 for BA 1-2-3, 0,04 for BA 4 and 0,05 for BA 6. From these results hand motor tasks with flexion/extension and finger tapping were counted as reproducible.

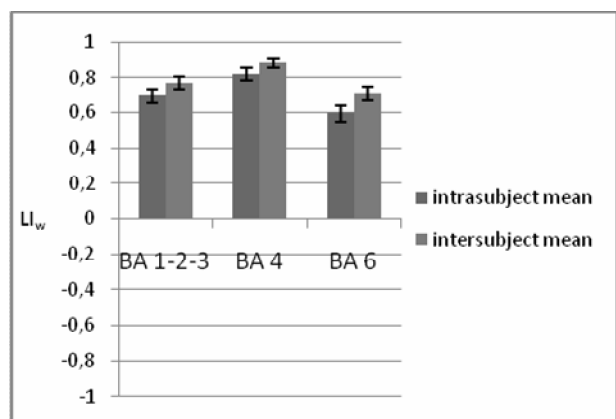


Fig. 9. Comparisons of standard deviations of mean weighted lateralisation indices at inter- and intrasubject of motor tasks at respective Brodmann areas.

In fig. 10 standard deviations of mean Z-score values were compared. Though Z-score values are often used in neurological studies mean Z-score standard deviations for intrasubject study were 0,90 for BA 1-2-3, 0,86 for BA 4 and 0,89 for BA 6. Relative standard uncertainties for intersubject study were 5% for BA 1-2-3, 5% for BA 4, 6% for BA 6 and for intrasubject study 15%, 13% and 14% respectively. This showed that maximum Z-score value of fixed region characterise more of concentration on task and this might not be the best characteristic of neurological differences.

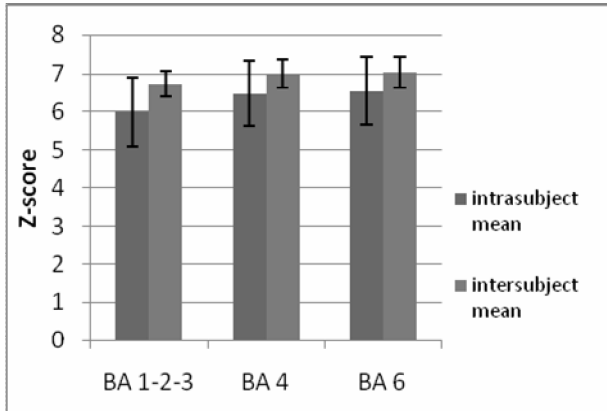


Fig. 10. Comparisons of standard deviations of mean maximum Z-score at inter- and intrasubject of motor tasks at respective Brodmann areas.

4.2. Cognitive task reproducibility

Fig. 11 shows the comparison of standard deviations of mean weighted lateralisation indices. The mean values of inter- and intrasubject test are not overlapping because of the age difference of subjects. Sentence comprehension test yielded a lower variation of results for intrasubject study with the standard deviation of 0,10 compared to 0,13 for BA 22 and 0,13 compared to 0,24 for BA 44-45. In intersubject study the results at BA 22 were equally variable with STD 0,15, and sentence comprehension test yielded more variability with STD of 0,19 compared to 0,13. The results showed that intrasubject results were all left lateral. For intersubject study word generation test yielded more interpretable results, because within STD BA 22 had bilateral activation and BA 44-45 left lateral activation. The mean results of intersubject sentence comprehension task are near the boundary limit of bi- and left laterality. It was concluded that word generation task would have higher reproducibility than sentence comprehension task for children.

The fig. 12 shows the comparison of standard deviation of inter- and intrasubject mean Z-score value where higher variation of intrasubject results are shown. Relative standard deviations of mean Z-score values in intersubject study with word generation task were 11% for BA 22, 11% BA 44-45 and for sentence comprehension 8% and 10% respectively. Relative standard uncertainty of mean Z-score values in intrasubject study with word generation task were 25%

for BA 22, 29% BA 44-45 and for sentence comprehension 14% and 25% respectively.

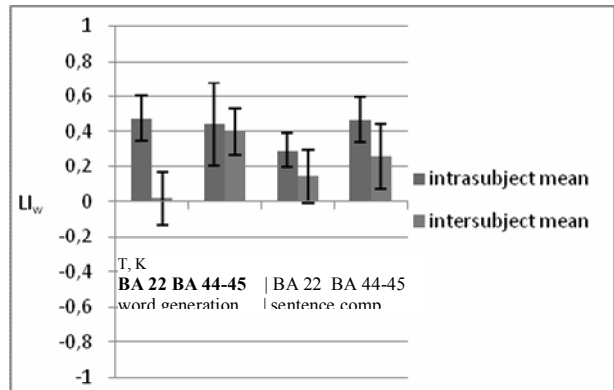


Fig. 11. Comparisons of standard deviations of mean weighted lateralisation indices of word generation and sentence comprehension tasks at respective Brodmann areas of inter- and intrasubject results.

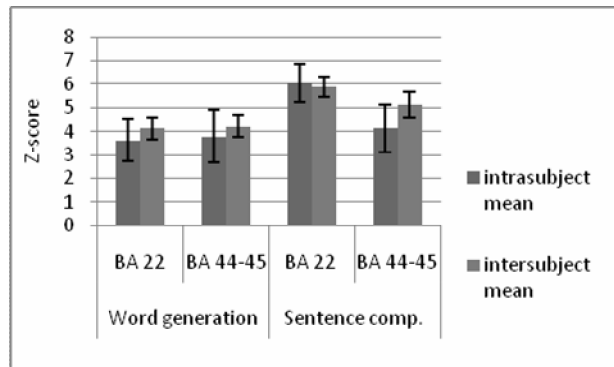


Fig. 12. Comparisons of standard deviations of mean maximum Z-score of word generation and sentence comprehension tasks at respective Brodmann areas of inter- and intrasubject results.

Fig. 12 shows that word generation task yielded lower maximum Z-score values from which was concluded that sentence comprehension task was more understandable to subjects and might need more logical thinking and interpretation of sentences which might need more concentration on task.

5. Conclusions

This study was about methodological reproducibility issues of functional magnetic resonance imaging. Reproducibility of methodology was assessed with both inter- and intrasubject results. Intersubject reproducibility was assessed with 24 motor area tests on healthy right handed adults and with 20 language area tests on healthy right handed children. Intrasubject reproducibility was assessed on one healthy right handed adult. Image pre-processing and analysis was done in SPM 8, where t-maps were masked by Brodmann area masks from MRICro and analyzed in prescribed area. Maximal Z-scores were noted and weighted lateralisation indices were calculated with

bootstrap/histogram algorithm in prescribed BA. The study yielded that motor test has good reproducibility with mean LI_w values (and standard deviation) of 0,77(0,04) for BA 1-2-3, 0,88(0,02) for BA 4 and 0,71(0,04) for BA 6 for hand motor test. For ankle motor test mean LI_w values and their standard deviation are 0,11(0,12), 0,59(0,04) and 0,23(0,06) respectively. Intrasubject repeatability yielded LI_w results with standard deviation between 0,04 and 0,05 for right hand finger tapping.

Cognitive word generation task results for intersubject study were 0,02(0,15) for BA 22 and 0,40(0,13) for BA 44-45 and 0,15(0,15), 0,26(0,19) respectively for sentence comprehension.

Mean maximum Z-scores had relative standard deviations for right hand test in intersubject study 5-6 % and for intrasubject study 13-15%. It was concluded that methodology of the motor task has good reproducibility. For language area methodological issues was concluded that stricter criteria for choosing subjects should be applied.

6. References

1. S. Ogawa, T. M. Lee, A. R. Kay, D. W. Tank „Brain magnetic resonance imaging with contrast dependent on blood oxygenation,“ *Proc. Natl. Acad. Sci. USA* 87(24): 9868–9872 (1990).
2. V. Renvall, „Functional magnetic resonance imaging reference phantom,“ *Magnetic Resonance Imaging* 27: 701–708 (2009).
3. J. Ashburner, C.-C. Chen, G. Flandin, R. Henson, S. Kiebel, J. Kilner, V. Litvak, R. Moran, W. Penny, K. Stephan, C. Hutton, V. Glauche, J. Mattout, C. Philips, „Statistical Parametric Mapping v.8,“ (The FIL Methods Group, London, UK, 2010), <http://www.fil.ion.ucl.ac.uk/spm/> (August, 2010).
4. International Consortium for Brain Mapping, „ICBM 452 T1 Atlas,“
5. http://www.loni.ucla.edu/ICBM/Downloads/Downloads_452T1.shtml (August, 2010).
6. K. J. Friston, P. Fletcher, O. Josephs, A. Holmes, M. D. Rugg, R. Turner, „Event-related fMRI: characterizing differential responses,“ *NeuroImage* 7: 30–40 (1998).
7. C. Rorden, „MRICro v.1.40,“ (Center for Advanced Brain Imaging, Atlanta GA, USA, 2005).
8. J. A. Maldjian, P. J. Laurienti, J. B. Burdette, R. A. Kraft, „An Automated Method for Neuroanatomic and Cytoarchitectonic Atlas-based Interrogation of fMRI Data Sets,“ *NeuroImage* 19: 1233-1239 (2003).
9. J. A. Maldjian, P. J. Laurienti, J. H. Burdette, „Precentral Gyrus Discrepancy in Electronic Versions of the Talairach Atlas,“ *NeuroImage* 21(1): 450-455 (2004).
10. M. Wilke, V. J. Schmithorst, „A combined bootstrap/histogram analysis approach for computing a lateralization index from neuroimaging data,“ *NeuroImage* 33: 522–30 (2006).
11. M. L. Seghier, „Laterality index in functional MRI: methodological issues“, *Magnetic Resonance Imaging* 26: 594–601 (2008).
12. H. Lohmann, M. Deppe, A. Jansen, W. Schwindt, S. Knecht, „Task repetition can affect functional magnetic resonance imaging-based measures of language lateralization and lead to pseudoincreases in bilaterality,“ *J. Cereb. Blood Flow Metab.* 24: 179–87 (2004).

EARLY DIAGNOSIS OF OSTEOARTHRITIS USING CONTRAST ENHANCED 3-DIMENSIONAL MRI

Carl SIVERSSON *, Carl-Johan TIDERIUS **, Leif DAHLBERG **, and Jonas SVENSSON *

* Department of Radiation Physics, Lund University, Malmö, Sweden,

** Department of Orthopedics, Lund University, Malmö, Sweden

Abstract: In this work the delayed Gadolinium Enhanced MRI of Cartilage (dGEMRIC) method, for early diagnosis of osteoarthritis, is described. A novel method for performing the dGEMRIC measurements using a 3-dimensional Look-Locker (3D-LL) MRI sequence is also described, together with the results from a study of 33 persons, for verification of this method. It is concluded that the 3D-LL sequence is robust enough for accurate dGEMRIC measurements.

Keywords: dGEMRIC, cartilage, osteoarthritis, MRI, T1, Look-Locker, 3D, B1 correction

1. Introduction

Osteoarthritis (OA) is a common chronic disease, resulting in degeneration of articular cartilage, causing pain and disabilities. The disease commonly affects the weight bearing joints, such as knee and hip joints. In a report [1], the World Health Organization (WHO) ranked OA as one of the ten diseases causing the most disease burden for people around the world. It was estimated that, at age 60, around 10 percent of the world population have joint problems that are related to OA.

There are yet no direct cures for OA and it is not clear which persons are at risk. To some extent, OA appears to be related to tearing of cartilage. Thus, overweighted people suffer from a higher risk of OA at a young age.

As the disease is not yet curable, treatment is primarily focused on prevention and symptom relief. Weight loss and appropriate exercise programs are the techniques that have been proved most effective. Only at a very late stage of the disease, when symptoms are very serious, transplants or implants may be considered as a treatment.

1.1. Cartilage diagnosis with dGEMRIC

Articular cartilage is a very complex tissue. Not only must the cartilage be able to absorb all forces that are generated as the body moves, but the cartilage surfaces must also be able to move without friction against each other, in order to not tear on the tissue.

Articular cartilage can be described as two different structures complementing each other. One structure is

collagen, holding the cartilage volume together and preventing it from expanding. The other structure consists of aggrecan, with strongly negatively charged glycosaminoglycans (GAGs) tightly bound. These strong charges will, through osmotic effects, attract water molecules, which will expand the cartilage structure and prevent it from collapsing. The result is an elastic tissue capable of absorbing large forces without being damaged. One of the early effects of OA is the amount of GAG in the cartilage being reduced. This will in turn affect the amount of water molecules in the cartilage, which over time will impair the mechanical properties of the cartilage.

Delayed Gadolinium Enhanced MRI of Cartilage (dGEMRIC) is a method for estimating the amount of GAG in the cartilage, thus providing a measurement of the degree of OA long before actual symptoms can be seen.

A negatively charged paramagnetic contrast agent (Magnevist, Gd-DTPA²⁻) is administered intravenously to the patient. The contrast agent distributes in the cartilage inversely proportional to the amount of GAG, due to repulsion between Gd-DTPA²⁻ and the GAG. Due to the paramagnetic properties of Gd-DTPA²⁻, the concentration of contrast agent can be determined by measuring the longitudinal relaxation time (T1) of the cartilage tissue using an MRI scanner. This is typically done at 60-120 minutes after injection, when the contrast agent has reached its peak concentration in the cartilage. Thus, the lower the measured T1 value is, the higher is the contrast agent uptake and the lower is the quality of the cartilage.

1.2. Traditional T1 quantification

T1 values for dGEMRIC is traditionally calculated from a series of equally positioned 2-dimensional Inversion Recovery spin echo (2D-IR) images with different inversion times. For each voxel a number of points, following the longitudinal magnetization recovery, is retrieved. By fitting the values of these points to an equation describing this recovery, the T1 of each voxel can be retrieved. Typically, an average T1 value is calculated for the region of the cartilage that is of interest.

In early dGEMRIC studies [2] it was investigated whether pre-contrast T1 measurements were also necessary, for relating the post-contrast T1 values to. However, it was concluded that the major T1 differences between patients primarily emerge after the contrast agent is added, thus making the pre-contrast measurements nonessential.

An early application of the dGEMRIC method [3, 4] was to measure the average T1 values for groups of people with expected differences in cartilage quality. Four such groups were examined (table 1), ranging from elite runners to groups of patients with early osteoarthritis. One conclusion from these studies was that the dGEMRIC method is a good indicator of cartilage quality and osteoarthritis.

Table 1. Previous dGEMRIC T1 results for four different groups of people.

	Elite runners	Average exercise	Sedentary	Early OA
Average T1	470 ms	410 ms	380 ms	305 ms

1.3. Three-dimensional dGEMRIC

During recent years, several methods for performing dGEMRIC in a three-dimensional (3D) volume of interest have emerged [5]. These are based on various techniques such as Inversion Recovery prepared Spoiled Gradient Echo (3D-IR SPGR), Look-Locker (3D-LL), and 2-point Variable Flip Angle (3D-VFA).

There are several advantages of using such 3D measurements, including improved possibilities for giving diagnoses regarding specific locations on the cartilage as well as improved possibilities for performing measurements that can more easily be reproduced.

Both the 3D-LL and the 3D-VFA techniques rely on a well-defined excitation pulse flip angle to obtain reliable measurements. A problem with this approach is that the flip angle is usually not very accurate outside of the centermost slices of the volume of interest, due to the radio frequency (RF) pulse excitation profile being nonrectangular. This typically renders erroneous T1 values outside of these slices, which limits the usefulness of such 3D measurement techniques. Local

flip angle variations may also be caused by B1-inhomogeneities, further reducing the accuracy of the T1-measurements. While the 3D-IR SPGR sequence does not suffer from these particular problems, it does instead suffer from long measurement times, typically twice that of other 3D sequences, which limits its usefulness for in vivo studies.

The aim of this work is to present the evaluation method we have developed [5] for 3D dGEMRIC, which resolves some of these previous issues. Our method has been used extensively during the past two years, proving it to be robust enough for clinical work [5, 6].

2. Materials and methods

2.1. The 3D Look Locker pulse sequence

The 3D Look-Locker sequence described here is based on the work by Look and Locker [5, 7]. A slice-selective adiabatic inversion pulse is applied followed by a train of low flip angle excitation pulses, separated by a small time t_f , to repeatedly sample the recovery of the longitudinal magnetization using a gradient echo. Remaining transversal magnetization is destroyed between the excitation pulses by means of RF and gradient spoiling.

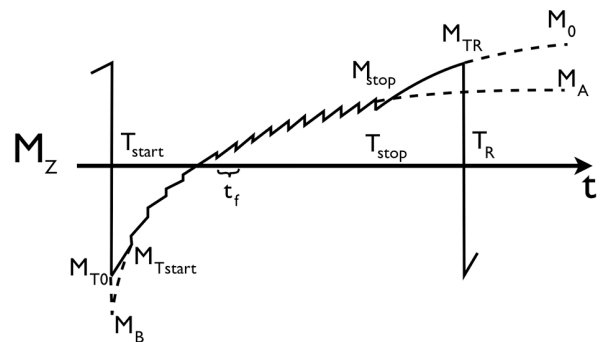


Fig. 1. The complete longitudinal magnetization evaluation throughout one repetition in a Look-Locker sequence.

By encoding each group of n successive gradient echoes into one of m separate k-spaces, a total of m separate set of image volumes are generated, each representing a specific temporal position (i.e. inversion time, TI) along the longitudinal relaxation curve. For each group of n successive gradient echoes the entire slice direction encodings are acquired using a linear encoding scheme. The process is repeated for new inversion pulses until all k-spaces are fully encoded. The actual TI for each image volume c ($1 \leq c \leq m$) is thus given by $TI_c = T_{start} + (c-1) \cdot n \cdot t_f + 0.5 \cdot n \cdot t$, where T_{start} is the time of the first excitation pulse, which is usually chosen as short as possible with respect to crusher gradients following the inversion pulse.

The signal $S(c)$ for a voxel in a given image volume c is proportional to the magnetization $M(TI_c)$ in the same voxel for the corresponding TI_c . This can be described by equation 1, where TI^* is the apparent longitudinal

relaxation time, and M_B and M_A are the extrapolated initial and steady-state longitudinal magnetization values respectively. By performing a three-parameter least square fit, using signal data from all image volumes, the parameters $T1^*$, M_B and M_A can be estimated for each voxel.

$$S(c) \propto M(TI_c) = M_A - (M_A - M_B) \cdot e^{-\frac{TI_c}{T1^*}} \quad (1)$$

Since the recovery of the magnetization is affected by the applied RF pulses, the resulting $T1^*$ is shorter than the true $T1$. Thus, the calculation of the true $T1$ is dependent on the excitation pulse flip angle, which must be properly corrected for.

2.2. Constant flip angle correction

This is the correction technique traditionally used with both 2D and 3D Look-Locker sequences. It has been previously described (8) that the resulting $T1^*$ can be corrected using equation 2.

$$\frac{1}{T1} = \frac{1}{T1^*} + \frac{\ln(\cos(\alpha))}{t_f} \quad (2)$$

However, one major drawback of this approach is that it requires the flip angle, α , to be well determined in every voxel being corrected. Commonly, the nominal flip angle from the user interface is used for all voxels and hence we refer to this method as constant flip angle (FA) correction.

2.3. Precalculated flip angle correction

If it can be assumed that the major source for flip angle variations within a sample is due to the shape of the RF-pulse excitation profile, the variations in flip angle will be mostly slice dependent. Thus, by calculating a flip angle slice profile, the acquired $T1^*$ can be effectively corrected, using equation (2), knowing only the slice origin for the corresponding region of interest. We call this method precalculated flip angle (FA) correction [5].

2.4. Calculation of a flip angle slice profile

We have shown [5] that during certain conditions the flip angle can be calculated directly from the 3D-LL data by combining equations (3), (4) and (5). These certain conditions include that the inversion pulse must be performing optimal, which is usually the case when scanning phantoms. Hence, once a flip angle slice profile has been acquired from phantom scans, this profile will be valid also for correction of *in vivo* data acquired using the exact same excitation pulse.

$$T1 = -\frac{t_f}{\ln\left(1 - \frac{M_A - M_A \cdot e^{-\frac{t_f}{T1^*}}}{M_0}\right)} \quad (3)$$

$$M_0 = \frac{M_{Tstart} + M_{Tstop} \cdot K \cdot e^{-\frac{Tstart}{T1}} \cdot e^{-\frac{TR - Tstop}{T1}}}{1 - e^{-\frac{Tstart}{T1}} - K \cdot e^{-\frac{Tstart}{T1}} + K \cdot e^{-\frac{Tstart}{T1}} \cdot e^{-\frac{TR - Tstop}{T1}}} \quad (4)$$

$$\alpha = \arccos\left(e^{t_f \cdot \left(\frac{1}{T1} - \frac{1}{T1^*}\right)}\right) \quad (5)$$

2.5. MR acquisition

All data was acquired on a 1.5 T Siemens Sonata whole-body scanner using a transmit-receive CP-Extremity coil. T1 was measured using a standard 2D-IR pulse sequence and an in-house developed 3D-LL sequence. The T1-evaluations were performed using custom in-house developed software.

For 2D-IR six images with TI ranging from 50 ms to 1600 ms was acquired. Resolution 256x256 pixels, field of view (FOV) 120 mm, slice thickness 3 mm, TE 15 ms, TR 2000 ms and Turbo factor 11. Duration for 2D-IR on both condyles was 10 minutes and 24 seconds.

For 3D-LL resolution was 256x256 pixels with 30 slices, FOV 160 mm, slice thickness 3 mm, nominal FA 6°, TE 2.15 ms, TR 2500 ms, 12 TIs. First TI was 98 ms and each excitation pulse was separated 4.84 ms. A hyperbolic secant pulse was used to achieve adiabatic inversion. Duration was 10 minutes and 42 seconds.

2.6. In vivo study

A study with 33 persons, likely to develop OA, was performed [5]. The subjects were injected with a triple-dose of Magnevist, after which the subjects were instructed to walk along a pre-determined route for ten minutes. The first measurement sequence was performed at 90 minutes after the contrast injection.

All sequences were executed consecutively without delays. First two sets of 2D-IR sequences were performed, positioned parallel to each other through the mid sections of the lateral and medial femur condyles in the knee with expected OA. Next, the 3D-LL sequence was performed on the same knee, positioned to cover both femur condyles.

Regions of interest (ROIs), in which an average T1 was calculated, were hand-drawn to cover the weight-bearing part of each femur condyle for both 2D-IR and 3D-LL (Fig 2).

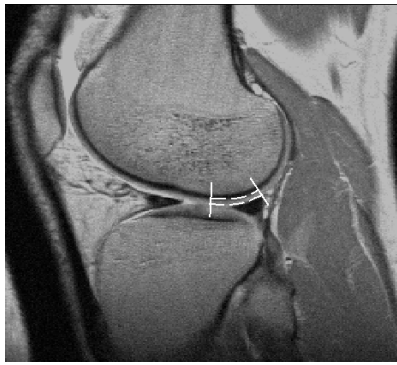


Fig 2. Weight bearing region of cartilage, from which an average T1 value is calculated.

The *in vivo* 3D-LL data was evaluated using both the constant FA correction method and the precalculated FA correction method, using a flip angle slice profile previously calculated from phantom measurements.

3. Results

T1 evaluations for both condyles were made, using each of the described methods, for all 33 subjects, resulting in a total of 66 measured ROIs for each method. When comparing to the 2D-IR T1 values, the 3D-LL T1 values are systematically overestimated by the constant FA correction method (Fig. 3a, table 2). However, the precalculated FA correction method is performing very well *in vivo* (Fig. 3b, table 2).

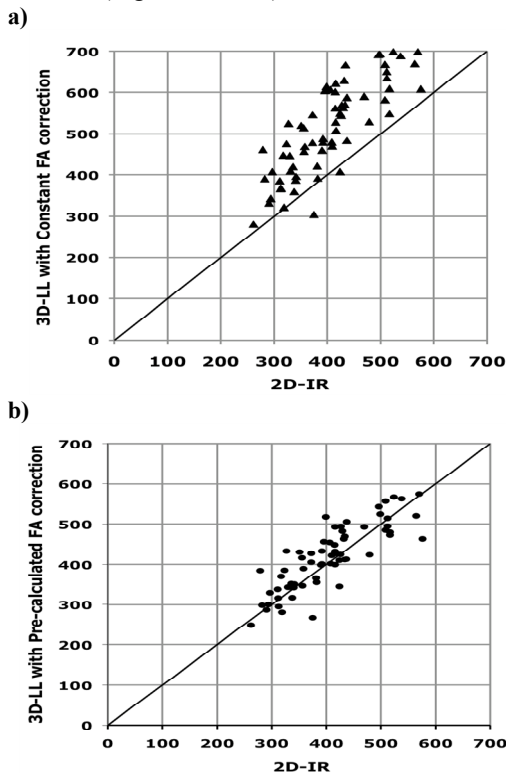


Fig 3. A total of 66 *in vivo* T1 measurements were made using both 3D-LL and 2D-IR. The figures show T1 measured using 3D-LL and evaluated using both evaluation methods, compared with T1 measured using 2D-IR. **a)** Constant FA correction versus 2D-IR; **b)** Precalculated FA correction versus 2D-IR.

Table 2. Comparison of *in vivo* results for the two 3D-LL evaluation methods.

	Constant FA correction	Pre-calculated FA correction
Systematic error	109.1 ms	13.3 ms
Random error (95%)	127.4 ms	90.1 ms

4. Discussion

Evaluating a 3D-LL sequence using the traditional constant FA correction method puts some severe restrictions on the reliability of the T1 measurements, mainly due to the flip angle slice profile not being perfectly rectangular. The method described here overcomes these problems and makes it possible to utilize a larger part of the acquired volume for reliable dGEMRIC measurements [5].

Thus it is shown that the 3D Look-Locker sequence is robust enough to perform reliable volumetric dGEMRIC measurements within clinical acceptable acquisition times. In order to perform such measurements it is however necessary to take the flip angle slice profile into account.

5. References

1. World Health Organization. World Health Report 2002. Reducing Risks, Promoting Healthy Life. Geneva: WHO, 2002.
2. Tiderius et al. Gd-DTPA2)-enhanced MRI of femoral knee cartilage: a dose-response study in healthy volunteers. *Magn Reson Med* 2001;46(6): 1067-1071.
3. Tiderius et al. Delayed gadolinium-enhanced MRI of cartilage (dGEMRIC) in early knee osteoarthritis. *Magn Reson Med* 2003;49(3):488-492.
4. Tiderius et al. dGEMRIC (delayed gadolinium-enhanced MRI of cartilage) indicates adaptive capacity of human knee cartilage. *Magn Reson Med* 2004;51(2): 286-290.
5. Siversson et al. Local flip angle correction for improved volume T1-quantification in 3D dGEMRIC using the Look-Locker technique. *J Magn Reson Imag* 2009;30:834-841.
6. Siversson et al. Repeatability of T1-quantification in dGEMRIC for three different acquisition techniques: 2D-Inversion Recovery, 3D-Look-Locker and 3D-Variable Flip Angle. *J Magn Reson Imag* 2010;31(5):1203-9
7. Look, Locker. Time saving in measurement of NMR and EPR relaxation times. *Rev Sci Instr* 1970;41(2):250-251.
8. Brix G, Schad LR, Deimling M, Lorenz WJ. Fast and precise T1 imaging using a TOMROP sequence. *Magn Reson Imaging* 1990;8(4):351-356

DOSIMETRY FOR THE LENS OF THE EYE, APPLICATIONS FOR MEDICAL STAFF INVOLVED IN INTERVENTIONAL PROCEDURES

Therése GEBER¹, Mikael GUNNARSSON¹, Sören MATTSSON¹

¹Department of Medical Radiation Physics, Lund University, Skåne University Hospital, Malmö, Sweden

Abstract: In interventional radiology the working physicians are exposed to scattered radiation. Recent studies indicate that the lens of the eye may be even more sensitive to ionizing radiation than previously thought. This makes good methods for estimating lens doses necessary. The relation between eye dose to physicians and patient dose-area product, absorbed dose to the lens and the dose to a measuring point at the forehead as well as the effect of eight different models of protective eyewear is measured. A correlation between physicians eye dose and patient dose-area product was found and a dosimeter at the forehead was found to underestimate the dose to the lens of the eye with 25 %. The effect of protective eyewear was shown to depend strongly on the angle in which the radiation strikes and the design of the eyewear.

Keywords: Interventional radiology, Staff doses, Cataract, Protective eyewear.

1. Introduction

During interventional procedures the present staff is exposed to scattered radiation from the patient. At particular risk are the eyes and hands of the physicians, which are not as easy to protect as the rest of the body (with lead aprons). Radiation exposure to the lens of the eye may lead to radiation-induced cataract [1]. The development of cataract has long been considered a deterministic effect, i.e. a threshold dose exists below which damage does not occur [2-4]. Recent studies however, suggest that the threshold is much lower or even that it does not exist at all and thus that cataract in fact is a stochastic effect [5-12]. This makes the issue of radiation exposure to the eyes even more significant since present dose limits [4], which are based on the deterministic data, then have to be reduced. If the absorbed dose to the lens is measured at all during medical procedures today it is usually done by placing a dosimeter at the side of the head near the eye or at the forehead [13, 14]. The question arises on how good is this approximation of the absorbed dose to the lens of the eye. To provide good protection for the lens of the eye it is important to have good knowledge of all aspects concerning the radiation situation. This report presents results from experimental measurements of the absorbed dose relation between the lens of the eye and a measuring point at the forehead. The dose distribution inside the head and thence the effect of eight different types of protective eyewear are investigated. Since

absorbed dose measurements are consuming it would be desirable to be able to estimate the dose to the lens of

the eye without performing measurements and therefore the presence of a relationship between the output from the X-ray tube and the absorbed dose to the lens is explored.

2. Materials and Methods

Measurements were made using a head phantom and a thorax phantom acting as a patient. The head phantom was an anthropomorphic Alderson phantom constructed around natural human bone, divided in discs with a thickness of 2.5 cm. Teeth and nasal cavities (sinuses) are also incorporated. To be able to place thermoluminescent dosimeters (TLDs) inside the head and not destroying the phantom, the disc where the eyes are located was replaced with a disc of polyethylene (PE) that has density and atomic number close to that of tissue. Small holes were made to fit the TLDs at the position of the lenses. The TLDs used were square chips made of LiF:Mg,Ti, TLD-100 (Thermo, Ohio, USA, www.thermo.com). The holes have a diameter of 4.2 mm and a depth of 13 mm to accommodate the dosimeters of 3x3 mm² and positioning the TLDs in the middle of the “eye disc”. The thorax phantom (model PBU-X-21, Kyoto Kagaku CO. Ltd, Kyoto, Japan, www.kyotokagaku.com) is an anthropomorphic phantom that closely resembles a real human chest and consists of materials that interact with radiation in the

same manner as do a real human being. During measurements the thorax phantom was placed on the operating table and the head phantom positioned where a physician would be expected to stand, figure 1. A headband with pockets for TLDs just above each eye was produced and placed on the head phantom during measurement without protective eyewear. The phantom measurements were performed on a clinically used X-ray unit (Philips MultiDiagnost Eleva, www.healthcare.philips.com). To easily be able to repeat the measurements the automatic exposure control was turned off and the exposure parameters set to 77 kV, 500 mA and 200 ms. No additional filter was used and the field size was set to it's maximum (about 13x16 cm² at a distance of 55 cm from focus). Below and above the PE disc sheets of radiochromic film (Gafchromic film, XR-QA2, www.gafchromic.com) was positioned. The film had been cut to fit precisely between the discs in the head phantom. To be able to convert the blackening of the film into absorbed dose the film was calibrated. This was done in the same radiation quality by irradiating a monitor detector (Unfors Xi, model 8201011-C, Unfors Instrument, Billdal, Sweden, www.unfors.com) and a piece of film simultaneously. Repeated exposures with increasing dose were made while exchanging films, giving darker and darker films. To scan the film an EPSON 4900 flatbed scanner was used and the images were read with the program ImageJ (<http://rsbweb.nih.gov/ij>). The mean pixel values were measured in each film, the background pixel value subtracted. The pixel values and the absorbed dose values from the detector was then plotted to obtain a dose-response diagram. A third degree polynomial was fitted to the measurement points and the equation for this was later used to convert net pixel values into absorbed dose distributions in the films used in the head phantom.

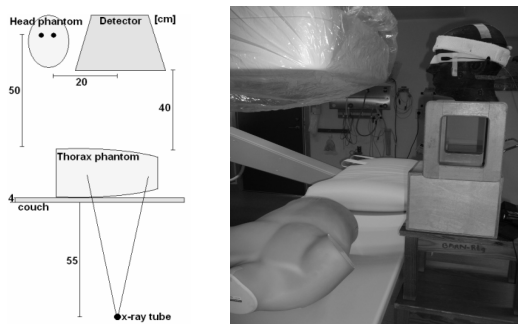


Fig. 1. Position of thorax and head phantom during measurements.

Measurements were made without protective eyewear as well as for eight different models of eyewear, irradiated both from the front and underneath from the left (as during interventional procedures). Measurements were also carried out on two senior physicians during a number of interventional procedures. They wore the same headband with TLDs as used in the phantom

measurements during the whole time of the procedures. The X-ray units used for measurements on the physicians were a Siemens Axiom Artis TA as well as a Siemens Axiom Artis see DF (www.medicalsiemens.com), X-ray units similar to the earlier used Philips Eleva. After each procedure the DAP value was noted and the TLDs in the headband read out.

3. Results

Figure 2 shows the relation between absorbed dose in the TLDs in the headband from the phantom measurements and the DAP value from the X-ray unit. The TLDs are located just above each eye respectively. Similarly figure 3 shows the relation between absorbed dose in the TLDs in the headband and the DAP value from the X-ray unit for the measurements on the physicians. A value of 7 μSv at the physicians' eyes for 1 Gy·cm² patient dose is found for the left lens in the phantom measurements and 1 μSv for 1 Gy·cm² in the measurements on the physicians. For the right lens the value is 5.5 μSv for 1 Gy·cm² in the phantom measurements and 0.7 μSv for 1 Gy·cm² in the measurements on the physicians.

Table 1 presents the absorbed dose to the TLD in the lens position related to the absorbed dose to the TLD at the corresponding position in the headband for the right and left eye respectively. For both eyes there is a 25 % higher dose in the lens than at the forehead.

In table 2 the absorbed dose to the TLD in the lens position with protective eyewear related to the absorbed dose to the TLD in the lens position without protective eyewear is presented. The number of the eyewear match one of the eight different models tested. For each pair of eyewear and without eyewear the phantom have been irradiated from the front as well as oblique from underneath, as during an interventional procedure. Figure 4 shows the dose distribution from the film sheets above and below the PE disc in the head phantom. The distribution without protective eyewear as well as the distribution from the worst and best working eyewear are presented.

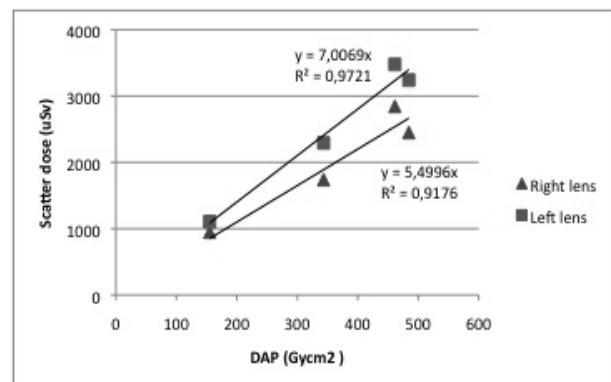


Fig. 2. Relation between absorbed dose in the TLDs in the headband from the phantom measurements and DAP value from the X-ray unit.

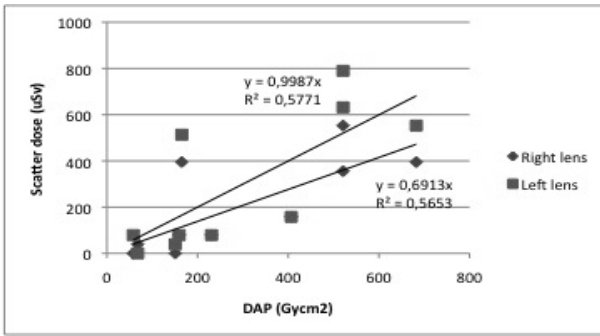


Fig. 3. Relation between absorbed dose in the TLDs in the headband from the measurements on physicians and DAP value from the X-ray unit.

Table 1. The absorbed dose to the TLD in the lens position related to the dose to the TLD at the corresponding position in the headband (at the forehead).

Left Lens/Headband over Left Eye (%)	125
Right Lens/Headband over Right Eye (%)	125

Table 2. The absorbed dose to the TLD in the lens position with protective eyewear related to the dose to the TLD in the lens position without protective eyewear, for the eight different models of protective eyewear. Irradiated oblique from underneath (as in interventional procedures) as well as from the front.

Eyewear #	1	2	3	4	5	6	7	8
Average Left TLD below (%)	72.4	43.0	77.5	84.8	86.1	22.4	35.1	69.7
Average Right TLD below (%)	98.2	89.1	96.8	93.8	96.6	89.2	87.6	92.0
Average Left TLD front (%)	17.8	14.4	27.1	26.0	22.5	14.3	15.5	20.0
Average Right TLD front (%)	17.0	13.0	24.7	26.1	23.7	17.1	18.9	16.6

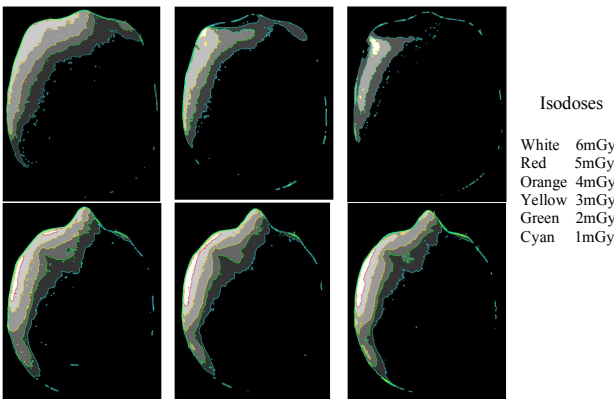


Fig. 4. Dose distribution from film sheets above (upper row) and below (lower row) the PE disc in the head phantom irradiated oblique from underneath. Leftmost is the distribution without protective eyewear, in the middle is the worst working eyewear and to the rightmost is the best working eyewear.

4. Discussion

The clear correlation between DAP value and absorbed dose to the right and left lens for the phantom measurements indicates the possibility of estimating the dose to the lenses without performing specific point

dose measurements for a given procedure, i.e. that a factor between DAP value and dose to the lens could be found. This would be of great use since it means that time consuming measurements would not be needed at all times and yet an estimation of the dose to the physicians' eyes would be obtained. In this case such a factor for the left lens would be about 7 µSv for 1 Gy·cm² and about 5.5 µSv for 1 Gy·cm² for the right lens. This is consistent with another study where the correlation between staff eye doses and patient doses were investigated [15]. They found a factor of 7 µSv for 1 Gy·cm² at the position of the eyes though with no scattering material at the head position and with a polymethylmethacrylate plate used to simulate a patient. For measurements on the physicians the correlation appear less clear. This is probably due to the fact that the physicians often work in pairs during procedures, the one not currently working standing behind the other, which means that the dose to the TLD does not correspond to the whole procedure in this case.

When the absorbed dose to the TLD in the lens position is related to the absorbed dose to the TLD at the corresponding position in the headband it turns out that the absorbed dose in the lens is 25 % higher than the absorbed dose in the headband. This means that a dosimeter at the forehead used for estimating the lens dose would underestimate the dose.

When the head phantom is irradiated from the front most of the protective eyewear works well and there are hardly any differences between the right and left eye. The absorbed dose to the lens is ranging between 13 % and 27 % of the dose without protective eyewear, which is considered as good. When the head phantom is irradiated oblique from underneath the situation is quite different. The remaining dose is much higher, between 22 % and 98 %, and there is a pronounced difference between the right and left eye. This is believed to be due to that radiation can slip through the gap created between the cheek and the eyewear because of the incident angle. The dose is consistently higher in the right lens suggesting that radiation also slips through at the nose. There is also a crucial difference between the different models, mainly for the left lens irradiated oblique from underneath. This suggests that how well the eyewear fit to the face is decisive. From figure 4 it can be seen that there is a big difference between the different models of protective eyewear. The effect of the protective eyewear seems to be best for the film sheet located above the PE disc. This is because the radiation strikes from underneath and therefore slips through the gap between the eyewear and the cheek at the bottom of the eyewear resulting in a higher dose there than at the top. It is important to bear in mind that the lens is located between these two sheets and so the real impact of wearing protective eyewear is some kind of average of the sheet below and above the PE disc. The dose distribution from figure 4 also show that a lot of radiation is deposited in the area of the left lens if protective eyewear is not used, which points out the importance of using protective eyewear.

5. Conclusions

It seems to be a clear relationship between DAP value and the dose to the physicians eyes. This relationship is most clear for phantom measurements but it is possible that a factor that correlates well even for physicians could be found. The meaning of such a factor would be that a lot of time could be saved since an approximation of the lens dose could be made from patient dose, given after each procedure, and therefore tedious measurements would not always be required.

When the absorbed dose to the lens of the eye is measured today it is usually done by placing a dosimeter at the side of the head or at the forehead and the assumption is made that this corresponds to the dose in the lens. When an approximation is made it is important to be aware of the errors that are introduced due to the approximation. This has most likely not been the case so far. This study shows that the dosimeters at the forehead underestimate the dose to the lens by 25 %. This has to be considered when estimating the dose to the lens of the eye. To underestimate the dose to the lens could lead to serious consequences, especially if the threshold dose turns out to be lower than previously thought.

When protective eyewear is irradiated from the front they seem to work as intended but when irradiated oblique from underneath the effect of the eyewear is poorer, especially for the right lens. This means that protective eyewear may provide a false sense of security when used under conditions where radiation does not strike from the front. The most important factor that determines whether a model of protective eyewear is effective or not seems to be the design. A good design minimizes gaps and moulds itself around the face, which can be highly individual. Each person on the staff ought therefore to have their own protective eyewear.

6. References

1. Merriam GR, Szechter A, Focht EF. The effects of ionizing radiation on the eye. *Front. Radiation Ther. Onc.* 1972;6:346-85.
2. Merriam GR, Jr., Worgul BV. Experimental radiation cataract- its clinical relevance. *Bull N Y Acad Med* 1983;59(4):372-92.
3. ICRP. Publication 60 1990 Recommendations of the International Commission on Radiological Protection: International Commission on Radiological Protection, 1991.
4. ICRP. Publication 103 The 2007 Recommendations of the International Commission on Radiological Protection: International Commission on Radiological Protection. 2007.
5. Chodick G, Bekiroglu N, Hauptmann M, Alexander BH, Freedman DM, Doody MM, et al. Risk of cataract after exposure to low doses of ionizing radiation: a 20-year prospective cohort study among US radiologic technologists. *Am J Epidemiol* 2008;168(6):620-31.
6. Cucinotta FA, Manuel FK, Jones J, Iszard G, Murrey J, Djojonegro B, et al. Space radiation and cataracts in astronauts. *Radiat Res* 2001;156(5 Pt 1):460-6.
7. Hall P, Granath F, Lundell M, Olsson K, Holm LE. Lenticular opacities in individuals exposed to ionizing radiation in infancy. *Radiat Res* 1999;152(2):190-5.
8. Minamoto A, Taniguchi H, Yoshitani N, Mukai S, Yokoyama T, Kumagami T, et al. Cataract in atomic bomb survivors. *Int J Radiat Biol* 2004;80(5):339-45.
9. Nakashima E, Neriishi K, Minamoto A. A reanalysis of atomic-bomb cataract data, 2000-2002: a threshold analysis. *Health Phys* 2006;90(2):154-60.
10. Neriishi K, Nakashima E, Minamoto A, Fujiwara S, Akahoshi M, Mishima HK, et al. Postoperative cataract cases among atomic bomb survivors: radiation dose response and threshold. *Radiat Res* 2007;168(4):404-8.
11. Wilde G, Sjostrand J. A clinical study of radiation cataract formation in adult life following gamma irradiation of the lens in early childhood. *Br J Ophthalmol* 1997;81(4):261-6.
12. Worgul BV, Kundiyevev YI, Sergiyenko NM, Chumak VV, Vitte PM, Medvedovsky C, et al. Cataracts among Chernobyl clean-up workers: implications regarding permissible eye exposures. *Radiat Res* 2007;167(2):233-43.
13. Lie OO, Paulsen GU, Wohni T. Assessment of effective dose and dose to the lens of the eye for the interventional cardiologist. *Radiat Prot Dosimetry* 2008;132(3):313-8.
14. Hausler U, Czarwinski R, Brix G. Radiation exposure of medical staff from interventional x-ray procedures: a multicentre study. *Eur Radiol* 2009;19(8):2000-8.
15. Vano E, Ubeda C, Leyton F, Miranda P, Gonzalez L. Staff radiation doses in interventional cardiology: correlation with patient exposure. *Pediatr Cardiol* 2009;30(4):409-13

EXTREMITY AND EYE LENS DOSES OF INTERVENTIONAL RADIOLOGY AND CARDIOLOGY WORKERS

Ausra URBONIENE, Birute GRICIENE
Radiation Protection Centre

Abstract: An interventional radiology and cardiology workers during interventional radiology procedures receive higher ionizing radiation doses in comparison with other groups of medical staff. This category of workers has higher potential risk of negative health effects (such as cataract) caused from occupational ionizing radiation exposure. It is known that external ionizing exposure distribution to the body of medical worker during interventional radiology procedures is non uniform. The aim of this work was to assess occupational exposure doses of extremities and eye lens of medical staff during interventional radiology procedures.

The doses of extremities and eye lens of interventional radiology and cardiology workers were measured during 55 interventional radiology procedures. The average eye lens dose of interventional radiology and cardiology physicians were about two times higher than the average dose near the neck above the protective apron. The maximum measured dose of physicians were: 0,79 mSv (left eye), 1,01 mSv (left shoulder), 1,29 mSv (finger), 1,50 mSv (left leg) per procedure. The study results show that annual dose of eyes and extremities of interventional radiology and cardiology physicians might result in more than 10 % of the annual dose limit to eyes and extremities.

Keywords: TLD, dosimetry, eye lens dose; extremity dose

1. Introduction

Sustained occupational exposure monitoring of workers exposed to ionizing radiation shows that medical staff during interventional radiology procedures receives much higher doses [1, 2]. This category of workers is more likely caused to negative effects (such as cataract) of ionizing radiation exposure to their health [3]. During interventional radiology procedures the individual protective aprons covers breast, waist, upper part of legs, however used additional radiation shielding in many cases do not help to avoid external exposure to eyes, hands and lower part of legs. The routine measurements of eye lens and extremity doses of interventional radiology and cardiology workers are not performed. The aim of this work was to assess exposure to eyes and extremities of medical staff during interventional radiology procedures.

2. Materials and Methods

Dose measurements were done with thermoluminescent whole body and ring dosimeters and separate thermoluminescent pellets placed into black packets (Fig. 1).

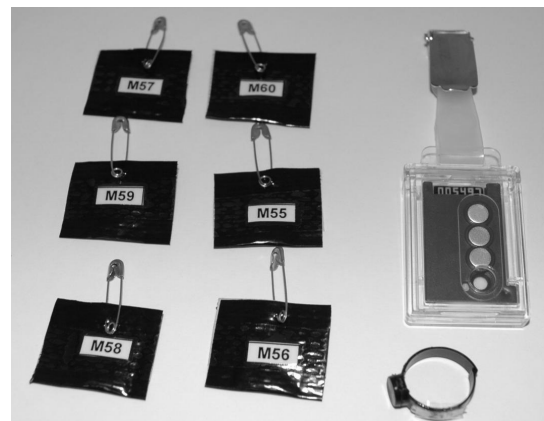


Fig. 1. Thermoluminescent dosimeters.

During interventional radiology procedures doses were measured in 8 places on the worker's body: above left and right eyebrows, on the left and right shoulders, on the left and right legs about 20 cm below knees, on the finger of right hand and near the neck above protective collar. The lithium fluoride (LiF:Mg,Ti) pellets were used. All doses were measured in terms of personal dose equivalent $H_p(0.07)$. $H_p(0.07)$ is operational dose quantity, it is equivalent dose in the depth of 0,07 mm.

Dosimeters after irradiation were read out with the RADOS thermoluminescent dosimetric system. The dosimeters for whole body dose measurement consist of two lithium fluoride pellets covered within 1 mm Al filter in a standard holder. The ring dosimeter has one lithium fluoride pellet. Preparing pellets for measurements annealing is performed at the temperature of 400°C for 1h and subsequently at 100°C for 2 h [4]. All pellets were calibrated for individual background and sensitivity. The minimum measured dose was 0.01 mSv. The total expanded measurement uncertainty is ± 25% with coverage factor k=2.

3. Results and discussion

During period of 2007-2008 34 interventional radiology and cardiology physicians and 30 workers of assisting staff (nurses, technicians and assistants) from the 6 hospitals participated in this study. 512 doses were measured during 55 interventional radiology procedures.

The results show wide range of variation in measured doses at different locations on the worker's body. Variation was influenced of wide range of fluoroscopy time and medical staff distance from the patient. Observed fluoroscopy time was in the range of 18 seconds – 30 minutes.

The measured doses of assisting staff were much lower than physicians. The doses above the minimum measured dose level for assisting staff were measured in three cases. The maximum measured dose for left leg of assisting nurse was 0,15 mSv per procedure. The lower doses assisting staff in comparison with physicians are received due to longer distance from X-ray equipment during interventional procedures.

The work place of physician during interventional procedure is close to the scattering area of patient however due to very short fluoroscopy time the doses of 11 physicians were less than minimum measured dose. The maximum measured doses of physicians were: 0,79 mSv (left eye), 1,01 mSv (left shoulder), 1,29 mSv (finger), 1,50 mSv (left leg) per procedure. The ranges of measured doses of interventional radiology and cardiology physicians are shown in Table 1.

Table 1. Ranges of measured doses per procedure of interventional radiology and cardiology physicians.

Interventional procedure (amount)	Left eye dose, mSv	Right eye dose, mSv	Left shoulder dose, mSv	Right shoulder dose, mSv	Hand dose, mSv	Left leg dose, mSv	Right leg dose, mSv
Coronariography and angioplasty (31)	0,01-0,79	0,01-0,45	0,01-1,01	0,01-0,17	0,04-1,29	0,01-1,50	0,01-0,92
Coronarograph (11)	0,01-0,09	0,01-0,03	0,01-0,08	0,01-0,06	0,03-0,18	0,01-0,94	0,01-0,73
Angiography of limb (6)	0,01	0,01	0,01-0,06	0,01	0,01-0,09	0,01-0,36	0,01-0,14
Embolization of head (1)	0,42	0,04	0,89	0,02	-	0,67	0,11

Other (6)	0,11-0,19	0,02-0,10	0,03-0,18	0,01-0,21	0,07-0,55	0,08-0,50	0,01-0,10
-----------	-----------	-----------	-----------	-----------	-----------	-----------	-----------

The average doses per procedure are shown in figure 2. The results show that the average left eye dose is about two times higher than the average dose near the neck above the protective apron. The average left eye dose per procedure was 0,19 mSv. The average extremity dose per procedure was 0,55 mSv (left leg) and 0,29 mSv (hand).

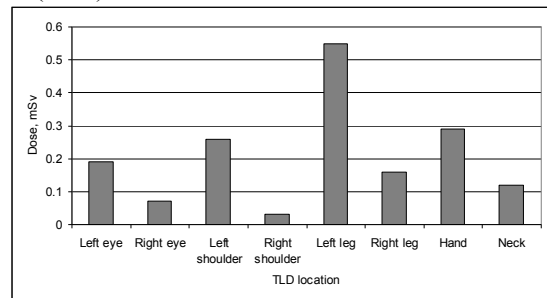


Fig. 2. Average dose per procedure of interventional radiology and cardiology physician.

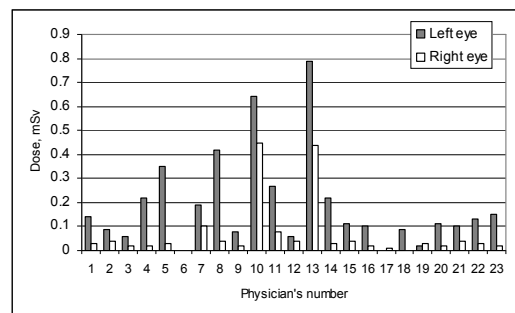


Fig. 3. Dose of the left and right eye of interventional radiology and cardiology physician.

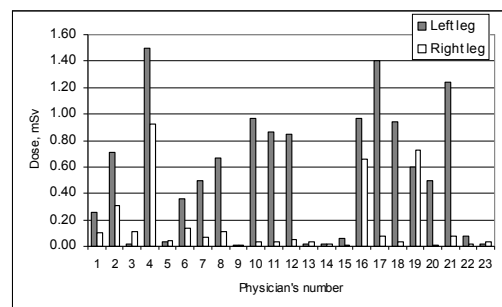


Fig. 4. Dose of the left and right leg of interventional radiology and cardiology physician.

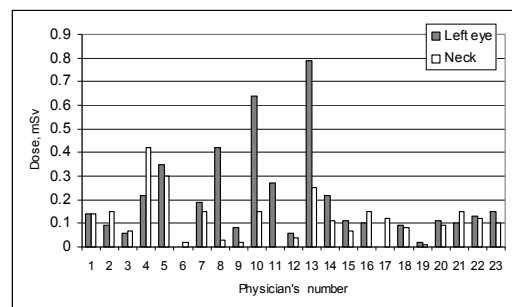


Fig. 5. Dose near the left eye and neck of interventional radiology and cardiology physician.

Generally the left side of the body receives higher doses than the right side (Fig. 3 and 4). Several authors state that dosimeter worn above the apron at neck level can be used to estimate the dose to the eyes [5, 6]. During present study it was observed more than five cases when left eye dose was more than 50 percent higher than the dose near the neck above collar (Fig. 5).

Taking into account that physician average fluoroscopy work time per month is 130 min. was calculated the annual average dose to eyes, legs and hands (table 2). The calculated average annual doses do not exceed dose limits, but results show that annual average dose of left eye and left leg could be more than 10 percent of the annual dose limit to eyes and extremities.

Table 2. Average dose for different parts of body comparison with annual dose limit.

Part of body	Average dose per procedure, mSv	Annual average dose, mSv	Annual dose limit, mSv	10 % of annual dose limit, mSv
Left eye	0,19	25,2	150	15
Hand	0,29	37,2	500	50
Left leg	0,55	72,0	500	50

4. Conclusion

The average eye lens dose of interventional radiology and cardiology physicians were about two times higher than the average dose near the neck above the protective apron. The study results show that annual doses of eyes

and extremities of interventional radiology and cardiology physicians might result in more than 10 percent of the annual dose limit to eyes and extremities. In such cases individual monitoring of extremities and eye lens of should be performed.

5. References

1. Radiation Protection Centre. Annual report 2007. Vilnius, 2008.
2. Radiation Protection Centre. Annual report 2009. Vilnius, 2010.
3. Vano E., Kleiman N. J., Duran A., Rehani M. M., Echeverri D., Cabrera M., Radiation Cataract Risk in Interventional Cardiology Personnel. Radiation Research In-Press, 2010.
4. Morkunas G., Gričienė B., Jankauskienė D. Current status of personal dosimetry in industry, research and medicine in Lithuania. Radiat. Prot. Dosim. 96(1-3), 2001. p. 57-59.
5. Covens P., Berus D., Buls N., Clerinx P. and Vanhavere F. Personal dose monitoring in hospitals: global assessment, critical applications and future needs. Radiat. Prot. Dosim. 124 (3), 2007. p. 250-259.
6. Clerinx P., Buls N., Bosmans H. and de May J. Double – dosimetry algorithm for workers in interventional radiology. Radiat. Prot. Dosim. 129 (1-3), 2008. p. 321-327.

DOSIMETRIC COMPARISON BETWEEN LINKED AND STRAND SEEDS FOR I-125 PERMANENT SEED PROSTATE BRACHYTHERAPY

Karolis JAKŠTAS*, Miglė ŠNIUREVIČIŪTĖ**

* Kaunas University of Technology, Physics Department; ** Kaunas Medical University Clinics;

Abstract: The purpose of the study is to compare two different types and activities of I-125 seeds used in low dose rate (LDR) prostate brachytherapy. Ten patients, whose treatment had been planned using linked (model STM1251) or strand (model 6711) seeds were selected. For each patient, the new treatment plans were created with another seeds type and activity. The number of seeds, needles and the parameters such as Vp100, D90, Vr100 and D1 were compared and analyzed.

Keywords: LDR brachytherapy, linked seeds, strand seeds, prostate.

1. Introduction

Brachytherapy history starts from 1901 when Pierre Curie suggested to Henri-Alexandre Danlos that a radioactive source could be inserted into a tumour and makes it shrink. More recent advancements in three dimension imaging modalities, computerised treatment planning systems and delivery equipment have made brachytherapy a safe and effective treatment for many types of cancer today. There are several types of brachytherapy, but the main target on this study is LDR (low dose rate) brachytherapy with I-125 seeds.

LDR prostate brachytherapy is a form of radiotherapy treatment for early, localized prostate cancer that has not spread outside the prostate gland. The treatment involves inserting tiny radioactive seeds into the prostate gland. This allows radiation to be targeted directly to the tumour and minimizes unwanted radiation effects. The homogeneous dose distribution in tumour depends on number of seeds and their activity. The activity of seeds used in prostate brachytherapy varying from 0.4 to 0.7 mCi. However, there are not many information about what source activity is the best for implantation.

The aim of our study was to compare linked (model STM1251) and strand (model 6711) seeds with different activity, find the most effective choice with less number of seeds and needles. The use of higher activity seeds could have some advantages – for example, we need smaller amount of seeds and needles that reduce operating time and harm of tissue, minimise edema for patient. Furthermore, there are some economical reasons, lower treatment cost

Here we report result of initial study of examining influence of the source activity to number of seeds and needles.

2. Methods and materials

Ten patients, whose treatment have been planned using linked (model STM1251) or strand (model 6711) seeds were selected. For each patient, the new treatment plans were created with another seeds type and activity. The volume of prostates varied from 22,22 to 47,42 cc (mean 33,33 cc) and prescribed dose was 145 Gy. Activity of the seeds ranged from 0,443 to 0,645 mCi. More detail information is given in Table 1.

The implantation were performed under general anesthesia An ultrasound (US) probe is placed in the rectum to obtain transversal and sagittal image of prostate, rectum and urethra. The software Variseed 8.0 was used for treatment planning. After the contours were obtained the plans were prepared The criteria were used for intra-operative planning dosimetry: for the prostate, D90 (minimum dose covering 90% of the prostate volume) >160 Gy, a Vp100 (prostate volume receiving 100% of the prescribed dose) ≥98%, for the rectum Vr100 (volume of the rectum receiving 100% of the prescribed dose) ≤0,5 cc, for the urethra D1 (maximum dose covering 1% of the urethra volume) ≤232 Gy.

As was mentioned above, we had real treatment plans with two types of seeds and later other plans with different type of seeds were made trying to reach similar dosimetry parameters. Table 2 summarises the parameters of planning dosimetry.

Table 2. Baseline characteristics of treatment plans: prostate volume, seed activity, number of seeds and needles

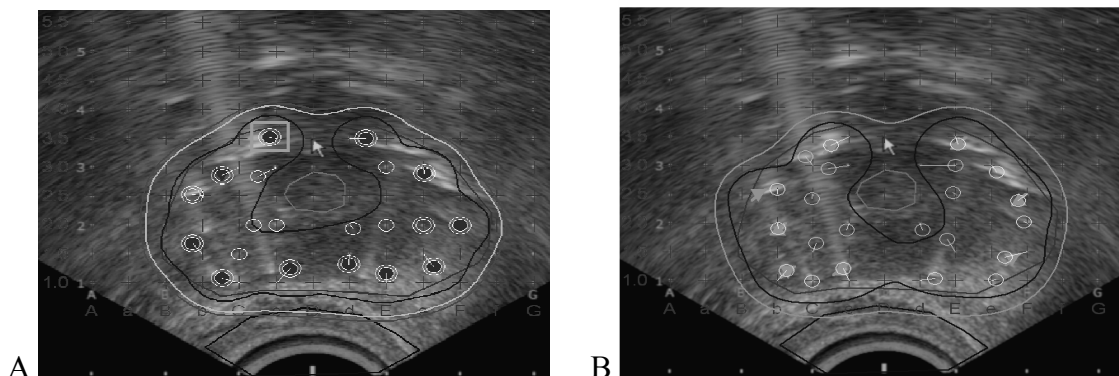
No.	Prostate volume (cc)	Seed activity (mCi)		Seed number		Number of needles	
		Linked	Strand	Linked	Strand	Linked	Strand
1	38.15	0.498	0.644	63	54	25	20
2	33.52	0.498	0.645	58	47	20	14
3	22.22	0.498	0.594	50	43	23	20
4	34.09	0.460	0.594	63	51	19	21
5	24.78	0.460	0.595	51	39	16	18
6	47.42	0.568	0.645	62	55	23	24
7	32.95	0.443	0.645	59	43	19	20
8	24.4	0.433	0.638	53	36	17	15
9	45.94	0.443	0.638	74	53	22	25
10	29.82	0.443	0.645	57	42	21	20

Table 3. Planning dosimetry parameters.

No.	Vp100% ¹		D90(Gy) ²		Vr100(cc) ³		D1(Gy) ⁴	
	Linked	Strand	Linked	Strand	Linked	Strand	Linked	Strand
1	99.59	99.76	181.35	188.51	0.21	0.25	228.28	235.01
2	99.14	99.59	181.22	177.88	0.37	0.15	196.17	201.6
3	99.86	99.94	198.07	191.74	0.09	0	208.17	229.18
4	99.4	98.43	188.87	182.88	0.34	0.38	207.3	227.52
5	98.87	98.35	191.12	181.73	0.19	0.17	216.55	223.46
6	98.44	99.5	182.39	184.34	0.4	0.1	211.45	203.58
7	98.9	99.06	189.67	178.88	0.19	0.32	208.27	223.48
8	99.93	98.69	193.2	182.21	0	0	213.12	219.11
9	98.92	99.26	182.48	183.38	0.25	0	190.89	214.51
10	98.76	99	184.7	186.65	0.23	0.19	206.87	203.91

1. Vp100 = prostate volume receiving 100% of the prescribed dose;
2. D90 = minimum dose covering 90% of the prostate volume;
3. Vr100 = rectum volume receiving 100% of the prescribed dose;
4. D1 = maximum dose covering 1% of the urethra volume.

Examples of the coverage of prostate gland using two different types of radioactive seeds are shown in Fig. 1.

**Fig. 1.** Dose coverage of prostate gland (a – strand seeds; b – linked seeds).

The lines mean different kind of dose coverage of prostate, for example, 100% of prescribed dose or 140% of prescribed dose. The manufacturing difference between these two kinds of radioactive materials is that the linked (model – STM1251) seeds are not initially connected and this process is made at the period of procedure. In this case the distances between seeds centres could be different and variable: the minimum distance between seeds could be 5 mm. However strand seeds (model – 6711) are connected by manufacture and the distance between them is fixed 10 mm, so you can't change the distance as you wish.

The planning system for seeds amount and dose distribution calculation converts source activity in mCi to the seed strength U. According to the recommendations in AAPM Report No. 21, Iodine-125 seed strength is specified as „air kerma strength“ having unit of microGray meter squared per hour, or $\mu\text{Gy}^2/\text{h}$. This unit corresponds to the dose imparted to air and is the product of the air kerma rate and the square of the distance in vacuum, in a direction perpendicular to and bisecting the long axis of the seed. For historical purposes, the strength is also stated in terms of „Apparent Activity“ having units of miliCurie (mCi). Apparent activity is determined from the stated air kerma strength using a conversion factor of 1.27 U/mCi. Both air kerma strength and apparent activity are a measure of output and not contained activity. The characterisation of the source in common use is activity. Therefore we use activity instead of strength units in our study.

3. Results

As shown in Figure 2, the most plans were made with seeds activity of 0.638– 0645 mCi, the plans with activity below 0.5 mCi reached 45%. The distribution of activity in the lower activity group is higher because the producer of linked seeds recommends seeds activity depending on the prostate volume. The volume of prostate was divided into three groups: from 20 to 30 cc, 30 – 40 cc and 40 – 50cc.

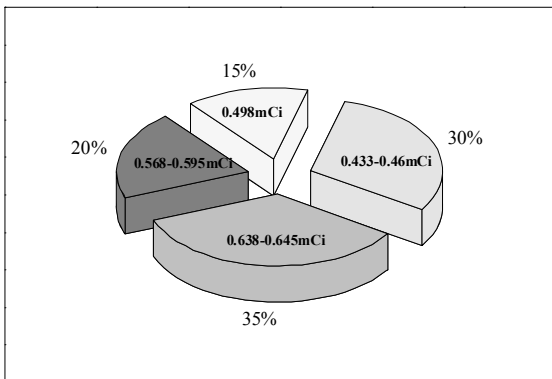


Fig. 2. Distribution of seeds radioactivity (percent)

One of the goals of this study was to compare number of seeds used in each kind of plans. Therefore, average number of seeds and needles in each volume of gland was evaluated. Figure 3 shows the average number of seeds in each volume of prostate. The average 52 seeds of lower activity were used for small volume prostate,

and 40 – higher activity strand seeds. The different between them is 12 seeds. The similar difference of seeds number is in bigger prostate group as well. It is quite big difference in seeds, however the planning dosimetry parameters, such as Vp100, D90, Vr100 and D1, are very close. This outcome gives an advantage in clinical and economical aspect

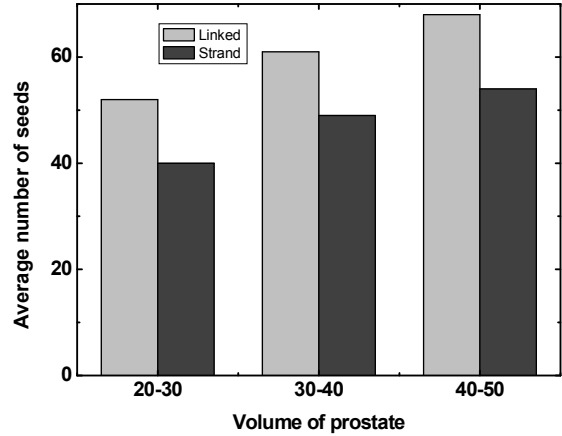


Fig. 3. The average number of seeds in each volume of prostate gland

Analyzing the number of seeds in one cc of prostate, there were found that smaller glands have bigger density of seeds, no matter it was lower or higher seeds activity (Fig.4).

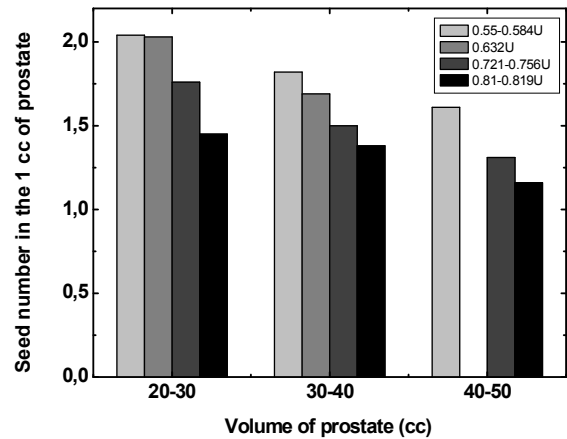


Fig. 4. Number of seeds in 1 cc of gland.

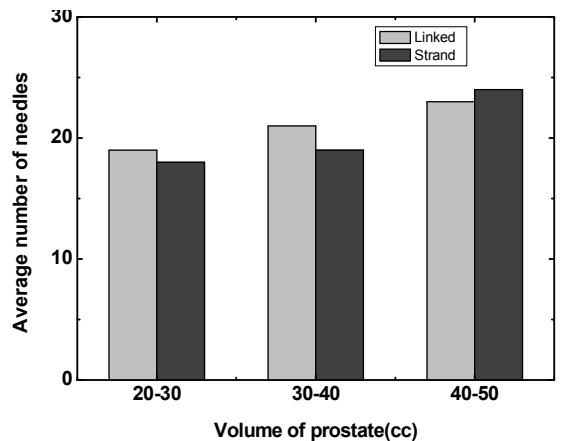


Fig. 5. The average number of needles in each volume of prostate gland.

Furthermore, the amount of needles is really important thing, because less number of needles translates into the shorter procedure time and reduces insult to patient. However, these results show small different in number of needles, only 1 – 2 needles (figure 5). It could be because we started to use the higher activity seeds recently and it needs more experience in planning.

4. Conclusion

Our analysis showed that it is possible to have good intraoperation treatment plans with higher activity seeds and it is possible to reduce amount of seeds and needles. However all these results require more precise evaluation – take more plans with each type of seeds, try to choose bigger interval between activities and to take more attention to the dose homogeneity. The next step would be comparing of the clinical results of patient after some period of implantation and evaluate the results of post implant dosimetry.

5. References

1. Giuseppina Laura Masucci, M.D., David Donath, M.D., Audrey Te' Treault-Laflame, Jean-Frank, Ois Carierr, PH.D., Yannick Hervieux, M.SC., Rene'e Xavie're Larouche, M.SC., Jean-Paul Bahary, M.D., Daniel Taussky, M.D., Comparison between high and low activity seeds for I – 125 permanent seed prostate brachytherapy, *Int. J. Radiation Oncology Biol. Phys.*, Vol. -, No. -, pp. 1–6, 2010
2. David C. Beyer, MD Fred Puente, CMD Kevin L. Rogers, MS Erdal M. Gurgose, PhD. Prostate brachytherapy: comparison of dose distribution with different I – 125 source design, *Radiology* 2001; 221:623–627.
3. Marion van Gellekom, Permanent prostate implants radiobiology and dosimetry.
4. R. Nath, L. L Anderson, G. Luxlon, K. A. Weaver, J. F. Williamson, A. S. Meigooni. “Dosimetry of interstitial brachytherapy sources: Recommendations of the AAPM Radiation Therapy Committee Task Group No. 43“ *Med. Phys.* 22, 209-303 (1984).
5. J. F. Wiliamson, B. M. Coursey, L. A. DeWerd, W. F. Hanson, R. Nath., G. Ibbot. Guidance to users of Nycomed Amersham and North American Scientific Inc. I–125 Interstitial sources: Dosimetry and calibration changes: Recommendation of the American Association Physicists in Medicine Radiation Therapy Committee and Ad Hoc Subcommittee on Low – Energy Seed Dosimetry” *Med. Phys.* 26. 570 – 573 (1999).
6. H. D. Kubo, B. M. Coursey, W.F. Hanson, R. W. Kline, S. M. Seltzer, R. E. Shuping and J. F. Wiliamson, “ Report of the Ad Hoc Committee AAPM Radiation Therapy Committee on I – 125 Sealed Source Dosimetry *Int. J. Radiat. Oncol., Biol., Phys.* 40. 697 – 702 (1998).

HEAT DISSIPATION INVESTIGATION BY THERMOVISION

Virgilijus MINIALGA, Rolandas PAULAUSKAS
Kaunas University of Technology, Physics department, Studentu st. 50, Kaunas LT-51368, Lithuania

Abstract: Heat dissipation occurs from heated area in accordance with heat diffusion law. The temperature will reduce, if there is no heat source. Heat spreads to material sides and to depth. The rate of this spread depends on conditions of thermal conductivity. Coefficients of thermal conductivity are included in temperature reduction describing equation. Materials were heated during laser’s beam exposure and temperature reduction was measured by non-contact method using thermovisor after switching-off of heating.

Keywords: Heat, temperature reduction, thermal conductivity, laser heating, thermovisor.

1. Introduction

Heat from heated area spreads in three ways: 1 - radiation, 2 - conductivity, 3 – convection. Radiation means that electromagnetic energy is emitted from the material to surrounding bodies. Conductivity is materials possibility to transfer heat through. Convection occurs when heat flows to the air (Fig. 1).

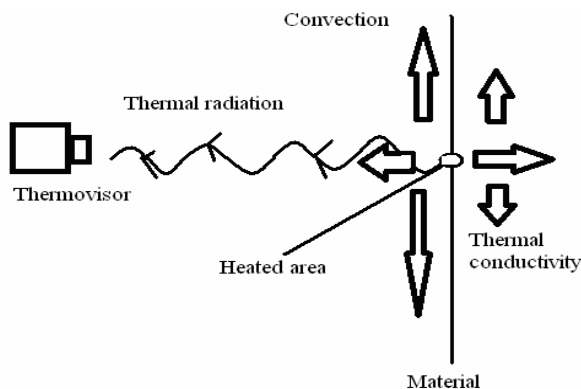


Fig. 1. The ways of heat spread from heated area.

Theoretical considerations and experimental measurements show that the main way of heat dissipation is thermal conductivity. Equation describing reduction of temperature by thermal conductivity is the following:

$$T = T_a + (T_0 - T_a) e^{\frac{-3 \lambda t}{4 c \rho d^2}}, \quad (1)$$

where T is temperature, T_a is environment temperature, λ is thermal conductivity constant, T_0 is initial temperature, c is specific heat, ρ is mass density, and d is diameter of heated zone.

The time constant τ_e of exponential reduction of temperature with time t strongly depends on thermal conductivity constant λ (2)

$$\tau_e = \frac{4 c \rho d}{3 \lambda} \quad (2)$$

Thermal conductivity constant λ is obtained from (2) by formula:

$$\lambda = \frac{4 c \rho d}{3 \tau_e} \quad (3)$$

2. Theoretical investigation

Examples from wood, ceramics, silicon, and carbon were taken for theoretical evaluations. The theoretical graphs were drawn using formula (1). Initial temperature T_0 was similar to temperature in experiment $T_0 = 300$ K. T_a was room temperature. In this investigation it was equal to 295 K. Parameters c and ρ were taken from [1, 2]. Parameter d equals to several millimeters of heated area.

Some results are presented in Fig. 2, Fig. 3, Fig. 4. Rate of temperature is the biggest in carbon examples, the second are silicon and ceramics.

Theoretical evaluation of radiation and convection influence on temperature reduction shows that the rate of these processes was much slower, therefore these processes were not taken into account because of their small contribution.

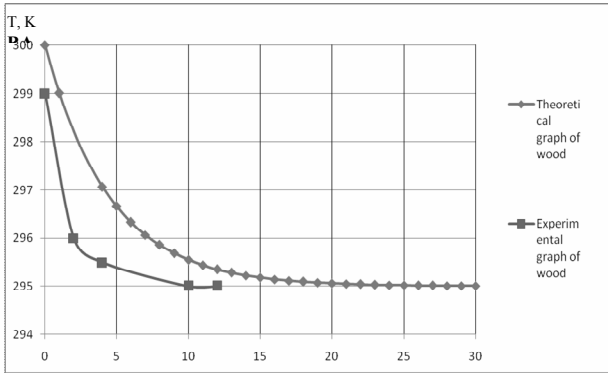


Fig. 2. Theoretical and experimental graphs of temperature reduction on the wood surface.

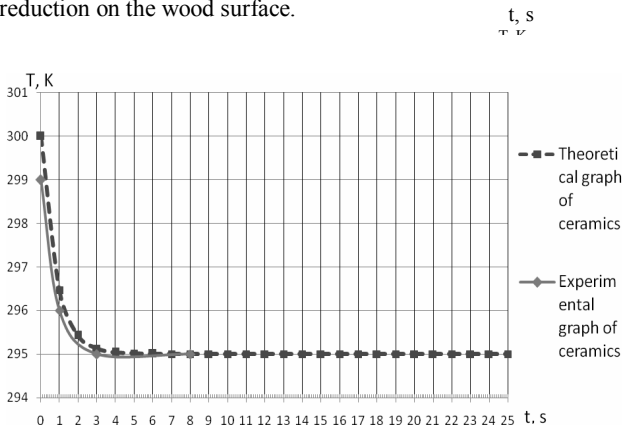


Fig. 3. Theoretical and experimental graphs of temperature reduction on the ceramics surface.

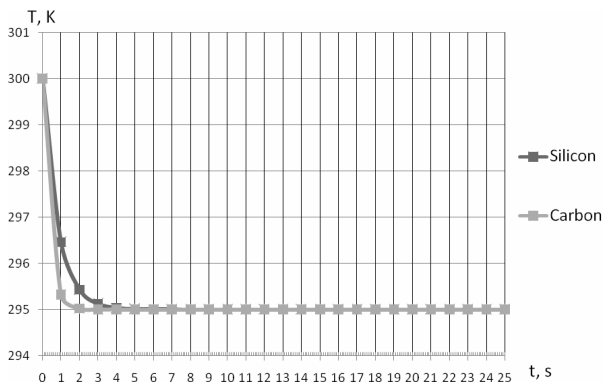


Fig. 4. Theoretical graphs of temperature reduction on the carbon and silicon surface.

3. Experimental investigations

Experimental measurements were done with wood and ceramics using thermovisor FLIR A20 (Fig.5). This device could take thermoimages and produce thermomovies of thermal radiation in 7,5 - 13μm wavelength region. Range of temperatures is -20°C -- 900°C with 2% error. The device has three changeable lenses for different distances of measurement. Thermovisor is connected to the computer over FireWare and data are saved as images or movies using ThermoCam Research Lab PRO 2.8 software.



Fig. 5. Thermovisor FLIR A20.

Three ways for heating surface area during the investigation were discussed. These ways are:

- a) Heating of surface by powerful laser beam;
- b) Temperature increase after hammer impact;
- c) Touching and contact heating.

The investigated materials were heated with 100mW laser in the first way (Fig. 6).

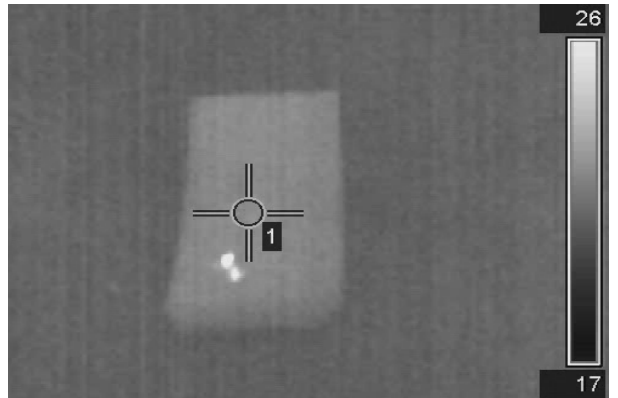


Fig. 6. Thermoimage of the wood heated by laser.

The white areas in Fig. 6 are laser beam heated places on the surface of object 1. The object is wooden board which was heated during ~ 10s laser beam exposure.

The measurements were repeated with the same materials but in the other way. The heat was given to the object by mechanical impact with hammer.

The kinetic energy was transformed into thermal energy so the heat was transferred additionally from the wood to the ground after impact as it is seen in Fig. 7.

Heated areas on the ground are bright places in the center part of thermoimage. The object 1 was moved to the right side of Fig. 7 after strong hammer impact. The white area of object 1 surface means the most heated place.

Mechanical impact could create a wider heated area in comparison with laser beam on the surface of material under investigation, but this impact could damage the material, for example break the bone in medical treatment.

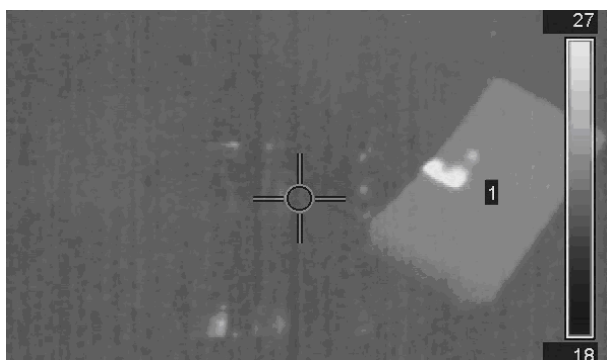


Fig. 7. Thermoimage of the wood after hammer impact.

The similar view is seen in thermoimage of human's body: the bruise area has higher temperature than other tissues.

The other way of measurement was to put close together two objects having different temperature. The heat was transferred from the hot material to the cold one because of heat diffusion (Fig. 8).

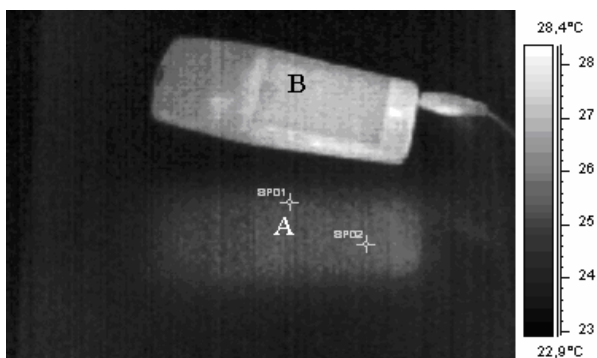


Fig. 8. Thermoimage of transferred heat to material's surface.

The area A is heated surface under investigation after contact with object B which has higher temperature. Difficulty of this way is the necessity of massive heated body. It should have good contact with object under investigation. This process takes long time comparing with earlier mentioned processes. Also the narrow places are not accessible for such heating.

The best way of these mentioned ways is heating by laser because of possibility to heat narrow places, to control laser beam's output power, direction and diameter. Therefore almost all experiments were carried out using laser heating.

Experimental graphs (Fig. 2, Fig. 3) were drawn using data from thermoimages of wood and ceramics. Investigated objects were heated for a short time by laser and the reduction of temperature was observed using thermovisor FLIR A20.

4. Results and discussions

The two different curves in Fig.2 correspond to different thermal conductivity for wood: evaluated theoretically experimentally. Similar changes of curves (Fig.3) show that thermal conductivity for ceramics is identical for theoretical model and for experimental sample. These measurements show that theoretical parameters have

been chosen identical to experimental samples. The parameters could be chosen more accurately in the case of Fig.2. Laser heating has the advantages in medical applications because of possibility to avoid infection and reach narrow places.

On the other hand the beam output power could damage surface of object under investigation in case of very powerful laser. This possibility is illustrated in Fig.9. Bright spot indicates laser beam and white circled area shows damaged surface.

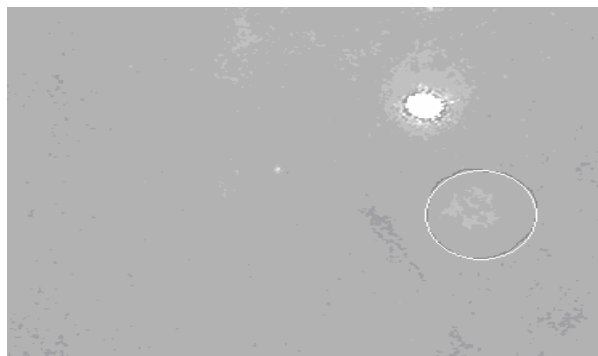


Fig. 9. Laser beam on material and circled area is damaged surface.

5. Conclusions

The best way of three investigated methods for heating object was laser heating. The possibilities to avoid infection and reach narrow places in medical applications are the main advantages of this method. Theoretical evaluation and thermovision investigation of laser heated material surfaces temperature reduction show that the main way of heat dissipation is conductivity. Thermal conductivity of real material can be calculated using experimental graphs of temperature reduction of heated area in time.

This method allows non-contact investigation of material thermal properties that is necessary for thin tissues and hard accessible places. Sometimes laser beam can damage the material's surface under investigation like body tissues, so it is important to take attention to laser's output power.

6. Acknowledgment

Authors acknowledge the Mechatronics Centre for research, studies and information at Kaunas University of Technology for the ability to use thermovisor FLIR A20 and notebook software.

7. References

1. <http://www.deltat.com/pdf/physical%20properties%20of%20materials.pdf>
2. http://www.engineeringtoolbox.com/thermal-conductivity-d_429.html

PATIENTS' DOSE ASSESSMENT IN DIGITAL DIAGNOSTIC RADIOGRAPHY

Rita PIKAITĖ*, Jurgita LAURIKAITIENĖ**, Diana ADLIENĖ*

*Kaunas University of Technology, Lithuania, **Kaunas Medical University Hospital, Lithuania

Abstract: Patients' irradiation doses during X-ray diagnostic examination procedures must be as low as reasonable possible, but sufficient for the diagnostics of diseases. The implementation of a new digital X-ray technique causes changes of the collective dose from medical exposures and absorbed dose to patients.

Doses received by patients during digital X-ray chest examinations (anterior and lateral projections) using a digital X-ray machine AXIOM MULTIX MP have been measured by DAP-meter and dose dependencies on patient's physical parameters (weight and size) investigated. It was shown that the dose area product depends exponentially on the patient's size. Optimization of the X-ray examination procedures for the individual patients is discussed on the basis of the obtained results.

1. Introduction

The benefits to mankind from medical x-ray diagnostic procedures in the past few decades have been substantial and the practice of modern medicine is highly dependent on their use. X-ray diagnostics is a medical procedure to get diagnostic view of testing field. There are ordinary and digital radiography. Ordinary X-ray image is obtained on the X-ray film and digital image is obtained on a computer screen. In the digital radiography the X-ray machine is installed in a close system, which uses digital technology to transform the detected X-radiation to digital image. Increasing of X-ray diagnostic techniques in the last years and implementation of new, mainly digital technologies cause the increasing of number of the X-ray examinations and influence collective dose from medical exposures over the world [1].

Doses received by patients are measured in different ways. Measurements depend on the available equipment and the method of the patients investigation. Anyhow the irradiation dose to patients should be as small as possible, but provide all necessary information about the investigated object.

One of the most important problems in the X-ray diagnostics is dosimetry. According to the registered dose a degree of risk for a patient could be evaluated. The absorbed dose to patient could be measured by various calorimetric, chemical, photographic, scintillation, thermoluminescent, semiconductor, ionization and other dosimeters, taking into account that

the accuracy of the dose registration depends on the measurement method.[2].

X-ray chest examination is most common diagnostics procedure in Lithuania and in the world, since the lung cancer is most common disease among men in many countries. 1200 new lung cancer cases are being determined every year in Lithuania. Because of the need and importance of lung radiography, the X-ray chest examination procedure was chosen for this investigation

2. Measurements

A group of randomly selected male patients undergoing X-ray examinations in the chest region was chosen for the dosimetric investigation. Doses to patients during 126 procedures have been measured. 86 procedures of them were X-ray chest examinations. Three examinations are possible in the chest X-ray radiography: a frontal plane (KL PA) radiography and side projection radiography (KL LAT) for the right and the left side

All investigated patients were weighted and their size was measured. The weight of the most analyzed patients was from the range of 61-70 kg. Standardized patient (an adult) weight is 60-80 kg.

X-ray chest examinations of patients were performed by digital X-ray machine AXIOM MULTIX MP with the integrated flat panel detector, which converts X-ray images to the digital data and sends them to the PC (Fig.1).

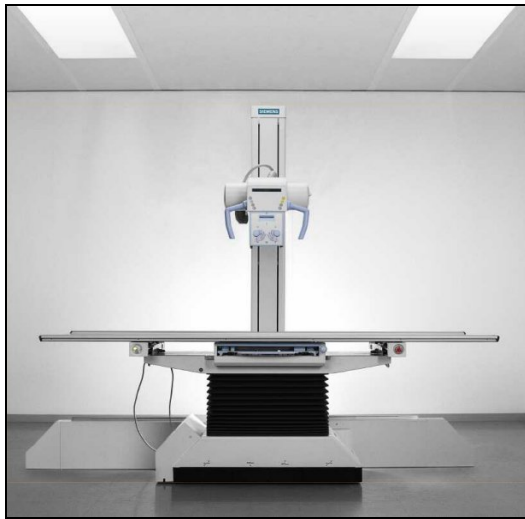


Fig. 1. Digital X-ray machine "AXIOM Multix MP"

The machine automatically adjusts the settings according to the chosen voltage, which depends on the area of the investigation (e.g chest radiography -125 kV, spine – 75 kV). Selected voltage was the same for the same region of the investigation regardless of the physical parameters of the patients. Adjusted parameter was exposure (mAs). It was dependent on the patient's parameters.

Dose-area product meter Diamentor 4M (PTW, Germany) was used for the dose measurements. Obtained dose area product values were used for the evaluation of the surface entrance doses received by patients [3]. Evaluated values were compared to those measured using TLD [4].

3. Results

Recommended surface entrance doses received by patient during chest x-ray examination are: 0.6 mGy or 0.2 Gy cm^2 (single PA exposure) and 1.7 mGy or 0.3 Gy cm^2 (single LAT exposure) [5]. Dose values are dependent on patient's physical parameters (weight, thickness).

The increasing tendency of the DAP values with the increased patient's thickness was observed. After the evaluation of the results it was found that this tendency was exponential one (Fig. 2) and was in accordance with the results discussed in the paper of T. Kiljunen et al [6].

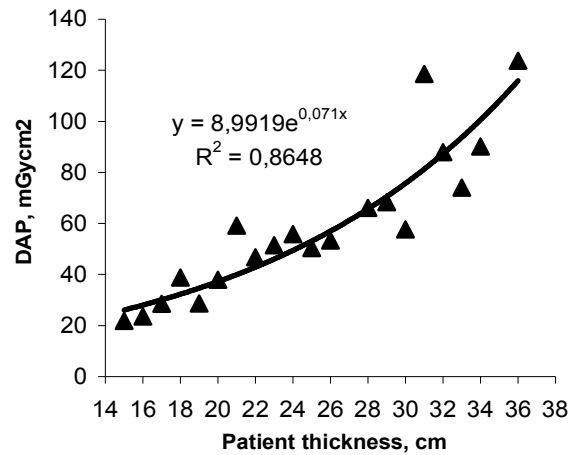


Fig. 2. Dose-area product versus patient's thickness

Since the X-ray tube voltage is set as a standard parameter for standard X-ray examination, the main parameter related to the patient's biometric data is exposure (mAs). The thicker is the patient, the higher is exposure: current strength and exposure time.

During the lung X-ray examinations higher exposure is applied when a patient is examined in LAT projection, as compared to the exposure in AP projection. The higher exposure corresponds to the higher dose received by patient. Measurement results on DAP variations for different patients exposed in KL AP and in KL LAT projections are provided in Fig. 3.

It is clearly seen that the doses to patients for KL LAT irradiation projection higher. This corresponds to the fact, that the thickness of patient in lateral projection is larger as in the case of front irradiation.

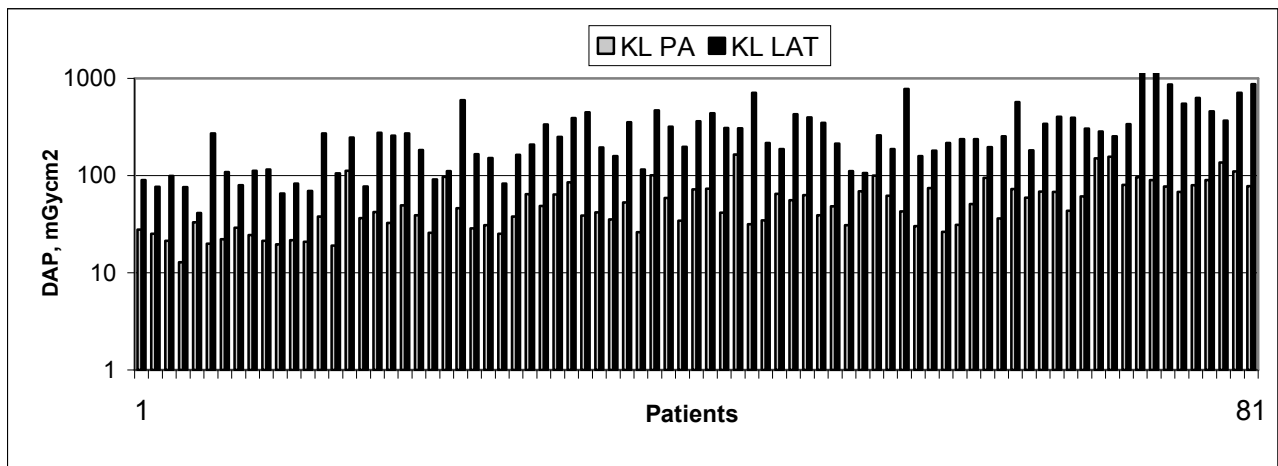


Fig. 3. Measured DAP values for patients exposed in two different thoracic projections

It is clearly seen that the doses to patients for KL LAT irradiation projection higher. This corresponds to the fact, that the thickness of patient in lateral projection is larger as in the case of front irradiation.

Intercomparisson of the dose measurements was performed together with Radiation Protection Centre of Lithuania, using both: DAP meter and TLD's. Intercomparisson results are presented in Fig.4.

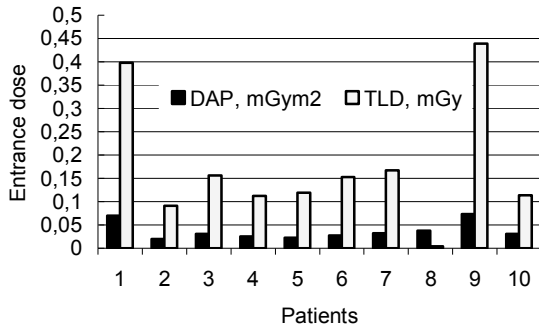


Fig. 4. Data obtained from the two dosimeters DAP, meter and thermoluminescent dosimeters

The same tendency of dose variations was observed using both methods of measurement. Some discrepancies (patient No.1 and patient No.9) in measured values could be attached to the not accurate positioning of Tlthermoluminescent dosimeter on the patient's surface.

4. Conclusions

Dose to the patient using digital X-ray diagnostics equipment is lower then in the case of conventional X-

ray examination. Exposure doses depend on the patient's biometric data (weight, thickness) and tend to increase exponentially with an increase of patient's thickness.

5. References

1. National collection of local diagnostic reference levels in Norway and their role in optimization of X-ray examinations/Eva Godske Friberg*, Anders Widmark and Ingrid Helen Ryste Hauge//Norwegian Radiation Protection Authority, P.O. Box 55, N-1332 Østerås, Norway.
2. Comparison of four methods for assessing patient effective dose from radiological examinations / N. Theocharopoulos, K. Perisinakis, J. Damilakis, H.Varvelis/
3. Measurements of skin entrance exposure with a dose-area-product meter at chest radiography / Cindy K. Parry, Robert Y. L. Chu, Bob. G. Eaton, Ching-Yuan Chen // Radiology. – Vol. 201, 1996, p. 574-575
4. Burinskienes V. Master's Work / Peculiarities of patient's dose evaluation using flat ionization chamber in X-ray diagnostic/2007
5. 2008-12-30 RSC Direktorius įsakymas Nr. 84 "Dėl rekomenduojamųjų rentgeno apšvitės lygių patvirtinimo. (in Lithuanian)
6. Diagnostic reference levels for thorax X-ray examinations of paediatric patients / T. Kiljunen, H. Jarvine's. Savolainen // British Journal of Radiology, 80 (2007), p. 452-459

RADIATION IMPACT ON POLYMER STRUCTURES

Algimantas MEŠKAUSKAS, Gediminas ADLYS, Simona MAČIULAITIENĖ
Kaunas University of Technology, Lithuania

Abstract: A sample of commercial semicrystalline polyethylene (PE), with the estimated crystallinity of 10% to 73%, was structurally characterized using constant wavelength X-ray powder diffraction. Degree of crystallinity and intermolecular distance of the amorphous component were measured for permeable samples. Changes in the crystalline orientation have been related to the load-extension curve. This was altered by changing the molecular weight, concentration of branches and strain rate. Structural changes of the polyethylene under exposure to cosmic radiation for a long time period have been investigated. Radiation induced changes and possibility to modify the properties using gamma source are discussed

Keywords: Radiation, Polymer, Polyethylene, XRD, GIXRD.

1. Introduction

Irradiation is an established tool for modifying the structure and properties of polymers [1, 2]. Modification possibility of polymers attracts growing interest [3, 4] due to the potential technological application of the modified polymers. Irradiation of the polymers generally leads to a radiation damage and modification of the surface and bulk properties of [5, 6]. This modification is the consequence of irreversible reaction mechanisms in polymers owing to processes like main chain scission, intermolecular cross-linking, creation of unsaturated bonds and emission of atoms, and molecules etc..

The overall picture of polyethylene bulk may be divided into two regions. In one region there is a high degree of disorder which is associated with the presence of a large number of structural defects. In the second region only a small number of defects are found. This region gives the structure a sufficiently high degree of order to enable the term "crystalline" to be applied.

The two regions are separated by a "semi-ordered" nematic zone where the level of disorder is intermediate. The basic techniques of infrared spectroscopy and x-ray diffraction have been used in the present work to determine the effect of electric fields on the morphology of LDPE and highly crystalline polyethylene.

The present work has been carried out to study the comparative influence of UV and hard electromagnetic radiation on the crystalline and optical properties of polymer materials. The effects induced by hard electromagnetic radiation have been investigated through the measurement of the degree of amorphization and crystallinity of polymers and

estimation of the crystallite size. When this powerful tool is applied to the organic materials, especially polymers, the actual challenge occurs due to the destruction of the specimens resulted from the irradiation damage by hard electromagnetic radiation.

2. Instruments and methods

X-ray diffractometer (Cu K_{α} radiation source) has been used in fixed θ of glancing angle incidence for 2θ scan (GIXRD) in depth profiling and conventional Bragg-Brentano geometry (θ - 2θ scanning) for wide scan. In conventional diffraction geometry the diffraction slit, Soller slit and receiving slit widths were 1° , 1° and 0.15min , respectively, and the scanning step was 0.01° . To avoid the direction influence when measuring crystal grains specimen rotation attachment has been used. The XRD measurements reported here were carried out using modified diffractometer (DRON-3M). Conventional X-ray diffraction (Fig.1.) can only reveal average structural characteristics such as lattice parameters for the investigated specimen and the diffraction is observed only from the planes parallel to the surface.

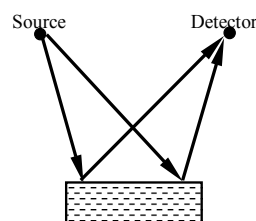


Fig.1. The experimental set up used for the measurement of diffraction patterns by conventional (B-B) geometry.

However in GIXRD (Fig. 2), the Bragg reflections originate from the crystals planes inside the sample and not parallel to its external surface, unlike in conventional Bragg–Brentano geometry where the incident angle θ is fixed and 2θ is rotating on a goniometer circle.

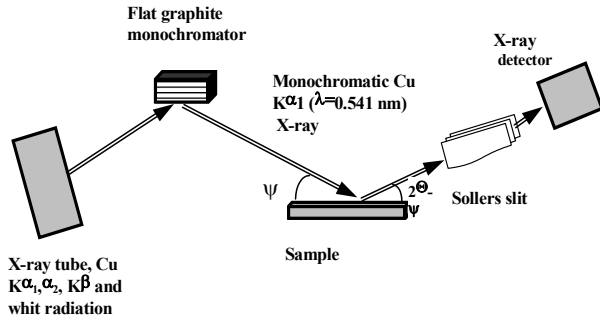


Fig.2. The experimental setup used for the measurement of diffraction patterns in grazing-incidence mode (GIXRD).

In the conventional $\theta/2\theta$ geometry [standard Bragg–Brentano (B-B) geometry], a parafocusing arrangement is used where the X-ray source and the detector slit are at the focal points of the incident and diffracted beams, respectively. For thin film arrangement, the incident and diffracted beams are made nearly parallel by means of a narrow slit on the incident beam and a long Soller slit on the detector side. In addition, the stationary incident beam makes a very small angle with the sample surface (typically 1° to 3°), which increases the path length of the X-ray beam through the film). This geometry is also referred to as asymmetric Bragg geometry.

A Ceylon graphite (002) reflection ($d_{hkl}=3.345 \text{ \AA}$, for Cu-K α - $\Theta=13.31^\circ$) monochromator was available for the incident beam in this work, and thus only the diffracted beam was collimated by a verticals Soller-slit assembly. The spectral resolution was usually reduced in this mode as compared with a focusing Bragg–Brentano geometry,

If the incident angle (α_i) is larger than the incident critical angle (α_c) of the material, the X-ray penetration depth changes very rapidly. If $\alpha_i > \alpha_c$ the refracted beam passes into the film and the diffraction from the near surface region is observed. If $\alpha_i \gg \alpha_c$ the refracted beam penetrates through the sample into the interface layer or substrate. This critical angle can be calculated for any material:

$$\alpha_c = (2.6 \times 10^{-6} \rho \lambda^2)^{1/2} \quad (1)$$

where ρ is the density in kilogram per cubic meter and λ is the wavelength of incident X-rays in Angstroms.

The X-ray beam penetration depths τ are calculated for each value α (since the depth changes for each α value) according to the following formula:

$$\tau = \frac{\cos \psi [\sin^2 \theta - \sin^2 (\theta - \alpha)]}{2\mu \cdot \sin \theta \cdot \cos (\theta - \alpha)} \quad (2)$$

where Ψ is the tilting angle; θ —the Bragg angle; α — X-ray beam incidence angle; μ —the absorption coefficient of the irradiated material corresponding to the applied X-ray wavelength. An example of the penetration depth variation with respect to the angle α of 2500 μm thick specimen is provided in figure 3.

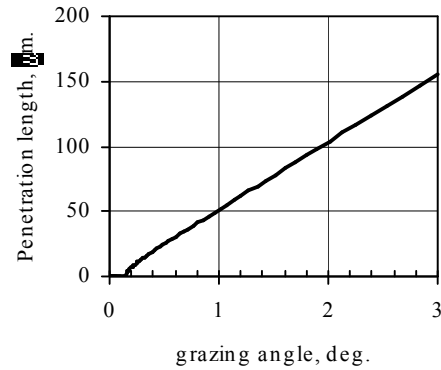


Fig.3. Penetration depth as a function of α angles

In GIXD geometry, the incident X-ray beam impinges on the surface at small angles ($<3^\circ$) of incidence.

The absorption function $\tau(z, \alpha)$ describes the attenuation of the incident wave and of the diffracted wave. For grazing incidence angle, it is expressed as:

$$\tau(z, \alpha) = \frac{4\pi B(\alpha)}{\lambda} + \frac{\mu}{\sin \beta} \quad (3)$$

where μ is the linear absorption coefficient and β is the angle between the diffraction beam and the sample surface, which is defined as: $\beta=2\theta-\alpha$.

$B(\alpha)$ is defined as:

$$B(\alpha) = \frac{1}{\sqrt{2} \left[\left(\alpha^2 - \alpha_c^2 \right) + 4\beta_\alpha^2 \right]^{1/2} - \left[\alpha^2 - \alpha_c^2 \right]^{1/2}} \quad (4)$$

Since rather broad spectral features are found in the polyethylene films, the reduced resolution does not present a major limitation for this work. A higher resolution is difficult to achieve with a laboratory setup, at least not within a reasonable time frame for the spectral acquisition process.

In basic theory related to isotropic two-phase systems it is stated that the scattering intensity is proportional to the Fourier transform of the autoconvolution of the electron-density profile, $\rho(r)$ as follows:

$$I = F(\Delta\rho^{*2}) \quad (5)$$

where symbol F means a three-dimensional Fourier transform, $\Delta\rho$ is the difference between the local and average electron density, and superscript *2 stands for the autoconvolution. When the ideal sharp profile of electron density is obtained due to the interface of two phases, the I values could be obtained from the Porod’s law. This law predicts the decreasing tendency of the intensity proportional to q^{-4} for large q values:

$$\lim_{q \rightarrow \infty} [I(q)] = \frac{K_p}{q^4} = I_p(q) \quad (6)$$

where q is the scattering vector:

$$q = (4\pi / \lambda) \cdot \sin(\theta/2),$$

λ is the wavelength of the incident X-ray beam, θ is the scattering angle, $I(q)$ is the observed scattering intensity, K_p is the so-called Porod-law constant, $I_p(q)$ is the Porod-law intensity.

3. Results

The absorption property of polymers exposed to X-rays is not high. Due to this, the reflection of the X-rays from the experimental samples has been investigated. In the present work initially unexposed 0.2 mm thick polyethylene fiber composite samples were investigated. The composite was fabricated by compaction of extended chain UHMWPE fibers under high pressure without any extraneous binder. The samples were exposures to the cosmic radiation X-ray diffractogram of LDPE (Fig.4), indicates characteristics peaks at 21.5° and 23.8° of 2θ scale.

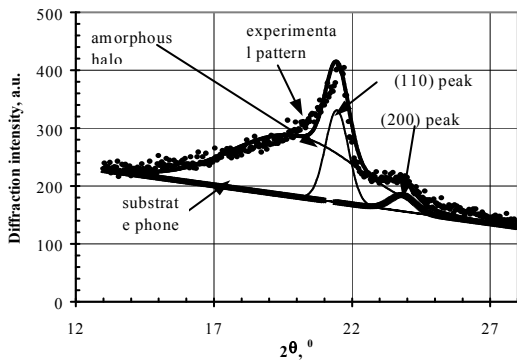


Fig. 4. Typical X-ray diffraction spectrum of polyethylene

X-ray diffractogram could be used for the evaluation of the sample crystallinity degree according to the formula (2)

Synthetic polymers almost never occur as single crystals. The diffraction pattern from polymers is almost always either a "powder" pattern (polycrystalline) or a fiber pattern (oriented polycrystalline).

The results presented in Fig.5 show that analysis of the shape and angular position of the amorphous halo in WAXS patterns of semicrystalline polymers is a sensitive and fruitful method for obtaining information on the amorphous phase's structure.

The integrated XRD intensity corresponds to the volume fraction crystallinity, ϕ_c . Other techniques such as density gradient columns (see Campbell and White or DSC) correspond to a mass fraction crystallinity ψ_c . The two fractions are related by the density ratios, where ρ_c is the crystalline density, ρ is

the bulk sample density and ρ_a is the amorphous part density,

$$\psi_c = \frac{\phi_c \cdot \rho_c}{\rho} \quad \text{and} \quad (1 - \psi_c) = \frac{(1 - \phi_c) \cdot \rho_a}{\rho} \quad (7)$$

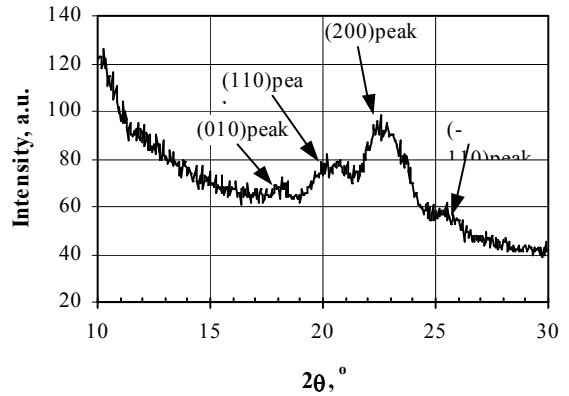


Fig. 5. X-ray diffraction pattern of polyethylene exposed to cosmic radiation

The peak at $2\theta = 21.11^\circ$ in diffraction pattern of the sample indicates the amorphous nature of the polymer. It was found that the diffraction intensity of polymer samples decreases after their long term exposure to cosmic rays. The increased intensity indicates the decrease in the amorphous nature of the polymer. The highest intensity peak was found to be shifted towards the small angles after the exposure (Fig.6a). It could be assumed that the diffraction peak occurs at about 0.2 degrees! This implies that the lattice parameters are changed during the irradiation of polyethylene.

If the time of measurement is long enough the X-ray diffraction could be observed from regularly spaced lamellae at very small angles using x-rays.

Small-angle x-ray scattering is a primary technique to describe the colloidal scale structure of such stacked lamellae. Since the lamellae are 2-D objects, a small angle pattern is multiplied by q^2 with the purpose to remove this dimensionality (Lorentzian correction) and the peak position is measured: $q = 4\pi/\lambda \sin(\theta/2)$, where q is the scattering angle. Bragg's law can be used to determine the period of crystalline structure: $L = 2\pi/q^*$. In some cases the X-ray data are being Fourier transformed to obtain a correlation function for the lamellae which indicate an average lamellar profile as it is shown in figure 6b.

The first broad diffraction peak corresponding to the period of 31.5nm is a distance between the polymeric fiber and 15.8 nm line corresponds to the crystal fiber layer thickness.

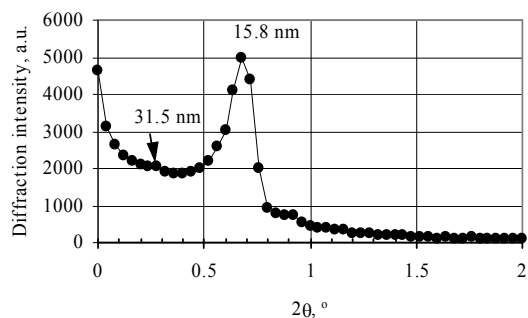


Fig. 6a. Experimental GISAXS measurement

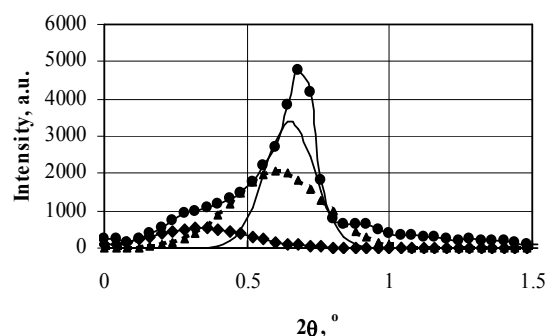


Fig. 6b. Theoretical fitting data

4. Conclusions

Polyethylene samples have been investigated after their long term exposure to cosmic rays. Observed changes in the crystalline orientation have been related to the exposure doses. It was found that the direct exposure to cosmic rays increase the crystallinity of polyethylene structure.

5. References

1. Sangeeta Prasher, Meenakshi Narwal, Shaveta Rana, and Mukesh Kumar, A Comparative Study on the Influence of IR Radiations to Some Polymers, Asian Journal of Chemistry Vol. 21, No. 10 (2009), S216-219.

2. Cristina-Delia Nechifor, Dana-Ortansa Dorohoi, Constantin Ciobanu, The Influence of Gamma Radiations on Physico-Chemical Properties of Some Polymer Membranes, Rom. Journ. Phys., Vol. 54, Nos. 3-4, P. 349-359, Bucharest, 2009.
3. T. Noon and D.K. Das-Gupta, Orphological Changes in Polyethylene Under Electrical Stress, (0-7803-3851 -0) 1997 IEEE Annual Report - Conference on Eiectrical Insulation and Dielectric Phenomena, Minneapolis, October 19-22, 1997.
4. Li Yin, Jianfeng Chen, Xiaoni Yang, Enle Zhou, Structure Image of Single Crystal of Polyethylene, Polymer 44 (2003) 6489-6493
5. L. Fontana, Diep Q. Vinh, M. Santoro, S. Scandolo, F. A. Gorelli, R. Bini, and M. Hanfland, High-pressure Crystalline Polyethylene Studied by X-Ray Diffraction and ab initio Simulations, PHYSICAL REVIEW B 75, 174112, 2007.
6. A. Aji,y S. Elkoun and X. Zhang, Biaxial Orientation Characterization in Pe and Pp Using WAXD X-Ray Pole Figures, FTIR Spectroscopy, and Birefringence, Journal of Plastic Film & Sheeting, VOL. 21—APRIL 2005
7. J. Majewski, T. L. Kuhl, K. Kjaer, M. C. Gerstenberg, J. Als-Nielsen, J. N. Israelachvili, and G. S. Smith, X-ray Synchrotron Study of Packing and Protrusions of Polymer-Lipid Monolayers at the Air-Water Interface, 1469 J. Am. Chem. Soc. 1998, 120, 1469-1473.
8. Yao Xua,1, Zhihong Lia, Wenhao Fana, Dong Wua, Yuhan Suna, Lixia Rongb, Baozhong Dongb, Density fluctuation in silica-PVA hybrid gels determined by small-angle X-ray scattering, Applied Surface Science 225 (2004) 116-123.
9. C. Pesqueraa, F. Gonzá'leza, C. Blancoa, L. Sanchezb, Synthesis and characterization of lanthanum incorporated mesoporous molecular sieves, Applied Surface Science 238 (2004) 320-323

PHYSICAL ASPECTS OF NEUTRON GENERATION IN MEDICAL ACCELERATORS

Gediminas Adlys
Kaunas University of Technology

Abstract: Neutron and proton separation energies as threshold energies of photonuclear reactions were calculated for typical materials used in medical accelerators and for radiation technologies. The values of nucleon binding energies in nucleus are defined within the range from 2.224 MeV for ^2H nuclide to 17.5 MeV for ^{13}C isotope are comparable to the energies of electrons produced in medical accelerators. The photo-neutron yield depends on neutron separation energy of nuclide and on natural isotopic composition of the element.

Keywords: nucleon separation energy, photonuclear reaction, photo-neutron and photo-proton generation, medical accelerators.

1. Introduction

Linear accelerators have evolved over the last decades to powerful devices having increasing role in medicine. Linear accelerators are used for generating both high-energy X-ray and electron beams for the treatment of tumours.

The maximum photon energy in linear accelerators can vary between 6 to 25 MeV. When the photons have energies above 10 MeV, they can interact with the atomic nuclei of the high-Z materials, which constitute the target and the head of the accelerator, and neutrons and protons can be ejected. Consequently, it is important to know the threshold energies of photo-neutron and photo-proton emissions from various materials.

The therapeutic beams with energies of over 10 MeV induce both photonuclear and electronuclear reactions. Different activation processes are likely to occur in products irradiated with high – energy photons or electrons. There are two direct processes: photo-proton (γ, p) and photo-neutron (γ, n) reactions. The remaining process is a neutron capture reaction after release of a neutron by a photo-neutron reaction [1].

Consequently as a result of these reactions undesirable radioisotopes and fast neutrons are produced. The main sources for photo-neutrons in a linear accelerator head are high atomic number components, including target, primary collimator, secondary collimators, wedges, blocks and multi-leaf collimators. These material include the lead (Pb), used as shielding in the collimator, tungsten (W) target used for the production of X-rays and iron (Fe) in the accelerator head [2].

The majority of the ejected neutrons reach the concrete walls of the accelerator bunker [3]. The neutron

production yield is related to the type of the beam, i.e. the cross-sections of photonuclear reactions are about three orders of magnitude greater than those for electronuclear reactions in the energy range of the therapeutic beams. Therefore, the neutron production is significantly higher for the therapeutic X-ray beams. The production of photo-neutrons may result in an additional irradiation of the patient [4] and exposure to the medical staff during treatments outside the treatment room due to the leakage neutron and photon radiation. Irradiation of personnel is possible also in treatment rooms due to the gamma and beta radiation emitted by decaying activation products [5].

At accelerator facilities, walls, floors and ceilings surrounding beam lines are exposed to secondary particles during machine operation and various radionuclides, such as ^3H , ^{22}Na , ^{54}Mn , ^{60}Co and ^{152}Eu , are produced and accumulated in the concrete. Quantitative estimation of these nuclides is important for radioactive waste management in the reconstruction or for evaluation of the decommissioning conditions of accelerator facilities [6, 7].

Natural isotopic abundance of elements is shown in a Table 1 [8].

2. The evaluation method

For photons with energies above the typical binding energy of nucleons, photonuclear interaction generally leads to emission of photo-neutrons as well as photo-protons. Absorption of the incident photons excites the nucleus to a higher discrete energy state, and the extra energy is emitted in the form of neutrons or protons.

The probability of neutron or proton emission depends on the last neutron or proton binding energy in nucleus.

Table 1. Natural abundance of elements

X	Isotope (natural abundance, %)
H	¹ H (99.985), ² H (0.015)
B	¹⁰ B (19.8), ¹¹ B (80.2)
C	¹² C (98.89), ¹³ C (1.11)
N	¹⁴ N (99.634), ¹⁵ N (0.366)
O	¹⁶ O (99.762), ¹⁷ O (0.038), ¹⁸ O (0.2)
F	¹⁹ F (100)
Na	²³ Na (100)
Mg	²⁴ Mg (78.99), ²⁵ Mg (10), ²⁶ Mg(11.01)
Al	²⁷ Al (100)
Si	²⁸ Si (92.23), ²⁹ Si (4.683), ³⁰ Si (3.087)
P	³¹ P (100)
S	³² S (95.02), ³³ S (0.75), ³⁴ S (4.21), ³⁶ S (0.02)
Cl	³⁵ Cl (75.77), ³⁷ Cl (24.23)
K	³⁹ K (93.2581), ⁴⁰ K (0.0117), ⁴¹ K (6.7302)
Ca	⁴⁰ Ca (96.94), ⁴² Ca (0.647), ⁴³ Ca (0.135), ⁴⁴ Ca (2.09), ⁴⁸ Ca (0.187)
Ti	⁴⁶ Ti (8.25), ⁴⁷ Ti (7.44), ⁴⁸ Ti (73.72), ⁴⁹ Ti (5.41), ⁵⁰ Ti (5.18)
Cr	⁵⁰ Cr (4.345), ⁵² Cr (83.789), ⁵³ Cr (9.501), ⁵⁴ Cr (2.365)
Mn	⁵⁵ Mn (100)
Fe	⁵⁴ Fe (5.845), ⁵⁶ Fe (91.754), ⁵⁷ Fe (2.119), ⁵⁸ Fe (0.282)
Co	⁵⁹ Co (100)
Ni	⁵⁸ Ni (68.077), ⁶⁰ Ni (26.223), ⁶¹ Ni (1.14), ⁶² Ni (3.634), ⁶⁴ Ni (0.926)
Cu	⁶³ Cu (69.17), ⁶⁵ Cu (30.83),
Zn	⁶⁴ Zn (48.63), ⁶⁶ Zn (27.9), ⁶⁷ Zn (4.1), ⁶⁸ Zn (18.75), ⁷⁰ Zn (0.62)
Mo	⁹² Mo (14.84), ⁹⁴ Mo (9.25), ⁹⁵ Mo (15.92), ⁹⁶ Mo (16.68), ⁹⁷ Mo (9.55), ⁹⁸ Mo (24.13), ¹⁰⁰ Mo (9.63)
Sn	¹¹² Sn (0.97), ¹¹⁴ Sn (0.66), ¹¹⁵ Sn (0.34), ¹¹⁶ Sn (14.54), ¹¹⁷ Sn (7.68), ¹¹⁸ Sn (24.22), ¹¹⁹ Sn (8.59), ¹²⁰ Sn (32.58), ¹²² Sn (4.63), ¹²⁴ Sn (5.79)
Ta	¹⁸¹ Ta (99.988)
W	¹⁸⁰ W (0.12), ¹⁸² W (26.5), ¹⁸³ W (14.31), ¹⁸⁴ W (30.64), ¹⁸⁶ W (28.43)
Pb	²⁰⁴ Pb (1.4), ²⁰⁶ Pb (24.1), ²⁰⁷ Pb (22.1) ²⁰⁸ Pb (52.4)

Masses of all nuclei are somewhat smaller than the sum of the masses of the N neutrons and Z protons contained in them. The mass difference is

$$\Delta m = Z m_p + N m_n - M_A, \quad (1)$$

where m_p the mass of free proton, m_n is the mass of a free neutron and M_A is the mass of the nucleus. Number of nucleons (mass number) is $A = Z + N$.

When Δm is expressed in energy units, this energy is known as a binding energy of the system, since it

represents the amount of energy keeping the particles in nucleus together.

The binding energy of a nucleus with Z protons and N neutrons $B(A, Z)$ is the energy needed to separate all the nucleons and end up with free protons and neutrons. According to the Einstein's theory, the difference of the the nucleus mass M_A and the sum of the masses of its protons and neutrons is equal to its binding energy:

$$B(A, Z) = [Z m_p + N m_n - M(A, Z)]c^2 \quad (2)$$

Frequently mass and energy are given by the same unit and in that case the factor c^2 in equation can be left out; On the other hand, when a nucleus is created from A nucleons, $B(A, Z)$ is equal to the energy released in the process.

The energy necessary to remove one particle from the nucleus is the separation or binding energy of that particle for that particular nuclide. A "particle" may be a neutron, a proton, an alpha particle, a deuteron, etc. The separation or binding energy of a nuclear particle is analogous to the ionization potential of an electron. If a particle enters the nucleus, an amount of energy equal to its separation energy is released [9].

The separation or binding energy of a neutron is

$$S_n = [M(A-1, Z) + m_n - M(A, Z)]c^2 \quad (3)$$

Such separation energy can be expressed in terms of the total binding energy [10]:

$$S_n = B_{tot}(A, Z) - B_{tot}(A-1, Z) \quad (4)$$

The separation or binding energy of a proton is

$$S_p = [M(A-1, Z-1) + m_p - M(A, Z)]c^2 \quad (5)$$

In many reference sources the tabulated quantity is the excess or mass defect rather than the mass. The mass excess Δ , is defined as $M(A, Z) - A$, and is usually given in units of energy equivalent of mass [10].

3. Results

Neutron separation energies (written in the brackets) are shown in the Table 2. Separation energy has the meaning of the neutron production energy thresholds for different isotopes of chemical element.

Neutron production thresholds are: 13.1 MeV for Al and between 8.9 MeV and 12 MeV for Fe isotopes; ~10 MeV for Cu and between 6,2 MeV and 8,7 MeV for W and Pb isotopes respectively..

The separation energy of the last neutron in the nucleus varies from 5 MeV to 17 MeV. As a consequence, the energy higher than 5 MeV would be necessary to produce neutrons from most of elements. However only for a few light elements, such as deuterium and beryllium, 5MeV energy is sufficient enough to produce neutrons. The (γ, n) cross section for these light elements is quite low, therefore the total process, electron-photon-neutron, has a low efficiency [11]

Tungsten has five stable isotopes with threshold energies for photo-neutron emission ranging from 6.190 MeV for ¹⁸³W to 8,416 MeV for ¹⁸⁰W and for

photoprotons emission from 6.568 for ^{180}W to 8.398 MeV for ^{186}W (Fig. 1).

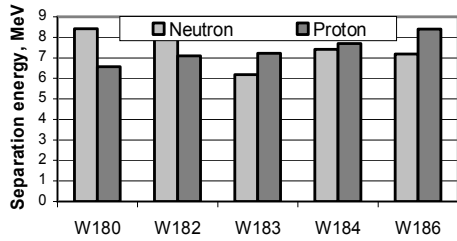


Fig. 1. Neutron and proton separation energies for tungsten isotopes.

Calculated proton separation energies from various nucleuses are shown in Table 3.

Table 2. Neutron separation energies

X	Neutron separation energy S_n , (MeV)
^1H	^2H (2.224)
^5B	^{10}B (8.436), ^{11}B (11.454)
^6C	^{12}C (18.721), ^{13}C (4.946)
^7N	^{14}N (10.553), ^{15}N (10.833)
^8O	^{16}O (15.664), ^{17}O (4.143), ^{18}O (8.043)
^9F	^{19}F (10.432)
^{11}Na	^{23}Na (12.419)
^{12}Mg	^{24}Mg (16.531), ^{25}Mg (7.330), ^{26}Mg (11.093)
^{13}Al	^{27}Al (13.058)
^{14}Si	^{28}Si (17.180), ^{29}Si (4.473), ^{30}Si (10.609)
^{15}P	^{31}P (12.311)
^{16}S	^{32}S (15.042), ^{33}S (8.642), ^{34}S (11.417), ^{36}S (9.889)
^{17}Cl	^{35}Cl (12.645), ^{37}Cl (10.31)
^{19}K	^{39}K (13.077), ^{40}K (7.799), ^{41}K (10.095)
^{20}Ca	^{40}Ca (15.643), ^{42}Ca (11.480), ^{43}Ca (7.933), ^{44}Ca (11.130), ^{48}Ca (9.945)
^{22}Ti	^{46}Ti (13.188), ^{47}Ti (8.880), ^{48}Ti (11.627), ^{49}Ti (8.142), ^{50}Ti (11.010)
^{24}Cr	^{50}Cr (12.999), ^{52}Cr (12.039), ^{53}Cr (7.939), ^{54}Cr (9.718)
^{25}Mn	^{55}Mn (10.227)
^{26}Fe	^{54}Fe (13.378), ^{56}Fe (11.197), ^{57}Fe (7.648), ^{58}Fe (10.044)
^{27}Co	^{59}Co (10.542)
^{28}Ni	^{58}Ni (12.217), ^{60}Ni (11.387), ^{61}Ni (7.820), ^{62}Ni (10.958), ^{64}Ni (9.657)
^{29}Cu	^{63}Cu (10.852), ^{65}Cu (9.911),
^{30}Zn	^{64}Zn (11.862), ^{66}Zn (11.058), ^{67}Zn (7.052), ^{68}Zn (10.198), ^{70}Zn (9.218)
^{42}Mo	^{92}Mo (12.676), ^{94}Mo (9.678), ^{95}Mo (7.368), ^{96}Mo (9.154), ^{97}Mo (6.821), ^{98}Mo (8.643), ^{100}Mo (8.289)
^{50}Sn	^{112}Sn (10.787), ^{114}Sn (10.299), ^{115}Sn (7.546), ^{116}Sn (9.563), ^{117}Sn (6.943), ^{118}Sn (9.327), ^{119}Sn (6.483), ^{120}Sn (9.108), ^{122}Sn (8.813), ^{124}Sn (8.487)
^{73}Ta	^{181}Ta (7.577)
^{74}W	^{180}W (8.416), ^{182}W (8.065), ^{183}W (6.190), ^{184}W (7.411), ^{186}W (7.190)
^{82}Pb	^{204}Pb (8.394), ^{206}Pb (8.086), ^{207}Pb (8.738), ^{208}Pb (7.368)

Table 3. Proton separation energies

X	Proton separation energy, MeV
^1H	^2H (2.224)
^5B	^{10}B (6.586), ^{11}B (11.228)
^6C	^{12}C (15.957), ^{13}C (17.533)
^7N	^{14}N (7.551), ^{15}N (10.204)
^8O	^{16}O (12.127), ^{17}O (13.782), ^{18}O (15.940)
^9F	^{19}F (7.995)
^{11}Na	^{23}Na (8.794)
^{12}Mg	^{24}Mg (11.693), ^{25}Mg (12.064), ^{26}Mg (14.146)
^{13}Al	^{27}Al (8.271)
^{14}Si	^{28}Si (11.585), ^{29}Si (12.334), ^{30}Si (13.507)
^{15}P	^{31}P (7.297)
^{16}S	^{32}S (8.864), ^{33}S (9.570), ^{34}S (10.884), ^{36}S (13.095)
^{17}Cl	^{35}Cl (6.371), ^{37}Cl (8.386),
^{19}K	^{39}K (6.381), ^{40}K (7.582), ^{41}K (7.808)
^{20}Ca	^{40}Ca (8.328), ^{42}Ca (10.277), ^{43}Ca (10.676), ^{44}Ca (12.164), ^{48}Ca (15.807)
^{22}Ti	^{46}Ti (10.344), ^{47}Ti (10.464), ^{48}Ti (11.445), ^{49}Ti (11.352), ^{50}Ti (12.164)
^{24}Cr	^{50}Cr (9.591), ^{52}Cr (10.505), ^{53}Cr (11.133), ^{54}Cr (12.372)
^{25}Mn	^{55}Mn (8.068)
^{26}Fe	^{54}Fe (8.853), ^{56}Fe (10.183), ^{57}Fe (10.559), ^{58}Fe (11.955)
^{27}Co	^{59}Co (7.364)
^{28}Ni	^{58}Ni (8.173), ^{60}Ni (9.533), ^{61}Ni (9.861), ^{62}Ni (11.137), ^{64}Ni (12.548)
^{29}Cu	^{63}Cu (6.122), ^{65}Cu (7.454),
^{30}Zn	^{64}Zn (7.714), ^{66}Zn (8.924), ^{67}Zn (8.911), ^{68}Zn (9.977), ^{70}Zn (11.118)
^{42}Mo	^{92}Mo (7.482), ^{94}Mo (8.491), ^{95}Mo (8.631), ^{96}Mo (9.297), ^{97}Mo (9.225), ^{98}Mo (9.795), ^{100}Mo (11.143)
^{50}Sn	^{112}Sn (7.554), ^{114}Sn (8.480), ^{115}Sn (8.753), ^{116}Sn (9.280), ^{117}Sn (9.439), ^{118}Sn (10.000), ^{119}Sn (10.127), ^{120}Sn (10.690), ^{122}Sn (11.395), ^{124}Sn (12.096)
^{73}Ta	^{181}Ta (5.943)
^{74}W	^{180}W (6.568), ^{182}W (7.095), ^{183}W (7.223), ^{184}W (7.700), ^{186}W (8.398)
^{82}Pb	^{204}Pb (6.638), ^{206}Pb (7.253), ^{207}Pb (7.488), ^{208}Pb (8.004)

Neutron and proton separation energies for four stable lead isotopes are shown in Figure 2.

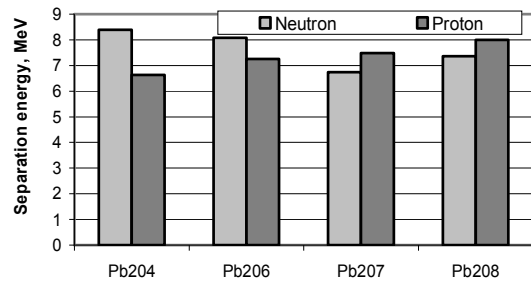


Fig. 2. Neutron and proton separation energies for lead isotopes.

The range of neutron emission threshold is from 6.738 MeV to 8.394 MeV and for photoprotons – from 6.638 MeV to 8.004 MeV.

For a given atomic number Z , the neutron separation energy S_n is larger for even N as compared to that for odd N . Similarly for a given N , proton separation energy S_p is larger for even Z compared to that for odd Z . This effect is caused by that part of the nuclear force that likes to have neutrons paired with neutrons (with antiparallel spin). This pairing of similar nucleons causes even-even nuclei (Z even, N even) to be more stable than even-odd or odd-even nuclei which, in turn, are more stable than odd-odd nuclei [10]. More stable nucleus is characterized by higher binding energies. In this case the larger amount of energy is required to separate the last particle (neutron or proton) from the nucleus.

It should be noted that nuclei containing 2, 6, 8, 14, 20, 28, 50, 82 or 126 neutrons or protons are especially stable. These nuclei are said to be magic. The associated numbers of neutrons or protons that are required to fill shells (or subshells) of nucleons in the nucleus behave in the same way as the electrons filling the shells of the atoms. Nuclei having a magic number of neutrons absorb neutrons to only a very small extent, so materials of this type could be used in the places where neutron absorption must be avoided.

4. Conclusions

Neutron and proton separation energies as threshold energies of photonuclear reactions were calculated for typical materials used in medical accelerators and for radiation technologies. The natural chemical elements consist of stable isotopes, differing by particle separation energies. As a consequence, with the increasing photon energy, more isotopes are participating in neutron or proton production.

The values of last nucleon separation energies vary from 2.224 MeV for ^2H nuclide to 17.5 MeV for ^{13}C isotope and are from the range of operation energies of medical electron accelerators used in medical therapy. The photo-neutron yield depends on neutron separation energy of nuclide and on natural isotopic composition of element.

5. References

1. O. Grégoire, M.R. Cleland, J. Mittendorfer, M. Vander Donskt, J. Meissner. Radiological safety of medical devices sterilized with X-rays at 7.5 MeV. *Radiation Physics and Chemistry* 67 (2003) 149-167.
2. H.Al-Ghamdi, Fazal-ur-Rehman, M.I. Al-Jarallah, N. Maalej. Photoneutron intensity variation with field size around radiotherapy linear accelerator 18-MeV X-ray beam. *Radiation Measurements* 43 (2008) S495-S499.
3. Konefal, A. Orlef, M. Dybek, Z. Maniakowski, K. Polaczek-Grelak, W. Zipper. Correlation between radioactivity induced inside the treatment room and the undesirable thermal/resonance neutron radiation produced by linac. *Physica Medica* (2008) 24, 212-218.
4. Facure, R.C, Falcão, A.X. Silva, V.R. Crispim, J.C. Vitorelli. A study of neutron spectra from medical linear accelerators. *Applied Radiation and Isotopes* 62 (2005) 69-72.
5. Donadille, F. Trompier, I. Robbes, S. Derreumaux, J. Mantione, B. Asselineau, K. Amgarou, A. Martin, J.F. Bottollier-Depois, F. Queinnec, B. Aubert, I. Clairand. Radiation protection of workers associated with secondary neutrons produced by medical linear accelerators. *Radiation Measurements* 43 (2008) 939-943.
6. K.Bessho, H. Matsumura, T. Miura, Q. Wang, K. Matsumoto, H. Hagura, Y. Nagashima, R. Seki, T. Takahashi, K. Sasa, K. Sucki, T. Matsuhiro, Y. Tosaki. Estimation of thermal neutron fluences in the concrete of proton accelerator facilities from ^{36}Cl production. *Nuclear Instruments and Methods in Physics Research B* 259 (2007) 702-707.
7. Jao-Peng Lin, Wei-chung Liu, Chun-Chih Lin. Investigation of photoneutron dose equivalent from high-energy photons in radiotherapy. *Applied Radiation and Isotopes* 65 (2007) 599-604.
8. J. K. Tuli. Nuclear Wallet Cards. National Nuclear Data Center. Brookhaven National Laboratory. 2005.
9. N. Tsoulfanidis. Measurement and Detection of Radiation. Taylor & Francis, 1995, 636 p.
10. W.Loveland, D. Morrissey, G. Seaborg. Modern Nuclear Chemistry. Wiley-Interscience, 2006, 671p.
11. L. Auditore, R.C. Barnà, D. De Pasquale, A. Italiano, A. Trifirò, M. Trimarchi. Study of a 5 MeV electron linac based neutron source. *Nuclear Instruments and Methods in Physics Research B* 229 (2005) 137-143.
12. J. R. Lamarsh. Introduction to Nuclear Reactor Theory. American Nuclear Society. 2002. 58

IMPLEMENTATION OF PATIENT PLAN CHECKING IN RADIATION THERAPY

R. Vilkas¹, M. Laurikaitis^{1,2}, D. Adlienė³, V. Andrijaitienė¹

¹Klaipėda University Hospital, Klaipėda, Lithuania

²Oncological Hospital of Kaunas Medical University Hospital, Kaunas, Lithuania

³Kaunas University of Technology, Physics Department, Kaunas, Lithuania

Abstract: The aim of this work was to check dose plans prepared using treatment planning system (TPS) before the first treatment of patient in linear accelerator applying percent depth dose (PDD) algorithm.

Dose plans of 166 patients prepared in the clinical routine work were checked. It was found that the dose deviations in the checked plans varied from -4.2 % to +6.7 %, with a mean deviation of 0.42 % and a standard deviation of 1.86 %. The sources of possible data variations are discussed on the basis of the obtained results.

Keywords: Radiotherapy, linear accelerator, quality control, dose calculation, plan check

1. Introduction

High energy radiation therapy is one of the most important methods to treat cancer patients. Therefore the requirements to deliver a prescribed dose to the certain target in modern radiotherapy are growing fast. Patient's treatment process is computerized, starting with the patient's data mapping and ending with the dose delivering to the patient. However errors can occur along the procedure chain. The prescribed dose errors larger than 5 % may influence the clinical outcome of the treatment [1]. This might be prevented if treatment plans are checked before the first treatment.

Usually dose plans are prepared using standard dose planning systems and the doses to patients are calculated using standard algorithms. Nevertheless different treatment complications may occur due to the incorrect dose calculations. The implementation of dose plan verification system in the clinical routine may help to ensure the high-quality treatment and avoidance of errors that might influence the clinical outcome of the treatment. However, the better way is to use independent calculation algorithm, which uses different from treatment planning system algorithms for the dose calculations.

The aim of this work was to check dose plans using percent depth dose algorithm before the first treatment of patient in linear accelerator.

2. The calculation method

The depth dose at a depth d on the central axis (CAX) can be calculated as [3]:

$$DD(d) = DD_m(d, A) \times CF_{dd}(d) \times CF_{inv} \times CF_{iso} \times CF_{sum} \times PLAN_FCT(p) \quad (1)$$

where, $DD(d)$ - the percentage depth dose (PDD) at any point on the beam central axis at depth d for patient geometry; $DD_m(d, A)$ - the depth dose at depth d for the equivalent field A on the surface, for reference beam geometry; $CF_{dd}(d)$ - the depth dose correction factor to convert from one Source to Skin Distance (SSD) to another; CF_{inv} - the Inverse Square Law (ISL) correction; CF_{iso} - the isocentric normalization correction; CF_{sum} - the weight factor, accounting for the weight of the beam (and the number of fields); $PLAN_FCT(p)$ - the plan normalization factor - this is used if the final distribution is renormalized to a particular isodose.

PDD method includes the inverse square correction in the depth dose calculation. Figure 1 shows the steps which are necessary for the calculation of a single isocentric beam in the patient (c) from reference beam geometry (fixed SSD) (a).

The depth dose correction factor used to convert from one SSD to another is given by:

$$CF_{dd}(d) = \frac{TPR(d, A_2)}{TPR(d, A_1)} \times \frac{(CSSD + D_{max})^2}{(CSSD + d)^2} \times \frac{(SPD + d)^2}{(SPD + D_{max})^2} \quad (2)$$

where, $TPR(d, A)$ - tissue-phantom ratio. TPR depends from depth d and for the equivalent field A ; $CSSD$ - the SSD on the central axis for the particular patient situation; D_{max} - the maximum dose depth; SPD - Source to Phantom Distance.

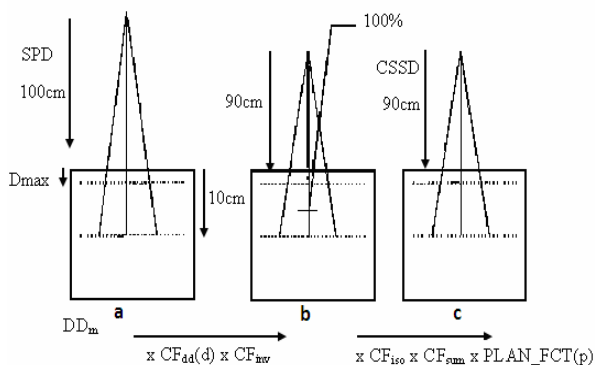


Fig. 1. The correction factors CF_{dd} and CF_{inv} are applied to the reference beam (a) to calculate the depth dose in the patient (b). The depth dose is then normalized in (c) by the application of the correction factors CF_{iso} , CF_{sum} , and $PLAN_FCT(p)$, such that (c) shows the actual on-screen isodose distribution. [3]

The Inverse Square Law correction is defined as:

$$CF_{inv} = \frac{(SSD_s + D_{max})^2}{(CSSD + D_{max})^2} \quad (3)$$

where, SSD_s - is equal to the SPD for standard fixed SSD and isocentric fields. For changed SSD fields, e.g., extended SSD, the SSD_s is equal to the changed SSD value.

The weighting factor, accounting for the weight of the beam is calculated using Eq.4. The weight of a beam is only relevant with respect to the other beam. The weight of a single field is meaningless. The correction factor CF_{sum} identifies the weight of the beam as:

$$CF_{sum} = \frac{F_{weight}}{N} \quad (4)$$

The PDD algorithm is used for the calculations performed in respect to the central axis. Only bulk densities are used for the lung (0.3 g/cm^3) and bone (1.2 and 1.5 g/cm^3).

Varian accelerators use an enhanced dynamic wedge (EDW) to generate a wedged beam. It is difficult to control this type of wedge, but it is advantageous since it provides constant energy distribution over the field. The wedge is generated by moving one of the collimators during irradiation. The number of monitor units required to deliver a wedged field is obtained multiplying the number of monitor units for the open field by a wedge factor (WF). This wedge factor is equal to the ratio between the number of monitor units delivered when the moving collimator passes the central axis (or the fan line through the point of calculation) and the final number of monitor units. This ratio can be estimated from the segmented treatment table (STT). The Kuperman model for the calculation of Varian enhanced dynamic wedge factors [2] calculation is used

Applying this model the wedge factor $WF_{\theta}(Y_c)$ is described as:

$$WF_{\theta}(Y_c) = \frac{MU(Y')}{MU_{total}} = STT(\theta, Y') \quad (5)$$

where Y' is considered to be a function of the centre-of-field coordinate Y_c and field size in the wedge-gradient direction. Note that equation (5) assumes that wedge factors are defined in the centre of the radiation field.

The above described algorithm was computerized and the "Radiotherapy Verification Program" (RVP) was developed by Swedish colleagues [4]. Working panel of RVP is presented in Fig. 2.

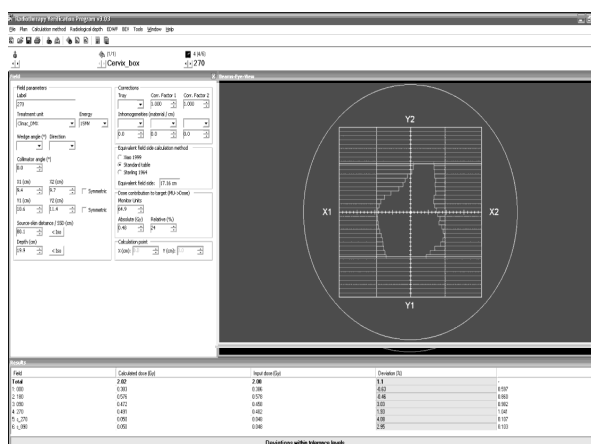


Fig.2 Working panel of Radiotherapy Verification Program.

All dose plans were checked at Radiotherapy department of Kaunas Medical University Hospital branch Oncology Hospital.

3. Results and discussion

Individual patient data (name, identification number), dose plan and irradiation details (irradiation unit, field size, distance from the source to irradiated surface, the depth in tissue, material heterogeneity and density, number of monitor units and the absolute dose) have been registered and calculation according to the selected data was performed.

Deviation between the results obtained using depth-dose calculation algorithm and calculated by TPS was estimated as:

$$Deviation = \left(\frac{D_{PDD}}{D_{TPS}} - 1 \right) \cdot 100\% \quad (6)$$

The program sets 5% tolerance limit. If the estimated deviation of checked plan exceeds the tolerance limit, the plan should be investigated. If investigation fails, the plan must be recalculated, and the reasons of discrepancy must be explored more deeply.

However it is quite difficult to check dose plans produced with sophisticated radiation treatment planning systems algorithms. Basic algorithm of RVP supports only calculations on a central beam axis. So it is impossible to check the dose plans where field central

axis is closed by a multi-leaf collimator or is a near the side of configured field, as it is shown in the Fig.3.

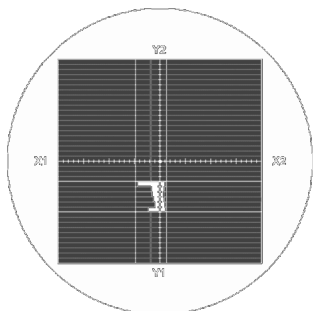


Fig.3 Field central axis is hidden

If that happens, it is necessary to recalculate the dose plan again changing the coordinates in the planning system so, that a central axis would be in the centre of the irradiated field. Of course, sometimes it is not possible if the planned location is surrounded by a number of critical organs that must be protected from additional exposure.

Also it is impossible to check plans if the irradiation fields with rotation are foreseen. Plans of this type require manual recalculation, dividing the calculation procedure according to the distinguished segments of rotation arc and calculating doses for each segment separately.

Dose plans for 166 cancer patients were produced using treatment planning system „ECLIPSE“ and checked by RVP using PDD method. Comparison of dose calculation results performed using different algorithms was processed statistically. The distribution of deviations obtained from the comparison of two algorithms is shown in Fig. 4.

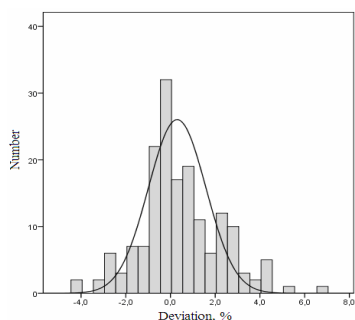


Fig. 4. The distribution of the deviation from comparison of two algorithms (PDD and TPS).

It was found that the deviations varied from -4.2 % to +6.7 %, with a mean deviation of 0.42 % and a standard deviation was 1.86 %. It was also found that 2% of plans did not fit in the 5% tolerance limit. These plans required an additional evaluation using manual check. The distribution of the deviations obtained from the comparison of PDD and TPS for different localizations are shown in Fig. 5 and Table 1.

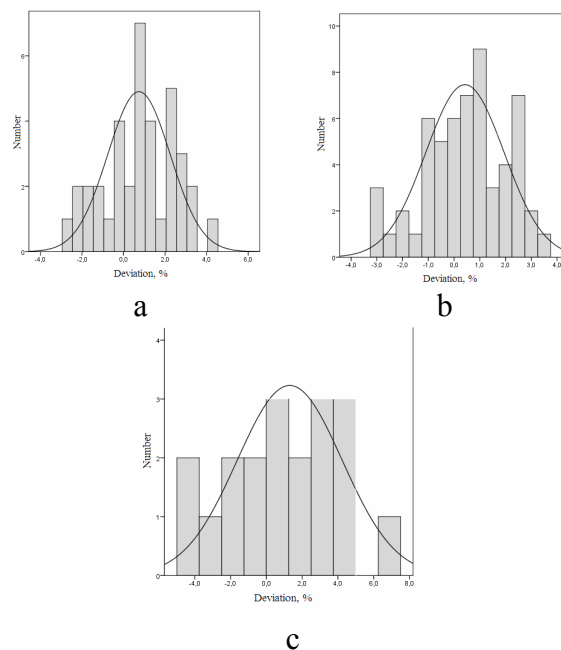


Fig. 5. The distribution of the deviation for different localization: head&neck (a), pelvis (b) and breast (c).

Table 1. Percentage deviation for different localization.

Localiazation	Patient	Min(%)	Max(%)	Mean	Standart deviation
Pelvis	67	-3	3,6	0,45	1,6
Head&Neck	37	-2,7	4,4	0,8	1,72
Breast	19	-4,2	6,7	1,1	3,05

4. Conclusions

Verification of dose plans was performed comparing dose calculation results obtained using planning system algorithm and verification algorithm. Total number of verified plans was 166. The deviations varied from -4,2 % to +6,7 %, with a mean deviation of 0,42 % and a standard deviation was 1,86 %. For the most treatment cases except breast treatment the deviation between percent depth - dose method and treatment planning system was in 5 % range.

5. References

1. ICRU Report No. 62. Prescribing, recording and reporting photon beam therapy. Bethesda, MD: ICRU, 1999.
2. Vadim Y Kuperman. A new analytical model for Varian enhanced dynamic wedge factors. Phys. Med. Biol. 49 (2004) p.2841–2851.
3. C. Huntzinger. Manual Calculations of Depth Dose and Monitor Units. (1999).
4. Johnsson S, (2003) Development and Evaluation of an independent system for absorbed dose calculations in radiotherapy. Thesis for the degree of Doctor of Philosophy. Lund.

DISTRIBUTION OF SCATTERED RADIATION IN SUPERFICIAL X-RAY THERAPY

Nikolajus MEDVEDEVAS*, Diana ADLIENĖ*, Jurgita LAURIKAITIENĖ**

*Kaunas University of Technology, Lithuania, **Kaunas Medical University Hospital, Lithuania

Abstract: Measurement and knowledge of dose delivered under lead eye shielding during superficial X-ray therapy allow to evaluate the irradiation effect on ocular structures. CT-Head phantom investigation of the lead shielding effectiveness in the typical superficial X-ray treatment procedure has shown that the side scattering of photons from the applicator are the main contributors to the additional dose to the patient as compared to the backscattered photons from the phantom surface or volume. Application of a lead shielding for reasonable eye protection is discussed.

Keywords: phantom, applicator, X-ray tube, superficial therapy, eye shielding, scattered photons.

1. Introduction

The application of superficial X-ray therapy doesn't anticipate the obligatory calculation of the doses delivered to critical organs as it is in case of computed tomography or LINAC. Despite the treatment doses are lower, they can cause radiation damage to the irradiated organs. Due to this the necessity exists to protect critical organs, especially during the superficial X-ray treatment of head skin.

It is known, that lead (Pb) shields are used in superficial radiotherapy of the periorbital region to reduce the dose delivered to critical structures beneath the area requiring treatment, which are close to or over the eye [1]. Treatment areas often include the nasal bridge, medical canthus and the eye lids [2, 3]. The protection efficiency of lead eye shields must be evaluated before their appliance in superficial X-ray therapy treatment.

One of the most recent evaluations of eye protection efficiency from direct X-rays for the case when the applicator is set in a certain distance from the irradiated area has been performed by M. J. Butson et al. [1].

However the superficial X-ray therapy is also performed when the applicator contacts with patient surface. In this case, the eye protection and the evaluation of protection efficiency raise some questions, because of the scattered photons, originating from the applicator, phantom and lead shielding. During the superficial X-ray therapy a photon interaction cross sections at keV energies are relatively large and dose enhancement is probable due to substantial backscattered photon fluence [4]. The evaluation of possible dose enhancement by backscattered photons from lead shielding is important,

because it may have a negative effect on ocular structures.

The purpose of this work was to investigate experimentally the angular surface dose distribution of scattered radiation of X-ray photons that were responsible for the doses registered on the head phantom surface without shielding and with a lead shielding during superficial X-ray therapy treatment, and to evaluate the efficiency of this shielding when the applicator contacts the phantom surface.

2. Methodology

GULMAY D3225 X-ray therapy unit with a acrylic conical applicator (orbicular exposure field - Ø4 cm) was used for the irradiation of PMMA head phantom (Cardinal Health Model 76-414-4150, Ø16 cm, h = 15.8 cm, $\rho = 1.190 \text{ g/cm}^3$).

X-ray shielding of PMMA phantom areas near the applicator was performed using pieces of lead ($4.12 \times 3.15 \times 0.183 \text{ cm}^3$).

A set of calibrated pencil dosimeters D-500 (dose range - $0.02 \div 5 \text{ Gy}$, Ø1 cm, h = 10 cm) was used for dose measurements. Dose values were estimated using analyser KID-6. The pieces of lead were placed beneath the applicator to cover the whole pencil dosimeter (Figure 1) and to avoid misinterpretation of the obtained results

Experimental set ups for angular dose distribution measurement on the phantom's surface (without shielding and with lead shielding) are presented in Figure 2 and Figure 3.

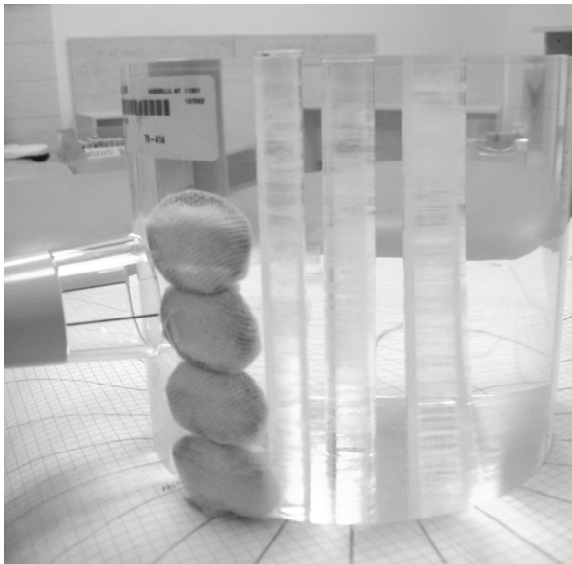


Fig. 1. Position of lead shielding on the PMMA phantom during the measurement of the angular surface dose distribution

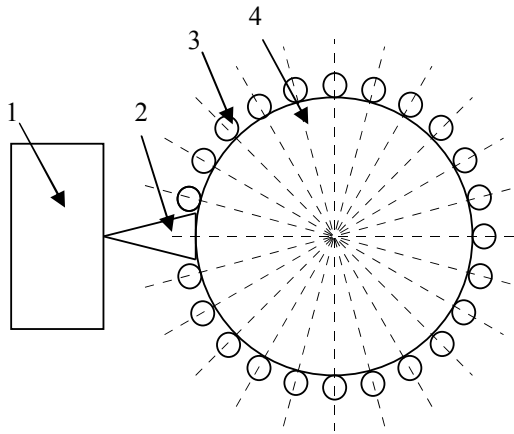


Fig. 2. Experimental set up for angular surface dose distribution measurement without shielding (1 – GULMAY D3225 X-ray therapy unit; 2 – conical applicator; 3 – pencil dosimeter D-500; 4 – PMMA head phantom)

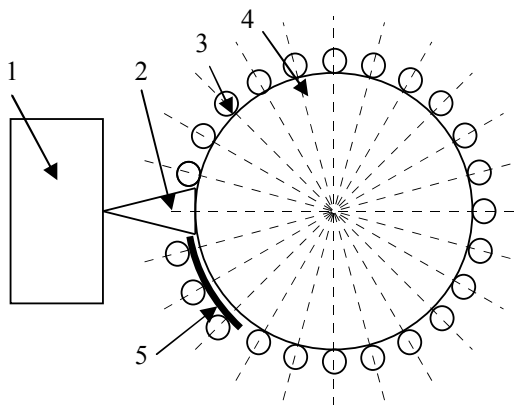


Fig. 3. Experimental set up for angular surface dose distribution measurement with lead shielding (5 - lead eye shield)

Central angle of 28.072° was estimated that corresponds to the irradiation field diameter, when the applicator contacts with the phantom. In order to include the contribution of side scattered photons from the

applicator to the phantom surface dose, dosimeters were placed around a phantom with an angular step of 15 degree. This arrangement enabled us to measure edge doses when the pieces of shielding lead were placed on the phantom's surface just beneath the applicator.

Angular surface dose distributions (without and with a lead shielding) were measured changing the beam quality (80 kVp, 100 kVp, 120 kVp). Irradiation dose to the target, $D_T = 4.0$ Gy at 0.5 cm depth was kept during all measurements. Irradiation parameters are provided in the Table 1.

Table 1. Irradiation parameters

Tube voltage, kVp	80	100	120
$D_{0.5cm}$, Gy	4,0		
D_{0cm} , Gy	4,56	4,50	4,45
Photon penetration depth, cm	0,5		
HVL	2,44 mm Al	2,97 mm Al	5,33 mm Al
Tube current, mA	20,0		
FSD, cm	20,0		

With reference to methods described in [5, 6, 7], the obtained dose values, measured in the shielded area (measuring point at 195°, 210° and 225°) without shielding and with lead shielding, were used to calculate the mass attenuation coefficients:

$$\mu / \rho = \frac{1}{\rho \cdot d} \ln \frac{D_0}{D} \quad (1)$$

where D_0 and D are the dose values measured without and with lead shielding, d (cm) is the thickness of lead shielding, ρ (g/cm^3) is density of lead and μ/ρ (cm^2/g) is the lead mass attenuation coefficient. The calculated values of lead mass attenuation coefficient were compared to theoretical values that were ascertained to energies of backscattered at 180 degrees photons using the XCOM database.

3. Results and discussion

The angular surface dose distributions measured without and with a lead shielding at different beam qualities of 80 kVp, 100 kVp and 120 kVp are presented in Fig.4 – Fig.6.

Performed measurements without shielding have shown that the doses in the neighbouring areas of applicator (165°-195°) are several times higher as compared to those measured near phantom surface at some distance from the applicator. This effect could be attributed to the side scattering of X-ray photons from the applicator. Application of lead eye shielding contributes to the reducing of the doses in the region of interest however the doses in the closest neighbourhood of applicator remain rather high. The most effective dose reduction (70.4% - 81%) was obtained at the angle of 210°, which corresponds to the distance of 4 cm from the edge (applicator side) of lead shielding plate. Average dose reduction of < 20% at 195 degrees is not satisfying and

was caused due to edge conditions (applicator - Pb plate). Average dose reduction of ~50% at further edge of lead shielding is appropriate. It seems that the shielding effectiveness could be enhanced if the lead plates would have a thickness

gradient. The thickness of the applied lead shielding must be larger in the area tightly closed to the applicator

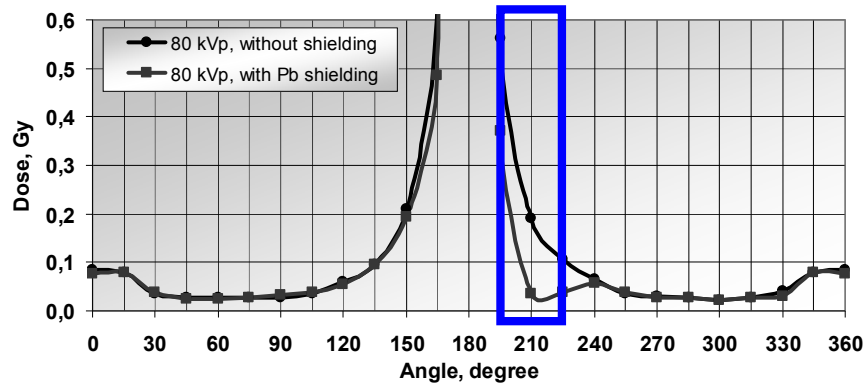


Fig. 4. Angular surface dose distribution, measured at 80 kVp without shielding and with lead shielding (rectangle marks the shielded area)

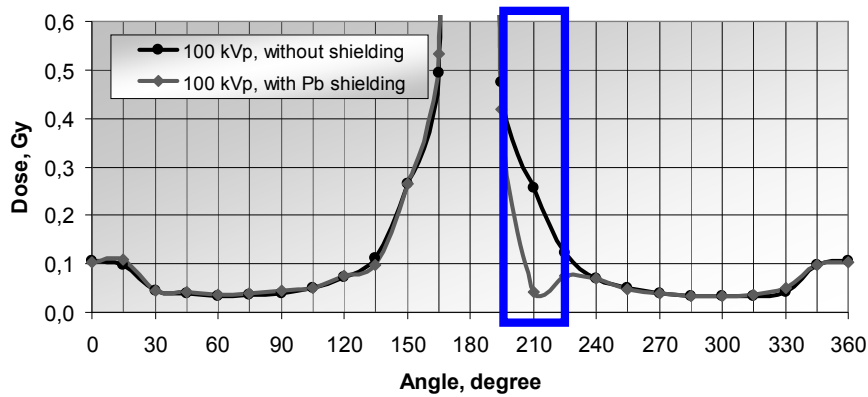


Fig. 5. Angular surface dose distribution, measured at 100 kVp without shielding and with lead shielding (rectangle marks the shielded area)

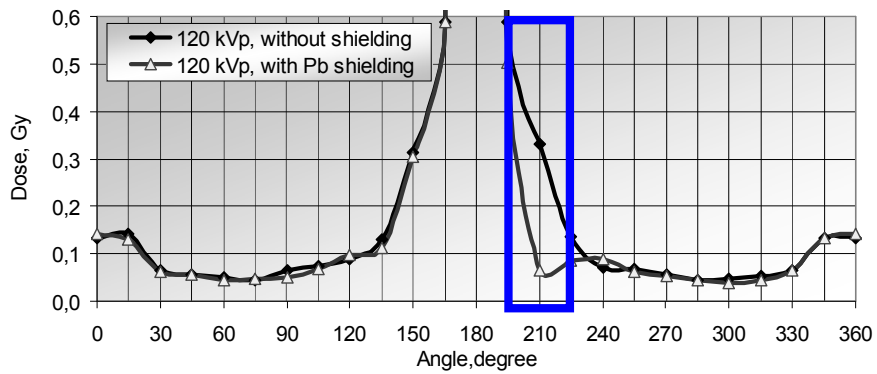


Fig. 6. Angular surface dose distribution, measured at 120 kVp without shielding and with lead shielding (rectangle marks the shielded area)

4. Conclusions

Investigation has shown that the lead shielding placed on the phantom surface near by the applicator of X-ray irradiation unit “narrows” side scattering range of X-ray photons and reduces the doses in the shielded area depending on the beam quality, photon penetration depth and angular position.

The most effective dose reduction of $> 70\%$ was obtained at the angle of 210° , which corresponds to the distance of 4 cm from the edge (applicator side) of Pb shielding plate. However due to the edge conditions (applicator - Pb plate) at 195° the dose reduction of $< 20\%$ was not satisfying. Dose reduction of $\sim 50\%$ at further from applicator edge of lead shielding is appropriate. Shielding effectiveness in these regions needs more detailed investigation.

5. References

1. Butson M. J., Cheung T., Yu P., Price S., Bailey M. Measurement of radiotherapy superficial X-ray dose under eye shield with radiochromic film. *Physica Medica* 2008 (24): p. 29-33.
2. Amdur R.J., Kalbaugh K.J., Ewald L.M., Parsons J.T., Mendenhall W.M., Bova F.J., et al. Radiation therapy for skin cancer near the eye: kilovoltage X-rays versus electrons. *Int J Radiat Oncol Biol Phys* 1992; 23(4): p. 769-779.
3. Wolstenholme V, Glees J. The role of kilovoltage X-rays in the treatment of skin cancers. *Eur Oncol Dis* 2006: p. 32-35.
4. Saiful Hug M., Venkataramanan N., Meli J. A. The effect on dose of kilovoltage x-rays backscattered from lead. *Int J Radiat Oncol Biol Phys* 1992; 24(1): p. 171-175.
5. Das I. J. Broad beam attenuation of kilovoltage photon beams: effect of ion chambers. *The British Journal of Radiology*, 1998 (71): p. 68-73.
6. Midgley S. M. Measurements of the X-ray linear attenuation coefficient for low atomic number materials at energies 32-66 and 140 keV. *Radiation Physics and Chemistry*, 2005 (72): p. 525-535.
7. Demir L., Han I. Mass attenuation coefficients, effective atomic numbers and electron densities of undoped and differently doped GaAs and InP crystals. *Annals of Nuclear Energy*, 2009 (36): p. 869-873.

THE INVESTIGATION OF CHERNOBYL CLEAN-UP WORKERS BLOOD BY EPR TECHNIQUE

Maksims POLAKOVŠ*, Nina MIRONOVA-ULMANE*, Andrejs PAVLENKO*, Tija ZVAGULE**, Natalija KURJANE**, Natalija GABRUSHEVA**

*Institute of solid State Physics, University of Latvia, Riga, Latvia

** Centre of Occupational and Radiological Medicine of P.Stradins Clinical University Hospital, Latvia

Abstract: Results of the blood investigation of Chernobyl clean-up workers examined by Electron paramagnetic resonance method in the Centre of Occupational and Radiological medicine of P.Stradins Clinical hospital of Latvia are reported in the present work.

Keywords: EPR (Electron paramagnetic resonance) hemoglobin, blood, Chernobyl clean-up worker.

1. Introduction

At the beginning of this century, when scientists began to apply the principles of quantum mechanics to describe the atoms or molecules, they found that a molecule or atom has discrete states, each with a corresponding energy. EPR (Electron paramagnetic resonance) was first discovered in Kazan State University by Soviet physicist Yevgeny Zavoisky in 1944, and was developed independently at the same time by Brebis Bleaney at the University of Oxford.

EPR spectroscopy is a measurement and interpretation of the energy differences between the electronic states. With knowledge of these energy differences, it is possible to gain insight into the identity, structure, and dynamics of the sample under study. It is possible to measure these energy differences, ΔE , because of an important relationship between ΔE and the absorption of electromagnetic radiation (Planck's law). EPR is the only technique that provides direct detection in the sample that contains free radicals and unpaired electrons. Common examples:

Transition metal ions – Fe^{3+} , Cu^{2+} , Mn^{2+} , Co^{2+}

Free Radicals – Typically carbon, nitrogen or oxygen containing compounds.

2. Materials and methods

The study of blood and hemoglobin radiation damage is very important in order to understand the biological effects of ionizing radiation [1-6]. Various physical techniques are used to determine structural damages of hemoglobin after irradiation: absorption spectroscopy

[8], IR spectroscopy [7], Mossbauer [6] and EPR spectroscopy [1, 7].

In present work we have studied the blood of Chernobyl clean-up workers by Electron paramagnetic resonance.

Between 1986 and 1991 approximately 6500 Latvian inhabitants were recruited for clean-up works at Chernobyl Nuclear Power Plant. Clinical investigations show high morbidity rate of clean-up workers compare with general population. Nowadays they represent group of chronically sick people with diseases prevalence of digestive, musculoskeletal and nervous system. Most of the Chernobyl' clean-up workers have poli-symptomatic sicknesses that exhibit tendency to progress, and their morbidity exceeds that observed in general population. Some of clean-up workers have erythrocytosis.

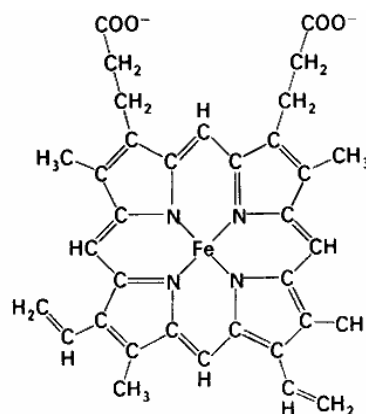


Fig.2. Chemical structure of porphyrin ring of the hemoglobin.

Erythrocytosis is defined as an excess of erythrocytes, or red blood cells (RBCs). RBCs in the blood are measured by the hematocrit (the percentage of the blood volume made up of RBCs) or by the hemoglobin (the essential oxygen-carrying protein in the RBC). Erythrocytosis occurs if either of these values is elevated. The normal limits on these blood values for males and females respectively are 52% and 47% for the hematocrit, and 17.7 g/dl and 15.7 g/dl for hemoglobin concentration. Many blood proteins use metal centres to bind and react with small molecules. For example hemoglobin contains iron (Fig.2) and gives to red blood cells their colour. The iron group in hemoglobin transports oxygen around the body. When the hemoglobin binds oxygen its does change charge but only changes its electronic configuration from high spin configuration to low spin configuration (Fig. 3).

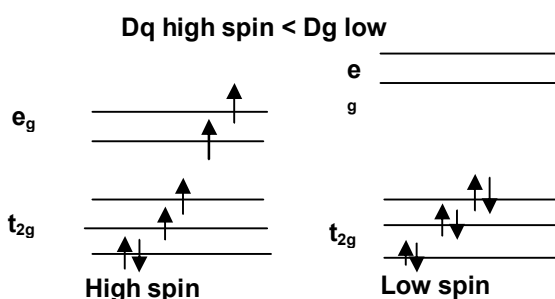


Fig. 3. Electronic configuration of Fe^{2+} (ferrous) $[Ar]3d^6$ in low and high spin states in hemoglobin.

Methemoglobin or (ferric form of hemoglobin) is the form of hemoglobin, when iron Fe^{2+} in the heme is oxidized to the Fe^{3+} ferric state (Fig. 4).

This form of hemoglobin is not able to bind oxygen. This compound is unable to deliver oxygen to tissues; therefore, it is advantageous to convert this Fe^{3+} form of hemoglobin into the Fe^{2+} ferrous state so that tissues can get the oxygen that they need.

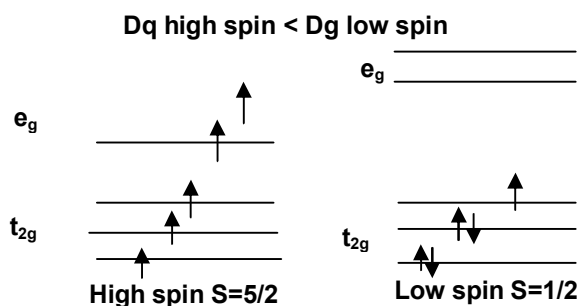


Fig. 4. Electronic configuration of Fe^{3+} (ferric) $[Ar]3d^5$ in low and high spin states in methemoglobin.

The samples of blood were received from the Centre of Occupational and Radiological medicine of P. Stradins Clinical hospital of Latvia, where Chernobyl "liquidators" are examined.

Venous blood was donated by consenting Chernobyl clean-up worker and collected under air in glass tubes containing a small amount of sodium citrate or heparin used as an anticoagulant. Blood without any

anticoagulant was also tested and showed no difference with respect to sodium citrate-treated or heparin blood. The samples for EPR measurements were rapidly frozen in liquid nitrogen.

The EPR spectra of frozen blood were measured on a BRUKER EMX-6/1 spectrometer equipped with an Aspect 2000 data system (Fig. 5). An ER 4102 ST Universal X-Band Resonator (TE_{102} mode) was used. The g-factors of EPR signals were determined by reference to the external magnetic field value measured by a Bruker ER 035 Gaussmeter and of the microwave frequency measured by a Systron Donner 6235A frequency counter.



Fig. 5. BRUKER EMX-6/1 spectrometer

The EPR signal intensities in blood were measured against fixed standard signals using the standard crystal $MgO (Cr^{3+})$ placed in resonant cavity.

The spectra were recorded at microwave power 6.2 mW, applying magnetic field modulation of 100 kHz and amplitude 1 mT. One spectrum is obtained averaging 20 scans with receiver time constant 25 ms. Documented dose for Chernobyl clean-up workers was taken from the register of the Centre of Occupational and Radiological medicine of P. Stradins Clinical hospital of Latvia.

3. Experimental results and discussion

In the present work we report results of investigations of blood of Chernobyl clean-up workers examined in the Centre of Occupational and Radiological medicine of P. Stradins Clinical hospital of Latvia by Electron paramagnetic resonance.

The important parameter of EPR spectra is g-factor. The g-factor of an EPR sample determines the position in the magnetic field (at a given microwave frequency) where an EPR transition will occur.

$$g = \frac{h\nu}{\beta B_0} \quad (1)$$

where h = Planck's constant, ν = microwave frequency; β = Bohr magneton, B_0 = magnetic field. The EPR spectra of human blood not participated in Chernobyl clean-up actions are present in the Fig. 6.

We can observe low intensity of EPR signal at g-factor 6.0, 4.3 and 2.00.

According to Table 4 [1, 11, 12] EPR signal with $g = 6.0$ is associated with methemoglobin (Fe^{3+} in high spin state), EPR signal with $g = 4.3$ is associated with transferrin (none-heme iron Fe^{3+}), signal with $g = 2.00$ is associated with methemoglobin (Fe^{3+} in low spin state), signal 1.98 is associated with used etalon MgO (Cr^{3+}).

Table 4. The indicators of EPR signal of the human blood [1].

Indicators of blood	Parameters of EPR signal
Fe^{3+} (methemoglobin)	Anisotropic signal $g_{\perp} = 6,0$ $g_{\parallel} = 2,0$
low-molecular complex of iron	Anisotropic signal $g_{\perp} = 4,52$
Fe^{3+} (transferrin)	Anisotropic signal $g_{\perp} = 4,3$ $g_{\parallel} = 9,3$
Cu^{2+} (ceruloplasmin)	$g_{\perp} = 2,056$ $g_{\parallel} = 2,209$ $A_{\parallel} = 155-200$ G
Radicals of adrenaline	singlet, $\Delta H = 14$ G $g = 2,003$
Radicals of adrenahroma	singlet, $\Delta H = 9$ G $g = 2,004$
Radicals of ascorbic acid	singlet at 77 K, $\Delta H = 9$ G $g = 2,004$ doublet at 300 K,

It is shown that it is difficult to analyze signal of g-factor at 2.00 since it is very close to EPR signal of MgO (Cr^{3+}) etalon with $g = 1.98$ which was used in this work. To investigate EPR signal of $g=2.00$ the other etalon with different g-factor is needed.

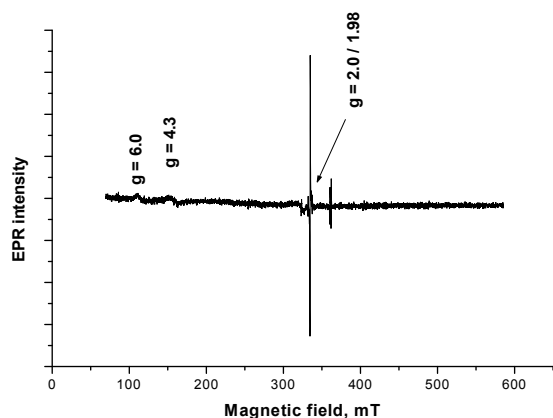


Fig. 6. The spectra of human blood not participated in Chernobyl clean-up actions.

It is shown in the Fig. 7 that this blood sample the level methemoglobin (Fe^{3+} in high spin state) is higher than normal. It is necessary to point out that the spectrum of blood sample corresponding to “not-participant” in Chernobyl clean-up action presented in the Fig. 6 is similar to the spectrum of a human blood sample, which was never exposed to radiation. We can observe correlation between EPR signal of

methemoglobin and activity of the $^{90}Sr/^{90}Y$ and documented dose in register (recorded from military passport) as well. The level of EPR signal of transferrin is higher than normal comparing with EPR spectrum of blood represented in Fig. 6.

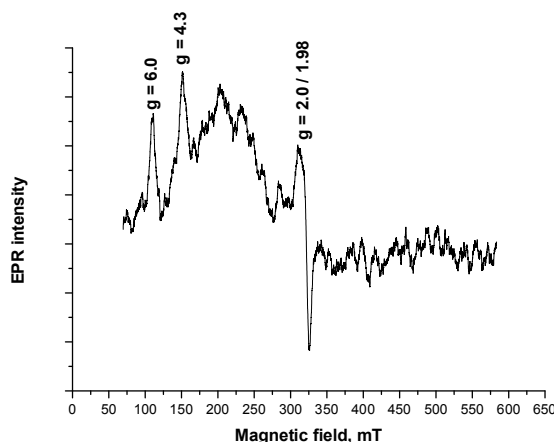


Fig. 7. EPR spectrum of blood of Chernobyl clean-up worker. (Documented dose in register - 0.195 Gy. $^{90}Sr/^{90}Y$ measured in tooth by EPR in 1997 year - 60 Bq/g).

It is shown (Fig. 8) that the level of methemoglobin (Fe^{3+} in high spin state) in this blood sample is higher than normal. We observe correlation between EPR signal of methemoglobin and activity of the $^{90}Sr/^{90}Y$ and documented dose in register as well. The level of EPR signal of transferrin is higher than normal. Comparing this level with EPR spectra (Fig. 7) it was found that relation between the levels of methemoglobin and transferrin are being changed.

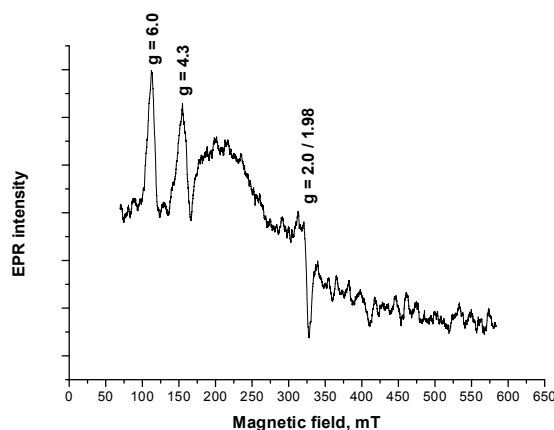


Fig. 8. EPR spectrum of blood of Chernobyl clean-up worker. (Documented dose in register 0.211 Gy. $^{90}Sr/^{90}Y$ measured in tooth by EPR in 1997 year - 80 Bq/g).

In the Fig. 9 it is shown that the level of EPR signal of methemoglobin (Fe^{3+} in high spin state) $g=6.0$ is close to the level of EPR signal registered for person who has not participated in Chernobyl clean-up work (Fig. 6). The activity measurement of the $^{90}Sr/^{90}Y$ related to the person who’s data is shown in the Fig. 9, equals to zero. The dose documented in register is 10 times smaller as compared to EPR spectra of human blood shown in Fig. 7 and Fig. 8. Despite the EPR signal

level corresponding to methemoglobin, which is presented in Fig. 9 is smaller than the EPR signal levels shown in Fig. 7 and Fig. 8, practically the same level of EPR signal of human blood $g = 4.3$ related to transferrin was observed.

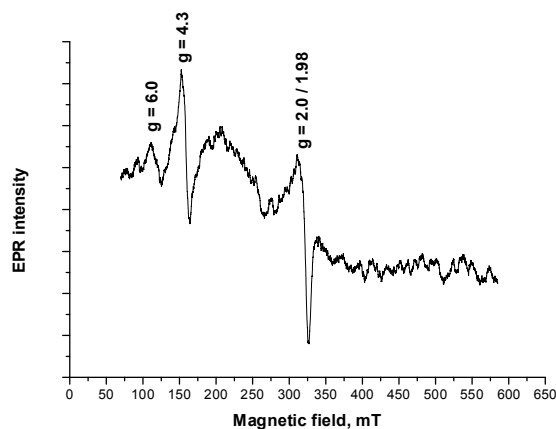


Fig. 9. EPR spectrum of blood of Chernobyl clean-up worker. (Documented dose in register - 0.02 Gy. $^{90}\text{Sr}/^{90}\text{Y}$ measured in tooth by EPR in 1997 year - 0 Bq/g).

Comparison of the EPR spectra of human blood of non-participants in Chernobyl clean-up action (Fig. 6) and spectra of Chernobyl clean-up workers (Fig. 7, Fig. 8 and Fig. 9), has confirmed the suggestion that Chernobyl clean-up workers have higher levels of methemoglobin (Fe^{3+} in high spin state) than other persons.

For the assessment of EPR spectra measured in blood samples of Chernobyl clean-up workers another etalon was used additionally. It was found that amount of Sr-90 presented in the teeth could serve as another etalon, since its contribution to the total absorbed dose varies from 20% to 50% [9, 10].

4. Summary and conclusion

These processed data show that methemoglobin level in the blood of Chernobyl clean-up workers is above normal. Maybe ion Fe^{2+} in hemoglobin is oxidized to the Fe^{3+} in human by radiation. In this case it is possible that the source of radiation is $^{90}\text{Sr}/^{90}\text{Y}$ or other radionuclides absorbed in teeth and bones of Chernobyl clean up workers during the clean-up action. Examining the health status of liquidators, determined pathologies can be related to the presence of higher levels of strontium and other radionuclides in the body.

The enhanced level of transferrin in the human blood is a subject of investigation since it plays a significant role in vital functions of human organism. EPR can detect the concentration of methaemoglobin and transferrin ions in human blood more precisely than any other technique does.

5. Acknowledgements

This work was supported by the Latvian Government grants (Nr. 09.1213), The Latvian State Research Program "Development of innovative multifunctional materials, signal processing and information technology for competitive science-intensive products" project No. 4 "New materials and technologies for evaluating biological tissue, and replace"

6. References

1. M.K. Pulatova, V.L. Sharygin, T.G. Shlyakova, A.E. Sipyagina, A.M. Wasserman, Use of EPR spectroscopy to check the changes in organism radioresistance. Clinical results Biophysics Volume 54, Number 2, 223-231, DOI: 10.1134/S0006350909020183 Original Russian Text © M.K. Pulatova, V.L. Sharygin, T.G. Shlyakova, A.E. Sipyagina, A.M. Wasserman, 2009, published in Biofizika, 2009, Vol. 54, No. 2, pp. 323–333.
2. Dreval', V.I., Sichevskaia, L.V., "Exposure to ionizing radiation decreases hemoglobin binding to erythrocyte membrane." Biofizika 45(6), 1086–1088 (2000).
3. Geoffrey, P., Jacobs, "A review on the effects of ionizing radiation on blood and blood components." Radiat. Phys. Chem. 53 (5), 511–523 (1998).
4. Puchala, M., Szweida-Lewandowska, Z., Kiefer, J., "The influence of radiation quality on radiation-induced hemolysis and haemoglobin oxidation of human erythrocytes." J. Radiat. Res. (Tokyo) 45 (2) 275–279 (2004).
5. H-Y.N. Holman, R. Goth-Goldstein, E.A. Blakely, K. Bjomstad, M. C. Martin and W.R. McKinney. "Individual human cell responses to low doses of chemicals studied by synchrotron infrared spectromicroscopy" In: Biomedical Spectroscopy: Vibrational spectroscopy and other novel techniques; A. Mahadevan-Janen, G.J.Puppels, eds., Proceedings of SPIE, 57-63 (2000).
6. Oshtrakh M.I., "Comparison of the oxyhemoglobin deoxygenation and radiolysis by γ -rays and electrons: Study by Mössbauer spectroscopy". Nucl. Instr. and Meth. in Phys. Res. B 185 129–135 (2001)
7. Ahmed Mohamed Maghraby, Maha Anwar Ali, "Spectroscopic study of gamma irradiated bovine haemoglobin" Radiation Physics and Chemistry 76 1600–1605 (2007).
8. Magdalena Komorowska, Anita Krokosz, Zo. a Szweida-Lewandowska, "Radiation damage to human erythrocytes: Influence of the composition of medium" Radiation Physics and Chemistry 76 1587–1593 (2007).

9. Mironova-Ulmane N, Pavlenko A, Zvagule T et al. (2001) Retrospective dosimetry for Latvian workers at Chernobyl. *Radiat. Prot. Dosim.* 96:237-240
10. Mironova-Ulmane N, Pavlenko A, Eglite M et al. (2005) Chernobyl clean-up workers: 17 years of follow-up in Latvia. *Recent Advances in Multidisciplinary Applied Physics*, pp.9-19, Elsevier 2005 (ISBN 0 08 0444 696-5)
11. Svistunenko, D.A., Davies, N.A., Wilson, M.T., Stidwill, R.P., Singer, M. and Cooper, C.E. (1997a). Free radical in blood: a measure of haemoglobin autoxidation in vivo? *J. Chem. Soc. Perkin Trans. II* 2539-2543
12. Svistunenko, D.A., Patel, R.P., Voloshchenko, S.V. and Wilson, M.T. (1997b). The globin-based free radical of ferryl hemoglobin is detected in normal human blood. *J. Biol. Chem.* 272, 7114-7121

BEHAVIOR OF BLOOD CELLS BEING IN CONTACT WITH HYDROXYAPATITE-COATED TITANIUM PLATE WITHIN AN HOUR

Alevtina LEICE*, Yuri DEKHTYAR**, Natalya BRITZINA***

*Latvian University P. Stradins Medical College, Latvia; **Riga Technical University, Latvia; ***Latvian University Institute of cardiology, Latvia

Abstract: Changes of 15 parameters in blood samples being in contact with the bioimplant (titanium plate, coated by hydroxyapatite layer) and undergoing blood ageing for an hour were investigated. Five consecutive measurements were analyzed. Blood exposure to the bioimplant resulted in statistically significant changes in 8 out of the 15 blood parameters. Ageing signs were obtained in 10 of them. Ageing process did not affect the influence of the bioimplant.

Keywords: blood cells, blood contact *in vitro* method, bio implant, blood ageing.

1. Introduction

The principal problem of biocompatibility of the material for tissue restitution is the issue of host response. Biomaterials can be either bio-inert or bioactive when coated by special layer creating bio surface [8, 4]. Hydroxyapatite is known as the bioactive one [1, 3, 5, 6, 8, 11]. The bio surface stimulates cell attachment and bone-implant contact in shorter time, [8] accelerates osseointegration [5], decreases platelet and erythrocytes adhesion [6, 11].

Therefore, it is very important to test implants for bioactivity by evaluating of host response [7]. Blood contact tests as initial testing for host response is usually done *in vitro*. Blood is variable material. [2]. Typically, blood samples stored with K2-EDTA at room temperature for 48 hours are aged [10, 12, 13]. The aim of this study is to reveal changes in blood parameters upon contact with titanium plate coated by hydroxyapatite layer as well as to evaluate whether these changes depend on blood ageing process which occurred during the storage for an hour. The dynamic method of consecutive measurements was applied.

2. Methods

The titanium plate deposited with hydroxyapatite (HAP) ceramic layer as bioactive material (Ti:HAP plate) was chosen for blood contact test. The 2 mm thick plates (1x2 cm²) were cut off from the titanium (grade A) tape. Then the titanium plates were washed carefully in acetone and ethanol and finally dried in air. To cover them by HAP, pulse laser deposition technique was used. A thickness of the HAP layer was equal to a couple of micrometers.

The blood specimens were tested by means of ABX Micros OT automated hematology analyzer, delivering

a standard package of 15 blood characteristics [9] including the count of red (RBC) and white (WBC) blood cells, platelets (PLT) as well as the percentages of 3 WBC subpopulations – lymphocytes (LY), monocytes (MON) and granulocytes (GRA), values of mean platelet volume (MPV), mean cell volume (MCV), mean cell hemoglobin (MCH), mean cell haemoglobin concentration (MCHC), content of hemoglobin (HGB), red cell distribution width (RDW), plateletcrit (PCT), platelet distribution width (PDW) and hematocrit (HCT). Subpopulations of white blood cells are recognized according to their size: LY are between 30 – 100 fl, MON are between 100 – 150 fl and GRA are between 150 – 450 fl [9]. The length of experiment was chosen to be an hour. The experiment was performed at room temperature. Venous blood specimens from 70 volunteers were collected in Vacutainer tubes (Becton-Dickinson) with K2-EDTA. The baseline test (1st test) of the collected specimens from each volunteer was performed. Then each of specimens was divided into two parts: "reference" (RP) and "experimental" (EP) samples.

The Ti:HAP plate was positioned within the EP, whereas, the RP was kept Ti:HAP plate free. Both EP and RP were tested simultaneously four times during an hour: on 10th, 20th 40th and 60th minute of experiment.

The differences (DIF) of 15 blood parameters from their baseline values were selected as the variables for statistics. Thus, the 1st test values were taken to be zero. DIF of the blood parameters calculated from the values at the corresponding time of testing in EP and RP samples were compared. Two-Factor analyze of variance with replication was used. This type of analysis provides 3 separate F_a - evaluates blood ageing process (time-dependent

changes), F_b – estimates the effect of the bioimplant (Ti:HAP) and F_{ab} – detects the interaction of the both. The latter confirms or rejects whether Ti:HAP influence depends on dynamic of blood ageing. Significance for F was at the $P \leq 0,05$ level.

3. Results

The differences of 15 blood parameters from their baseline values obtained within an hour are illustrated in figures 1-15.

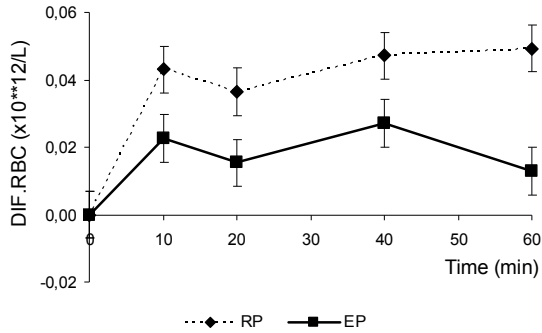


Fig.1. Changes in DIF.RBC number obtained in EP and RP blood samples

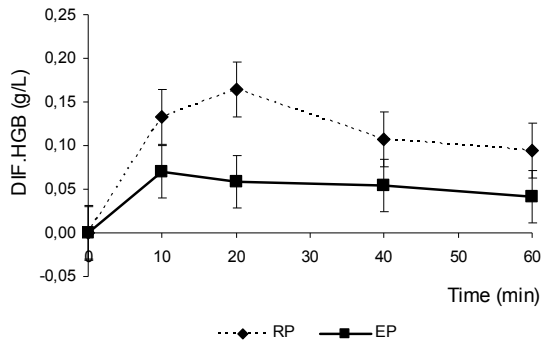


Fig.2. Changes in DIF.HGB values obtained EP and RP blood samples

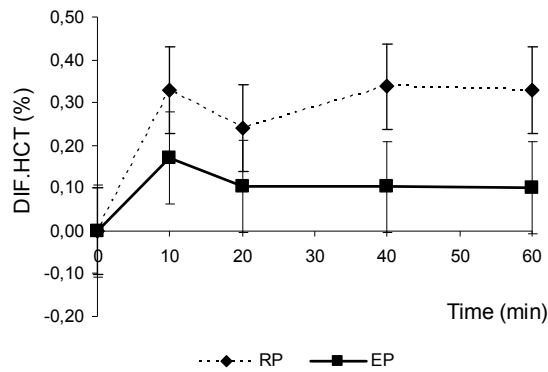


Fig.3. Changes in DIF.HCT values obtained EP and RP blood samples

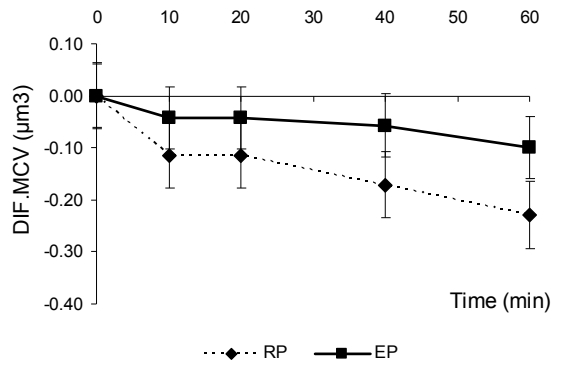


Fig.4. Changes in DIF.MCV values obtained EP and RP blood samples

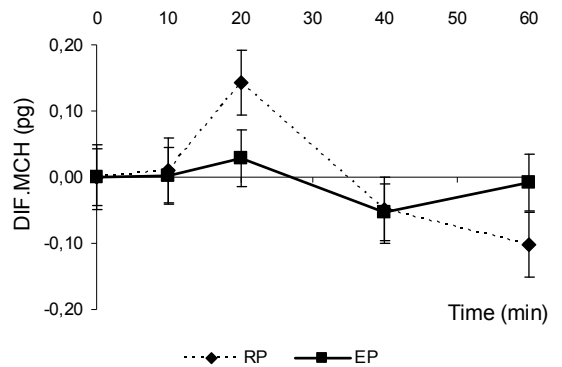


Fig.5. Changes in DIF.MCH values obtained EP and RP blood samples

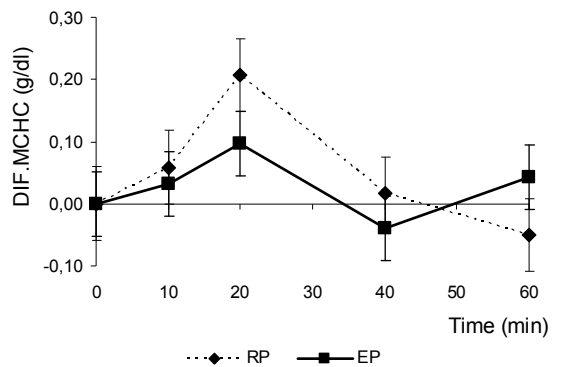


Fig.6. Changes in DIF.MCHC values obtained EP and RP blood samples

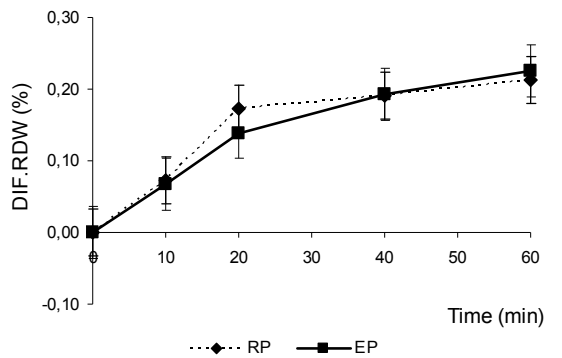


Fig.7. Changes in DIF.RDW number obtained EP and RP blood samples

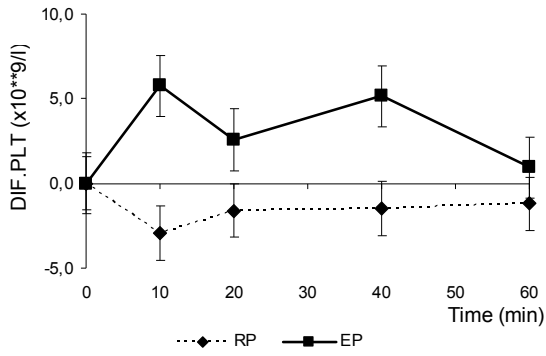


Fig.8. Changes in DIF.PLT number obtained EP and RP blood samples

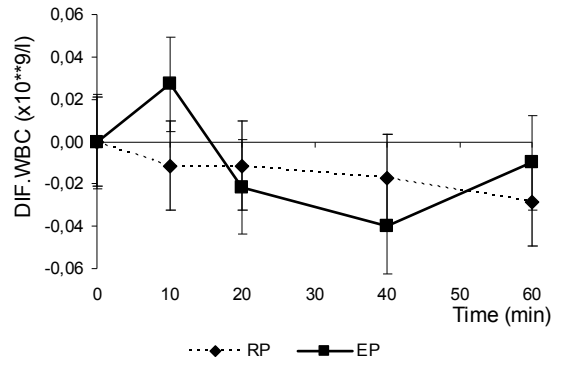


Fig.12. Changes in DIF.WBC number obtained EP and RP blood samples

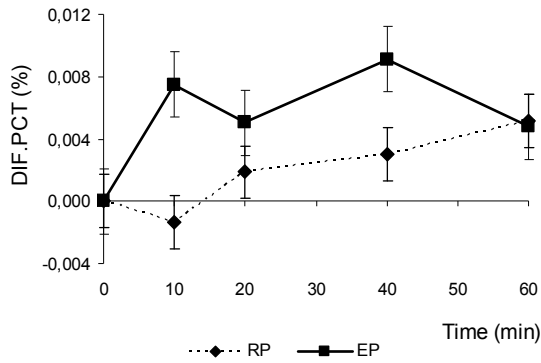


Fig.9. Changes in DIF.PCT values obtained EP and RP blood samples

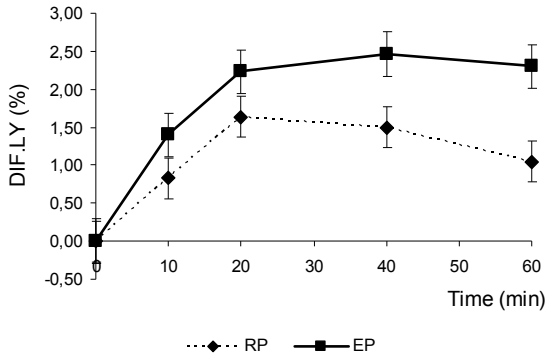


Fig.13. Changes in DIF.LY percentage obtained EP and RP blood samples

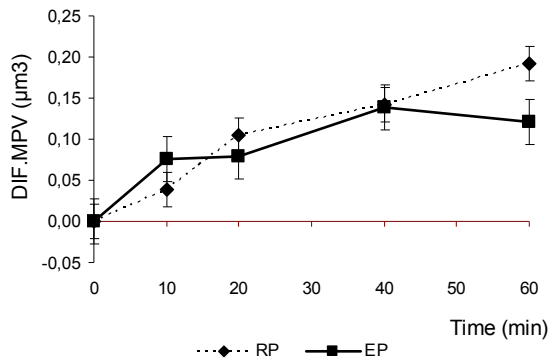


Fig.10. Changes in DIF.MPV values obtained EP and RP blood samples

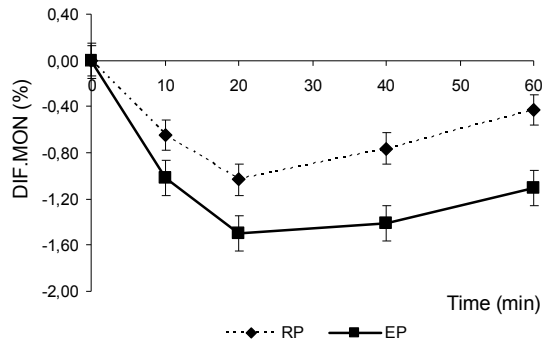


Fig.14. Changes in DIF.MON percentage obtained EP and RP blood samples

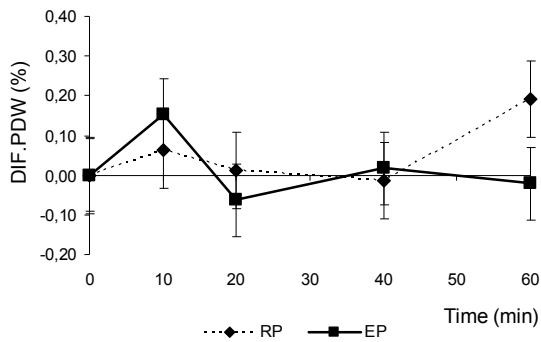


Fig.11. Changes in DIF.PDW values obtained EP and RP blood samples

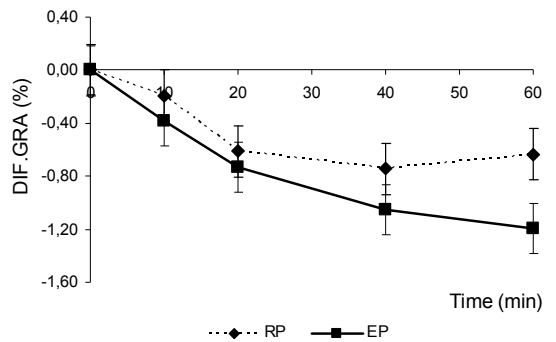


Fig.15. Changes in DIF.GRA percentage obtained EP and RP blood samples

The two-factor analysis of variances with replication provided evaluation of separate factors as well as their interaction. Analysis of five consecutive measurements allowed concluding that the blood parameter changes are time-dependent. Statistically significant F_a was revealed for five of blood parameters related to the red blood cells (DIF.RBC, DIF.HGB, DIF.MCH, DIF.MCHC, DIF.RDW), and for two of them related to platelet (i.e. DIF.PCT and DIF.MPV). There were stated statistically significant time-dependent changes in three WBC subpopulations percentages without any changes in the total WBC number (Table.1.).

Table 1. Changes in blood parameters occurring during its storage for 1 hour. Comparison of 5 consecutive measurements, obtained in blood exposed to Ti:HAP and free of it.

Blood parameter	F_b	p_b	F_a	p_a
DIF.RBC [$10^{12}/l$]	6.72	0.01	3.05	0.02
DIF.HGB [g/l]	6.69	0.01	3.42	0.01
DIF.HCT [%]	4.27	0.04	1.48	0.21
DIF.MCV [μm^3]	3.02	0.08	1.46	0.21
DIF.MCH [pg]	0.04	0.84	2.46	0.04
DIF.MCHC [g/dl]	0.25	0.62	2.4	0.05
DIF.RDW [%]	0.05	0.83	11.93	0.01
DIF.PLT [$10^9/l$]	12.88	0.01	0.41	0.80
DIF.PCT [%]	6.89	0.01	2.34	0.05
DIF.MPV [μm^3]	0.53	0.47	11.21	0.01
DIF.PDW [%]	0.26	0.61	0.62	0.65
DIF.WBC [$10^9/l$]	0.10	0.75	0.75	0.56
DIF.LY [%]	12.53	0.01	14.90	0.01
DIF.MON [%]	20.52	0.01	20.74	0.01
DIF.GRA [%]	3.24	0.03	7.40	0.01

F_a – F statistic of time-dependent changes (blood ageing);

p_a – significance level for F_a

F_b - F statistic of Ti:HAP influence;

p_b - significance level for F_b

Table 2. Changes in blood parameters occurring during its storage for 1 hour. Analysis of Ti:HAP/ageing interaction: 5 consecutive measurements, obtained in blood exposed to Ti:HAP and free of it.

Blood parameter	F_{ab}	p_{ab}
DIF.RBC [$10^{12}/l$]	0.59	0.67
DIF.HGB [g/l]	0.63	0.64
DIF.HCT [%]	0.33	0.86
DIF.MCV [μm^3]	0.25	0.91
DIF.MCH [pg]	1.02	0.40
DIF.MCHC [g/dl]	0.72	0.58
DIF.RDW [%]	0.11	0.98
DIF.PLT [$10^9/l$]	1.65	0.16
DIF.PCT [%]	1.72	0.14
DIF.MPV [μm^3]	1.08	0.37
DIF.PDW [%]	0.62	0.65
DIF.WBC [$10^9/l$]	0.50	0.74
DIF.LY [%]	1.22	0.30
DIF.MON [%]	1.65	0.16
DIF.GRA [%]	0.52	0.72

F_{ab} – F statistic of Ti:HAP/blood ageing interaction;

p_{ab} – significance level for F_{ab}

To estimate the effect of blood/Ti:HAP contact, F_b was calculated for each blood parameter simultaneously. Four of blood parameters related to erythrocytes (DIF. RBC, DIF.HGB and DIF.HCT) changed their values in different ways after having being in contact with Ti:HAP. The same was stated for DIF.PLT and DIF.PCT (platelet parameters), as well as for WBC subpopulations percentage. The changes in the total number of WBC remained statistically insignificant

To check whether Ti:HAP effect depends on dynamic of blood ageing, F statistic of interaction of both factors (F_{ab}) was calculated. The results are shown in the Table2. There was not found any statistically significant F_{ab} in any of the 15 analyzed blood parameters. This indicated that changes in blood parameters affected by the bioimplant are not related to time-dependent changes, i.e., the both processes were independent.

4. Discussion

Using host response *in vitro* as the initial testing of biomaterials faces two problems: the evaluation of changes in tissue and development of suitable methods for this purpose. The method of blood contact testing is one of the most widespread and inexpensive one. Blood tests performed *in vitro* are usually directed towards the issue of blood coagulation and lyses of blood cells. However, more detailed information about changes of blood parameters can be of interest as well.

Blood is extremely variable material. Its properties depends on many factors of individual donors, as well as on accuracy of blood drawing act, that may change the host response capabilities [2] Besides, it is well known that blood storage at room temperature is accompanied by the process that is considered as blood ageing [10,12,13].

So, the aim of the experiment was, firstly, to evaluate time-dependent changes in 15 blood parameters in condition, when blood samples were stored at room temperature for an hour, secondly, to compare changes in blood samples being in contact with the bioimplant to contact free ones and finally, to judge whether the difference in both samples depends on blood ageing process.

The titanium plate, coated by hydroxyapatite (HAP) ceramic layer is considered as bioactive material [1, 3, 5, 6, 8, 11]. Thus, it was chosen for testing. Changes in blood parameters over time of exposure to bio-implants were the subject of interest, so the differences from baseline values of blood parameters (DIF) were selected as the variables for statistics. This approach allowed ignoring the individual variances in the baseline values of blood parameters. To obtain more reliable results, 5 consecutive measurements of each blood sample have been performed.

The results of two-factor analysis of variances with replication showed that changes in 6 out of the 15 parameters differed in blood samples exposed to

Ti:HAP from exposure free ones. These 6 parameters demonstrated the signs of ageing during the storage for an hour. Platelet numbers and values of hematocrit differed in blood samples being in contact with Ti:HAP plate from contact free samples, at the same time there were no signs of systemic time-dependent changes in those parameters. On the other hand, there were 4 parameters (DIF.MCH, DIF.MCHC, DIF.RDW and DIF.MPV) with signs of blood ageing process (statistically significant F_a) but without any changes related to contact with the bioimplant.

Thus, it can be stated that changes in blood parameters under experimental conditions can be either only time-dependent or bioimplant-dependent, or both factor dependent. The obtained data suggest that blood ageing process and bioimplant-dependent process develop in different ways. This is confirmed by the lack of any statistically significant Ti:HAP/ageing factor interaction.

This phenomenon can probably be explained by changes in cytoplasmic membrane properties of blood cells. This suggestion comes from the behavior of WBC subpopulation during the experiment: pronounced changes in WBC subpopulation percentage without any changes in total WBC number. Leukocyte subpopulation measurement principles are based on different reaction of their cytoplasmic membranes to treatment by two reagents Diluent and Lyse. Those actions make the sizes of three cell types more different (one from the other) and this is the base for recognition them by hemoanalyzer [9]. The alteration of cell membrane properties that leads to the modifying reaction to Diluent and Lyse is the possible way how the automated cell classification can be changed. Those alterations take place both in the processes of blood ageing and during the contact with Ti:Hap but their modes are probably different.

5. Conclusions

1. Blood exposure to titanium coated by hydroxyapatite layer resulted in statistically significant changes in erythrocyte and platelet number as well as in alteration of leukocyte subpopulation percentages leaving unchanged the total white blood cell numbers.
2. Blood sample storage at room temperature for an hour evokes changes in the number of red blood cell and percentage distribution of subpopulations of leukocytes. The changes in the number of total white blood cells remained statistically insignificant.
3. Two-factor analysis of variances showed the lack of statistically significant interaction between time-dependent and bioimplant-dependent changes in all tested blood parameters.
4. The proposed dynamic method of several consecutive measurements because of special statistical approach appeared to be sensitive for detecting changes in blood cells, occurring within an hour of contact with bio-implant.

6. References

1. Bermúdez-Reyes B., Espinoza- Beltrán F. J., Espitia-Cabrera I. and Contreras- García M. E. Characterization of HA/ZrO₂-Base Bilayer on 316L Stainless Steel Substrates for Orthopedic Prosthesis Applications. *Advances in Technology of Materials and Materials Processing Journal*, 9[2] (2007) 141-148.
2. Black J. and Hasting G. *Handbook of Biomaterial Properties*. CHAPMAN HALL, 1998; 590p.
3. Cannas M., Denicolat P., Webb L.X., Gristina A.G. 1988. Bioimplant surfaces: Binding of fibronectin and fibroblast adhesion. *J.Orthop. Res.* 7. pp. 316–325.
4. Kononen M., Hornia M., Kivilahti J., Hautaniemi J., et al. Effect of surface processing on the attachment, orientation, and proliferation of human gingival fibroblasts on titanium. *J. Biomed. Mater. Res.* 1992. 26, No 10. pp. 1325–1341.
5. Nishimura Ichiro et al. Discrete deposition of hydroxyapatite nanoparticles on a titanium implant with predisposing substrate microtopography accelerated osseointegration. *2007 Nanotechnology* 18 245101 (9. pp).
6. Pakr JY. Davies JE. Red blood cell and platelet interactions with titanium implant surfaces. *Clin Oral Implants Res.* 2000 Dec;11(6):530-9.
7. Sajuata V. Bhat. *Biomaterials*. 2002, Springer, 265p.
8. Schuler M., Gethin Rh. Owen, Douglas W. Hamilton, Michael de Wild, Marcus Textor. Biomimetic modification of titanium dental implant model surfaces using the RGDSP-peptide sequence: A cell morphology study. *Biomaterials Volume 27, issue 21, July 2006*. pp. 4003 – 4015.
9. Hematoloģijas analizators ABX MICROS OT. (Hematology analyzer ABX MICROS OT). Invitros SIA. Lietotāja instrukcija., 2000. 98 lpp.
10. LaFayette N., et al. An *in vitro* method for assessing biomaterial-associated platelet activation. *ASAIO J.*, 2007. 53. pp.159–162.
11. Viayanand K., Deepak K. Pattanayak, T.R. Rama Mohan and R.Banerjee. Interpreting Blood-Biomaterial Interactions from Surface Free energy and work of Adhesion. In: *Trends Biomater. Artif. Organs*. 2005. Vol 18 (2).
12. Vienken J. The need for a systems approach in biomaterials testing. *MDT*. 2007. September , Germany. <http://www.device-link.com/mdt/archive/07/09/004.html>
13. Vogelaar, S.A., Posthurma, D., Boomsma, D. & Kluff, C. Blood sample stability at room temperature for counting red and white blood cells and platelets. *Vascular Pharmacology*, 2002, 39, pp. 123-125.

DATA PROCESSING FOR CONNECTION BETWEEN HARD COSMIC RAY FLUX VARIATIONS AND HUMAN HEALTH DISORDER ANALYZING

Dmitrijus STYRA*, Ana USOVAITĖ*, Jelena STANKEVIČ*
* Vilnius Gedimino Technical University, Saulėtekio al. 11, LT-10223

Abstract: The prognostic connection between a decrease of hard cosmic ray flux (HCRF) and human health, especially leaps in cardiovascular disease (CVD) occurrence within 1–3 days is well known. In addition, now the authors begin to analyze the relationship between geomagnetic parameters (HCRF) and other human state parameters - trauma cases and the total number of emergency calls. HCRF and medical data are analyzed in period 2001 – 2010 and it is a large amount of data. Authors offer data processing system design with three main parts: database management system, client part and results visualization by the suitable method.

Keywords: Hard cosmic rays flux, medical calls, cardio-vascular diseases, database.

1. Introduction

Hard cosmic rays flux (HCRF) variations can be used as an indirect human health indicator. The prognostic relationship between a decrease of HCRF and subsequent leaps in cardiovascular disease (CVD) occurrence within 1–3 days is well known (Styra et al. 2005, 2008, 2009).

HCRF can be use for human health warning pathology prediction. People, who have any cardiovascular pathology, are very sensitive to the environment and its obvious changes. In addition, now the authors analyze the relationship between geomagnetic parameters (HCRF) and trauma cases and the number of total emergency medical calls. The similar information (e.g. solar radiation) for research frequently are obtained from different free access databases (Pagola et al. 2010, De Ruysscher et al. 2010).

Therefore, for analysis the database system is necessary. This systems implementation is described in the paper.

2. HCRF values data processing

HCRF values are measured continuously through 15 minutes intervals by computerized gamma spectrometer. The special software AnGamma 3.24 manages spectrometer work. Data of many years was accumulated and it was necessary to transform in XLS (Excel) format.

2001-2010 HCRF data was analyzed in four ranges of energies. Altogether initial HCRF data contained more than 700,000 records. So, nine years of real data are available with a high quality. These are large amounts of data and that must be prepared for further processing and using. This is the only way possible to make the proper, intended for current research, data array. The main feature of developed system of data processing is requirement to work with very large volumes of the data though there isn't any concerning difficult mathematical calculations (Styra et al. 2005, 2008, 2009).

Initial data of HCRF measurements must be arranged so that we must continue to work with its and it would be possible:

- 1) To use HCRF measurements value of certain date;
- 2) To show how HCRF change in different time intervals: one hour, day, month and year;
- 3) To prepare the data for further work.

For this purpose the original database was created, allowing work with the data in period 2001 – 2010. The database consists of three data sets:

- 1) For each hour HCRF values;
- 2) For each day HCRF 1-h time interval averages;
- 3) For each month HCRF 1-h time interval averages.

At first, it was developed an algorithm for the intermediate calculations - for each hour of each HCRF values and each day HCRF 1-h time interval averages data arrays formation.

Three main data arrays were developed. The general data-processing algorithm is shown in Figure 1.

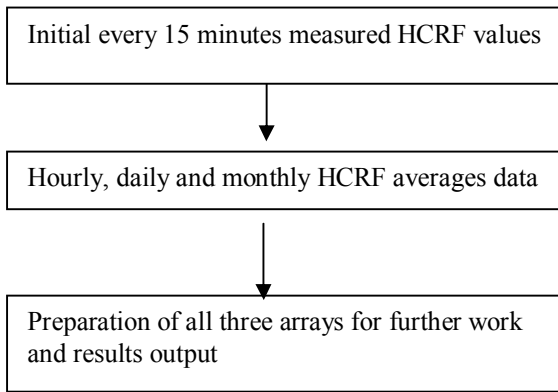


Fig. 1 HCRF data processing algorithm

3. Human health disorder data arrays formation

Medical data were obtained from the Vilnius ambulance service. In this paper used 2001 January - July 2010 period data:

1. Total number of emergency calls;
2. Cardio-vascular diseases data;
3. Trauma cases data.

Emergency calls data array formation algorithm is shown in Figure 2:

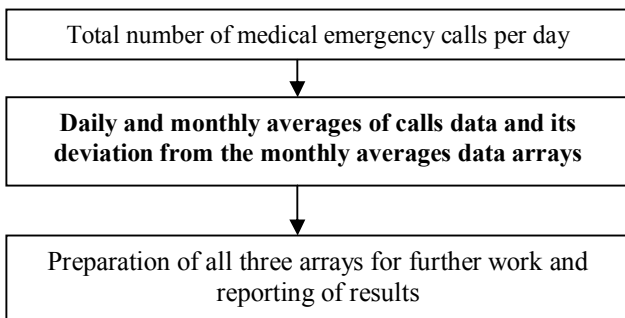


Fig. 2 Emergency calls data processing algorithm

In the same way cardiovascular diseases data and trauma cases data are processed. All incidence data is stored in XLS file format.

4. System design and implementation

For computerized work with the given data it was necessary to choose software components.

The main requirements for the system are:

1. To store large data arrays;
2. To use only the computer equipment in our disposition;
3. To process and visualize the data;
4. To allow concurrent access by multiple users;
5. To offer usable interface.

System functionality is given in use case diagram (Fig. 3).

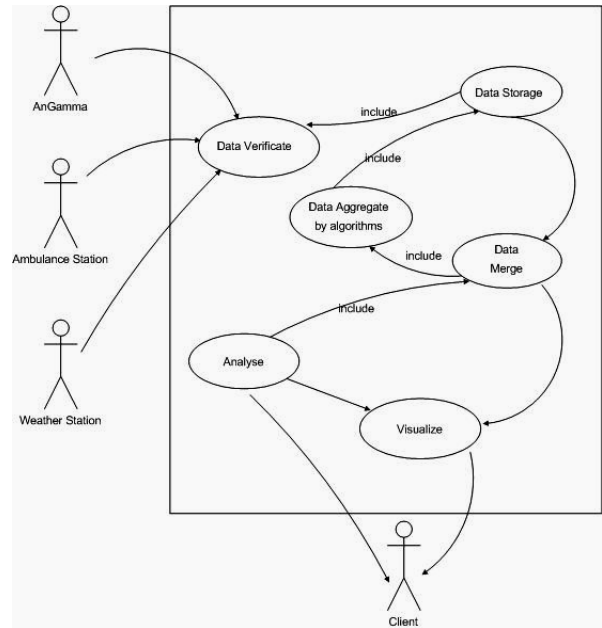


Fig. 3 System functionality

Client-server architecture was chosen for this system (Fig. 4).

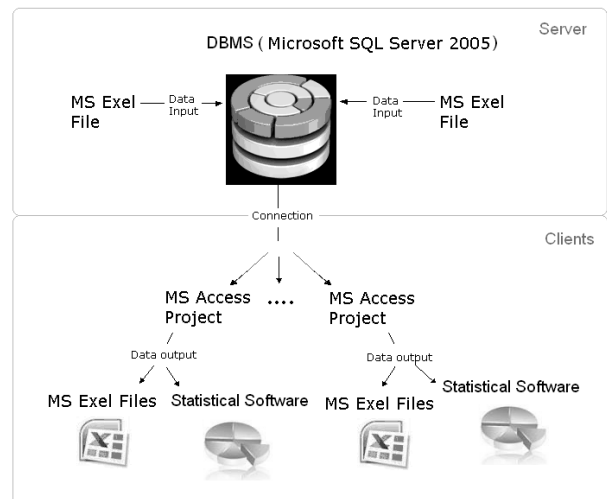


Fig. 4 System architecture

System implementation consists of three parts:

1. To choose database management system (DBMS) and create database for storing the data. This data are imported into the database from MS Excel files.

2. To develop MS Access project connected to the created database. This is system client part which can be installed on several users' computers. Therefore, such a solution of the task was chosen. Forms and reports are used for interface creation. If it is necessary the results may be exported to Excel file or to statistical software chosen one.

3. Then the results are visualized by the suitable method.

The combination of all these different program components makes the system appropriate for almost any our needs.
The system report with data visualization example is given in Figure 5.

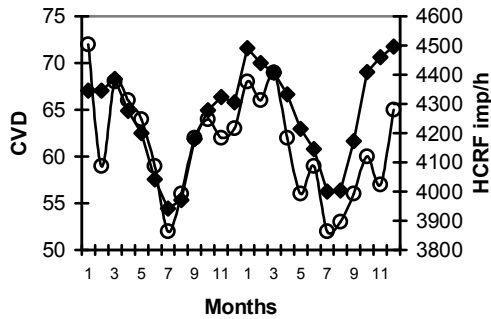


Fig. 5 Average monthly values in Vilnius in 2008 – 2009; ○ - cardiovascular diseases (1), ■ - hard cosmic ray flux (2).

The results of average monthly value produce analogical course of HCRF and CVD with maximum in winter and minimum in summer time (Fig. 5, curves 1 and 2).

Changes of HCRF values on 2 January 2001 are shown in Figure 6.

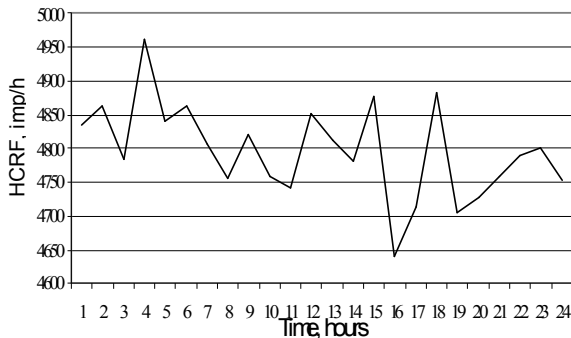


Fig. 6 HCRF values in hourly intervals on 2 January 2001.

5. Conclusions

HCRF and medical data are analyzed in period 2001 – 2010 and it is a large amount of data. In this work the data processing system to quick and simple work the data from different source has been proposed. Originally, HCRF data were in 15 minutes frequency, medical data were in daily one, therefore the respective data integrates and daily and monthly values were calculated to do the analysis. The obtained results show the usefulness of the system for initial studies of relationship between hard cosmic rays flux variations and medical data.

6. References

1. De Ruyscher D et al. First report on the patient database for the identification of the genetic pathways involved in patients over-reacting to radiotherapy: GENEPI-II. Radiotherapy and Oncology, 2010.
2. Pagola I., Gastón G., Fernández-Peruchena C., Moreno S., Ramírez L. New methodology of solar radiation evaluation using free access databases in specific locations “Renewable Energy”, 35 (2010), p. 2792-2798.
3. Styra D, Chuchelis A, Usovaite A, Damauskaite J. On possibility of short-term prognosis of cyclonic activity after-effects in Vilnius by variation of hard cosmic rays flux. J Environ Eng Landsc Manage 16, 2008, 159–167.
4. Styra D, Gaspariunas J, Usovaitė A, Juozulynas A. On the connection between hard cosmic ray flux variation and changes in cardiovascular disease in Vilnius city. Int J Biometeorol 49, : 2005. 267–272.
- Styra D, Usovaitė A, J. Damauskaite, Juozulynas A. Leaps in cardiovascular diseases after a decrease of hard cosmic ray flux and atmospheric pressure in Vilnius city in 2004–2007. Int J Biometeorol 53, 2009. 471–477

THE RADIATION SAFETY OF EDUCATIONAL NEUTRON LABORATORY

Rita PLUKIENĖ, Artūras PLUKIS, Laurynas JUODIS, Vidmantas REMEIKIS
Center for Physical Sciences and Technology, Savanoriu 231, 02300 Vilnius, Lithuania

Abstract. Exposure from radioactive nuclear substances can pose a risk of adverse health effects. All employees of educational institution and students involved with the use of nuclear substances and radiation devices are required to follow established procedures for the possession, safe use, transfer and disposal of these substances and devices. According to the IAEA recommendations the radiation dose levels should be kept as low as reasonably achievable (ALARA Principle) and below the allowed exposure limits [1].

In this work we address the above introduced problem concerning the future neutron laboratory, which is previewed in the CPST (Center for Physical Sciences and Technology) for educational purposes. The possible risk in terms of dose levels was estimated at the PuBe and Cf neutron sources storage container, experimental hall with neutron sources and adjacent laboratory room for equipment and student practical works. These estimations also serve as guidelines for the neutron laboratory design in the preparation stage.

Keywords: neutrons, dose rate.

1. Introduction

Neutrons are neutral particles with no charge and because of this they can penetrate many materials very easily. They do not produce ionization directly, but their interaction with atoms can give rise to alpha, beta, gamma or X rays which produce ionization. Neutrons can only be stopped by thick masses of concrete, water, polyethylene or paraffin.

The Educational Neutron Laboratory (ENL) at the CPST will be created to house PuBe and Cf neutron sources (together forming 10^8 n/s of total activity) and possibly the neutron generator. It will be situated on the first floor of the building which construction initially was designed for work with various kinds of radiation. In the neutron laboratory the student practical works of specimen irradiation, life time experiments, coincidence measurements and other experiments will be performed. The goal of the work is to estimate the dose levels of the laboratory and evaluate the radiation safety condition because this influences different routine and monitoring scheme. If radiation dose does not exceeds $12 \mu\text{Sv/h}$ it is accepted as common laboratory without additional means of radiation controlling system, if the dose level exceeds $56 \mu\text{Sv/h}$ – the requirements for such II category laboratory is more strict and includes additional monitoring and radiation control system with time limit for work in the place, special permissions to enter the zone, safety control, personal dose monitoring etc. We have evaluated the dose levels at the PuBe and Cf neutron sources storage container, experimental hall

and adjacent laboratory room for equipment and student practical works.

2. Modeling

For radiation safety assessment we have used MCNPX code [2] and ENDF-VI [3] cross-section libraries. The Monte Carlo N-Particle Code MCNPX was applied for neutron transport calculation and dose rate evaluation. In brief, particle transport using the Monte Carlo technique is based on the explicit tracking of particles following each particle from a source throughout its life to its death (by parasitic absorption or escape). Probability distributions are randomly sampled using transport data. In calculations these distributions are used to determine the type of interaction, energy of particles if it scatters, leakage of particles and number of neutrons produced if fission occurs. The dose rate was obtained using detector calculation tallies and energy deposition to dose conversion factors. For the neutron sources, secondary gamma photons mostly produced in the (n,γ) reactions must be taken into account. It is possible to do simultaneous coupled neutron-gamma transport calculations using MCNPX code.

MCNPX was used in evaluation of radiation shielding of RBMK-1500 reactor spent nuclear fuel containers [4] and in modeling of several nuclear experiments: AVF 65 γ^0 -ray beam (1-10 MeV) transport, HIMAC and ISIS 800 – high energy neutron (20-800 MeV) transport in iron and concrete [5].

The neutron sources of two types are previewed in the laboratory – 4 $^{239}\text{PuBe}$ sources of the total activity of $5.7 \cdot 10^7$ n/s and one spontaneous fission ^{252}Cf source ($\sim 2 \cdot 10^7$ n/s). The total activity of neutron sources was taken conservatively 10^8 n/s. The neutron source storage container is the 1.8 m depth underground cylindrical well of 0.6 m diameter, filled by polyethylene matrix as moderator. The neutron sources are placed in central channel of the well and two vertical experimental channels are situated 15 cm and 20 cm from the source to obtain different neutron flux characteristics during irradiation experiments. The simplified scheme of storage container of the neutron sources is presented in Fig. 1.

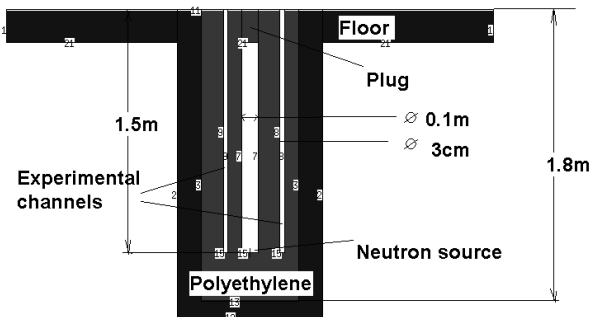


Fig. 1. The simplified scheme of the underground storage container for neutron sources.

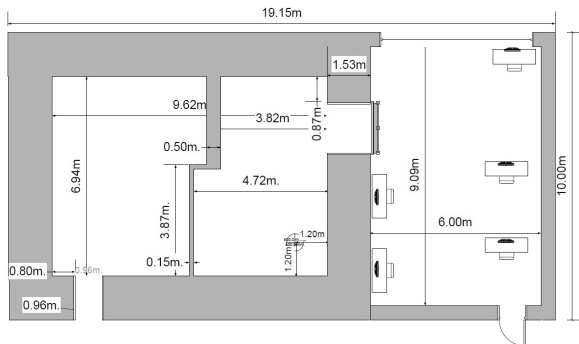


Fig. 2. The neutron laboratory scheme with underground neutron source in the middle (marked by circle).

The ENL scheme is presented in Fig. 2. The neutron sources storage container is placed in the right corner of the experimental hall, which concrete walls are 1.54 m of thickness specially designed for the radiation shielding purposes. The experimental hall is subdivided in two rooms by thin walls (part of wall is 50 cm and other part is 15 cm thickness) for neutron generator or other equipment. The equipment and student room is behind the experimental hall and connected by the door 1.74 m of width. This door is additionally shielded by the movable trolley filled with polyethylene or paraffin. The second door opening is from the experimental hall to the corridor. In this calculation concrete density was taken 3 g/cm^3 and polyethylene density – 0.9 g/cm^3 .

3. Results

The radiation safety has been evaluated in terms of neutron and photon doses in case of inserted in the storage container and open neutron source as well as

neutron flux distribution in the experimental hall and surrounding.

The calculated neutron doses rates in the case of inserted in the storage container and neutron source are presented in Table 1. The central channel of the moderator tube can be plugged with the 50 cm of polyethylene. In this case one or two of the side channels will be used for activation of samples. The dose rates are less than $0.1 \mu\text{Sv/h}$, when the plug is inserted. In order to obtain the high fluxes of the fast neutrons, plug must be removed. In this case dose rate on the ground level above the source is more than 0.6 mSv/h . Fortunately, one does not need to stay directly above central hole, and time for changing samples is less than 10 seconds. The neutron dose rates for unshielded neutron source situated on the ground level are presented in Table 2. At vicinity of the source they are in order of few mSv/h , but on the other side of the shielding wall and if door is closed by the polyethylene shield (trolley) of 30 cm thickness, dose rates are less than $0.01 \mu\text{Sv/h}$. One must take into account, that experiments outside shielding most probably will use one smallest PuBe source with 10^5 n/s activity, so resulting doses will be two orders of magnitude lower, but for the 10^8 n/s activity neutron source – the additional shielding means should be implemented.

Table 1. Neutron dose rates in the various positions of the laboratory when neutron source is placed in the storage container.

Position	Dose rate $\mu\text{Sv/h}$
At ground level unplugged	640
At 1.5 m height unplugged	140
At ground level with 50 cm of thickness polyethylene plug	0.07
At 1.5 m height polyethylene plug	0.02
At ground level 0.5 m from the source channel	0.01

Table 2. Neutron dose rates in the various positions of the experimental hall during experiment with open neutron source* on the ground level.

Position	Dose rate $\mu\text{Sv/h}$
At 3.64 m height above neutron source (on the ceiling)	461
At ground level on the wall 1.2m from the source	$2.1 \cdot 10^3$
At 1.5 m height on the wall 1.2m from the source	$1.5 \cdot 10^3$
At ground level behind the wall	0.009
At 1.5 m height behind the wall	0.0035
At 1.5 m height behind the open door	37
At 1.5 m height behind the closed door	0.002
At 1.5 m height behind 50cm of thickness wall opposite the door	22
At 1.5 m height in the corner of thin walls intersection	83
At 1.5 m height behind 15 cm wall	118
At 1.5 m height behind the open door to the corridor	3

*the ^{252}Cf ($\sim 10^8$ n/s) neutron source was used in the present calculation

The photon dose rates for unshielded neutron source are presented in Table 3. The photons make additionally about 1% of the neutron dose in the case of weak (i.e. thin wall) or no shielding (i.e. open door), on the other hand in the case of strong shielding (i.e. 1.53 m concrete wall) the photons dose is comparable (makes about one third of the neutron dose).

Table. 3. Photon dose rates for various positions in the experimental hall during experiment with open neutron source on the ground level.

Position	Dose rate $\mu\text{Sv/h}$
At 1.5 m height behind the wall	0.001
At 1.5 m height behind 50 cm wall opposite the door	0.3
At 1.5 m height in the corner of thin walls intersection	0.6
At 1.5 m height behind 15 cm wall	0.6
At 1.5 m height behind the open door to the corridor	0.05

The neutron distribution in the experimental hall and around in the case of open neutron source is presented in Fig. 3. It is obvious that the highest neutron propagation is in the ambience of the neutron source, but also in the room separated by the thin wall and in the adjacent laboratory. The neutron leakage is observed behind the door – the larger shielding should be implemented at the entrance to the laboratory and also the shielded or permanently closed with concrete wall door opening from the experimental hall to the corridor should be considered. The neutron flux distribution also shows that the building construction of the experimental hall is sufficient to block the neutron propagation in the surrounding premises.

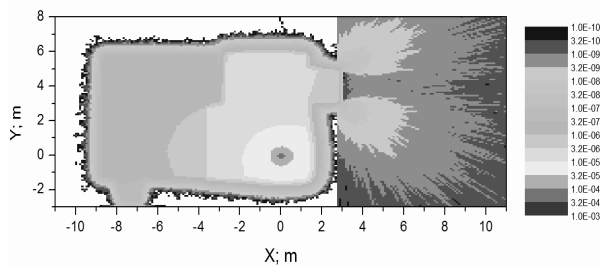


Fig. 3. The neutron flux (a.u.) distribution in the experimental hall, adjacent laboratory and corridor in the case of open neutron source.

4. Conclusions

The radiation safety evaluation of the future neutron laboratory (CPST, Vilnius) has been performed using MCNPX code. During activation experiments, if the central experimental channel with neutron source is plugged, the neutron dose rate is less than $0.1 \mu\text{Sv/h}$ i.e. less than natural background. There is no potential risk for students or personnel in adjacent laboratory or corridor even using unshielded 10^5 n/s source, but in case of 10^8 n/s activity neutron sources (i.e., ^{252}Cf source is used) – the additional shielding means should be implemented. It was estimated, that photons forms about one third of the dose when neutron shielding is strong, but their input is negligible (about 1%) in case of weak shielding. The neutron flux distribution shows that the building construction of the experimental hall is sufficient to block the neutron propagation in the surrounding premises, but the special attention should be paid on the door openings, they should be shielded carefully to avoid neutron leakage at the edges.

5. References

1. "Safety Assessment for Facilities Activities" IAEA Safety Standards Series No. GSR Part 4 International Atomic Energy Agency, Vienna (2009).
2. Briesmeister, J.F., A General Monte Carlo Code for Neutron and Photon Transport, Version 4B. Report LA-12625-M. Los Alamos National Laboratory, New Mexico (1997).
3. J.S. Hendricks, S.C. Frankle, and J.D. Court, *ENDF / B-VI data for MCNP*, Los Alamos National Laboratory Report LA-12891 (1994).
4. A. Plukis, R. Plukienė, V. Remeikis, R. Davidonis, P. Kučinskis and D. Ridikas "Evaluation of radiation shielding of RBMK-1500 reactor spent nuclear fuel containers using MCNP5", *Lithuanian Journal of Physics* Vol. 46, No. 3, pp. 367-374. (2006).
5. A. Žukauskaitė, R. Plukienė, A. Plukis, and D. Ridikas „Modelling of neutron and photon transport in iron and concrete radiation shieldings by the Monte Carlo method” *Lithuanian Journal of Physics* Vol. 47, No. 1, pp. 97-102. (2007).

TEACHING OF MEDICAL PHYSICS TO MEDICAL, DENTAL, HEALTHCARE AND BIOMEDICAL ENGINEERING STUDENTS IN THE CZECH REPUBLIC

Vojtěch MORNSTEIN*, Daniel VLK*, Carmel J. CARUANA**

*Department of Biophysics, Medical Faculty, Masaryk University, Brno, Czech Republic; **Biomedical Physics, Faculty of Health Sciences, University of Malta, Malta

Abstract: We present an overview of the development of the biomedical physics component of programmes for medical, dental, healthcare and biomedical engineering students in faculties of medicine in the Czech Republic. With medical, dental and healthcare students, we focus on the effective and safe use of biomedical devices, whilst for engineering students we concentrate on general biophysics and on devices which are not encountered in engineering courses such as optical devices (e.g., endoscopes and microscopes).

Keywords: Biomedical physics, Medical physics, Biophysics, Biomedical engineering, Education, Czech Republic

1. Introduction – history

In the Austro-Hungarian Empire, the teaching of medical physics (i.e. physics for medical students) started in the 50' of 19th century. The teachers were physicists working in philosophical faculties at this time. At the beginning, the same syllabus was delivered to both students of medicine and physics. This led to complaints from students of both medicine and physics. The situation changed after the arrival of the famous professor Ernst Mach from Graz to Prague. Special lectures on physics were introduced for students of medicine and pharmacy. They were of relatively small extent – 2 semesters, each with 5 hours of lectures for both the German and Czech part of Charles University.

Masaryk University in Brno was founded in 1919 and its Medical Faculty in 1920. Physics became a regular part of curriculum, and was taught by Czech professors of physics coming from the Faculty of Sciences of the university or from Brno Technical University. The first author of a Czech textbook on Medical Physics was professor Viktor Teissler (published in 1937). He worked in Bratislava and later also in Brno (after World War II, as Czech universities were closed by Nazis for six years).

The other Czech medical faculties were founded after the war and the development of medical biophysics was accelerated. The educational process was completed with the introduction of practical laboratory classes. Originally experiments consisted of measurements of basic physico-chemical, electrical and optical quantities. Starting from about the 70' of the 20th century the practical exercises were gradually oriented to problems closer to medicine, demonstrations of medical devices started, and later the

students could perform also some simple physical examinations as regular laboratory tasks (e.g., measurement of blood pressure, determination of visual acuity or skin impedance).

The departments of Medical physics were also growing, and started involving themselves in research activities. Before the World War II. the departments were usually represented only by one professor, 1-2 volunteer assistants and one craftman or academic technician. Today numbers of employees exceed ten in most departments. Partly due to Soviet influence, partly due to major progress in molecular sciences, Medical Physics was renamed as Medical Biophysics. Its syllabus was also oriented more in direction of general, molecular and physiological biophysics. This trend was finally broken in the last 10-15 years in most of the departments, and the subject (denoted still as biophysics) is gradually reorienting on the safe, efficient and effective use of medical devices. Thus, we are in full agreement with the latest recommendations published by Caruana et al. [1,2]. The Czech community of medical biophysicists was informed about this activity also in a Czech language journal [3]. The latest achievement of our community is the foundation of the Czech Society of Medical Physics which is associated with the Czech medical society of Jan Evangelista Purkyně.

2. Situation today

Eight medical faculties exist in the Czech Republic today and all include a medical biophysics department. They are listed in Table 1. (teaching General Medicine courses) and Table 2. (teaching also Dental Medicine courses).

Table 1. Medical Biophysics for General Medicine in Czech medical faculties

Medical Faculty (MF)	additional content	semester	lectures – labs ¹
<i>Charles Univ. Prague</i>	xxx	xxx	xxx
1st MF in Prague	-	1st	2-4
2nd MF in Prague	-	1st	2-3
3rd MF in Prague	informatics	1st	0-53 (total)
MF in Pilsen	-	2nd	3-4
MF in Hradec Králové	biostatistics	1st	41-69 (total)
MF of <i>Masaryk Univ. in Brno</i>	informatics	1st	3-4
MF of <i>Palacký Univ. in Olomouc</i>	informatics, biostatistics	1st and 2nd	60-60 (total)
MF of <i>Univ. Ostrava</i> ²	informatics	1st and 2nd	2-2

¹hours per week or total number of hours²starting this year (new faculty)**Table 2.** Medical Biophysics for Dental Medicine in Czech medical faculties

Medical Faculty (MF)	additional content	semester	lectures – labs ¹
<i>Charles Univ. Prague</i>			
1st MF in Prague	-	1st	2-2
MF in Pilsen	-	1st	2-2
MF in Hradec Králové	biostatistics	1st	23-60 (total)
MF of <i>Masaryk Univ. in Brno</i>	informatics	1st	2-0-4
MF of <i>Palacký Univ. in Olomouc</i>	informatics, biostatistics	1st	15-45 (total)

¹hours per week or total number of hours

Notice the specific situation in Charles University – there are five medical faculties, three of them in Prague. Historically, the 1st medical faculty has been oriented on General Medicine, the 2nd on Paediatrics and the 3rd on Hygiene and Preventive Medicine. Today this differentiation of focus has been reduced. The curriculum at the 3rd Medical Faculty in Prague is partly delivered using problem based learning techniques. English study programmes, identical with the Czech ones, are taught everywhere, except at the newer Medical Faculty in Ostrava, where courses started in September 2010. It is also necessary to mention that besides the students of general and dental medicine, almost all these faculties have big numbers of bachelor students of health care professions like nursing, laboratory assistants, optometrists, radiological assistants, nutrition specialists, midwives, rescuers, physiotherapists and some others. Except for physiotherapists, radiological assistants and optometrists, these study programmes involve less physics and biophysics compared to medicine, however they always include some physics in their curriculum.

The teachers in the departments of medical biophysics have background in medicine, biophysics, physics, electrical engineering and other professions such as, computer sciences, as health informatics is also often taught by these departments. The faculties in Hradec Králové and Olomouc deal also with the teaching of basic biostatistics so that they have more lectures and laboratory hours. In some faculties, health informatics or biostatistics is taught in separated courses by the same or different departments.

3. What we teach – a typical syllabus

The main task of departments of Medical Biophysics is to provide students with basic knowledge of physical principles encountered in medicine both as a background of physiological processes and as working principles of biomedical devices. Of course, to assess the risks connected with operation of diagnostic or therapeutic systems it is also necessary to understand interaction of many physical agents on the human organism. Safety problems due to ionising radiation and electric currents are emphasized. Our programme also includes health informatics which includes a wide range of topics from PC hardware and software to data mining, sharing and processing with emphasis on web tools and resources. Since the practical laboratory tasks are discussed in another contribution, we will concentrate on the content of lectures. Although there are small differences between individual faculties depending on the research interests of individual academic members of staff we are convinced that the following syllabus of lectures at Brno Medical Faculty is typical to what is found at other universities in the Czech Republic.

A) Medical biophysics in General medicine programmes

Device-oriented lectures: Medical devices - introduction, X-ray imaging, Biosignals and their processing. Thermometry, Protection of the patient from ionizing radiation and image quality outcomes in X-ray imaging, Biomolecular and cellular research devices, Magnetic resonance imaging (MRI), Infrared

imaging (thermography), Devices for electrochemical analysis, Auxiliary laboratory devices (e.g., centrifuges), Microscopy, Nuclear medicine and radiotherapy, Sensory perception examination and aids, Physical therapy, Endoscopes, tissue ablation devices and lithotripters, Nanomedical devices, Occupational safety when using medical devices, Devices for substitution and support for body organs, Ultrasound diagnostics.

Lectures on general and physiological biophysics: Structure of matter, Thermodynamic principles, Thermodynamics and life, Structure of living matter, Resting and action membrane potential, Biophysics of cardiovascular system, Biophysics of breathing, Introduction to biophysics of receptors, Biophysics of hearing and vestibular sense, Biophysics of visual perception, Safety aspects of air pressure, gravity changes and ultrasound, Biocybernetics, Healthcare informatics.

B) Medical biophysics in Dental medicine programmes

Device-oriented lectures: Medical devices - introduction, X-ray imaging, Protection of the patient from ionizing radiation and image quality outcomes in X-ray imaging, Magnetic resonance imaging (MRI), Infrared imaging (thermography), Biosignals and their processing, Thermometry, Microscopy, Nuclear medicine and radiotherapy, Physical therapy, Sensory perception examination and aids, Ultrasound diagnostics.

Lectures on general and physiological biophysics: same as in general medicine.

The syllabus used for dental medicine is rather reduced and not so strongly device-oriented. The reason is that fewer medical devices are used in dentistry. However, in some cases, diagnostic or therapeutic methods are explained for better understanding of themes taught in other courses. An overview of medical biophysics as it is taught in the Czech Republic, is internationally accessible in our textbook used in the English study programme [4].

Rigorous quality assurance has become an unavoidable part of the educational process in medicine. Unfortunately it is a time consuming activity which is considered as an obstacle for scientific research by many our colleagues. It results in abundant use of written tests and, generally, in the degradation of the teacher's role. We are convinced that student assessment in the form of written tests or essays on their own is not sufficient for accurate student appraisal. Our assessment tradition also includes an oral exam, which gives good feedback to the teacher, and the written test is used to act as an impetus for the students to prepare seriously for the oral part of the exam. After the first experiences obtained in the English study programme, we have introduced such tests also in the Czech study programme.

4. Medical physics for biomedical engineering programme

The second large group of students taught in some medical faculties are biomedical technicians. These will soon be joined also by biomedical engineers. In the past, these study programmes were fully managed by Technical Universities in Prague and Brno. To improve the understanding of medical problems, medical terminology and the health care services, these study programmes now include units taught at medical faculties. About ten biomedical science subjects are now taught and examined by departments at medical faculties. Since biomedical engineers receive tuition regarding medical devices at their own faculty we emphasize different topics such as Microscopy, Sensory perception examination and aids, Physical therapy, Endoscopes, tissue ablation devices and lithotripters, Devices for substitution and support of body organs, Structure of matter, Thermodynamic principles, Thermodynamics and life, Structure of living matter, Resting and action membrane potential, Biophysics of cardiovascular system, Biophysics of breathing, Introduction to biophysics of receptors, Biophysics of hearing and vestibular sense, Biophysics of visual perception, Safety aspects of air pressure, gravity changes, and ultrasound.

5. Perspectives

The SWOT audit methodology thoroughly performed at the European level by Caruana et al. [2] has been applied by ourselves at the local (faculty) level and used for future planning. The situation can be different in various countries so that it is not easy to give advices. Perhaps, the situation in the Czech Republic is not yet critical, because the stakeholders are aware of the need of physics as a part of the theoretical background for medicine. The main danger for Czech medical biophysics is to ignore overlapping of subject matter taught in other departments or to concentrate too much on medical informatics. The department of medical biophysics can maintain a strong position only when teaching subjects which are difficult for other departments such as physiology, chemistry or biology to deliver. It is our personal experience that such a strategy is accepted as a role our departments should play. It is becoming difficult for faculty management to ignore warnings that without certain (bio)physical (and technical) knowledge the use of biomedical devices by medical and healthcare professionals is dangerous both for patients as well as for the medical and healthcare professionals themselves. Many renowned clinicians are aware that their own ability to use physical knowledge for the improvement of patients' treatment is not sufficient for effective and safe practice. This can lead to occasional or even regular cooperation with biophysical departments.

To maintain or regain academic acceptance of medical biophysics within faculties of medicine we need to base our curricula on device oriented teaching and internationally accepted research. The academic milieu is very competitive and a biophysics which is weak on

strategy can easily be absorbed by new departments arising from the boom in basic biomolecular sciences. It is already evident (we can see that when teaching in the English study programme) that too many medical students study in medical faculties throughout different European countries without understanding basic physical concepts like energy, power, electric voltage or radioactivity. These students are coming from high schools without classes in physics and when the lack of physics is not made up in medical curricula life-threatening situations arise for patients when a communication is needed between the medical doctor and a medical physicist or technician particularly in critical care medicine situations.

Acknowledgment

This contribution is supported by a development project of the Czech Ministry of Education, Youth and Sports entitled "C42 - Inter-university co-operation in biomedical techniques and biomedical engineering using state-of-the-art technologies".

References

1. Caruana C.J., Wasilewska-Radwanska M., Aurengo A., Dendy P.P., Karenauskaite V. Malisan M.R., Meijer J.H., Mornstein V., Rokita E., Vano E., Wucherer M., The role of the biomedical physicist in the education of the healthcare professions: An EFOMP project. *Physica Medica*, 2009, vol. 25, no. 3, p. 133-140.
2. Caruana C.J., Wasilewska-Radwanska M., Aurengo A., Dendy P.P., Karenauskaite V. Malisan M.R., Meijer J.H., Mihov D., Mornstein V., Rokita E., Vano E., Weckstrom M., Wucherer M., A comprehensive SWOT audit of the role of biomedical physicist in the education of healthcare Professional in Europe, *Physica Medica: European Journal of Medical Physics*, 2010, vol. 26, p. 98-110.
3. Mornstein V., Caruana C.J., Vlk D., Škorpíková J., Forýtková L., Grec P. Teaching medical biophysics for health care profession in future, What should we teach? (in Czech) *Lékař a technika*, 2008, č. 1, s. 22-29.
4. Hrazdira I., Mornstein V., Bourek A., Škorpíková J., *Fundamentals of biophysics and medical technology*, Masarykova Universita, Brno, 2007, 317 p.

METHOD OF THE RADIONUCLIDE ACTIVITY DETERMINATION IN NUCLEAR MEDICINE SOURCES OF COMPLEX GEOMETRIES

Andrej ROŽKOV, Ruslan JERENKEVIČ, Vadim ČESONIS
JSC Lokmis Radiometry department, Visorių str. 2, LT-08300 Vilnius, Lithuania
andrejus.r@lokmis.lt

Abstract: The possibility to use the high purity germanium (HPGe) detector with a package of software for the semi-empirical modeling of the radionuclide registration efficiency and the analysis of gamma energy spectra in routine measurements in nuclear medicine laboratory is demonstrated.

Keywords: Gamma spectrometry, registration efficiency, HPGe detector, ANGLE modeling software

1. Introduction

In nuclear medicine liquid radiopharmaceutical drugs are administered to patients during diagnostic or therapeutic treatments reaching 33 million procedures worldwide annually. Radionuclide activities in most popular drug samples may be as large as 0.37-7.4 GBq per single delivery to the patient. Although the increase of radionuclide activities in drugs improves the quality of imaging procedures and may lead to the success of the radiotherapy treatment, it cannot be compromised by ionizing radiation doses given to persons [1].

The internal exposure doses to the patient due to the drug treatment may be evaluated using complicated models of the radionuclide distribution in organs of the human body. In routine laboratory operations the patient exposure is monitored by measuring the radionuclide activity prior to its administration using dose calibrators. Dose calibrators are ionization chambers coupled to a digital electronic system which gives a direct reading in units of the activity by means of calibration factors previously established by the manufacturer. Commercially available dose calibrators enable determination of radionuclide activities in drug samples with the typical measurement error of about 5% (compared to a NIST SRM geometry, 5 ml of the solution in a glass ampoule with 0.6 mm wall thickness) [2].

However, the accuracy of the radionuclide activity measurement depends on many factors, most important of them being related to the attenuation of the ionizing radiation in the container material (e.g. the type of the container, its filling volume, container position inside the ionization chamber, container material and wall thickness)

and to the measured radionuclide decay scheme. Underestimation of the above mentioned parameters may lead to the inaccurate determination of the radionuclide activity in a drug sample up to several times and, thus, may result in false results of the internal exposure dose to the patient [3, 4].

The aim of this work is to demonstrate the possibility to apply the semi-empirical modeling of radionuclide registration efficiency in order to improve the procedure of the determination of radionuclide activities in nuclear medicine samples of complex geometries.

2. Methods

The radionuclide photo peak registration efficiency in the defined measurement geometry was calculated using the semi-empirical model ANGLE (ORTEC) [5]. It uses reference efficiency curves, detector geometrical parameters and gamma attenuation coefficient databases as input data to calculate effective solid angles between the escaping gamma ray and the detector and, thus, to determine the radionuclide registration efficiency values. In this work HPGe detector parameters, used as input data in the modeling – detector height/radius, core top type/height/radius, inactive germanium top/side thickness, contact top/side thickness, contact (pin) material, end-cap top/side thickness and material, vacuum top/side thickness and housing side/top material – were taken from the detector manufacturer design records.

In order to validate modeling data, radionuclide registration efficiencies were modeled for the Marinelli beaker geometry (GA-MA Associates, model 530 G-E,

matrix density 1.0 g/cm^3) using the reference curve obtained for the certified ionizing radiation source in a close geometry (Czech metrological institute, model CBSS) The modeled radionuclide efficiency registration curve was used to calculate radionuclide activities in the certified calibration ionizing radiation source (Eckert&Ziegler Nuclitec, model EG-ML), and then compared with certified values (Table 1). The gamma energy spectrum was obtained using a coaxial HPGe detector (end-cap diameter 76 mm) and analyzed using the software GammaVision (ORTEC).

Table 1. Radionuclide activities in the reference ionizing radiation source, according to its certificate, C_r , Bq, and radionuclide activities in the source calculated using the modeled radionuclide registration efficiency curve, C_m , Bq.

Radionuclide	C_r , Bq	C_m , Bq
^{57}Co	107 ± 3	110 ± 10
^{60}Co	548 ± 16	500 ± 30
^{85}Sr	664 ± 20	660 ± 40
^{88}Y	1050 ± 30	1000 ± 60
^{109}Cd	2840 ± 91	3000 ± 20
^{113}Sn	509 ± 15	510 ± 30
$^{123\text{m}}\text{Te}$	136 ± 4	130 ± 10
^{137}Cs	459 ± 13	460 ± 30
^{241}Am	303 ± 11	290 ± 20

Results show that radionuclide activities, calculated using the semi-empirical registration efficiency curve, are in a good agreement with certified values in the range of the total measurement uncertainty.

3. Results and discussions

Registration efficiencies of radionuclides, used in nuclear medicine gamma imaging procedures, were modeled for the 10 ml serum vial (Kimble, diameter 24 mm) geometry of a varying filling volume 1-10 ml. Radionuclides included: a) ^{123}I ($T_{1/2}=13.2 \text{ h}$) emitting 158.97 keV gamma ray with the decay probability of 83.3 % and b) ^{111}In ($T_{1/2}=2.80 \text{ d}$) emitting a couple of coincident gamma rays, of which one is a 245.35 keV photon with the decay probability 94.1 %. Modeling results are given in Fig. 1.

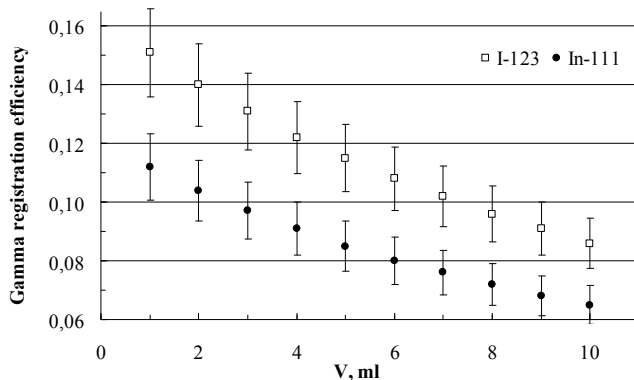


Fig. 1. Modeled ^{123}I and ^{111}In registration efficiency curves for the serum vial geometry.

Modeled curves were integrated into the gamma spectra analysis software to produce automatic reports on

radionuclide activities in samples. Apparently, ^{123}I medical source of about 1 MBq activity, placed in 10 ml serum vial, would yield a statistically reliable photo peak ($> 10\,000 \text{ cps}$) in less than a minute of the measurement time, resulting in radionuclide activity values with the total uncertainty up to 10 %, that is comparable with the performance of dose calibrators. However, in a case of complex measurement geometries (e.g. different type of the vial, its filling volume, vial position towards the detector, different vial material and wall thickness), the ANGLE software would generate the curve typically in 5 minutes, with the possibility for the immediate application in the gamma spectra analysis software – faster than compared with dose calibrator calibration and operation procedures, that may take considerable time and require additional certified calibration sources. That will result in less time for calibration procedures and, thus, in lower ionizing radiation doses obtained by the operator and in lower errors in radionuclide activity determination due to the decay half-life correction. Probably, the combination of a dose calibrator (for well defined measurement geometries) and the HPGe detector with a package of ANGLE and GammaVision software (for complex measurement geometries) would accelerate the determination of radionuclide activities with reasonable precision in drugs prior to administration to patients.

4. Conclusion

Radionuclide activity determination in medical drugs using the HPGe detector with a package of software for the semi-empirical modeling of radionuclide registration efficiency and the analysis of gamma energy spectra may be used in nuclear medicine laboratories as an additional tool to accelerate the determination of radionuclide activities with reasonable precision in medical sources of complex geometries prior to their administration to patients.

5. References

1. United Nations Scientific Committee on the Effects of Ionizing Radiation. Sources and effects of ionizing radiation. New York: United Nations, vol. 1, 202 p. (2008).
2. Capintec CRC-25R dose calibrator owner's manual. Ramsey: Capintec, rev. B, 220 p. (2007).
3. Cahoun J., Golas D., Harris S. Effects of varying geometry on dose calibrator response: cobalt-57 and technetium-99m. Journal of Nuclear Medicine, vol. 28 (9), 1478-1483 (1987).
4. Strigari L. *et al.* Comparison of methods to determine accurate dose calibrator activity measurements. Journal of Experimental and Clinical Cancer Research, vol. 27 (14), p. 1-6 (2008).
5. ORTEC ANGLE Semiconductor Detector Efficiency Calculation User Guide, 931077, 44 p. (2008).

AUTHOR INDEX

- Adlienė D., 119, 130, 133
Adlys G. A., 122, 126
Andrijaitienė V., 130
Aurengo A., 87
Back S. A. J., 14
Britzina N., 142
Bumbure L., 25
Caruana C. J., 78, 83, 87, 153
Česonis V., 157
Dahlberg L., 101
Dekhtyar Yu., 25, 142
Dendy P. P., 87
Gabrusheva N., 137
Geber T., 105
Gillis S., 35
Gricienė B., 109
Griškevičius R., 11
Gunnarsson M., 105
Holstein H., 31
Ilie A., 62
Ilves P., 95
Jakštas K., 112
Jakubovskij E., 11
Jerenkevič R., 157
Juodis L., 150
Juzėnas P., 71
Karabanovas V., 77
Karenauskaitė V., 87
Kasulaitytė L., 7
Katashev A., 25
Kepler J., 95
Kepler K., 19, 95
Kirsanova T., 25
Kišonas J., 51
Kulvietis V., 45, 51
Kurjane N., 137
Laurikaitienė J., 119, 133
Laurikaitis M., 130
Leice A., 142
Lukoševičiūtė S., 71
Mačiukaitienė S., 122
Malisan M. R., 87
Mattsson S., 18, 105
Matulionytė M., 67
Medvedevas N., 133
Meijer J. H., 87
Meškauskas A., 122
Mihov D., 87
Miller A., 7, 11
Minialga V., 116
Mironova – Ulmane N., 137
Mornstein V., 83, 87, 153
Nordstrom F., 14
Olsson M.L., 31
Pacukevich E., 25
Pašukonienė V., 71
Paulauskas R., 116
Pavlenko A., 137
Petrošiūtė S., 71
Pikaitė R., 119
Plukienė R., 150
Plukis A., 150
Poderys V., 62, 67
Polakovs M., 137
Pupkaitė V.,
Purviniene R., 71
Remeikis V., 150
Rokita E., 87
Rotomskis R., 39, 45, 59, 62, 67, 71, 77
Rožkov A., 157
Selskis A., 62
Shuvalova L., 25
Siversson C., 101
Skripka A., 59
Soderberg M., 18
Srivastava R., 35
Stankevič J., 147
Stašys K., 77
Styra D., 147
Svensson J., 101
Šniurevičiūtė M., 112
Tiderius C. J., 101
Tingberg A., 31
Tomberg T., 95
Urbonienė A., 109
Usovaitė A., 147
Valančiūnaitė J., 39, 59
Valius M., 77
Vano E., 87
Vilkas R., 130
Vladimirov A., 19
Vlk D., 83, 153
de Wagter C., 35
Wasilewska – Radwanska M., 87
Weckstrom E., 87
Wettersted AF S., 14
Wucherer M., 87
Zvagule T., 137

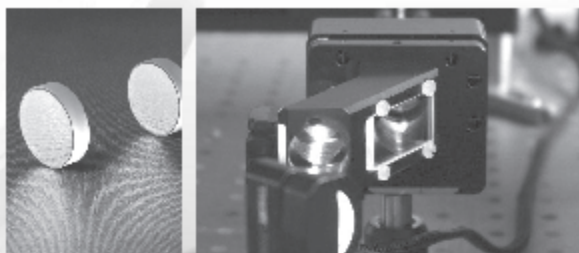
CONTENT

CONFERENCE & WORKSHOP PROGRAM	3
A. Miller, L. Kasulaitytė. IMRT FOR CRANIOSPINAL IRRADIATION: CHALLENGES AND RESULTS	7
E. Jakubovskij, R. Griškevičius, A. Miller. IMRT COMMISSIONING: BALTIC INSTITUTIONS PLANNING AND DOSIMETRY COMPARISONS	11
Fredrik Nordström, Sacha AF Wettersted, Sven ÅJ Bäck. QUALITY ASSURANCE METHODS IN RADIOTHERAPY	14
Sören Mattsson, Marcus Söderberg. PATIENT DOSE MANAGEMENT IN CT, SPECT/CT AND PET/CT IMAGING	18
Anatoli Vladimirov, Kalle Kepler. ANALYSIS OF AEC CALIBRATION METHODS FOR COMPUTED RADIOGRAPHY BY ESTIMATING TCDD AT DIFFERENT TUBE POTENTIALS	24
Lada Bumbure, Yuri Dekhtyar, Alexey Katashev, Tatyana Kirsanova, Ella Pacukevich, Lubova Shuvalova. DIGITAL QA METHOD'S CALIBRATION IN DIGITAL RADIOGRAPHY	30
Hanna Holstein, Anders Tingberg, Marie-Louise Olsson. OPTIMIZATION OF IMAGE QUALITY AND DETERMINATION OF EFFECTIVE DOSE TO ASSISTING PERSONS IN VETERINARY RADIOLOGY	34
Raju Srivastava, Sofie Gillis, Carlos de Wagter. RADIOGRAPHIC FILM: STILL A VIABLE DOSIMETER? ..	38
Jurga Valančiūnaitė, Ričardas Rotomskis. QUANTUM DOTS AS ENERGY DONORS FOR PHOTOSENSITIZERS: PERSPECTIVES FOR PHOTODYNAMIC THERAPY OF CANCER	44
Vytautas Kulvietis, Ričardas Rotomskis. ACCUMULATION OF QUANTUM DOTS IN EHRlich ASCITES TUMOURS IN MICE	50
Juras Kišonas, Vytautas Kulvietis. SPECTROSCOPIC STUDY OF QUANTUM DOTS DISTRIBUTION IN VIVO	54
Artiom Skripka, Jurga Valančiūnaitė, Ričardas Rotomskis. SPECTRAL STUDY OF THE FORMATION OF QUANTUM DOTS AND CHLORIN E6 COMPLEX IN THE PRESENCE OF PROTEIN	59
Vilius Poderys, Algirdas Selskis, Adelina Ilie, Ričardas Rotomskis. RING LIKE TPPS₄ J-AGGREGATE STRUCTURE	62
Matulionytė Marija, Vilius Poderys, Ričardas Rotomskis. INFLUENCE OF SURFACE COATING ON CDTE QUANTUM DOTS STABILITY AND INTERACTION WITH BOVINE SERUM ALBUMIN	67
Simona Petrošiūtė, Rasa Purvinienė, Vita Pašukonienė, Simona Lukoševičiūtė, Petras Juzėnas, Ričardas Rotomskis. CHARACTERIZATION OF CANCER STEM CELLS AND THEIR RESPONSE TO CDTE QUANTUM DOTS	71
Karolis Stašys, Vitalijus Karabanovas, Ričardas Rotomskis, Mindaugas Valius. SURFACE MODIFICATION OF (CDSE)ZNS QUANTUM DOTS USING THIOLS – CHARACTERIZATION, PHOTOPHYSICAL AND BIOLOGICAL STUDIES	77
Carmel. J. Caruana. EUROPEAN COMMISSION PROJECT 'GUIDELINES ON MPE': PROPOSED QUALIFICATION AND CURRICULUM FRAMEWORKS	82
Daniel Vlk, Vojtěch Mornstein, Carmel. J. Caruana. MEDICAL PHYSICS AND BIOMEDICAL ENGINEERING AT THE FACULTY OF MEDICINE, MASARYK UNIVERSITY, BRNO	86
C.J. Caruana, M. Wasilewska-Radwanska, A. Aurengo, P.P. Dendy, V. Karenauskaite, M.R. Malisan, J.H. Meijer, D. Mihov, V. Mornstein, E. Rokita, E. Vano, M. Weckstrom, M. Wucherer. EFOMP PROJECT 'BIOMEDICAL	

PHYSICS EDUCATION FOR THE MEDICAL/HEALTH CARE PROFESSIONS' – AN UPDATE FOR MEDPHYS2010	90
Joosep Kepler, Kalle Kepler, Tiiu Tomberg, Pilvi Ilves. UNCERTAINTY IN FUNCTIONAL MAGNETIC RESONANCE IMAGING METHODS FOR CORTEX MOTOR AND LANGUAGE AREA EXAMINATIONS	95
Carl Siverson, Carl-Johan Tiderius, Leif Dahlberg, Jonas Svensson. EARLY DIAGNOSIS OF OSTEOARTHRITIS USING CONTRAST ENHANCED 3-DIMENSIONAL MRI	101
Therese Geber, Mikael Gunnarsson, Sören Mattsson. DOSIMETRY FOR THE LENS OF THE EYE, APPLICATIONS FOR MEDICAL STAFF INVOLVED IN INTERVENTIONAL RADIOLOGY PROCEDURES	105
Aušra Urbonienė, Birutė Gričienė. EXTREMITY AND EYE LENS DOSES OF THE INTERVENTIONAL RADIOLOGY AND RADIOLOGY WORKERS	109
Karolis Jakštas, Miglė Šniurevičiūtė. DOSIMETRIC COMPARISON BETWEEN LINKED AND STRAND SEEDS FOR I-125 PERMANENT SEED PROSTATE BRACHYTHERAPY	112
Virgilijus Minialga, Rolandas Paulauskas. HEAT DISSIPATION INVESTIGATION BY THERMOVISION ...	116
Rita Pikaitė, Jurgita Laurikaitienė, Diana Adlienė. PATIENTS' DOSE ASSESSMENT IN DIGITAL DIAGNOSTIC RADIOGRAPHY	119
Algimantas Meškauskas, Gediminas Adlys, Simona Mačiulaitienė. RADIATION IMPACT ON POLYMER STRUCTURES	122
Gediminas Adlys. PHYSICAL ASPECTS OF NEUTRON GENERATION IN MEDICAL ACCELERATORS	126
R. Vilkas, M. Laurikaitis, D. Adlienė, V. Andrijaitienė. IMPLEMENTATION OF THE PATIENT PLAN CHECKING IN RADIOTHERAPY	130
Nikolajus Medvedevas, Diana Adlienė, Jurgita Laurikaitienė. DISTRIBUTION OF SCATTERED RADIATION IN SUPERFICIAL X-RAY THERAPY	133
Maksims Polakovs, Nina Mironova-Ulmane, Andrejs Pavlenko, Tija Zvagule, Natalija Kurjane, Natalija Gabrusheva. THE INVESTIGATION OF CHERNOBYL CLEAN - UP WORKERS BLOOD BY EPR TECHNIQUE	137
Alevtina Leice, Yuri Dekhtyar, Natalya Britzina. BEHAVIOUR OF BLOOD CELLS BEING IN CONTACT WITH HYDROXYAPATITE-COATED TITANIUM PLATE WITHIN AN HOUR	142
Dmitrijus Styra, Ana Usovaitė, Jelena Stankevič. DATA PROCESSING FOR CONNECTION BETWEEN HARD COSMIC RAY FLUX VARIATIONS AND HUMAN HEALTH DISORDER ANALYZING	147
Rita Plukienė, Artūras Plukis, Laurynas Juodis, Vidmantas Remeikis. THE RADIATION SAFETY OF EDUCATIONAL NEUTRON LABORATORY	150
Vojtěch Mornstein, Daniel Vlk, Carmel. J. Caruana. TEACHING OF MEDICAL PHYSICS TO MEDICAL, DENTAL, HEALTH CARE AND BIOMEDICAL ENGINEERING STUDENTS IN THE CZECH REPUBLIC	153
Andrej Rožkov, Ruslan Jerenkevič, Vadim Česonis. METHOD OF THE RADIONUCLIDE ACTIVITY DETERMINATION IN NUCLEAR MEDICINE SOURCES OF COMPLEX GEOMETRIES	157
AUTHOR INDEX	159

ALTECHNA

UAB „Altechna“ – Lietuvos lazerinių technologijų įmonė, nuo 1996 m. dirbanti fotonikos ir laboratorinių tyrimų srityse. Mes siūlome platų optikos produktų pasirinkimą ir lazerinių technologijų pritaikymą moksle ir pramonėje.



PAGRINDINĖS ALTECHNA VEIKLOS:

- Lazerinių technologijų komponentų prekyba
- Diodais kaupinami kieto kūno lazeriai
- Mikrofabrikavimas femtosekundiniu lazeriu
- Inovaciniai sprendimai mokslo ir pramonės atstovams
- Optomechaninių įrenginių dizainas

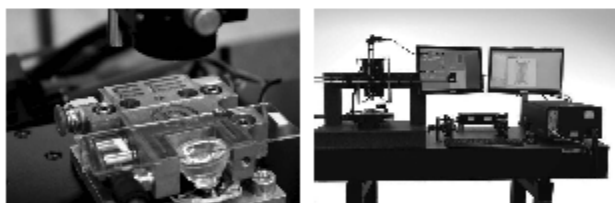
ALTECHNA PRODUKTAI:

- Lazerinė optika
- Kristalai
- Lazerinė įranga
- Lazeriai
- Mikrofabrikavimo sistemos

Altechna bendradarbiauja ir teikia produktus mokslinėms įstaigoms bei lazerinėms kompanijoms daugiau nei 40-yje pasaulio valstybių. Tarp kurių Europos Sąjungos šalys, JAV, Japonija, Kanada, Indija, Brazilija, Australija ir kitos.

Glaudus bendradarbiavimas su tarptautiniais verslo partneriais įgalina įmonę teikti individualius bei kokybiškus aukštųjų technologijų sprendimus.

Altechna taip pat aktyviai dalyvauja nacionaliniuose projektuose ir teikia profesionalią pagalbą renkantis įrangą laboratorijoms.



MES ATSTOVAUJAME:



ANDOR TECHNOLOGY
www.andor.com



OCEAN OPTICS
www.oceanoptics.com



AEROTECH
www.aerotech.com

SHEAUMANN

SHEAUMANN
www.sheumann.com

semrock

SEMROCK
www.semrock.com

PI

PHYSIK INSTRUMENTE
www.pi.ws